

Efficient first-principles modeling of complex molecular crystals at sub-chemical accuracy

Benjamin X. Shi,¹ Kristina M. Herman,^{2, a} Flaviano Della Pia,³ Venkat Kapil,^{4, 5} Andrea Zen,^{6, 7} Péter R. Nagy,^{8, 9, 10} Sotiris Xantheas,^{2, 11, 12, *} and Angelos Michaelides^{3, *}

¹*Initiative for Computational Catalysis, Flatiron Institute,
160 5th Avenue, New York, NY 10010*

²*Department of Chemistry, University of Washington,
Seattle, Washington 98195, United States*

³*Yusuf Hamied Department of Chemistry,
University of Cambridge, Lensfield Road,
Cambridge CB2 1EW, United Kingdom*

⁴*Department of Physics and Astronomy, University College London,
7-19 Gordon St, London WC1H 0AH, UK*

⁵*Thomas Young Centre and London Centre for
Nanotechnology, 9 Gordon St, London WC1H 0AH*

⁶*Dipartimento di Fisica Ettore Pancini, Università di Napoli Federico II,
Monte S. Angelo, I-80126 Napoli, Italy*

⁷*Department of Earth Sciences, University College London,
Gower Street, London WC1E 6BT, United Kingdom*

⁸*Department of Physical Chemistry and Materials Science,
Faculty of Chemical Technology and Biotechnology,
Budapest University of Technology and Economics,
Műegyetem rkp. 3., H-1111 Budapest, Hungary*

⁹*HUN-REN-BME Quantum Chemistry Research Group,
Műegyetem rkp. 3., H-1111 Budapest, Hungary*

¹⁰*MTA-BME Lendület Quantum Chemistry Research Group,
Műegyetem rkp. 3., H-1111 Budapest, Hungary*

¹¹*Advanced Computing, Mathematics and Data Division,
Pacific Northwest National Laboratory, 902 Battelle Boulevard,
MS J7-10, Richland, Washington 99352, United States*

¹²*Computational and Theoretical Chemistry Institute (CTCI),*

*Pacific Northwest National Laboratory,
Richland, Washington 99352, United States*

(Dated: March 3, 2026)

Abstract

Molecules can form myriad crystalline polymorphs, each with distinct properties affecting their performance across diverse applications, from pharmaceuticals to functional materials and more. Predicting the thermodynamically most stable polymorph from first principles remains a formidable challenge. It requires methods that scale to large, technologically-relevant molecules while achieving very high accuracy (below 1 kJ/mol) on relative lattice energies. Such accuracy, often termed sub-chemical accuracy, is generally beyond the reach of the workhorse density functional theory (DFT). In this work, we introduce a framework, combining advances in correlated wavefunction theory (cWFT) and the many-body expansion, to deliver accurate, cost-effective predictions of complex molecular crystals. For 23 organic molecules and 13 ice polymorphs, we predict crystal lattice energies to within experimental uncertainties at costs comparable to hybrid DFT, while being several orders of magnitude more efficient than previous cWFT approaches. We extend this approach to a set of large, drug-like molecules including axitinib and ROY, previously inaccessible to cWFT and where DFT is insufficient, achieving sub-chemical accuracy on the relative energies between challenging polymorphs. With the reference data generated throughout this work, we have been able to further parametrize a DFT functional with unprecedented accuracy aligning with our predictions. This cWFT framework as well as DFT functional are made openly available, providing new ranking tools to facilitate efficient high-throughput screening of molecular crystal polymorphs.

INTRODUCTION

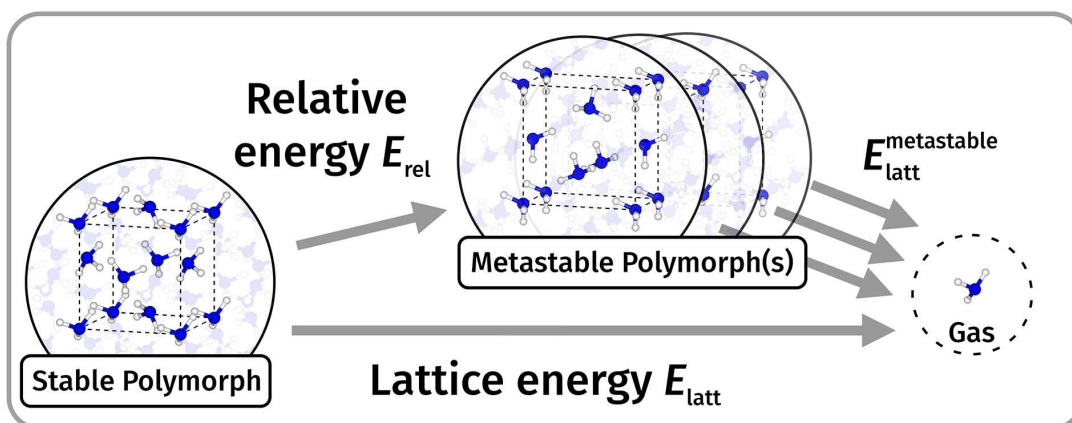
The constituent molecules in a molecular crystal can adopt numerous possible crystallographic arrangements [1, 2], with each polymorph characterized by distinct properties. This diversity offers exciting opportunities to design molecular crystals tailored for its widespread applications across pharmaceuticals [3, 4], agrochemicals [5], gas storage materials [6], functional devices [7, 8], and the food industry. More fundamentally, molecular crystals underpin many natural phenomena, from biological sugars such as glucose and sucrose [9] to heat and mass transport in high-pressure planetary ices [10, 11]. Mapping the relative stability of these polymorphs [12] and identifying the thermodynamically most stable form is essential towards these applications. However, experimental determination is often hindered by inaccessible thermodynamic conditions or high synthesis costs. Consequently, substantial effort has focused on addressing this

challenge through computational modeling, giving rise to the field of organic crystal structure prediction [13–15].

Predicting polymorph stability from first principles remains a longstanding challenge [16]. The key computational quantities (Figure 1), within a zeroth-order approximation [17] neglecting thermal [18] and quantum nuclear effects [19], are the lattice (E_{latt}) and relative (E_{rel}) energies. The former compares the energy per molecule of a crystalline polymorph to the gas phase, $E_{\text{latt}} = E^{\text{crys}} - E^{\text{gas}}$, while the latter compares the energy between two polymorphs (e.g., A and B), $E_{\text{rel}} = E^{\text{crys,A}} - E^{\text{crys,B}}$. The value of E_{rel} is often less than 2 kJ/mol, observed within more than half of previously examined polymorph pairs [20]. Thus, reliably distinguishing polymorph stability requires methods that achieve sub-chemical accuracy [21] (1 kJ/mol). In addition to this exceptionally stringent accuracy, such a method must also scale efficiently to large, complex molecular crystals of technological importance. While challenging, if these demands can be met, the resulting methods will offer major technological, economic, and public health benefits [22, 23]. Beyond enabling materials discovery and exploration of experimentally inaccessible phases [24], such methods can also be used to de-risk [25] existing applications, especially pharmaceuticals, where late-emerging stable polymorphs (notably rotigotine) have led to costly recalls [23, 26].

Density functional theory (DFT) has become the primary tool for modeling molecular crystals [27]. Recently, its scope has been greatly expanded by machine-learning interatomic potentials (MLIPs) that aim to reproduce its accuracy at a fraction of the cost [28, 29]. The development of advanced dispersion corrections now allow DFT to attain chemical accuracy for a relatively wide range of properties [30–33] (4 kJ/mol). However, achieving sub-chemical accuracy across broad sets of molecular crystals remains difficult. Results can vary significantly [34] with the choice of density functional approximation (DFA) to the exchange-correlation functional [35] and dispersion correction [36]. Notably, systems prone to delocalization error [37] pose challenges for DFT, such as ionic co-crystals [38], flexible molecular crystals [39, 40] and tautomeric polymorphs [41]. These challenges are exemplified by the prototypical ROY molecule - named for its red, orange, and yellow polymorphs [42–44] - with DFT consistently overstabilizing the red forms over stable yellow ones [16, 45, 46]. Developing methods that overcome these limitations of DFT represents a major frontier in computational modeling [47].

Methods from correlated wavefunction theory (cWFT), notably coupled cluster with single, double and perturbative triple excitations [48] [CCSD(T)] and quantum diffusion Monte Carlo [49] (DMC), can achieve sub-chemical accuracy on molecular crystal predictions. Both methods have



$$E_{\text{latt}} = E_{\text{latt}}^{\text{HF}} + \left[E_{\text{latt}}^{\text{CCSD(T)}} - E_{\text{latt}}^{\text{HF}} \right]$$

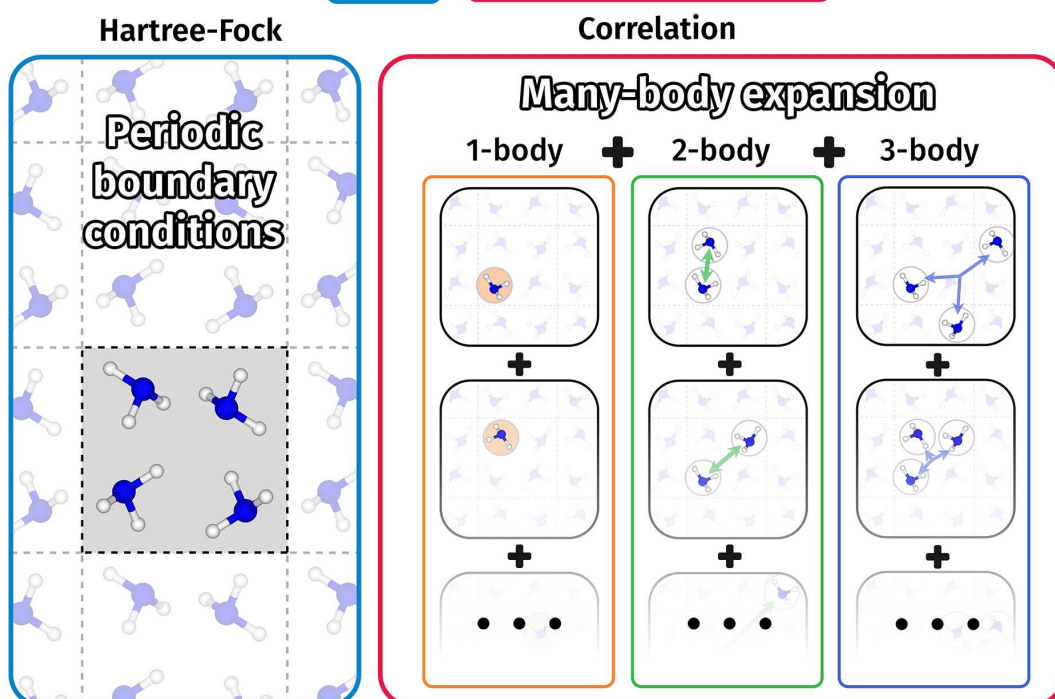


Figure 1: Reliable and efficient procedure for molecular crystal energetics. We employ a divide-and-conquer approach to reach ‘gold-standard’ CCSD(T) estimates of the lattice E_{latt} and relative E_{rel} energies (shown schematically in the top panel and defined in the Methods). As a post-Hartree-Fock (HF) method, the CCSD(T) E_{latt} is composed of a (mean-field) HF and an (electron-electron) correlation contribution. We treat HF under periodic boundary conditions (PBC) while the correlation energy is treated with the many-body expansion (MBE). This division provides a natural description for each component, allowing us to leverage new developments in solid-state modeling under PBCs together with molecular quantum chemistry for the MBE.

been shown to agree with experimental E_{latt} measurements for several organic molecules [50–53] and polymorphs of ice [54, 55]. However, their computational cost has limited these methods to small systems, where we show in this work that a single polymorph treated with DMC can require hundreds of thousands of CPU core-hours. This cost is comparable to a full DFT search over thousands of polymorphs for a large molecule [56]. Conventional CCSD(T) features a steeper computational scaling than DMC and is typically applied to crystals through a many-body expansion (MBE)[57]. Here, the total energy of the full periodic system is decomposed into many smaller calculations of monomer (one-), dimer (two-), trimer (three-) and higher-body contributions. Although this expansion is exact when all body-order terms are included, its practicality comes from the fact that high-order (beyond tetramer) and long-range contributions (i.e., dimers or trimers that are far apart) can be neglected or approximated with cheaper methods. Nonetheless, attaining sub-chemical accuracy in the MBE remains challenging, requiring *tour-de-force* efforts only achievable for model systems such as benzene [21, 58, 59]. In fact, recent studies [60, 61] show that dimers of moderate-sized molecules like anthracene ($C_{14}H_{10}$) already exceed practical limits for conventional CCSD(T).

In this work, we introduce LNO-MBE-CCSD(T), a framework that combines recent methodological developments in CCSD(T) with modeling advances in the MBE to enable accurate and efficient treatment of molecular crystals. Notably, this framework extends CCSD(T) to the regime of large drug-like molecules that are more than two times the size of anthracene. We employ a divide-and-conquer approach (discussed in the Methods) that treats the Hartree-Fock (HF) contribution [to the CCSD(T) total energy] under periodic boundary conditions (PBCs) - made highly efficient by recent GPU implementations and sparsity-based algorithms [62] - and the remaining CCSD(T) correlation energy with the MBE. The main advance employed in this work is an improved local natural orbital (LNO) approximation for CCSD(T) [63, 64] that makes it practical to use within MBE calculations for large molecular crystals. As described in Supplementary Section 2D, our modifications to LNO-CCSD(T) prevent the accumulation of local-approximation errors from the numerous two- and three-body terms in the MBE, enabling reliable and affordable convergence. In addition, we show that the number of MBE calculations can be greatly reduced by combining new formulations that exploit translational symmetry [65] with machine-learning descriptors [66] to eliminate all redundant terms. Together, the resulting LNO-MBE-CCSD(T) framework can make E_{latt} predictions at orders of magnitude lower cost than DMC, comparable to hybrid DFT with PBCs.

We apply LNO-MBE-CCSD(T) to study an unprecedented set of molecular crystals to high accuracy. We predict E_{latt} for 23 molecular crystals and 13 ice phases to an accuracy that surpasses experimental uncertainties. Furthermore, we demonstrate agreement with experiments on E_{rel} to sub-chemical accuracy for competing polymorphs of ROY ($\text{C}_{12}\text{H}_9\text{N}_3\text{O}_2\text{S}$), axitinib ($\text{C}_{22}\text{H}_{18}\text{N}_4\text{OS}$) and rotigotine ($\text{C}_{19}\text{H}_{25}\text{NOS}$), with the latter two being currently marketed pharmaceuticals. Using the reference-quality datasets generated here, we benchmark and parametrize a new functional, B86bPBE50-revXDM, that outperforms existing DFAs, and use it to train cost-efficient MLIPs to capture thermal and nuclear quantum effects missing from static E_{latt} and E_{rel} estimates. As a final outlook, this work delivers an efficient toolkit - all freely available and well-documented (see Methods) - for high-throughput screening and ranking of molecular crystal polymorphs, ranging from high-accuracy LNO-MBE-CCSD(T) for final-stage refinement to a cost-effective B86bPBE50-revXDM functional suitable for intermediate stages.

RESULTS AND DISCUSSION

Agreement with experiments across diverse datasets

We first assess LNO-MBE-CCSD(T) at predicting E_{latt} for the X23 dataset of small organic molecular crystals. This dataset has been a fundamental benchmark for new methods, whether semi-empirical [67, 68], DFT [33, 69] or machine-learning [34, 70] based. As shown in Figure 2, X23 consists of 23 systems spanning a wide range of lattice energies (-25 to -170 kJ/mol) from weak dispersion to strong hydrogen-bonding. They are well-characterized by experimental [50–52] references, with LNO-MBE-CCSD(T) yielding mean absolute deviations (MADs) of 3.4 kJ/mol. As experimental uncertainties exceed 4 kJ/mol for 21 systems in the X23 dataset [53] (see Supplementary Section 4 A), we conclude that both LNO-MBE-CCSD(T) and recent DMC estimates [53] are accurate to within experimental uncertainty, with DMC also having a MAD of 3.4 kJ/mol relative to experiment. On the other hand, the differences between DMC and LNO-MBE-CCSD(T) are below 2 kJ/mol for most systems (15 of 23), yielding a MAD of 3.1 kJ/mol relative to DMC. Consistent with recent observations on dimers [71, 72], CCSD(T) predicts slightly stronger binding for van der Waals systems and weaker binding for H-bonded systems. Anthracene and naphthalene are notable exceptions, where the source of their discrepancies remains presently debated [71, 73] and we show in Supplementary Section 4 D that higher-order

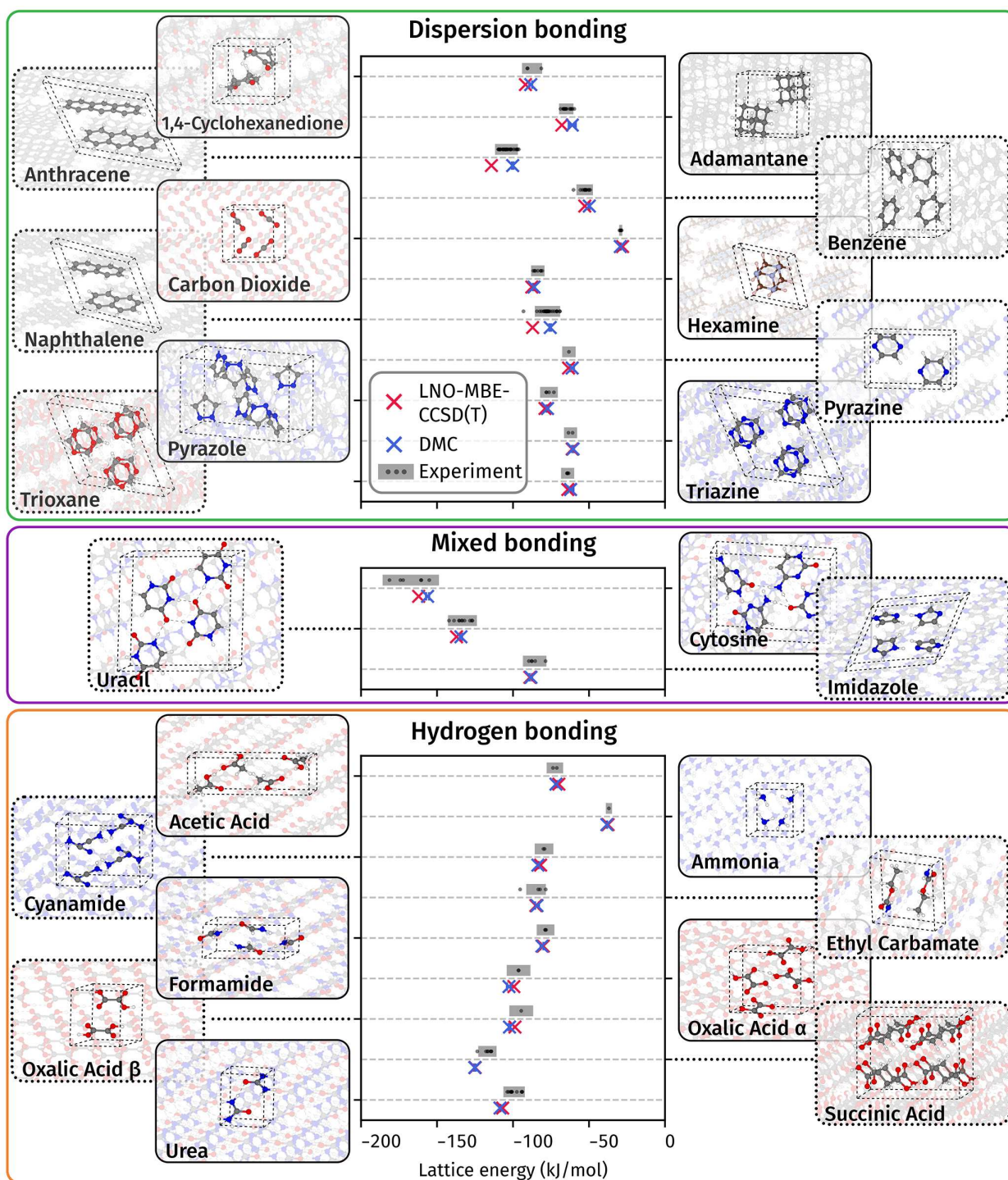


Figure 2: Agreement across diverse molecular crystals. Comparison of the lattice energy predicted by LNO-MBE-CCSD(T) against previous DMC estimates [53] as well as experimental measurements for the 23 organic molecular crystals in the X23 dataset. The full dataset is split into crystals held primarily by dispersion, hydrogen-bonding, or a mixture in the top, bottom and middle panels, respectively. The experimental sublimation enthalpies were converted to lattice energies using corrections computed with DFT-trained machine-learning interatomic potentials in Ref. 34 and expressed as a range based on the set of previous measurements (see Supplementary Section 4 A).

correlation effects beyond CCSD(T) [74] may not be negligible.

We briefly highlight the capabilities enabled by our methodological developments introduced in the Methods. The systems from the X23 dataset have been the focus of numerous MBE-based studies, summarized and compared in Supplementary Section 4 F. The high-cost of going beyond DFT [to CCSD(T)] has typically limited these studies to only subsets of the X23. In addition, multilevel approaches are often required, where CCSD(T) is applied only to two-body terms (sometimes to short cutoff distances) while using lower-level methods for higher-body terms. Examples include the random phase approximation (RPA) [61], second-order Møller-Plesset perturbation theory (MP2) [30, 75], HF [76], DFT [77] or force fields [78, 79]. These neglected terms can introduce uncontrolled errors which can be significant [75, 80] (exceeding 4 kJ/mol on E_{latt}) in some cases. Our optimizations to the LNO approximation within this work enable all dimers to be treated accurately with LNO-CCSD(T), while also allowing three-body terms to be computed directly at the same level of theory. As a result, this study is the most comprehensive to date. It is the only work to apply (LNO-)CCSD(T) up to the trimers for the entire X23 dataset, needed for an accurate CCSD(T)-quality E_{latt} estimate, while ensuring a cost competitive with DFT (discussed later). In Supplementary Section 4 F, we have used LNO-MBE-CCSD(T) to benchmark the previous MBE estimates, showing that some multi-level approximations [61] can reach MADs as low as 2 kJ/mol.

We next examine 13 ice polymorphs (out of more than 20 polymorphs experimentally characterized to date) which comprise the ICE13 dataset [55] in Figure 3. These systems are challenging due to the small relative energy differences (<5 kJ/mol) and the need for large unit cells to capture hydrogen disorder [82, 83] present in several anti-ferroelectric polymorphs, including Ih, III, VI, VII, and XVII [84]. LNO-MBE-CCSD(T) resolves these small energy differences, yielding an MAD of 0.5 kJ/mol on E_{latt} (and 0.6 kJ/mol on E_{rel} ; see Supplementary Section 6) relative to DMC for the ICE13 dataset, within experimental uncertainties where available [81]. This agreement surpasses that of any DFA [55], which can show deviations up to 10 kJ/mol. For hydrogen-disordered polymorphs in Figure 3, we move beyond the small ferroelectric unit cells (typically ≤ 12 water molecules) used in most high-level studies [55, 85, 86], toward experimentally observed anti-ferroelectric, hydrogen-disordered structures of medium (~ 16 molecules) and large (>80 molecules) sizes. The linear scaling of LNO-MBE-CCSD(T) enables efficient treatment of these larger systems while retaining high accuracy, owing to our optimizations that prevent error accumulation across the many three-body contributions. The importance of modeling hydrogen

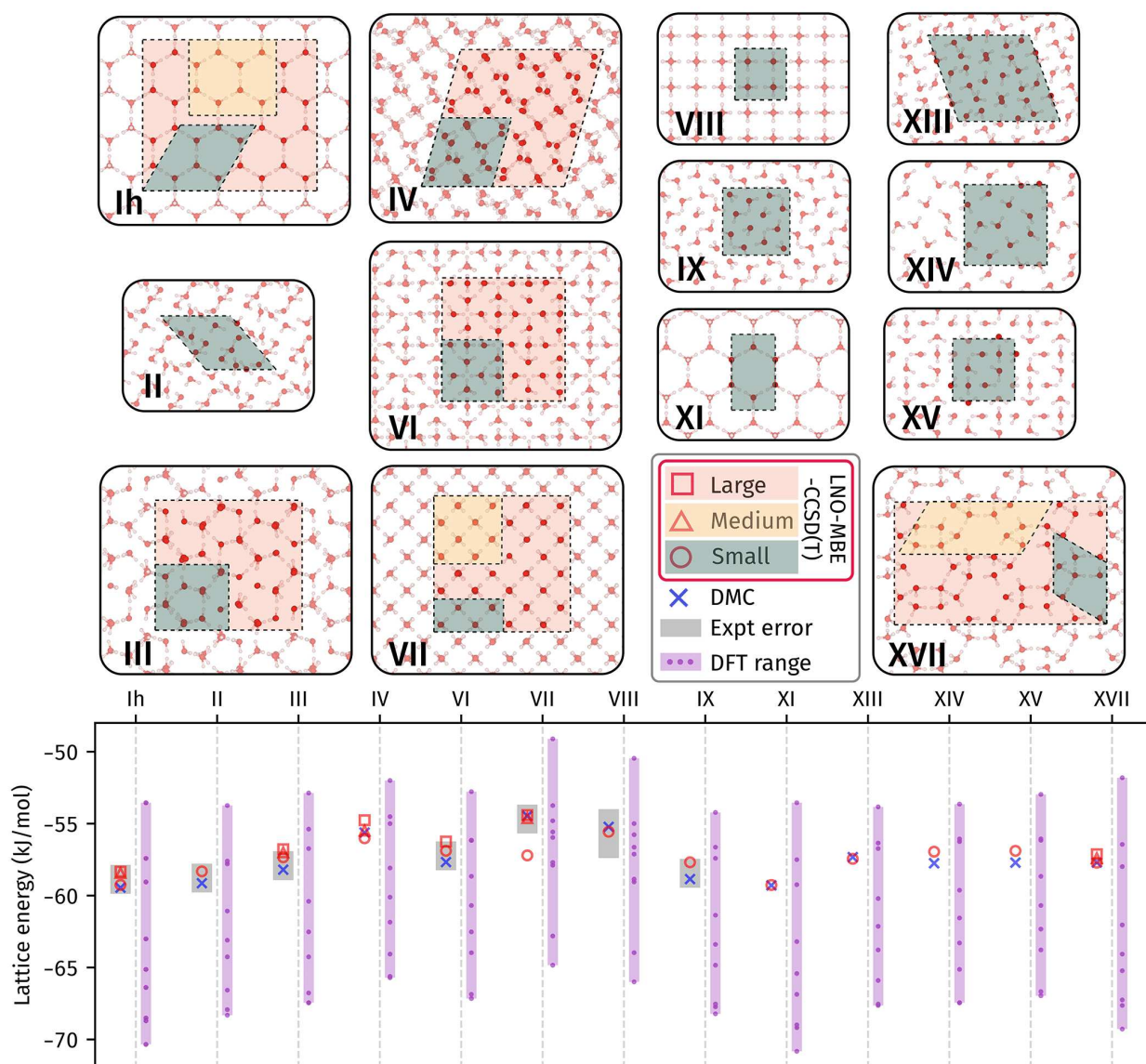


Figure 3: Agreement across 13 polymorphs of ice. Comparison of the lattice energy predicted by LNO-MBE-CCSD(T) against previous DMC estimates [55] and experiments [81] (when available) for the 13 ice polymorphs in the ICE13 dataset. The lattice energy for a range of widely-used density functional approximations [B3LYP-D4, revPBE0-D3, PBE0-MBD, SCAN+rVV10, optB86b-vdW, revvdW-DF2, vdW-DF, revPBE-D3, PBE-D3(BJ)] from Ref. 55 is illustrated in purple. We extend beyond standard small ferroelectric ordered cells (6–16 water molecules) to increasingly hydrogen-disordered antiferroelectric cells of medium (12–16 molecules) and large (>80 molecules) sizes.

disorder is evident for ice VII: the small unit cell yields poor agreement with experiment due to its large dipole moment (see Supplementary Section 1 A), whereas the medium and large cells - whose dipole moments are near zero - restore agreement.

Efficient benchmarks for lower-level theories

We now assess the computational cost of LNO-MBE-CCSD(T) on the X23 dataset. Developing methods that improve the accuracy-cost Pareto front is essential for high-throughput applications [27, 56, 87] such as materials screening and training machine-learning interatomic potentials. Figure 4a compares the cost of LNO-MBE-CCSD(T) with periodic DFT using GGAs and hybrid DFAs (i.e., functionals), as well as with DMC (tabulated in Supplementary Section 5). Remarkably, LNO-MBE-CCSD(T) is comparable in cost to periodic hybrid DFT. Specifically, using stringent (dubbed “high”) distance cutoffs (to converge 2B and 3B terms to within 0.5 kJ/mol each) leads to costs that are on average 4,762 CPU core hours (CPUh) compared to 2,412 for periodic hybrid DFT. It is two orders of magnitude lower than DMC, where $\sim 200,000$ CPUh is needed on average to achieve a 95% confidence interval of 1 kJ/mol on statistical uncertainties in the X23 dataset, reaching up to 700,000 CPUh for some systems.

As discussed in Supplementary Section 5, the cost of LNO-MBE-CCSD(T) can be lowered substantially by relaxing 2B and 3B distance cutoffs. We have defined “moderate” and “low” settings that yield MADs of 1.0 and 1.8 kJ/mol relative to the high setting, with average costs of 1,906 and 502 CPUh, respectively. Moreover, our method runs efficiently (and if needed massively parallel) on commodity hardware, requiring as little as 46 GB of memory and 8 CPU cores per calculation - significantly less than the demands of a recent periodic MP2 study [88] on the X23 dataset. We have not included the cost of periodic HF calculations within our analysis of CPU times as the HF part is greatly accelerated via new GPU implementations, discussed in Supplementary Section 4 B; this can also be used to accelerate periodic hybrid DFT.

The extensive reference data (from X23 and ICE13) computed within this work provide a reliable benchmark for lower-cost methods, like DFAs or MLIP foundation models [89], free from thermal, quantum nuclear and geometric errors. On the other hand, using experiments as benchmarks imposes fundamental limits on precision of the obtained MAD due to the wide range of values [53]. For example, experimental uncertainties exceed 4 kJ/mol for 21 systems within the X23 dataset (see Supplementary Section 4 A). Figure 4b compares commonly used DFAs

against our CCSD(T) references, ranging from PBE with various flavors of dispersion corrections to the B86bPBE-based GGA and hybrid functionals, along with trusted DFAs such as r^2 SCAN-D4 and PBE0-MBD. As in earlier studies [33], balancing performance across X23 and ICE13 is difficult for DFT. For example, while revPBE-D3 performs best for ICE13 (MAD = 0.5 kJ/mol), its performance is worse for X23 (4.2 kJ/mol). The good overall performance of PBE0-MBD [90] and B86bPBE25-XDM [33] on both sets is also notable.

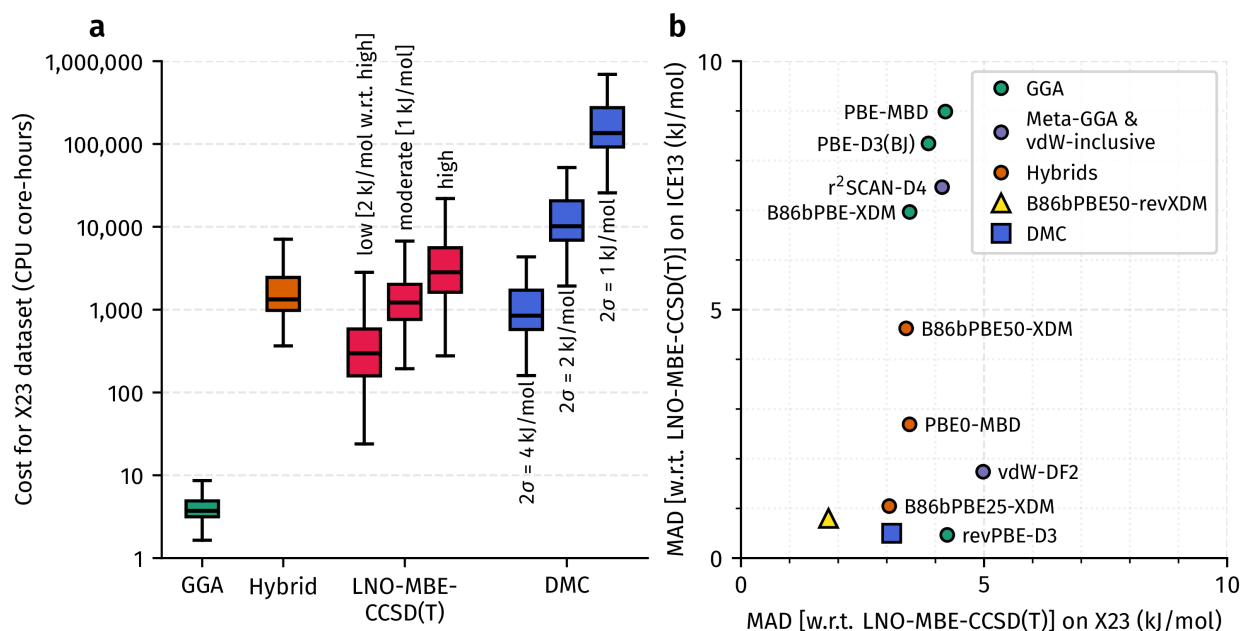


Figure 4: High accuracy benchmarks at affordable costs. **a** Comparison of the cost of LNO-MBE-CCSD(T) against periodic DFT, for both the generalized gradient approximation (GGA) and hybrids, as well as DMC. We report LNO-MBE-CCSD(T) results using low, moderate, and high settings defined by different two- and three-body cutoff distances, where the low and moderate settings have a mean absolute deviation (MAD) of 1 and 2 kJ/mol to the high settings, respectively. DMC costs are also reported for different levels of statistical sampling corresponding to 95% confidence intervals (2σ) of 1, 2, and 4 kJ/mol. The DMC costs neglect the costs to generate the trial wave-function and optimize the Jastrows while the CCSD(T) cost is only for the correlation energy. **b** We have computed the mean absolute deviation (MAD) to our LNO-MBE-CCSD(T) estimates for a wide set of density functional approximations to benchmark their performance on the ICE13 and X23 datasets. These benchmarks have been further used to reparameterize the XDM coefficients of the B86bPBE50 functional, yielding B86bPBE50-revXDM with unprecedented accuracy across both X23 and ICE13.

Until now, the lack of condensed phase references have meant that dispersion corrections are parametrized only to binding energies of gas-phase dimers [91] or trimers. Our LNO-MBE-CCSD(T) references here allow for optimization towards molecular crystal E_{latt} and in Supplementary Section 7, we have revised the XDM coefficients for B86bPBE50 to our X23 benchmarks. As shown in Figure 4, this new DFA, dubbed B86bPBE50-revXDM, reduces the MAD for X23 from 3.4 to 1.8 kJ/mol and on the out-of-training ICE13 set from 1.8 to 0.8 kJ/mol. Its high fraction (50%) of exact-exchange makes it more robust [92] towards treating delocalization error-prone systems, which we will discuss for ROY and axitinib in Figure 5. Furthermore, we have optimized these coefficients for the small, cost-effective ('lightdense') basis sets, allowing for the X23 dataset to be computed by this hybrid DFT within 10 CPUh on average - comparable to a GGA. These qualities of B86bPBE50-revXDM - enabled through optimization against the LNO-MBE-CCSD(T) references - makes the functional a robust and effective tool, e.g., for initial screening in high-throughput searches. In Supplementary Section 9, we show that B86bPBE50-revXDM can be integrated into recent MLIP frameworks [34], requiring ~ 900 small-cell geometries (under 40,000 CPUh) to train robust models for axitinib and ROY. These models capture the full thermodynamics of the polymorph pairs [31], including anharmonic and nuclear quantum effects via path-integral molecular dynamics. As a result, these contributions can be removed from experimental relative enthalpies (as we have done for ROY and axitinib in Figure 5), enabling direct comparison with 0 K estimates.

Resolving complex and challenging systems

We now show that the LNO-MBE-CCSD(T) framework can be used to predict E_{rel} for large drug-like molecules. Compared to E_{latt} , converging E_{rel} requires looser LNO-MBE-CCSD(T) parameters (demonstrated in Supplementary Section 3B) - including smaller basis sets, looser local thresholds, and shorter distance cutoffs in the MBE - enabling further cost reductions. The specific systems examined include competing polymorphs pairs of ROY [16] (R and Y) as well as axitinib [96, 97] (VI and XLI) and rotigotine [94] (I and II). While ROY represents a moderate-sized molecule with 27 atoms, axitinib and rotigotine represent large drug-like molecules with 46 and 47 atoms, respectively, and are currently marketed drugs used for treating cancer and Parkinson's disease, respectively. In Figure 5, we compare LNO-MBE-CCSD(T) E_{rel} predictions against experimental measurements (with thermal and vibrational contributions removed, as

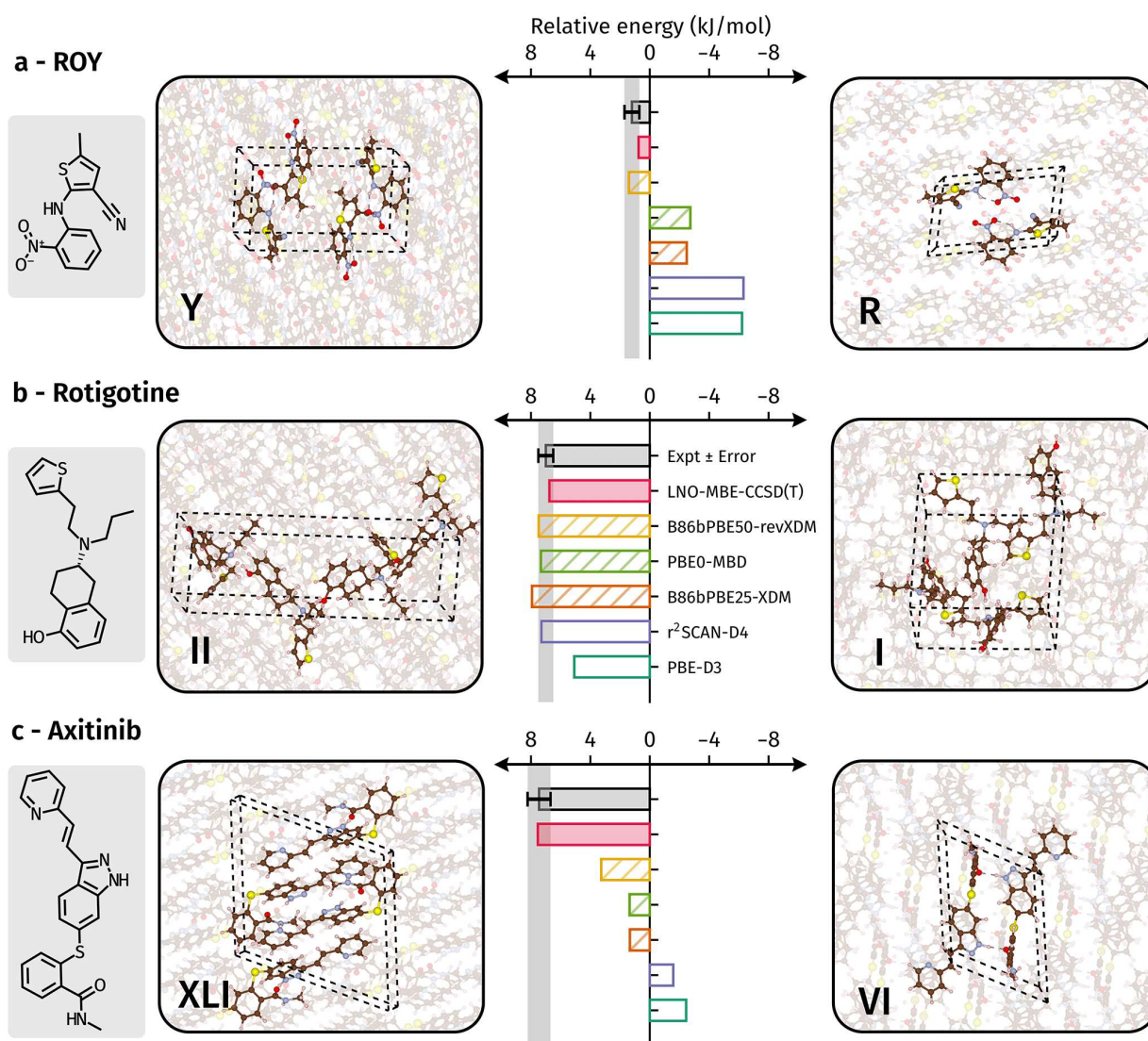


Figure 5: Sub-chemical accuracy on pharmaceutical-scale polymorph pairs. Comparison of the relative energy predicted by LNO-MBE-CCSD(T) against experiments (where the gray bar indicates uncertainties) for competing polymorphs of **a** ROY [93] (Y and R), **b** rotigotine [94] (II and I) and **c** axitinib [95] (XLI and VI). The experimentally observed form is given to the left, with a negative relative energy favoring its formation while a positive value favoring the (incorrect) metastable form. We also report the predictions for a set of commonly-employed density functional approximations and also the B86PBE50-revXDM parametrized in this work.

described in Supplementary Section 9). The values of E_{rel} range from 1.2 kJ/mol for the ROY polymorph pair up to ~ 8 kJ/mol for the axitinib and rotigotine polymorph pairs. In all cases, LNO-MBE-CCSD(T) reproduces these differences to within experimental uncertainty (all less

than 1 kJ/mol).

The level of agreement on E_{rel} achieved with LNO-MBE-CCSD(T) is not trivial, with the polymorphs of ROY and axitinib representing long-standing challenges for DFT [98]. Both systems feature conformations with varying π conjugation, with DFT tending to overstabilize planar conformations due to delocalization error [37, 99]. Figure 5 illustrates this challenge across widely used functionals/DFAs for the competing polymorph pairs of these two systems. We include representative DFAs from the generalized gradient approximation (GGA), given by PBE-D3(BJ) and r^2 SCAN-D4, to hybrids (B86bPBE25-XDM and PBE0-MBD), with a more comprehensive list tabulated in Supplementary Section 8 D. The GGAs predict incorrect polymorphs for both systems, with errors exceeding 7 kJ/mol on the E_{rel} , and while hybrids reduce these errors, they still deviate by more than 3 kJ/mol from experimental and LNO-MBE-CCSD(T) values. Here, the higher exact exchange in B86bPBE50-revXDM allow for the correct polymorph to be predicted in all cases, albeit with remaining quantitative errors on E_{rel} . Similarly, quantitative agreement to experiment cannot be achieved by lower-level cWFT methods such as MP2 and CCSD (see Supplementary Sections 4 C, 6 A, and 8 C) nor more approximate MBE-based methods which only correct up to CCSD(T) for one-body contributions [97, 98].

CONCLUSION

To conclude, we have introduced the LNO-MBE-CCSD(T) framework within this work, delivering sub-chemical accuracy on relative energies for molecular crystals at costs competitive with periodic hybrid DFT and two orders of magnitude lower than other high-level methods. For 23 organic molecular crystals and 13 ice polymorphs, comprising the X23 and ICE13 datasets, respectively, we reproduce lattice energies to within the uncertainties of experiments. Its low cost significantly expands the scope and complexity of systems that can now be tackled with high accuracy, enabling sub-chemical-accuracy predictions on the relative energies of drug-like molecules such as ROY (forms R and Y), axitinib (forms VI and XLI), and rotigotine (forms I and II). The first two systems challenge existing density functional approximations [16, 98], with agreement to experimental relative energies achieved only by LNO-MBE-CCSD(T).

Our ability to address technologically relevant molecular crystals with the LNO-MBE-CCSD(T) framework builds on a combination of advances developed over the past decade, both within our groups and by others. This represents a natural progression from a landmark study [21] in 2014,

which achieved sub-chemical accuracy for the lattice energy of benzene using advances from the preceding decade. Since then, efficient linear-scaling local approximations [63, 100, 101] have significantly expanded the range of accessible systems. However, their application within the MBE has been limited by the accumulation of small errors across many-body terms, an issue we address here. We also significantly decrease the large number of MBE calculations by combining a recently developed formulation exploiting translational-symmetry [65] with machine-learning descriptors [102, 103]. Finally, we reduce MBE distance cutoffs, leading to a further reduction of calculations, through subtractive embedding with modern dispersion corrections [104] fitted to CCSD(T) data.

The relatively low computational cost of the LNO-MBE-CCSD(T) framework - requiring only tens of thousands of CPU core-hours for drug-like molecular crystals - makes it well suited for high-throughput workflows such as crystal structure prediction (CSP) and computational benchmarking [105, 106]. The systems studied here, including rotigotine and axitinib, are comparable to those from the latest CSP Blind Test [56], where some DFT-based protocols required millions of CPU hours to screen thousands of polymorphs. We anticipate that LNO-MBE-CCSD(T) can be an economical choice for studying a final shortlist of candidate structures. Moreover, the B86bPBE50-revXDM functional parametrized from our LNO-MBE-CCSD(T) data can be used to replace existing functionals within the initial stages to filter generated polymorphs [107–109]. It achieves unprecedented accuracy on molecular crystals for a DFA, while reliably predicting the qualitative ordering of difficult systems such as ROY and axitinib. Together, we anticipate that these advances will enable reliable and practical identification of late-emerging stable polymorphs, as exemplified by rotigotine and axitinib. In the case of rotigotine, a new polymorph discovered decades after clinical use led to mass recalls with major economic and public-health consequences [110], while a late-emerging polymorph similarly delayed the development of axitinib [95].

To support its broad use in molecular crystal modeling, the LNO-MBE-CCSD(T) framework will be released as an open-source GitHub package upon publication. It will include worked examples from this study, enabling immediate adoption by users. More broadly, these tools are expected to facilitate applications beyond organic molecular crystals to a wide range of systems in computational chemistry and materials science, including inorganic materials. With routine CCSD(T) static calculations becoming feasible with LNO-MBE-CCSD(T), the next frontier is to develop CCSD(T)-level machine-learning interatomic potentials that capture finite-temperature [111] and

anharmonic effects, to understand thermodynamic stability [17, 112, 113] as a function of pressure and temperature.

ACKNOWLEDGEMENTS

The Flatiron Institute is a division of the Simons Foundation. A.M. and B.X.S. acknowledges support from the European Union under the “n-AQUA” European Research Council project (Grant No. 101071937). P.R.N. acknowledges support from ERC Starting Grant No. 101076972, “aCCuracy”, the National Research, Development, and Innovation Office (NKFIH, Grant No. FK142489), and the János Bolyai Research Scholarship of the Hungarian Academy of Sciences. A.Z. acknowledges support from the European Union under the Next Generation EU (Project Nos. 20222FXZ33 and P2022MC742). K.M.H. and S.S.X. acknowledge support from the Center for Scalable Predictive Methods for Excitations and Correlated Phenomena (SPEC), which is funded by the U.S. Department of Energy (DOE), Office of Science, Basic Energy Sciences (BES), Chemical Sciences, Geosciences, and Biosciences Division (CSGB), as part of the Computational Chemical Sciences (CCS) program under FWP 70942 at Pacific Northwest National Laboratory (PNNL), a multi-program national laboratory operated for DOE by Battelle. The authors are grateful for resources provided by the Cirrus UK National Tier-2 HPC Service at EPCC (<http://www.cirrus.ac.uk>) funded by the University of Edinburgh and EPSRC (EP/P020267/1) and computational support from the UK national high performance computing service, ARCHER 2, as obtained via the UKCP consortium and funded by EPSRC grant ref EP/P022561/1 We also acknowledge the EuroHPC Joint Undertaking for awarding this project access to the EuroHPC supercomputer LEONARDO, hosted by CINECA (Italy) and the LEONARDO consortium through an EuroHPC Regular Access call. This research also used resources of the National Energy Research Scientific Computing Center, which is supported by the Office of Science of the U.S. Department of Energy under Contract No. DE-AC02-05CH11231.

COMPETING INTERESTS STATEMENT

The authors declare no competing interests.

METHODS

The divide-and-conquer approach

We employ a divide-and-conquer approach to reach a CCSD(T)-level of accuracy in an efficient manner. As a post-Hartree-Fock (HF) method, CCSD(T) builds on the HF approximation to the Schrödinger equation by incorporating electron-electron interactions neglected in the mean-field treatment of HF. The resulting total CCSD(T) energy consists of the HF and (electron) correlation energy: the former (qualitatively) captures electrostatic, exchange, and induction effects, while the latter accounts for van der Waals dispersion, charge transfer and other correlation effects. It is known that HF leads to slow and erratic convergence with cutoff distance in the MBE [114, 115] (see Supplementary Section 2 A), necessitating higher body orders (up to five molecules). In contrast, the correlation energy converges smoothly within the MBE, requiring only up to three-body terms and shorter cutoff distances, even for the challenging high-pressure ice VIII phase. Given these considerations, we treat HF under periodic boundary conditions (PBC) while only the correlation energy is treated with the MBE. This division further allows us to leverage methodological advances from the past decade to enhance these methods.

In (periodic) solid-state electronic structure modeling, major progress has been achieved in reducing the costs of calculations with hybrid DFAs. Here, the HF-like exchange term dominates, where most development has been focused on. Specifically, these developments include GPU implementations [116, 117] and efficient sparsity-based [118] or low-rank decomposition methods such as the adaptively compressed exchange (ACE) operator [62], included in multiple popular solid state DFT packages [117]. These advances can be readily utilized in periodic HF calculations, enabling accurate computation of large molecular crystals within tens of GPU hours, as shown in Supplementary Section 4 B.

For CCSD(T), local correlation approximations [63, 100, 101, 119–121] pioneered within the molecular quantum chemistry community have greatly expanded the size of molecules that are now accessible [64]. For example, the local natural orbital (LNO)[63, 121] approximation used in this work has been used to evaluate the binding energy of a protein-ligand complex of 1023 atoms [63, 64] However, the application of local CCSD(T) to the MBE was limited previously by the accumulation of individually small errors due to the large number of three-body terms. As described in Supplementary Section 2 D, we have optimized the LNO approximation for the

MBE, eliminating this error accumulation while enabling a more affordable overall treatment.

There have also been new advances to the efficiency of the MBE. Symmetrically-equivalent body terms can now be identified using new formulations exploiting crystal translational symmetry [65]. In addition, recently-developed machine-learning descriptors [102] allow for a further reduction. We also introduce a subtractive embedding of the correlation energy with Grimme’s D4 dispersion [104], a negligible-cost addition that reduces cutoff distances. Together, these developments lower the number of required CCSD(T) calculations by orders of magnitude compared to a full enumeration and significantly expand the scope of molecular crystals that can be tackled by CCSD(T) with the MBE.

We combine all these developments within several packages that will be released upon publication. Our MBE implementation - combining translation symmetry with machine-learning descriptors - is provided as a separate standalone Python dependency, pMBE. It generates and manages the two- and three-body (or beyond) terms, storing them in a database file. The LNO-MBE-CCSD(T) framework interfaces with pMBE to generate an efficient set of MBE fragments, while using the QuAcc workflow library [122] to manage the full set of calculations to compute their final contributions to the lattice energy. Our optimizations to the LNO-CCSD(T) approximation is available in the latest 2025 version of MRCC [123, 124], with the necessary options needed for the MBE turned on within the LNO-MBE-CCSD(T) package by default. The use of the QuAcc workflow library also means that in principle, it is modular and can be interfaced with other (local) CCSD(T) implementations [101, 125] as well as MBE codes [61, 69, 102, 126]. In addition, the inputs to perform B86bPBE50-revXDM are provided and we have also made it available as a custom calculator for the atomic simulation environment (ASE).

Coupled cluster theory

All CCSD(T) calculations were performed in MRCC [123, 124], accelerated by the local natural orbital (LNO) [63, 64, 121, 127] approximation. The aug-cc-pVXZ basis set family [128] was used to compute E_{latt} while the jul-cc-pVXZ basis set family was used for E_{rel} . The complete basis set (CBS) limit was reached using a two point extrapolation [129] of the triple (TZ) and quadruple-zeta (QZ) pair for the two-body contributions, while the double-zeta (DZ) and TZ pair was used for three-body contributions. We use a composite scheme whereby CCSD(T) was calculated with the smaller basis set in the CBS pair, and a correction to the CBS limit was

performed with (canonical) MP2. For E_{latt} calculations, we performed a two-point extrapolation to the local approximation free (i.e., conventional) CCSD(T) limit from Tight and vTight LNO settings, while we used Tight LNO settings only for E_{rel} . Counterpoise corrections were employed when calculating all terms.

Many-body expansion

The many-body expansion fragmentation was performed using the periodic implementation of Herman and Xantheas [65]. We truncated the MBE to the three-body level, with distance cutoffs (as well as convergence plots) described in Supplementary Section 1 D. The Coulomb Matrix (CM) global descriptor, computed with DScribe [103, 130], was further used to identify redundant terms. As described in Supplementary Section 2 C 2, we have made additional modifications to enable permutational and rotational symmetry of the CM descriptor, together with a regularizing term based on the distance cutoff.

Density functional theory

The periodic HF calculations were performed in the GPU implementation of the Vienna *ab-initio* simulation package [131–133] (VASP) version 6.4.2. We used the hard (denoted by X_h, where X is the element) PBE projector augmented wave (PAW) potentials and an energy cutoff of 1000 eV. A Γ -centered k -point mesh was used with the k -point density (KSPACING) of 0.2 \AA^{-1} . We used the truncated Coulomb potential (HFRCUT=-1) and the ACE [62] operator. For the DFT benchmarks in Figure 4, the calculations for PBE-D3(BJ), revPBE-D3(0), r^2 SCAN-D4, optB86b-vdW and vdW-DF2 were performed in VASP, while some of the DFT functionals (B86bPBE-XDM, B86bPBE-XDM-25, B86bPBE-XDM-50, PBE0-MBD, PBE+TS) were performed in the Fritz Haber Institute *ab initio* molecular simulations (FHI-aims) package [134]. In the latter, we aim to reach the ‘tight’ basis set level, using a composite process described in Supplementary Section 1 B for hybrid functionals. The CPU costs for both the GGA and hybrid DFT in Figure 4a were performed in Quantum Espresso [135] as described in Supplementary Section 1 B.

DATA AVAILABILITY

See the supplementary information for a detailed compilation of the obtained results as well as further data and analysis to support the points made throughout the text. The input and output files associated with this work and all analysis will be made available on Github and Zeonodo upon publication.

CODE AVAILABILITY

The LNO-MBE-CCSD(T) framework and the standalone pMBE software will be made freely available on Github upon publication, with documentation containing instructions and examples on how to run the two codes.

^a Present address: Department of Chemistry, University of Chicago, Chicago, IL 60637, United States

* Electronic address: sotiris.xantheas@pnnl.gov

* Electronic address: am452@cam.ac.uk

- [1] J. Maddox, Crystals from first principles, *Nature* **335**, 201 (1988).
- [2] S. M. Woodley and R. Catlow, Crystal structure prediction from first principles, *Nat. Mater.* **7**, 937 (2008).
- [3] M. A. Neumann, J. van de Streek, F. P. A. Fabbiani, P. Hidber, and O. Grassmann, Combined crystal structure prediction and high-pressure crystallization in rational pharmaceutical polymorph screening, *Nat. Commun.* **6**, 7793 (2015).
- [4] R. M. Bhardwaj, J. A. McMahon, J. Nyman, L. S. Price, S. Konar, I. D. H. Oswald, C. R. Pulham, S. L. Price, and S. M. Reutzel-Edens, A prolific solvate former, galunisertib, under the pressure of crystal structure prediction, produces ten diverse polymorphs, *J. Am. Chem. Soc.* **141**, 13887 (2019).
- [5] C. Lamberth, S. Jeanmart, T. Luksch, and A. Plant, Current challenges and trends in the discovery of agrochemicals, *Science* **341**, 742 (2013).
- [6] J. T. A. Jones, T. Hasell, X. Wu, J. Bacsa, K. E. Jelfs, M. Schmidtman, S. Y. Chong, D. J. Adams, A. Trewin, F. Schiffman, F. Cora, B. Slater, A. Steiner, G. M. Day, and A. I. Cooper,

- Modular and predictable assembly of porous organic molecular crystals, *Nature* **474**, 367 (2011).
- [7] M. A. Baldo, D. F. O'Brien, Y. You, A. Shoustikov, S. Sibley, M. E. Thompson, and S. R. Forrest, Highly efficient phosphorescent emission from organic electroluminescent devices, *Nature* **395**, 151 (1998).
- [8] O. Bolton, K. Lee, H.-J. Kim, K. Y. Lin, and J. Kim, Activating efficient phosphorescence from purely organic materials by crystal design, *Nat. Chem.* **3**, 205 (2011).
- [9] G. M. Brown and H. A. Levy, α -D-glucose: Precise determination of crystal and molecular structure by neutron-diffraction analysis, *Science* **147**, 1038 (1965).
- [10] J. Sun, B. K. Clark, S. Torquato, and R. Car, The phase diagram of high-pressure superionic ice, *Nat. Commun.* **6**, 8156 (2015).
- [11] J.-A. Hernandez, M. Bethkenhagen, S. Ninet, M. French, A. Benuzzi-Mounaix, F. Datchi, M. Guarguaglini, F. Lefevre, F. Occelli, R. Redmer, T. Vinci, and A. Ravasio, Melting curve of superionic ammonia at planetary interior conditions, *Nat. Phys.* **19**, 1280 (2023).
- [12] S. L. Price, Predicting crystal structures of organic compounds, *Chem. Soc. Rev.* **43**, 2098 (2014).
- [13] G. J. O. Beran, Modeling polymorphic molecular crystals with electronic structure theory, *Chem. Rev.* **116**, 5567 (2016).
- [14] A. Pulido, L. Chen, T. Kaczorowski, D. Holden, M. A. Little, S. Y. Chong, B. J. Slater, D. P. McMahon, B. Bonillo, C. J. Stackhouse, A. Stephenson, C. M. Kane, R. Clowes, T. Hasell, A. I. Cooper, and G. M. Day, Functional materials discovery using energy–structure–function maps, *Nature* **543**, 657 (2017).
- [15] N. Marzari, A. Ferretti, and C. Wolverton, Electronic-structure methods for materials design, *Nat. Mater.* **20**, 736 (2021).
- [16] G. J. O. Beran, I. J. Sugden, C. Greenwell, D. H. Bowskill, C. C. Pantelides, and C. S. Adjiman, How many more polymorphs of ROY remain undiscovered, *Chem. Sci.* **13**, 1288 (2022).
- [17] S. L. Price, Is zeroth order crystal structure prediction (CSP_0) coming to maturity? What should we aim for in an ideal crystal structure prediction code?, *Faraday Discuss.* **211**, 9 (2018).
- [18] J. Hoja, A. M. Reilly, and A. Tkatchenko, First-principles modeling of molecular crystals: Structures and stabilities, temperature and pressure, *WIREs Comput. Mol. Sci.* **7**, e1294 (2017).
- [19] V. Kapil and E. A. Engel, A complete description of thermodynamic stabilities of molecular crystals, *Proc. Natl. Acad. Sci. U. S. A.* **119**, e2111769119 (2022).

- [20] J. Nyman and G. M. Day, Static and lattice vibrational energy differences between polymorphs, *CrystEngComm* **17**, 5154 (2015).
- [21] J. Yang, W. Hu, D. Usvyat, D. Matthews, M. Schütz, and G. K.-L. Chan, Ab initio determination of the crystalline benzene lattice energy to sub-kilojoule/mole accuracy, *Science* **345**, 640 (2014).
- [22] J. Kaiser, Shortages of cancer drugs put patients, trials at risk, *Science* **332**, 523 (2011).
- [23] D.-K. Bučar, R. W. Lancaster, and J. Bernstein, Disappearing polymorphs revisited, *Angew. Chem. Int. Ed.* **54**, 6972 (2015).
- [24] J. Johal and G. M. Day, Exploring organic chemical space for materials discovery using crystal structure prediction-informed evolutionary optimisation, *Nat. Commun.* **16**, 10540 (2025).
- [25] A. V. Kazantsev, P. G. Karamertzanis, C. S. Adjiman, C. C. Pantelides, S. L. Price, P. T. A. Galek, G. M. Day, and A. J. Cruz-Cabeza, Successful prediction of a model pharmaceutical in the fifth blind test of crystal structure prediction, *Int. J. Pharm. A Priori Performance Predictions*, **418**, 168 (2011).
- [26] C. R. Taylor, M. T. Mulvee, D. S. Perenyi, M. R. Probert, G. M. Day, and J. W. Steed, Minimizing polymorphic risk through cooperative computational and experimental exploration, *J. Am. Chem. Soc.* **142**, 16668 (2020).
- [27] D. Firaha, Y. M. Liu, J. van de Streek, K. Sasikumar, H. Dietrich, J. Helfferich, L. Aerts, D. E. Braun, A. Broo, A. G. DiPasquale, A. Y. Lee, S. Le Meur, S. O. Nilsson Lill, W. J. Lunsman, A. Mattei, P. Muglia, O. D. Putra, M. Raoui, S. M. Reutzel-Edens, S. Rome, A. Y. Sheikh, A. Tkatchenko, G. R. Woollam, and M. A. Neumann, Predicting crystal form stability under real-world conditions, *Nature* **623**, 324 (2023).
- [28] B. Kalita, H. Gokcan, and O. Isayev, Machine learning interatomic potentials at the centennial crossroads of quantum mechanics, *Nat. Comput. Sci.* **5**, 1120 (2025).
- [29] V. Gharakhanyan, L. Barroso-Luque, Y. Yang, M. Shuaibi, K. Michel, D. S. Levine, M. Dzamba, X. Fu, M. Gao, X. Liu, H. Ni, K. Noori, B. M. Wood, M. Uyttendaele, A. Boromand, C. L. Zitnick, N. Marom, Z. W. Ulissi, and A. Sriram, Open Molecular Crystals 2025 (OMC25) dataset and models, *arXiv [physics.chem-phy]*, arXiv:2508.02651 (2025).
- [30] G. J. O. Beran and K. Nanda, Predicting organic crystal lattice energies with chemical accuracy, *J. Phys. Chem. Lett.* **1**, 3480 (2010).
- [31] J. Hoja, H.-Y. Ko, M. A. Neumann, R. Car, R. A. DiStasio, and A. Tkatchenko, Reliable and practical computational description of molecular crystal polymorphs, *Sci. Adv.* **5**, eaau3338 (2019).

- [32] A. J. A. Price, R. A. Mayo, A. Otero-de-la-Roza, and E. R. Johnson, Accurate and efficient polymorph energy ranking with XDM-corrected hybrid DFT, *CrystEngComm* **25**, 953 (2023).
- [33] A. J. A. Price, A. Otero-de-la-Roza, and E. R. Johnson, XDM-corrected hybrid DFT with numerical atomic orbitals predicts molecular crystal lattice energies with unprecedented accuracy, *Chem. Sci.* **14**, 1252 (2023).
- [34] F. Della Pia, B. X. Shi, V. Kapil, A. Zen, D. Alfè, and A. Michaelides, Accurate and efficient machine learning interatomic potentials for finite temperature modelling of molecular crystals, *Chem. Sci.* **16**, 11419 (2025).
- [35] J. P. Perdew and K. Schmidt, Jacob's ladder of density functional approximations for the exchange-correlation energy, *AIP Conf. Proc.* **577**, 1 (2001).
- [36] S. Grimme, A. Hansen, J. G. Brandenburg, and C. Bannwarth, Dispersion-corrected mean-field electronic structure methods, *Chem. Rev.* **116**, 5105 (2016).
- [37] K. R. Bryenton, A. A. Adeleke, S. G. Dale, and E. R. Johnson, Delocalization error: The greatest outstanding challenge in density-functional theory, *WIREs Comput. Mol. Sci.* **13**, e1631 (2023).
- [38] L. M. LeBlanc, S. G. Dale, C. R. Taylor, A. D. Becke, G. M. Day, and E. R. Johnson, Pervasive delocalisation error causes spurious proton transfer in organic acid–base co-crystals, *Angew. Chem. Int. Ed.* **57**, 14906 (2018).
- [39] J. Bernstein and A. T. Hagler, Conformational polymorphism. The influence of crystal structure on molecular conformation, *J. Am. Chem. Soc.* **100**, 673 (1978).
- [40] A. Chattopadhyay, A. R. Hill, S. E. Wright, G. J. O. Beran, and A. J. Cruz-Cabeza, Lattice energy partitions in crystals of flexible molecules and the 40% limit, *J. Am. Chem. Soc.* [10.1021/jacs.5c09997](https://doi.org/10.1021/jacs.5c09997) (2025).
- [41] C. J. Perry, S. A. Ramos, M. C. Phelps, L. J. Mueller, and G. J. O. Beran, Taming tautomerism in organic crystal structure prediction, *J. Am. Chem. Soc.* **147**, 26865 (2025).
- [42] S. Chen, I. A. Guzei, and L. Yu, New polymorphs of ROY and new record for coexisting polymorphs of solved structures, *J. Am. Chem. Soc.* **127**, 9881 (2005).
- [43] A. Lévesque, T. Maris, and J. D. Wuest, ROY reclaims its crown: New ways to increase polymorphic diversity, *J. Am. Chem. Soc.* **142**, 11873 (2020).
- [44] J. Weatherston, M. R. Probert, and M. J. Hall, Polymorphic ROYalty: The 14th ROY polymorph discovered via high-throughput crystallization, *J. Am. Chem. Soc.* **147**, 11949 (2025).

- [45] J. Nyman, L. Yu, and S. M. Reutzel-Edens, Accuracy and reproducibility in crystal structure prediction: The curious case of ROY, *CrystEngComm* **21**, 2080 (2019).
- [46] C. Greenwell, J. L. McKinley, P. Zhang, Q. Zeng, G. Sun, B. Li, S. Wen, and G. J. O. Beran, Overcoming the difficulties of predicting conformational polymorph energetics in molecular crystals via correlated wavefunction methods, *Chem. Sci.* **11**, 2200 (2020).
- [47] G. J. O. Beran, Frontiers of molecular crystal structure prediction for pharmaceuticals and functional organic materials, *Chem. Sci.* **14**, 13290 (2023).
- [48] R. J. Bartlett and M. Musiał, Coupled-cluster theory in quantum chemistry, *Rev. Mod. Phys.* **79**, 291 (2007).
- [49] W. M. C. Foulkes, L. Mitas, R. J. Needs, and G. Rajagopal, Quantum Monte Carlo simulations of solids, *Rev. Mod. Phys.* **73**, 33 (2001).
- [50] A. Otero-de-la-Roza and E. R. Johnson, A benchmark for non-covalent interactions in solids, *J. Chem. Phys.* **137**, 054103 (2012).
- [51] A. M. Reilly and A. Tkatchenko, Understanding the role of vibrations, exact exchange, and many-body van der Waals interactions in the cohesive properties of molecular crystals, *J. Chem. Phys.* **139**, 024705 (2013).
- [52] G. A. Dolgonos, J. Hoja, and A. D. Boese, Revised values for the X23 benchmark set of molecular crystals, *Phys. Chem. Chem. Phys.* **21**, 24333 (2019).
- [53] F. Della Pia, A. Zen, D. Alfè, and A. Michaelides, How accurate are simulations and experiments for the lattice energies of molecular crystals?, *Phys. Rev. Lett.* **133**, 046401 (2024).
- [54] A. Zen, J. G. Brandenburg, J. Klimeš, A. Tkatchenko, D. Alfè, and A. Michaelides, Fast and accurate quantum Monte Carlo for molecular crystals, *Proc. Natl. Acad. Sci. U. S. A.* **115**, 1724 (2018).
- [55] F. Della Pia, A. Zen, D. Alfè, and A. Michaelides, DMC-ICE13: Ambient and high pressure polymorphs of ice from diffusion Monte Carlo and density functional theory, *J. Chem. Phys.* **157**, 134701 (2022).
- [56] L. M. Hunnisett, N. Francia, J. Nyman, N. S. Abraham, S. Aitipamula, T. Alkhidir, M. Almehairbi, A. Anelli, D. M. Anstine, J. E. Anthony, J. E. Arnold, F. Bahrami, M. A. Bellucci, G. J. O. Beran, R. M. Bhardwaj, R. Bianco, J. A. Bis, A. D. Boese, J. Bramley, D. E. Braun, P. W. V. Butler, J. Cadden, S. Carino, C. Červinka, E. J. Chan, C. Chang, S. M. Clarke, S. J. Coles, C. J. Cook, R. I. Cooper, T. Darden, G. M. Day, W. Deng, H. Dietrich, A. DiPasquale, B. Dhokale,

- B. P. van Eijck, M. R. J. Elsegood, D. Firaha, W. Fu, K. Fukuzawa, N. Galanakis, H. Goto, C. Greenwell, R. Guo, J. Harter, J. Helfferich, J. Hoja, J. Hone, R. Hong, M. Hušák, Y. Ikabata, O. Isayev, O. Ishaque, V. Jain, Y. Jin, A. Jing, E. R. Johnson, I. Jones, K. V. J. Jose, E. A. Kabova, A. Keates, P. F. Kelly, J. Klimeš, V. Kostková, H. Li, X. Lin, A. List, C. Liu, Y. M. Liu, Z. Liu, I. Lončarić, J. W. Lubach, J. Ludík, N. Marom, H. Matsui, A. Mattei, R. A. Mayo, J. W. Melkumov, B. Mladineo, S. Mohamed, Z. Momenzadeh Abardeh, H. S. Muddana, N. Nakayama, K. S. Nayal, M. A. Neumann, R. Nikhar, S. Obata, D. O'Connor, A. R. Oganov, K. Okuwaki, A. Otero-de-la-Roza, S. Parkin, A. Parunov, R. Podeszwa, A. J. A. Price, L. S. Price, S. L. Price, M. R. Probert, A. Pulido, G. R. Ramteke, A. U. Rehman, S. M. Reutzel-Edens, J. Rogal, M. J. Ross, A. F. Rumson, G. Sadiq, Z. M. Saeed, A. Salimi, K. Sasikumar, S. Sekharan, K. Shankland, B. Shi, X. Shi, K. Shinohara, A. G. Skillman, H. Song, N. Strasser, J. van de Streek, I. J. Sugden, G. Sun, K. Szalewicz, L. Tan, K. Tang, F. Tarczynski, C. R. Taylor, A. Tkatchenko, R. Tom, P. Touš, M. E. Tuckerman, P. A. Unzueta, Y. Utsumi, L. Vogt-Maranto, J. Weatherston, L. J. Wilkinson, R. D. Willacy, L. Wojtas, G. R. Woollam, Y. Yang, Z. Yang, E. Yonemochi, X. Yue, Q. Zeng, T. Zhou, Y. Zhou, R. Zubatyuk, and J. C. Cole, The seventh blind test of crystal structure prediction: Structure ranking methods, *Acta Cryst. B* **80**, 548 (2024).
- [57] M. S. Gordon, D. G. Fedorov, S. R. Pruitt, and L. V. Slipchenko, Fragmentation methods: A route to accurate calculations on large systems, *Chem. Rev.* **112**, 632 (2012).
- [58] A. L. Ringer and C. D. Sherrill, First principles computation of lattice energies of organic solids: The benzene crystal, *Chem. - Eur. J.* **14**, 2542 (2008).
- [59] C. H. Borca, Z. L. Glick, D. P. Metcalf, L. A. Burns, and C. D. Sherrill, Benchmark coupled-cluster lattice energy of crystalline benzene and assessment of multi-level approximations in the many-body expansion, *J. Chem. Phys.* **158**, 234102 (2023).
- [60] C. T. Sargent, D. P. Metcalf, Z. L. Glick, C. H. Borca, and C. D. Sherrill, Benchmarking two-body contributions to crystal lattice energies and a range-dependent assessment of approximate methods, *J. Chem. Phys.* **158**, 054112 (2023).
- [61] K. Syty, G. Czekają, K. N. Pham, and M. Modrzejewski, Multi-level coupled-cluster description of crystal lattice energies, *J. Chem. Theory Comput.* **21**, 5533 (2025).
- [62] L. Lin, Adaptively compressed exchange operator, *J. Chem. Theory Comput.* **12**, 2242 (2016).
- [63] P. R. Nagy and M. Kállay, Approaching the basis set limit of CCSD(T) energies for large molecules with local natural orbital coupled-cluster methods, *J. Chem. Theory Comput.* **15**, 5275 (2019).

- [64] P. R. Nagy, State-of-the-art local correlation methods enable affordable gold standard quantum chemistry for up to hundreds of atoms, *Chem. Sci.* **15**, 14556 (2024).
- [65] K. M. Herman and S. S. Xantheas, A formulation of the many-body expansion (MBE) for periodic systems: Application to several ice phases, *J. Phys. Chem. Lett.* **14**, 989 (2023).
- [66] M. Rupp, A. Tkatchenko, K.-R. Müller, and O. A. von Lilienfeld, Fast and accurate modeling of molecular atomization energies with machine learning, *Phys. Rev. Lett.* **108**, 058301 (2012).
- [67] M. Mortazavi, J. G. Brandenburg, R. J. Maurer, and A. Tkatchenko, Structure and stability of molecular crystals with many-body dispersion-inclusive density functional tight binding, *J. Phys. Chem. Lett.* **9**, 399 (2018).
- [68] S. P. Thomas, P. R. Spackman, D. Jayatilaka, and M. A. Spackman, Accurate lattice energies for molecular crystals from experimental crystal structures, *J. Chem. Theory Comput.* **14**, 1614 (2018).
- [69] J. Hoja, A. List, and A. D. Boese, Multimer embedding approach for molecular crystals up to harmonic vibrational properties, *J. Chem. Theory Comput.* **20**, 357 (2024).
- [70] D. P. Kovács, J. H. Moore, N. J. Browning, I. Batatia, J. T. Horton, Y. Pu, V. Kapil, W. C. Witt, I.-B. Magdău, D. J. Cole, and G. Csányi, MACE-OFF: Short-range transferable machine learning force fields for organic molecules, *J. Am. Chem. Soc.* **147**, 17598 (2025).
- [71] Y. S. Al-Hamdani, P. R. Nagy, A. Zen, D. Barton, M. Kállay, J. G. Brandenburg, and A. Tkatchenko, Interactions between large molecules pose a puzzle for reference quantum mechanical methods, *Nat. Commun.* **12**, 3927 (2021).
- [72] B. X. Shi, F. Della Pia, Y. S. Al-Hamdani, A. Michaelides, D. Alfè, and A. Zen, Systematic discrepancies between reference methods for noncovalent interactions within the S66 dataset, *J. Chem. Phys.* **162**, 144107 (2025).
- [73] V. Fishman, M. Lesiuk, J. M. L. Martin, and A. Daniel Boese, Another angle on benchmarking noncovalent interactions, *J. Chem. Theory Comput.* **21**, 2311 (2025).
- [74] T. Schäfer, A. Irmeler, A. Gallo, and A. Grüneis, Understanding discrepancies in noncovalent interaction energies from wavefunction theories for large molecules, *Nat. Commun.* **16**, 9108 (2025).
- [75] Y. Xie, Z. L. Glick, and C. D. Sherrill, Assessment of three-body dispersion models against coupled-cluster benchmarks for crystalline benzene, carbon dioxide, and triazine, *J. Chem. Phys.* **158**, 094110 (2023).

- [76] A. Hermann and P. Schwerdtfeger, Ground-state properties of crystalline ice from periodic Hartree–Fock calculations and a coupled-cluster-based many-body decomposition of the correlation energy, *Phys. Rev. Lett.* **101**, 183005 (2008).
- [77] A. D. Boese and J. Sauer, Embedded and DFT calculations on the crystal structures of small alkanes, notably propane, *Cryst. Growth Des.* **17**, 1636 (2017).
- [78] R. Bukowski, K. Szalewicz, G. C. Groenenboom, and A. van der Avoird, Predictions of the properties of water from first principles, *Science* **315**, 1249 (2007).
- [79] S. Wen and G. J. O. Beran, Accurate molecular crystal lattice energies from a fragment QM/MM approach with on-the-fly ab initio force field parametrization, *J. Chem. Theory Comput.* **7**, 3733 (2011).
- [80] P. M. Nelson and C. D. Sherrill, Convergence of the many-body expansion with respect to distance cutoffs in crystals of polar molecules: Acetic acid, formamide, and imidazole, *J. Chem. Phys.* **161**, 214105 (2024).
- [81] E. Whalley, Energies of the phases of ice at zero temperature and pressure, *J. Chem. Phys.* **81**, 4087 (1984).
- [82] J. D. Bernal and R. H. Fowler, A theory of water and ionic solution, with particular reference to hydrogen and hydroxyl ions, *J. Chem. Phys.* **1**, 515 (1933).
- [83] L. Pauling, The structure and entropy of ice and of other crystals with some randomness of atomic arrangement, *J. Am. Chem. Soc.* **57**, 2680 (1935).
- [84] C. G. Salzmann, P. G. Radaelli, B. Slater, and J. L. Finney, The polymorphism of ice: Five unresolved questions, *Phys. Chem. Chem. Phys.* **13**, 18468 (2011).
- [85] B. Santra, J. Klimeš, D. Alfè, A. Tkatchenko, B. Slater, A. Michaelides, R. Car, and M. Scheffler, Hydrogen bonds and van der Waals forces in ice at ambient and high pressures, *Phys. Rev. Lett.* **107**, 185701 (2011).
- [86] M. Macher, J. Klimeš, C. Franchini, and G. Kresse, The random phase approximation applied to ice, *J. Chem. Phys.* **140**, 084502 (2014).
- [87] S. Wengert, G. Csányi, K. Reuter, and J. T. Margraf, Data-efficient machine learning for molecular crystal structure prediction, *Chem. Sci.* **12**, 4536 (2021).
- [88] Y. H. Liang, H.-Z. Ye, and T. C. Berkelbach, Can spin-component scaled MP2 achieve kJ/mol accuracy for cohesive energies of molecular crystals?, *J. Phys. Chem. Lett.* **14**, 10435 (2023).

- [89] E. C.-Y. Yuan, Y. Liu, J. Chen, P. Zhong, S. Raja, T. Kreiman, S. Vargas, W. Xu, M. Head-Gordon, C. Yang, S. M. Blau, B. Cheng, A. Krishnapriyan, and T. Head-Gordon, Foundation models for atomistic simulation of chemistry and materials, *Nat. Rev. Chem.* , **1** (2026).
- [90] A. Tkatchenko, R. A. DiStasio, R. Car, and M. Scheffler, Accurate and efficient method for many-body van der Waals interactions, *Phys. Rev. Lett.* **108**, 236402 (2012).
- [91] J. Řezáč and P. Hobza, Benchmark calculations of interaction energies in noncovalent complexes and their applications, *Chem. Rev.* **116**, 5038 (2016).
- [92] D. R. Broderick and J. M. Herbert, Delocalization error poisons the density-functional many-body expansion, *Chem. Sci.* **15**, 19893 (2024).
- [93] L. Yu, Polymorphism in molecular solids: An extraordinary system of red, orange, and yellow crystals, *Acc. Chem. Res.* **43**, 1257 (2010).
- [94] M. Mortazavi, J. Hoja, L. Aerts, L. Quéré, J. van de Streek, M. A. Neumann, and A. Tkatchenko, Computational polymorph screening reveals late-appearing and poorly-soluble form of rotigotine, *Commun. Chem.* **2**, 70 (2019).
- [95] A. M. Campeta, B. P. Chekal, Y. A. Abramov, P. A. Meenan, M. J. Henson, B. Shi, R. A. Singer, and K. R. Horspool, Development of a targeted polymorph screening approach for a complex polymorphic and highly solvating API, *J. Pharm. Sci.* **99**, 3874 (2010).
- [96] M. Vasileiadis, C. C. Pantelides, and C. S. Adjiman, Prediction of the crystal structures of axitinib, a polymorphic pharmaceutical molecule, *Chem. Eng. Sci. 2013 Danckwerts Special Issue on Molecular Modelling in Chemical Engineering*, **121**, 60 (2015).
- [97] G. J. O. Beran, From polymorphs to cocrystals and salts: Successfully predicting axitinib's challenging crystal forms, *Chem. Sci.* **16**, 23026 (2025).
- [98] C. Greenwell and G. J. O. Beran, Inaccurate conformational energies still hinder crystal structure prediction in flexible organic molecules, *Cryst. Growth Des.* **20**, 4875 (2020).
- [99] G. J. O. Beran, S. E. Wright, C. Greenwell, and A. J. Cruz-Cabeza, The interplay of intra- and intermolecular errors in modeling conformational polymorphs, *J. Chem. Phys.* **156**, 104112 (2022).
- [100] C. Riplinger, P. Pinski, U. Becker, E. F. Valeev, and F. Neese, Sparse maps—A systematic infrastructure for reduced-scaling electronic structure methods. II. Linear scaling domain based pair natural orbital coupled cluster theory, *J. Chem. Phys.* **144**, 024109 (2016).

- [101] A. Jiang, Z. L. Glick, D. Poole, J. M. Turney, C. D. Sherrill, and H. F. Schaefer, III, Accurate and efficient open-source implementation of domain-based local pair natural orbital (DLPNO) coupled-cluster theory using a t1-transformed Hamiltonian, *J. Chem. Phys.* **161**, 082502 (2024).
- [102] C. H. Borca, B. W. Bakr, L. A. Burns, and C. D. Sherrill, CrystaLattE: Automated computation of lattice energies of organic crystals exploiting the many-body expansion to achieve dual-level parallelism, *J. Chem. Phys.* **151**, 144103 (2019).
- [103] L. Himanen, M. O. J. Jäger, E. V. Morooka, F. Federici Canova, Y. S. Ranawat, D. Z. Gao, P. Rinke, and A. S. Foster, Dscribe: Library of descriptors for machine learning in materials science, *Comput. Phys. Commun.* **247**, 106949 (2020).
- [104] E. Caldeweyher, S. Ehlert, A. Hansen, H. Neugebauer, S. Spicher, C. Bannwarth, and S. Grimme, A generally applicable atomic-charge dependent London dispersion correction, *J. Chem. Phys.* **150**, 154122 (2019).
- [105] D. Zhou, I. Bier, B. Santra, L. D. Jacobson, C. Wu, A. Garaizar Suarez, B. R. Almaguer, H. Yu, R. Abel, R. A. Friesner, and L. Wang, A robust crystal structure prediction method to support small molecule drug development with large scale validation and blind study, *Nat. Commun.* **16**, 2210 (2025).
- [106] L. S. Price, M. Paloni, M. Salvalaglio, and S. L. Price, One size fits all? Development of the CPOSS209 data set of experimental and hypothetical polymorphs for testing computational modeling methods, *Cryst. Growth Des.* **25**, 3186 (2025).
- [107] M. Habgood, I. J. Sugden, A. V. Kazantsev, C. S. Adjiman, and C. C. Pantelides, Efficient handling of molecular flexibility in *ab initio* generation of crystal structures, *J. Chem. Theory Comput.* **11**, 1957 (2015).
- [108] R. Nikhar and K. Szalewicz, Reliable crystal structure predictions from first principles, *Nat. Commun.* **13**, 3095 (2022).
- [109] N. Galanakis and M. E. Tuckerman, Rapid prediction of molecular crystal structures using simple topological and physical descriptors, *Nat. Commun.* **15**, 9757 (2024).
- [110] I. B. Rietveld and R. Céolin, Rotigotine: Unexpected polymorphism with predictable overall monotropic behavior, *J. Pharm. Sci.* **104**, 4117 (2015).
- [111] E. Olehnovics, Y. M. Liu, N. Mehio, A. Y. Sheikh, M. R. Shirts, and M. Salvalaglio, Accurate lattice free energies of packing polymorphs from probabilistic generative models, *J. Chem. Theory Comput.* **21**, 2244 (2025).

- [112] C. Červinka and G. J. O. Beran, Ab initio prediction of the polymorph phase diagram for crystalline methanol, *Chem. Sci.* **9**, 4622 (2018).
- [113] G. B. Correa, S. Konstantinopoulos, B. I. Tan, Y. Zhang, F. W. Tavares, C. S. Adjiman, and E. J. Maginn, Assessing polymorph stability and phase transitions at finite temperature: Integrating crystal structure prediction, lattice dynamics, and molecular dynamics, *J. Chem. Theory Comput.* **21**, 12197 (2025).
- [114] P. J. Bygrave, N. L. Allan, and F. R. Manby, The embedded many-body expansion for energetics of molecular crystals, *J. Chem. Phys.* **137**, 164102 (2012).
- [115] J. Hofierka and J. Klimeš, Binding energies of molecular solids from fragment and periodic approaches, *Electron. Struct.* **3**, 034010 (2021).
- [116] M. Hacene, A. Anciaux-Sedrakian, X. Rozanska, D. Klahr, T. Guignon, and P. Fleurat-Lessard, Accelerating VASP electronic structure calculations using graphic processing units, *J. Comp. Chem.* **33**, 2581 (2012).
- [117] P. Giannozzi, O. Baseggio, P. Bonfà, D. Brunato, R. Car, I. Carnimeo, C. Cavazzoni, S. de Gironcoli, P. Delugas, F. Ferrari Ruffino, A. Ferretti, N. Marzari, I. Timrov, A. Urru, and S. Baroni, Quantum ESPRESSO toward the exascale, *J. Chem. Phys.* **152**, 154105 (2020).
- [118] S. Kokott, F. Merz, Y. Yao, C. Carbogno, M. Rossi, V. Havu, M. Rampp, M. Scheffler, and V. Blum, Efficient all-electron hybrid density functionals for atomistic simulations beyond 10 000 atoms, *J. Chem. Phys.* **161**, 024112 (2024).
- [119] N. Niemeyer, P. Eschenbach, M. Bensberg, J. Tölle, L. Hellmann, L. Lampe, A. Massolle, A. Rikus, D. Schnieders, J. P. Unsleber, and J. Neugebauer, The subsystem quantum chemistry program Serenity, *WIREs Comput. Mol. Sci.* **13**, e1647 (2023).
- [120] Q. Ma and H.-J. Werner, Explicitly correlated local coupled-cluster methods using pair natural orbitals, *Wiley Interdiscip. Rev.: Comput. Mol. Sci.* **8**, e1371 (2018).
- [121] P. R. Nagy, G. Samu, and M. Kállay, Optimization of the linear-scaling local natural orbital CCSD(T) method: Improved algorithm and benchmark applications, *J. Chem. Theory Comput.* **14**, 4193 (2018).
- [122] A. S. Rosen, *Quacc – The Quantum Accelerator*: <https://zenodo.org/records/13921187>, Zenodo (2024).
- [123] M. Kállay, P. R. Nagy, D. Mester, Z. Rolik, G. Samu, J. Csontos, J. Csóka, P. B. Szabó, L. Gyevi-Nagy, B. Hégyely, I. Ladjánszki, L. Szegedy, B. Ladóczki, K. Petrov, M. Farkas, P. D. Mezei, and

- Á. Ganyecz, The MRCC program system: Accurate quantum chemistry from water to proteins, *J. Chem. Phys.* **152**, 074107 (2020).
- [124] D. Mester, P. R. Nagy, J. Csóka, L. Gyevi-Nagy, P. B. Szabó, R. A. Horváth, K. Petrov, B. Hégyel, B. Ladóczki, G. Samu, B. D. Lőrincz, and M. Kállay, Overview of developments in the MRCC program system, *J. Phys. Chem. A* **129**, 2086 (2025).
- [125] F. Neese, F. Wennmohs, U. Becker, and C. Riplinger, The ORCA quantum chemistry program package, *J. Chem. Phys.* **152**, 224108 (2020).
- [126] L. A. Burns, C. D. Sherrill, and B. P. Pritchard, QCManyBody: A flexible implementation of the many-body expansion, *J. Chem. Phys.* **161**, 152501 (2024).
- [127] P. R. Nagy and M. Kállay, Optimization of the linear-scaling local natural orbital CCSD(T) method: Redundancy-free triples correction using Laplace transform, *J. Chem. Phys.* **146**, 214106 (2017).
- [128] K. A. Peterson and T. H. Dunning, Accurate correlation consistent basis sets for molecular core-valence correlation effects: The second row atoms Al–Ar, and the first row atoms B–Ne revisited, *J. Chem. Phys.* **117**, 10548 (2002).
- [129] F. Neese and E. F. Valeev, Revisiting the atomic natural orbital approach for basis sets: Robust systematic basis sets for explicitly correlated and conventional correlated *ab initio* methods?, *J. Chem. Theory Comput.* **7**, 33 (2011).
- [130] J. Laakso, L. Himanen, H. Homm, E. V. Morooka, M. O. J. Jäger, M. Todorović, and P. Rinke, Updates to the DScibe library: New descriptors and derivatives, *J. Chem. Phys.* **158**, 234802 (2023).
- [131] G. Kresse and J. Hafner, Ab initio molecular dynamics for liquid metals, *Phys. Rev. B* **47**, 558 (1993).
- [132] G. Kresse and J. Furthmüller, Efficiency of ab-initio total energy calculations for metals and semiconductors using a plane-wave basis set, *Comput. Mater. Sci.* **6**, 15 (1996).
- [133] G. Kresse and J. Furthmüller, Efficient iterative schemes for ab initio total-energy calculations using a plane-wave basis set, *Phys. Rev. B* **54**, 11169 (1996).
- [134] V. Blum, R. Gehrke, F. Hanke, P. Havu, V. Havu, X. Ren, K. Reuter, and M. Scheffler, *Ab Initio* molecular simulations with numeric atom-centered orbitals, *Comput. Phys. Commun.* **180**, 2175 (2009).

- [135] P. Giannozzi, S. Baroni, N. Bonini, M. Calandra, R. Car, C. Cavazzoni, D. Ceresoli, G. L. Chiarotti, M. Cococcioni, I. Dabo, A. D. Corso, S. de Gironcoli, S. Fabris, G. Fratesi, R. Gebauer, U. Gerstmann, C. Gougousis, A. Kokalj, M. Lazzeri, L. Martin-Samos, N. Marzari, F. Mauri, R. Mazzarello, S. Paolini, A. Pasquarello, L. Paulatto, C. Sbraccia, S. Scandolo, G. Sclauzero, A. P. Seitsonen, A. Smogunov, P. Umari, and R. M. Wentzcovitch, QUANTUM ESPRESSO: A modular and open-source software project for quantum simulations of materials, *J. Phys.: Condens. Matter* **21**, 395502 (2009).

Supplementary information: Efficient first-principles predictions of complex molecular crystals at sub-chemical accuracy

Benjamin X. Shi,¹ Kristina M. Herman,² Flaviano Della Pia,³ Venkat Kapil,^{4,5} Andrea Zen,^{6,7} Péter R. Nagy,^{8,9,10} Sotiris Xantheas,^{2,11,12,*} and Angelos Michaelides^{3,*}

¹*Initiative for Computational Catalysis, Flatiron Institute,
160 5th Avenue, New York, NY 10010*

²*Department of Chemistry, University of Washington,
Seattle, Washington 98195, United States*

³*Yusuf Hamied Department of Chemistry,
University of Cambridge, Lensfield Road,
Cambridge CB2 1EW, United Kingdom*

⁴*Department of Physics and Astronomy, University College London,
7-19 Gordon St, London WC1H 0AH, UK*

⁵*Thomas Young Centre and London Centre for
Nanotechnology, 9 Gordon St, London WC1H 0AH*

⁶*Dipartimento di Fisica Ettore Pancini, Università di Napoli Federico II,
Monte S. Angelo, I-80126 Napoli, Italy*

⁷*Department of Earth Sciences, University College London,
Gower Street, London WC1E 6BT, United Kingdom*

⁸*Department of Physical Chemistry and Materials Science,
Faculty of Chemical Technology and Biotechnology,
Budapest University of Technology and Economics,
Műegyetem rkp. 3., H-1111 Budapest, Hungary*

⁹*HUN-REN-BME Quantum Chemistry Research Group,
Műegyetem rkp. 3., H-1111 Budapest, Hungary*

¹⁰*MTA-BME Lendület Quantum Chemistry Research Group,
Műegyetem rkp. 3., H-1111 Budapest, Hungary*

¹¹*Advanced Computing, Mathematics and Data Division,
Pacific Northwest National Laboratory, 902 Battelle Boulevard,
MS J7-10, Richland, Washington 99352, United States*

¹²*Computational and Theoretical Chemistry Institute (CTCI),
Pacific Northwest National Laboratory,*

Richland, Washington 99352, United States

(Dated: March 3, 2026)

CONTENTS

1. Computational details	6
A. Geometries	6
B. Periodic HF and DFT	7
1. VASP	7
2. FHI-AIMs	8
3. Quantum Espresso	8
C. Correlated wavefunction theory	9
D. Many-body expansion	10
2. Lowering computational cost of MBE	12
A. Removing HF contribution to handle only electron correlation	12
B. Enhancing distance convergence using empirical dispersion corrections	14
C. Identifying symmetrically and translationally redundant terms	24
1. Periodic MBE	24
2. Coulomb-matrix filter	25
D. Optimizing the local natural orbital approximation for the MBE	33
3. Cost-efficient electronic structure parameters	35
A. Lattice energy	35
1. Basis set dependence	35
2. Effect of core electrons	37
3. Beyond-CCSD(T) contributions	38
4. Convergence with many-body terms in the MBE	38
5. Local approximation convergence	39
6. Final parameters	42
B. Relative energy	45
1. Final parameters	45
2. Experimental and vanEijck-3 forms of molecule X	47
3. Ice Ih and VIII	49
4. Lattice energy of X23 Dataset	52

* Electronic address: sotiris.xantheas@pnnl.gov

* Electronic address: am452@cam.ac.uk

A. Experimental analysis	52
B. Periodic HF	56
C. MBE cWFT correlation	59
D. Effects from CCSD(cT)-fit	61
E. Final estimates and comparison to DMC	64
F. Comparison to other work	69
G. Validating CCSD(T) estimates	71
5. Cost comparison for X23 dataset	73
A. Calculating cost of hybrid DFT	75
B. Calculating cost of LNO-MBE-CCSD(T)	75
C. Calculating the cost of DMC	77
6. Lattice and relative energy of ICE13 Dataset	81
A. Final lattice energies	81
B. Final relative energies	83
7. Towards optimized density functional approximations for molecular crystals	86
8. Relative energy calculations on pharmaceutical molecular crystals	92
A. Convergence of 2B and 3B terms as a function of cutoff	93
B. MBE contributions to the relative energies	98
C. Final relative energies	100
D. Density functional approximation comparison	101
E. Estimation of geometrical errors	102
9. Thermal contributions from machine-learning interatomic potentials	104
A. The framework	104
B. Computational and dataset details	106
C. Convergence of the relative sublimation enthalpies	106
D. Final experimental relative energy estimates	112
10. Benchmarking density functional and wave function methods	114
A. X23 lattice energy	115
B. ICE13 lattice energy and relative energy	118

1. COMPUTATIONAL DETAILS

A. Geometries

The geometries used for all of the molecular crystals studied in this work were taken from previous work. For ease of reproduction, we have provided these geometries in our GitHub data repository (available upon publication). The geometries for the X23 dataset were compiled by Della Pia *et al.* [1], with most geometries taken from Klimeš [2] for the optB88-vdW [3] density functional approximation (DFA) besides hexamine and succinic acid, which come from Reilly and Tkatchenko [4] optimised using the PBE+TS [5, 6] DFA. The ICE13 geometries in Figure 3 of the main text were also taken from Della Pia *et al.* [7] for the ‘small’ unit cells. The ‘medium’ and ‘large’ unit cells were generated with Genlce [8, 9] then optimized within this work using the PBE [5] DFA, using the same input parameters as Ref. 7. The large unit cells exhibit greater proton disorder, more closely approximating antiferroelectric unit cells with zero net dipole, as shown in Table 1. The geometries for forms I and II of rotigotine were taken from Mortazavi *et al.* [10]. Within experiments, this system has a disordered crystal structure, where its thiophene rings randomly takes on two alternative orientations that are related by a 180° rotation, as visualized in Supplementary Figure 2 of Ref. 10. We have modeled this system using a 50%:50% average of the two respective configurations, meaning we compute the two configurations for each form, following the procedure of Mortazavi *et al.* [10]. We have considered the experimental and vanEijck-3 forms of molecule X from the Third CSP Blind Test [11], with the geometries provided by Prof. Erin Johnson from Ref. 12. This system was used for testing purposes and the only one not visualized in the main text, add we display it in Figure 1 here. These geometries were optimized by the B86bPBE-XDM [13, 14] DFA. The geometries for forms VI and XLI of

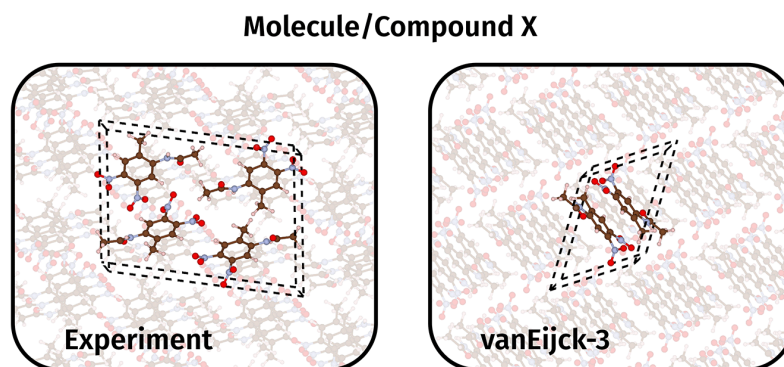


FIG. 1: Visualization of the vanEijck-3 and experimental forms of molecule X.

axitinib geometries were provided by Prof. Greg O. Beran from Ref. 15, optimized using the B86bPBE-XDM DFA. The geometries for forms Y and R of ROY were taken from Beran *et al.* [16], optimized using the B86bPBE-XDM DFA.

TABLE 1: Estimated dipole moment per monomer in the unit cell (in Debye) for the 13 ice systems in the ICE13 dataset for the large, medium and small sizes. We used the TTM2.1-F [17] polarizable water model to compute the dipole moments. We generated $3 \times 3 \times 3$ supercell in a box with large vacuum and computed the net dipole of the inner unit cell.

	Large	Medium	Small
Ih	0.00	0.00	1.39
II	0.01	0.02	1.21
III	0.05	0.54	0.96
IV	0.02	-	0.00
VI	0.00	0.02	1.54
VII	0.00	0.02	0.80
VIII	-	-	0.00
IX	-	-	0.01
XI	-	-	0.00
XIII	-	-	1.46
XIV	-	-	0.00
XV	-	-	0.02
XVII	-	-	0.00

B. Periodic HF and DFT

1. VASP

The periodic HF calculations were all performed in the GPU implementation of the Vienna *ab-initio* simulation package [18–20] (VASP) 6.4.2. We used version 54 of the hard (denoted by X_h, where X is the element) PBE projector augmented wave (PAW) potentials, together with an energy cutoff of 1000 eV. A Γ -centered k -point mesh was used in all the systems, with the k -point density set (via the KSPACING parameter) to 0.2 \AA^{-1} and the truncated Coulomb potential

(HFRCUT=-1). We also utilized the Adaptively Compressed Exchange [21] (ACE) operator to accelerate the HF calculations, enabled by setting ALGO=Normal. In Section 10, the benchmarks for the PBE-D3(BJ) [5, 22], revPBE-D3(0) [22, 23], r²SCAN-D4 [24, 25], optB86b-vdW [26] and vdW-DF2 [27, 28] DFAs were performed in VASP, utilizing the same parameters as the periodic HF calculations.

2. FHI-AIMs

The benchmarking for a subset of DFAs (B86bPBE-XDM, B86bPBE-XDM-25 [29], B86bPBE-XDM-50 [29], PBE0-MBD [30, 31] and PBE+TS [5, 6] in Section 10 was performed in the Fritz Haber Institute *ab initio* molecular simulations (FHI-aims) package [32]. We used slightly different procedures to reach the basis set limit depending on the type (i.e., cost) of the underlying DFA. B86bPBE-XDM was performed with the `tight` basis sets, while we approximated the `tight` limit for B86bPBE-XDM-25 and B86bPBE-XDM-50 using the procedure of Price *et al.* [29]:

$$E_{\text{hybrid}}^{\text{tight}} \approx E_{\text{hybrid}}^{\text{lightdense}} + \left(E_{\text{GGA}}^{\text{tight}} - E_{\text{GGA}}^{\text{lightdense}} \right), \quad (1)$$

where the GGA is B86bPBE-XDM and the hybrid is either B86bPBE-XDM-25 or B86bPBE-XDM-50, which were performed with the `lightdense` basis sets. We make use of a similar composite process for PBE0-MBD, which were also both performed with the `lightdense` basis set and subsequently corrected to the `tight` basis set using PBE-MBD and PBE-D3(BJ) DFAs, respectively. PBE-TS was performed directly at the `tight` basis set level. The DFT calculations were performed with scalar relativistic effects and a Γ -centred k-point density (using the parameter `k_grid_density` of 4, increased to 6 for MBD-based DFAs).

3. Quantum Espresso

We used Quantum Espresso [33] to benchmark the cost of hybrid DFT on the CPU with the ACE operator in Section 5. We used the Precision Standard Solid State Pseudopotentials [34], together with an energy cutoff of 80 Ry and charge density cutoff of 320 Ry. We used the same k -point grids as used for the corresponding VASP calculations.

C. Correlated wavefunction theory

We leverage developments in the local natural orbital (LNO) [35–38] approximation to coupled cluster theory with single, double, and perturbative triple excitations [CCSD(T)] [39] in MRCC [40–42]. In addition, we also performed density-fitted second-order Møller-Plesset perturbation theory (DF-MP2) [43] to correct for local correlation and basis set errors as described in Section 3 A 6. LNO-CCSD(T) was performed with a patched 2023 version of the MRCC [40–42] program, described in Section 2 D, that has been optimized for many-body expansion calculations. The improvements described in Section 2 D are available and made to be the default setting for LNO methods since the 2025 version of MRCC. To reach the local approximation free (LAF) limit, we use the following formula from Refs. 37, 38:

$$E^{\text{LAF N-T}} = E^{\text{Tight}} + 0.5 (E^{\text{Tight}} - E^{\text{Normal}}). \quad (2)$$

We used the Dunning family [44] of correlation consistent basis sets, specifically the aug-cc-pVXZ basis set family for lattice energies and jul-cc-pVXZ basis set family for relative energies. The latter corresponds to only using cc-pVXZ on the H atoms, while using the aug-cc-pVXZ basis set on the other atoms. We have tested the CBS(DZ/TZ) and CBS(TZ/QZ) two-point complete basis set (CBS) extrapolations for the double-zeta (DZ), triple-zeta (TZ) and quadruple-zeta (QZ) basis sets. We employed the following two-point-extrapolation formulae:

$$E_{\text{corr}}^{\text{CBS}} = \frac{X^\beta E_{\text{corr}}^X - Y^\beta E_{\text{corr}}^Y}{X^\beta - Y^\beta}, \quad (3)$$

$$E_{\text{HF}}^{\text{CBS}} = E_{\text{HF}}^X - \frac{E_{\text{HF}}^Y - E_{\text{HF}}^X}{\exp(-\alpha\sqrt{Y}) - \exp(-\alpha\sqrt{X})} \exp(-\alpha\sqrt{X}), \quad (4)$$

for the correlation and HF components of the energy, with X and $Y = X + 1$ denoting the (zeta) size of the basis set. We use $\alpha = 5.79$ and $\beta = 3.05$ when using the aug-cc-pVXZ and $\alpha = 5.625$ and $\beta = 3.05$ when using the jul-cc-pVXZ, as adapted from Ref. 45. We use the def2-QZVPP-RI-JK auxiliary basis function for density-fitting/resolution-of-identity Hartree-Fock (HF) computations, and the RI auxiliary basis sets from Weigend [46, 47] corresponding to the atomic orbital basis sets for subsequent cWFT calculations. Counterpoise corrections were employed when calculating all terms.

D. Many-body expansion

The cWFT calculations described in the preceding section were performed on molecular clusters generated by the many-body expansion [48–50] (MBE). The MBE allows for the interaction or total energy of a system formed of (molecular) monomers to be expressed as a sum of 1-body, 2-body, 3-body, and higher-order terms:

$$E = \sum_i E_i + \sum_{i>j} \Delta^2 E_{ij} + \sum_{i>j>k} \Delta^3 E_{ijk} + \dots \quad (5)$$

Here, the first term is a sum over the total energy E_i minus a reference energy E_{ref} (typically taken as the optimized gas-phase energy) for each molecule which makes up the unit cell. The second term sums over the 2-body (2B) interaction energies for each enumerated pair of molecules i and j :

$$\Delta^2 E_{ij} = E_{ij} - E_i - E_j. \quad (6)$$

The third term gives the 3-body contributions involving molecules i , j , and k which are nonadditive (i.e., beyond the sum of the individual pairwise interactions):

$$\Delta^3 E_{ijk} = E_{ijk} - \Delta^2 E_{ij} - \Delta^2 E_{ik} - \Delta^2 E_{jk} - E_i - E_j - E_k. \quad (7)$$

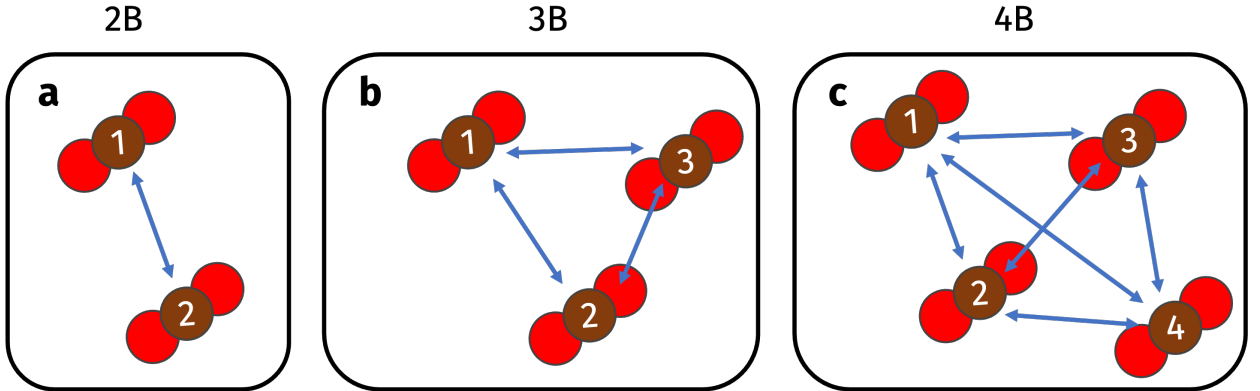


FIG. 2: Schematic describing the distance metrics used for the (a) two-body (2B), (b) three-body (3B) and (c) four-body (4B) terms.

The main advantage of this approach is that it restricts the (expensive) cWFT calculations to smaller fragments as opposed to a full calculation of the whole unit cell. For example, for ice, it has been shown that the total lattice energy converges at the 4-body term [51]. Furthermore, it is possible to truncate the distance required to compute each of these contributions, lowering

the cost more. While the distance metric between two monomers is straightforward – being the distance between their center of masses or a specific atom within each molecule – it is less clear for three or four bodies. We follow the convention of Herman and Xantheas [51], where the distance metric is formed as the product of pairwise distances between all monomers. We have described the standard MBE here, but we explore further methods to lower its cost in Section 2.

We report the final 2B and 3B distance cutoffs for the system studied within this work in Table 2. These cutoffs were selected based upon convergence of these terms for the various systems reported throughout, given in the table.

TABLE 2: Two (2B) and three (3B) body cutoffs for the systems studied within this work.

System	2B cutoff (Å)	3B cutoff (Å ³)	Convergence	Reference
X23	12	300	Section 2 B	Table 26
ICE13	9	150	Section 2 A	Table 33
ROY	16	800	Section 8 B	Table 44
Axitinib	20	720	Section 8 B	Table 44
Rotigotine	19	750	Section 8 B	Table 44
Molecule X	16	450	Section 8 B	Table 44

2. LOWERING COMPUTATIONAL COST OF MBE

In this section, we describe the techniques employed within this work to lower the cost of standard MBE – dubbed ‘full enumeration’. In particular, these approaches enhance the efficiency of the MBE by decreasing the number of terms and maximum order contribution required in the MBE. We emphasize here that several of these approaches have been explored within previous work (and we will endeavour to highlight the prior work). The key development here is that we have combined all these approaches to make the most efficient MBE strategy to date for studying molecular crystals that can reach sub-chemical accuracy on E_{rel} . When combined with an LNO-CCSD(T) approach that has been further optimized for the MBE within this work, it has allowed for complex (pharmaceutical-sized) molecular crystals to be studied. We have dubbed this framework LNO-MBE-CCSD(T) in this paper. The final comparison of the cost to perform LNO-MBE-CCSD(T) is tabulated and discussed in Section 5.

A. Removing HF contribution to handle only electron correlation

As a post-HF method, the CCSD(T) total energy is made up of HF energy contribution as well as the CCSD(T) correlation energy contribution. These two terms account for different types of physical interactions [52]. The HF contribution primarily accounts for the electrostatic, exchange, and induction components of the lattice energy. The CCSD(T) correlation energy includes van der Waals dispersion, charge-transfer effects and the electron correlation contribution to the higher order coupling of all the above. As such, they have differing behaviors in their separate MBE. In fact, the MBE for HF is significantly more challenging than the MBE for the CCSD(T) correlation energy as it (1) requires longer distance cutoffs to converge any of the terms and (2) higher-order many-body terms.

We illustrate the differing behavior of HF and CCSD(T) in Figure 3 for the two-body (2B) and three-body (3B) contribution to the total energy of ice VIII. As seen for both the 2B and 3B contributions, the HF energy converges non-monotonically as a function of distance while the correlation energy components converge rapidly with distance cutoffs. For example, the CCSD(T) correlation energy contribution to the two-body terms has converged to sub ~ 0.1 kJ/mol by a 7 Å while there are still 4 kJ/mol jumps for the HF energy, which manifest in the total energy as well. Beyond just a slower convergence with the distance cutoff, there is also a worse convergence with number of body terms for the total energy. In Table 3, we show for ice VIII that the total energy

contribution of four-body terms – computed with MBpol [53, 54] from Herman and Xantheas [51] – still has a significant contribution of ~ 0.8 kJ/mol while the correlation energy we have computed with CCSD(T) contributes less than 0.1 kJ/mol.

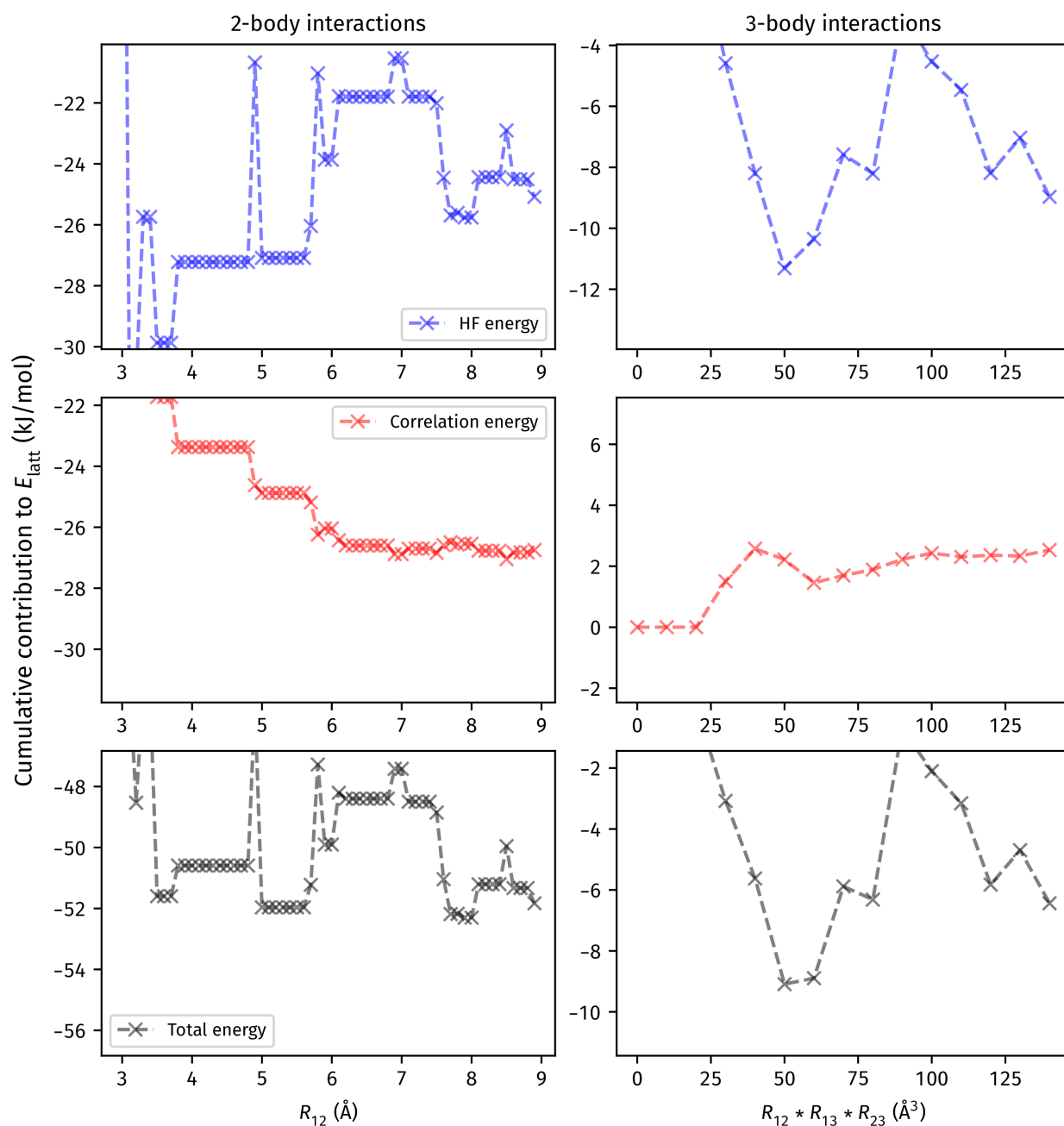


FIG. 3: Comparison of the convergence behaviour of the HF, CCSD(T) correlation and total energy for the two-body and three-body contributions to the lattice energy of ice VIII. The aug-cc-pVTZ and aug-cc-pVDZ basis sets were used for the 2B and 3B contributions, respectively. CCSD(T) calculations are accelerated with the LNO approximation using vTight thresholds.

These observations thus highlight the advantage of separating the treatment of both HF and

TABLE 3: MBE contributions up to four-body (4B) for the total and correlation energy contribution to ice VIII. The correlation energy contribution comes from the ‘Canonical’ approach described in Section 3 A 6.

Contribution (kJ/mol)	Correlation	Total (MBpol [51])
1B	-5.3	1.2
2B	-31.0	-53.9
3B	2.5	-6.7
4B	-0.1	3.2

CCSD(T). Furthermore, as we highlight in Section 5, advancements in the treatment of HF under periodic boundary conditions now make it economical to treat this component directly without resorting to the MBE.

It should be emphasized here that the idea to separate the treatment of HF and CCSD(T) correlation has been explored across several different studies for various systems. For ice Ih, it was shown by Hermann [55] that correlation energies up to only 2B terms are needed to compute the total energy of this system. This has also been further demonstrated for both water clusters and ice clusters by Gillan *et al.* [56] as well as for driving molecular dynamics simulations of water clusters by Heindel and Xantheas [57]. For molecular crystals, this has been recently used by Syty *et al.* [58] for the X23 dataset, with 2B contributions computed by LNO-CCSD(T) and 3B contributions from the random phase approximation (RPA). Similarly, such subtractive embedding approaches have been shown earlier for diverse molecular crystal systems by Müller and Usvyat [59] as well as Beran and co-workers [60–62]. Such an approach has also been employed to study hydrates [63]. Separate from the goal to reach cWFT accuracy, Boese and co-workers [64, 65] have demonstrated its usefulness to bring GGA-level DFT calculations up to the hybrid-DFT level from 2B contributions.

B. Enhancing distance convergence using empirical dispersion corrections

The CCSD(T) correlation energy is largely dominated by van der Waals dispersion interaction. There exist widely-used force-fields [66–70] that approximate this contribution, most relevantly to the present work through a family of dispersion corrections developed by Grimme [22, 71–73] for DFT. The D4 dispersion correction has also been parametrized for HF and we used

this parametrization as it corresponds to a direct approximation of the dispersion contributions from the correlation energy. This family of dispersion corrections are trivial and cost-effective to compute as they only depend on atomic numbers and positions. The latest is the D4 correction [73], which improves upon the previous D3 correction by incorporating an atomic-charge dependence (based on atomic charges computed using classical electronegativity equilibration partial charges). In addition, three-body dispersion effects are described using an Axilrod-Teller-Muto term [74, 75]. We remove the D4 term from the CCSD(T) correlation energy and instead compute the difference between the CCSD(T) and D4 energy ($\Delta_{D4}^{CCSD(T)}$), which we can converge instead. The full D4 term with periodic boundary conditions can be trivially computed and added onto the periodic HF calculation.

In Figs. 4 to 26, we illustrate the convergence of the 2B and 3B terms as a function of distance cutoffs relative to the converged value of both the CCSD(T) correlation energy and $\Delta_{D4}^{CCSD(T)}$ for all 23 molecules in the X23 dataset. Here, we have used $R_{12} = 12 \text{ \AA}$ and $R_{12} * R_{23} * R_{13} = 300 \text{ \AA}^3$ distance cutoffs as the converged value for the 2B and 3B terms, respectively. It can be seen that $\Delta_{D4}^{CCSD(T)}$ converges faster with distance cutoff than the CCSD(T) correlation energy, allowing shorter truncation distances and fewer overall calculations. For the latter, by a 9 \AA cutoff on the 2B terms, 18 out of 23 were converged to within 1 kJ/mol for $\Delta_{D4}^{CCSD(T)}$ while only 4 were converged for the CCSD(T) correlation energy. Similarly, by a 200 \AA^3 cutoff on the 3B terms, 20 out of 23 were converged to within 1 kJ/mol with $\Delta_{D4}^{CCSD(T)}$ while 18 were converged for the CCSD(T) correlation energy.

Part of the faster convergence of $\Delta_{D4}^{CCSD(T)}$ arises from the fact that it has a smaller value than the CCSD(T) correlation energy. For example, its lies in the range between -5.6 to 12.3 kJ/mol for the 2B terms, an order of magnitude smaller range than the correlation energy, which lies between -171.7 to -26.9 kJ/mol for the 2B terms. The resulting decrease in required cutoff distance allows us to decrease the number of terms required. For example, the number of 2B terms at 9 \AA is half that at 12 \AA for most systems in Table 4, and there is a similar decrease in number of 3B terms between 250 \AA^3 and 300 \AA^3 distance cutoff in Table 5.

A final outcome is that we now have two approaches that converge systematically towards the final result with distance cutoff, given a means to validate our results. In Table 30 of Section 4, we show that there is a small difference in the resulting lattice energy E_{latt} at for 2B and 3B cutoffs of 12 \AA and 300 \AA^3 , respectively, when using either the $\Delta_{D4}^{CCSD(T)}$ or CCSD(T) correlation energy in the MBE treatment. Specifically, we find a mean-absolute-deviation (MAD) of 0.42 kJ/mol and root-mean-square-deviation of 0.79 kJ/mol, confirming the sub-kJ/mol convergence of the

chosen distance cutoffs.

It is instructive to highlight again that this type of subtractive embedding between two levels of theory in the MBE has been explored by other authors. For example, Sherrill and co-workers [76–79] have considered several variations of second-order Møller-Plesset perturbation theory. Similarly, this has been explored by Beran and co-workers [60, 61, 67, 80] through their Hybrid Many-body Interaction (HMBI) approach. Klimes and Modrzejewski [58, 81–83] have explored subtractive embedding on top of variants of the random phase approximation (RPA). Finally, the partitioning of the CCSD(T) total energy into the HF and correlation energy described in the preceding section is itself a type of subtractive embedding. To our knowledge, no study has used the D4 dispersion (on top of HF) proposed within this work.

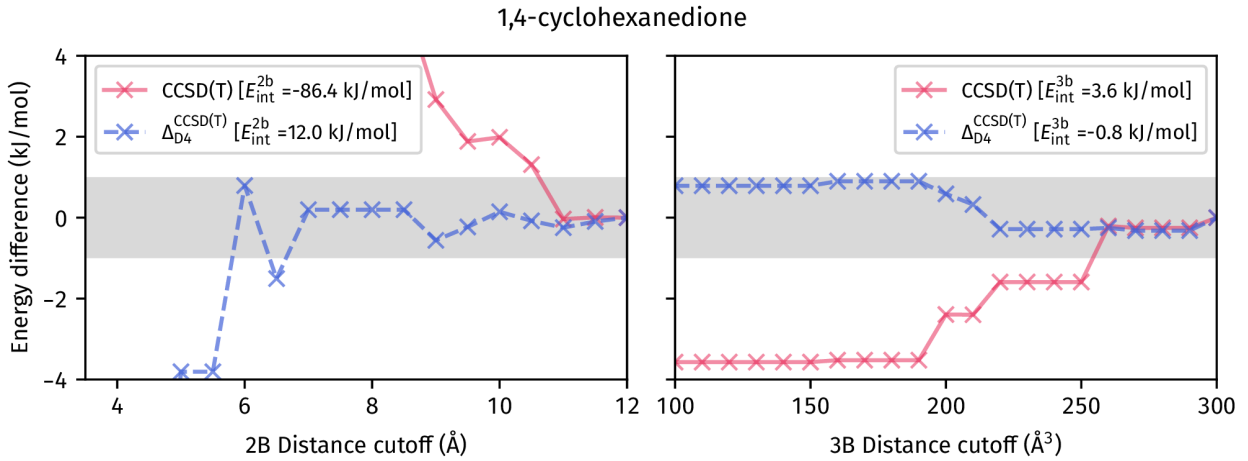


FIG. 4: The convergence with distance cutoff of the two-body (2B) and three-body (3B) components of the many-body expansion (MBE) for the lattice energy E_{latt} of 1,4-cyclohexanedione from the X23 dataset. The red line shows the CCSD(T) result, while the blue line shows the difference to the D4 result. The shaded area indicates the range of energies between -1 and 1 kJ/mol. We use the pairwise distance R_{12} between the two monomers in the 2B case, and the product of the pairwise distances $R_{12} * R_{13} * R_{23}$ in the 3B case.

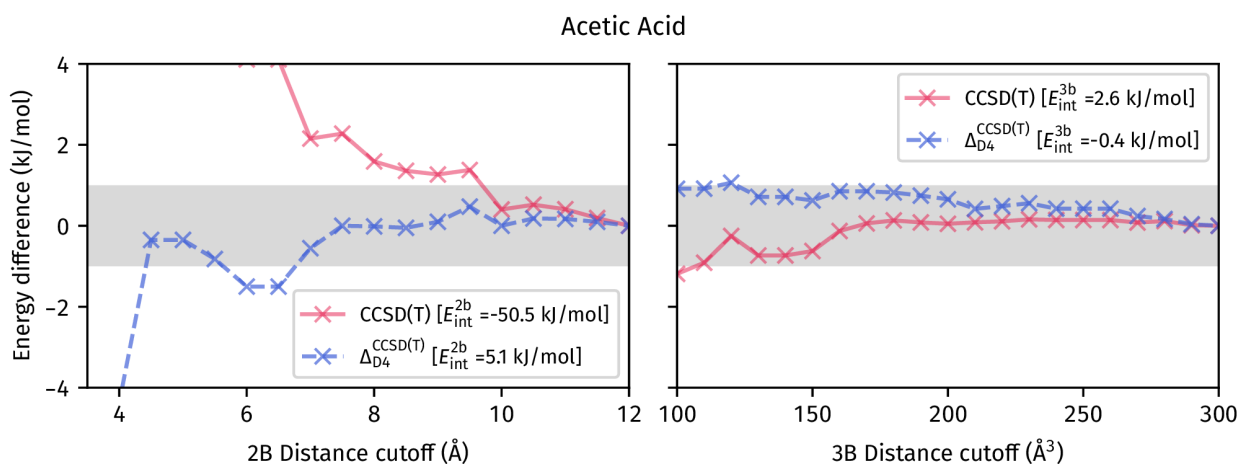


FIG. 5: The convergence of the 2B and 3B MBE components to the E_{latt} of acetic acid.

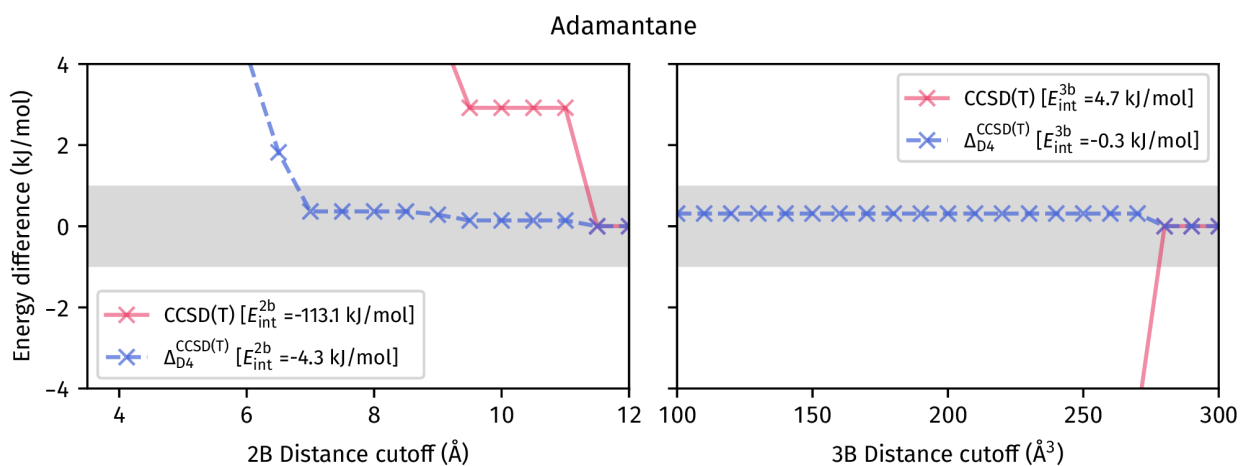


FIG. 6: The convergence of the 2B and 3B MBE components to the E_{latt} of adamantane.

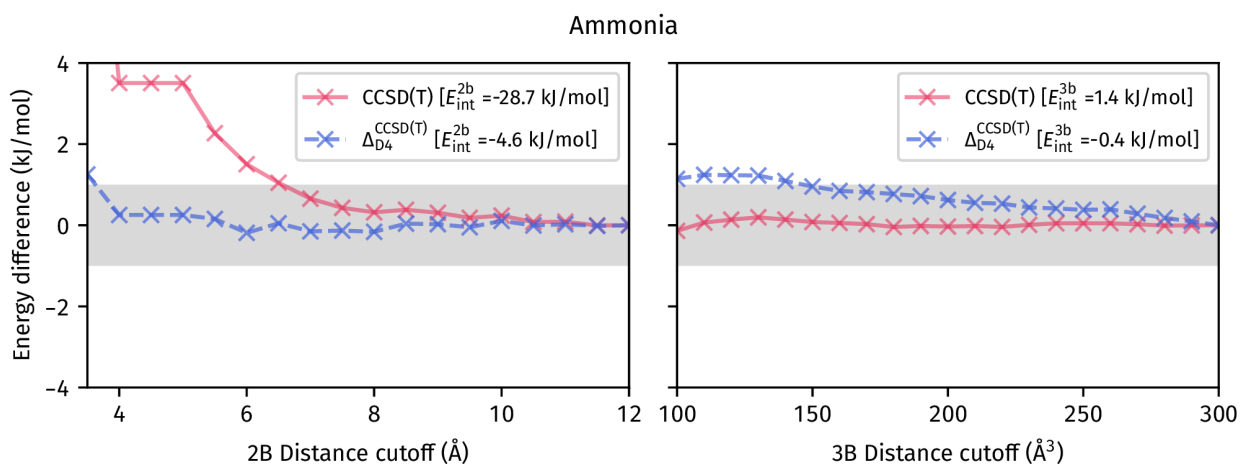


FIG. 7: The convergence of the 2B and 3B MBE components to the E_{latt} of ammonia.

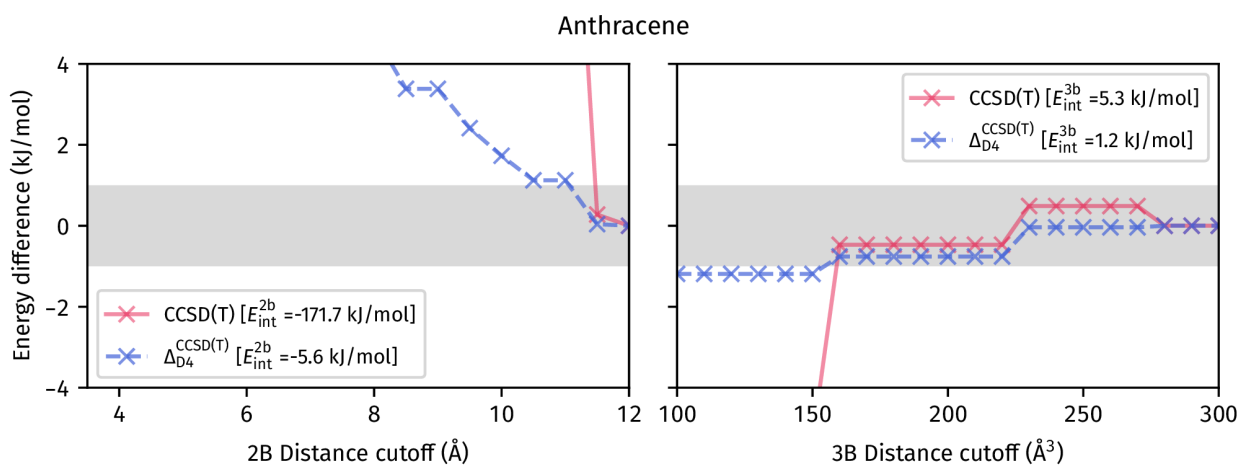


FIG. 8: The convergence of the 2B and 3B MBE components to the E_{latt} of anthracene.

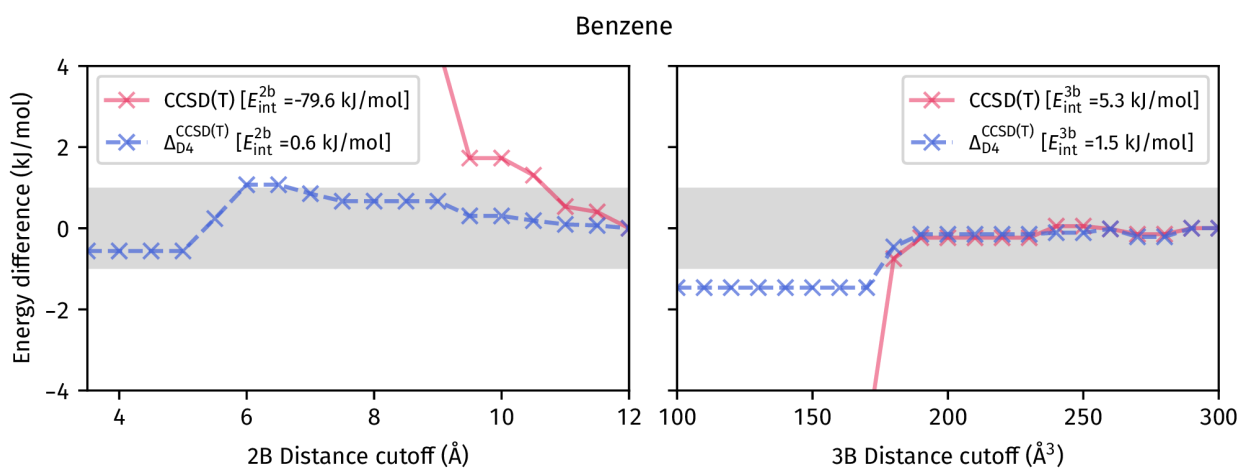


FIG. 9: The convergence of the 2B and 3B MBE components to the E_{latt} of benzene.

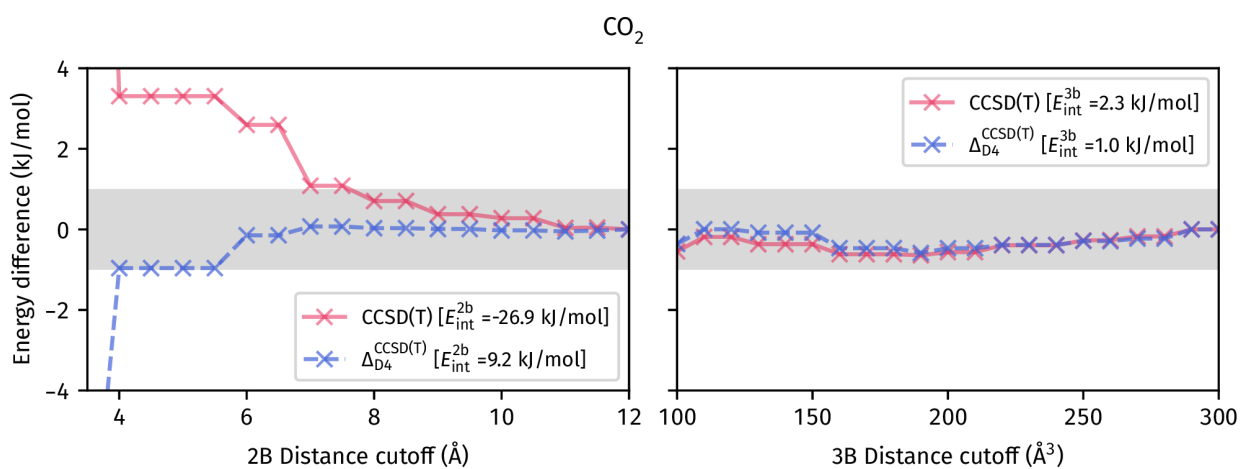


FIG. 10: The convergence of the 2B and 3B MBE components to the E_{latt} of CO₂.

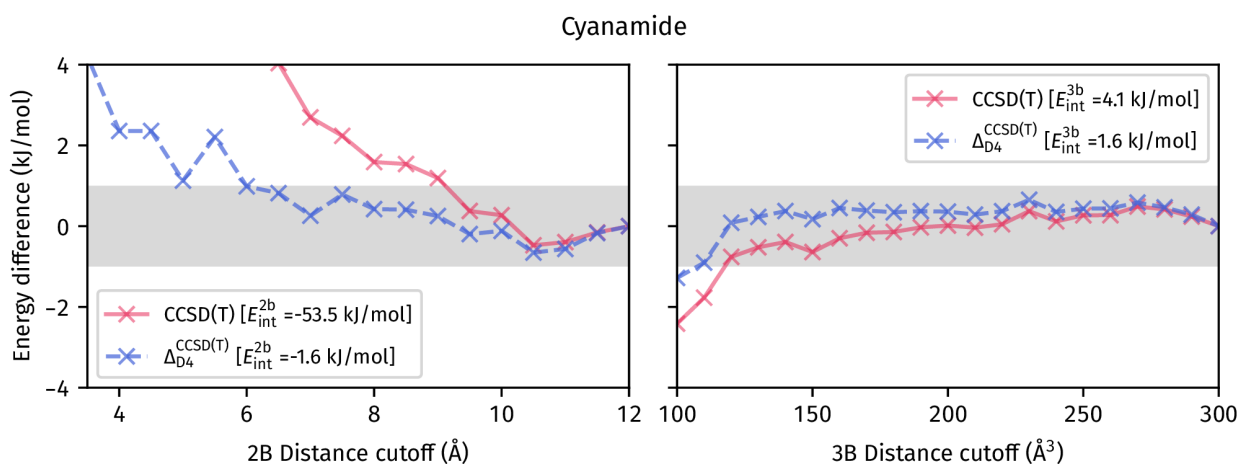


FIG. 11: The convergence of the 2B and 3B MBE components to the E_{latt} of cyanamide.

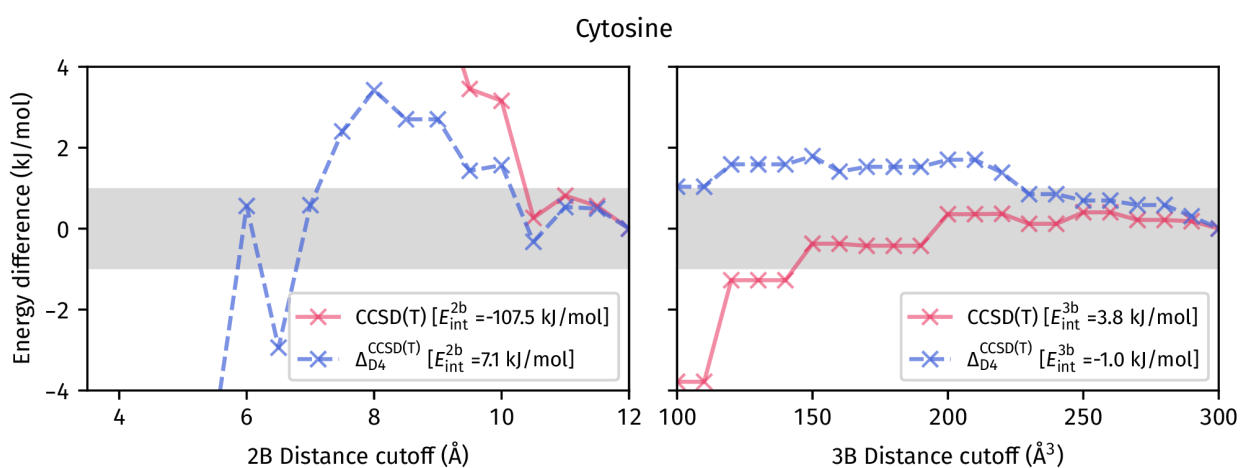


FIG. 12: The convergence of the 2B and 3B MBE components to the E_{latt} of cytosine.

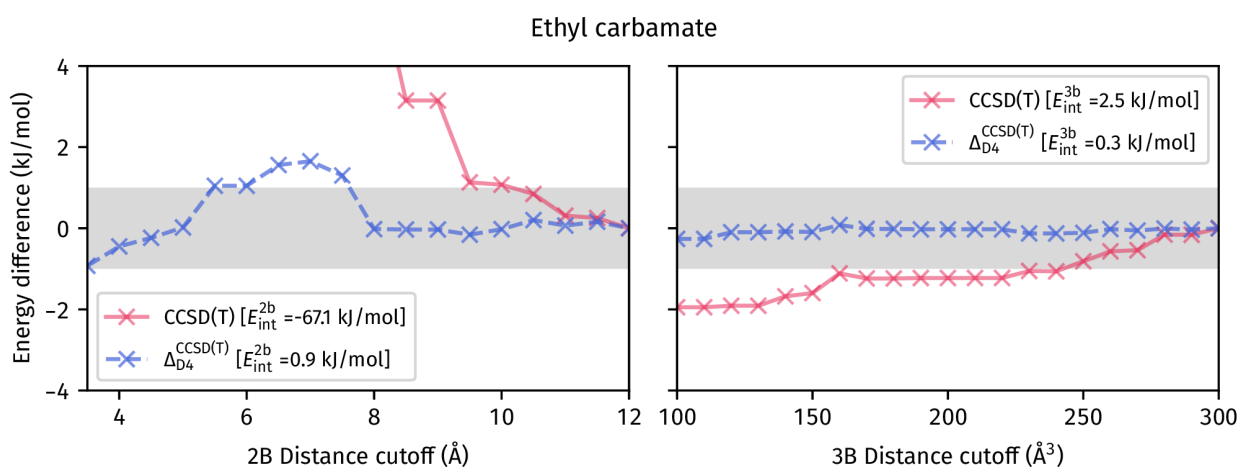


FIG. 13: The convergence of the 2B and 3B MBE components to the E_{latt} of ethyl carbamate.

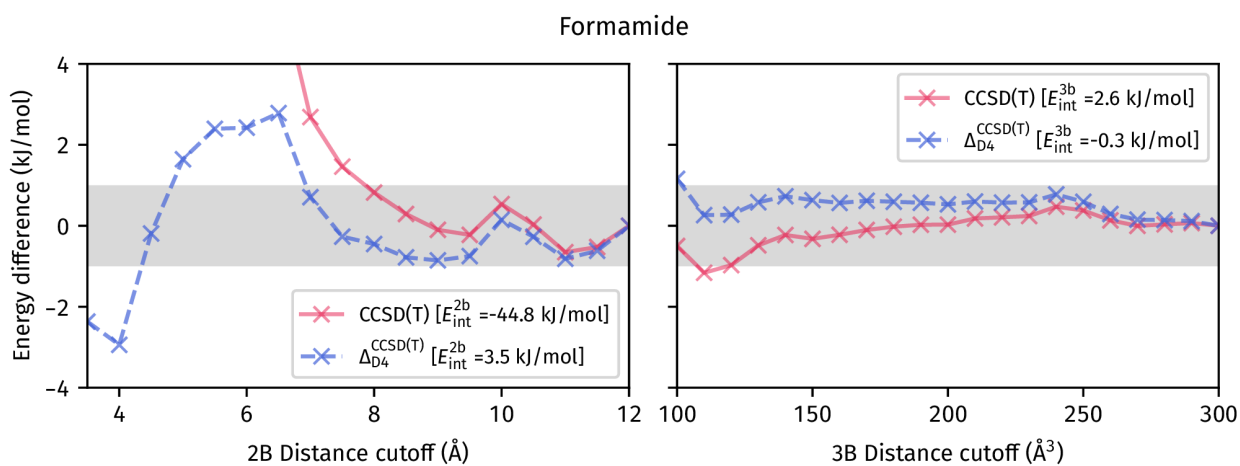


FIG. 14: The convergence of the 2B and 3B MBE components to the E_{latt} of formamide.

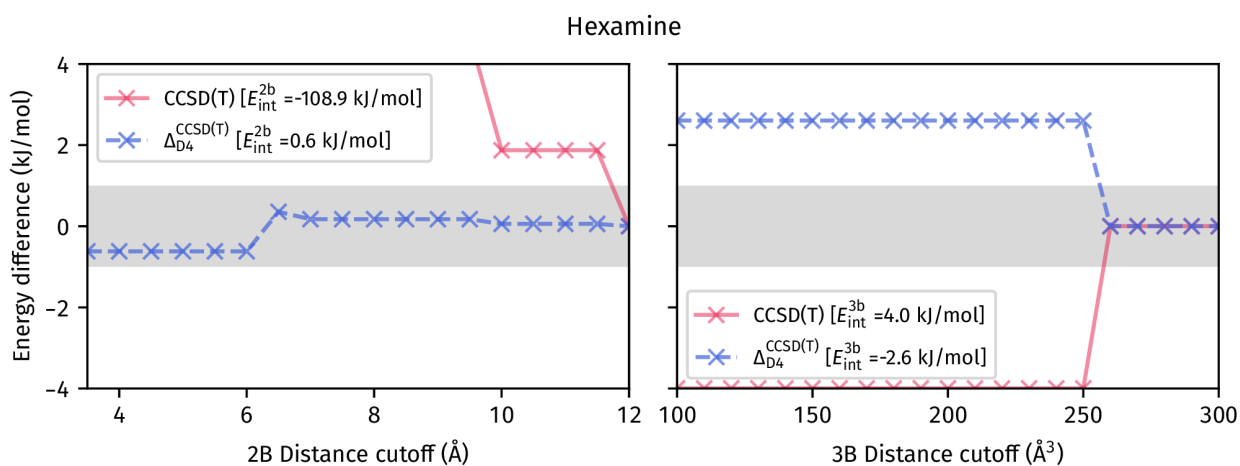


FIG. 15: The convergence of the 2B and 3B MBE components to the E_{latt} of hexamine.

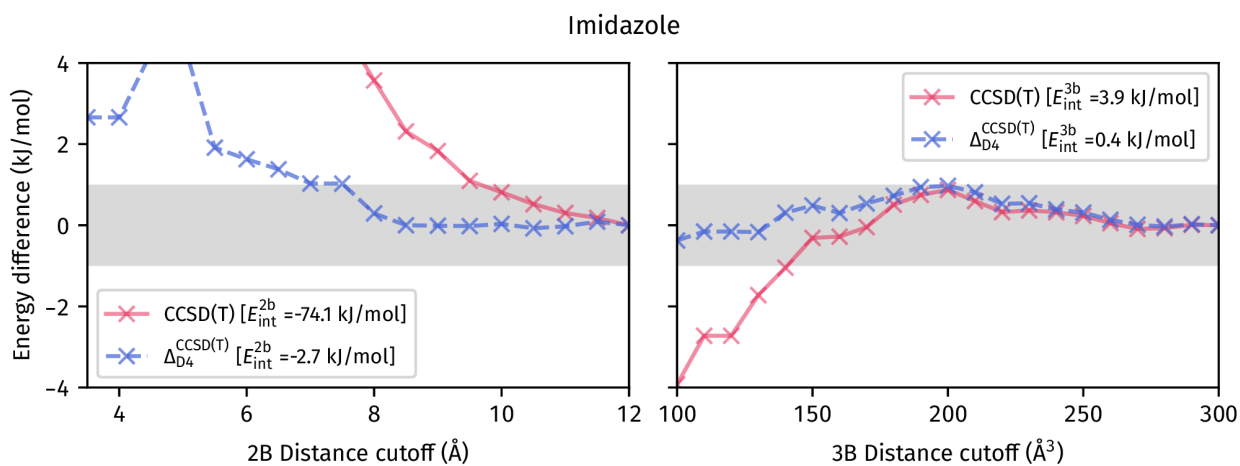


FIG. 16: The convergence of the 2B and 3B MBE components to the E_{latt} of imidazole.

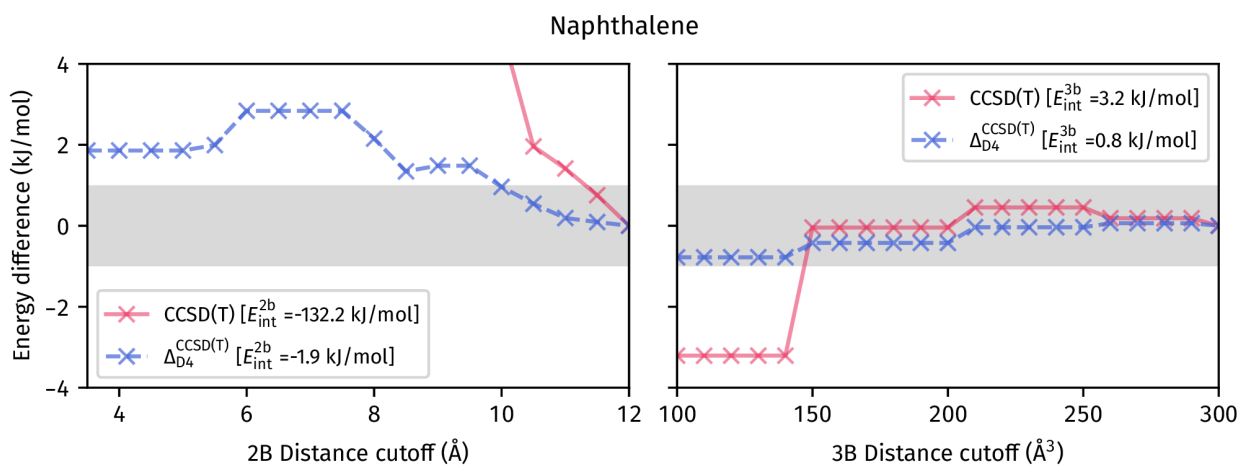


FIG. 17: The convergence of the 2B and 3B MBE components to the E_{latt} of naphthalene.

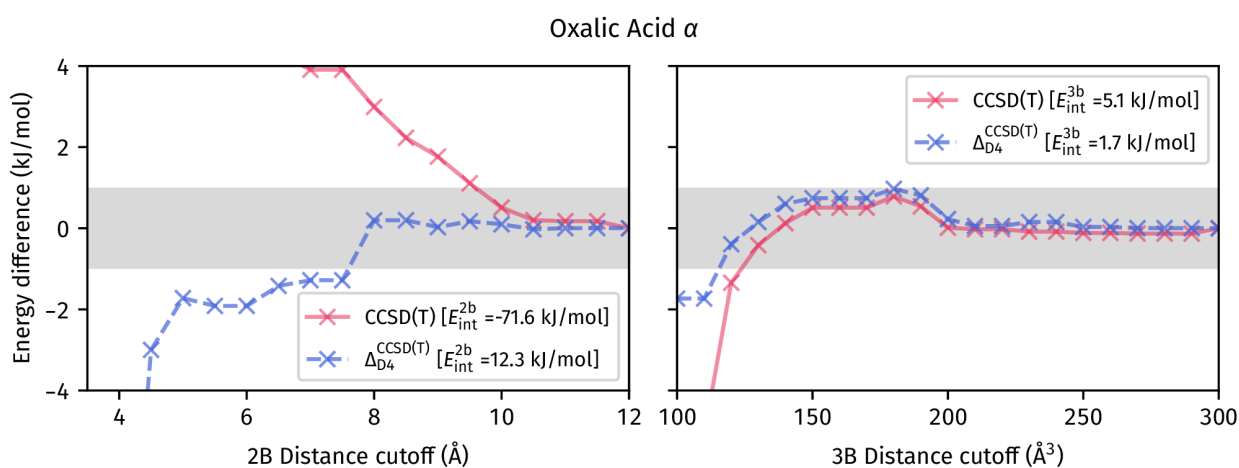


FIG. 18: The convergence of the 2B and 3B MBE components to the E_{latt} of oxalic acid α .

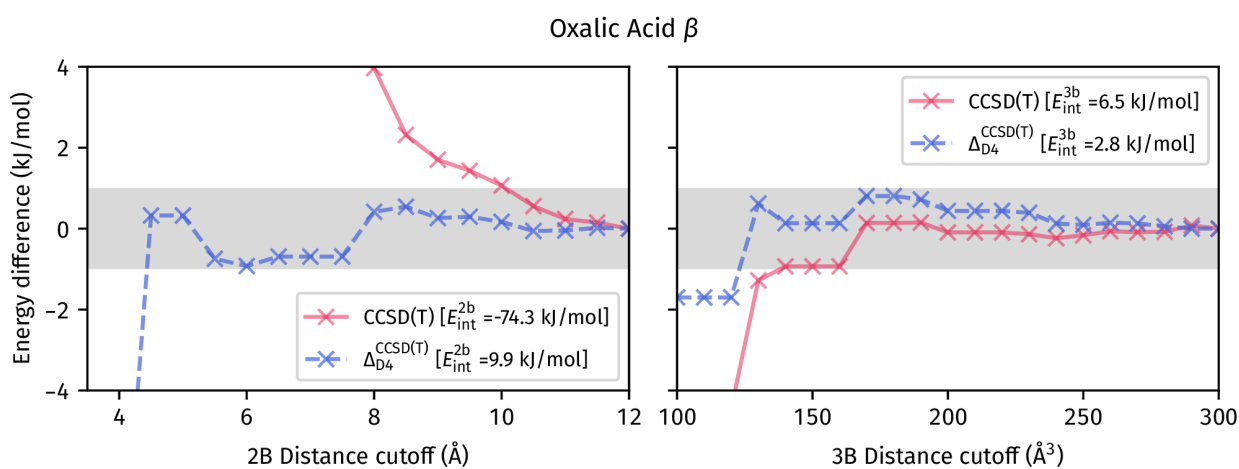


FIG. 19: The convergence of the 2B and 3B MBE components to the E_{latt} of oxalic acid β .

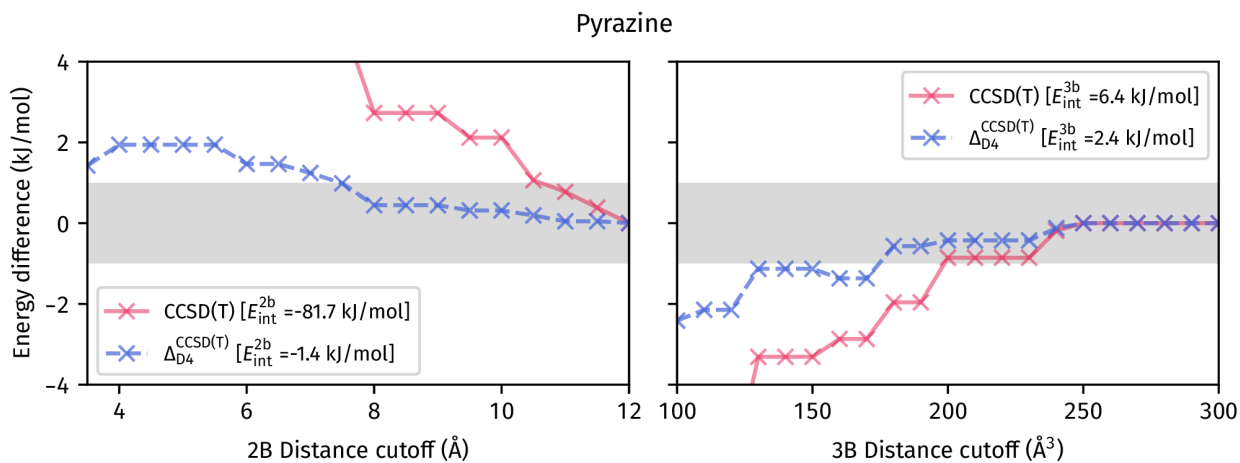


FIG. 20: The convergence of the 2B and 3B MBE components to the E_{latt} of pyrazine.

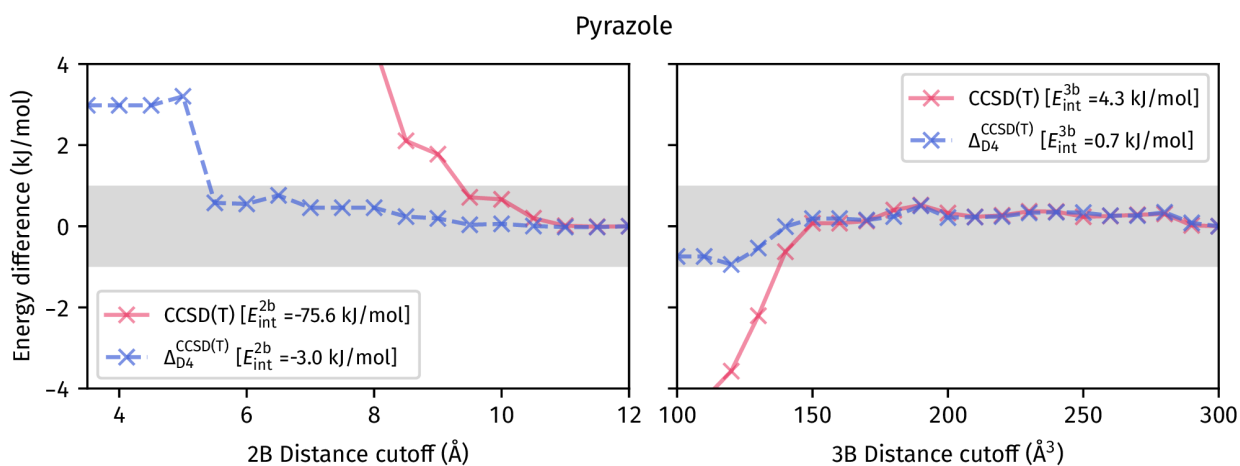


FIG. 21: The convergence of the 2B and 3B MBE components to the E_{latt} of pyrazole.

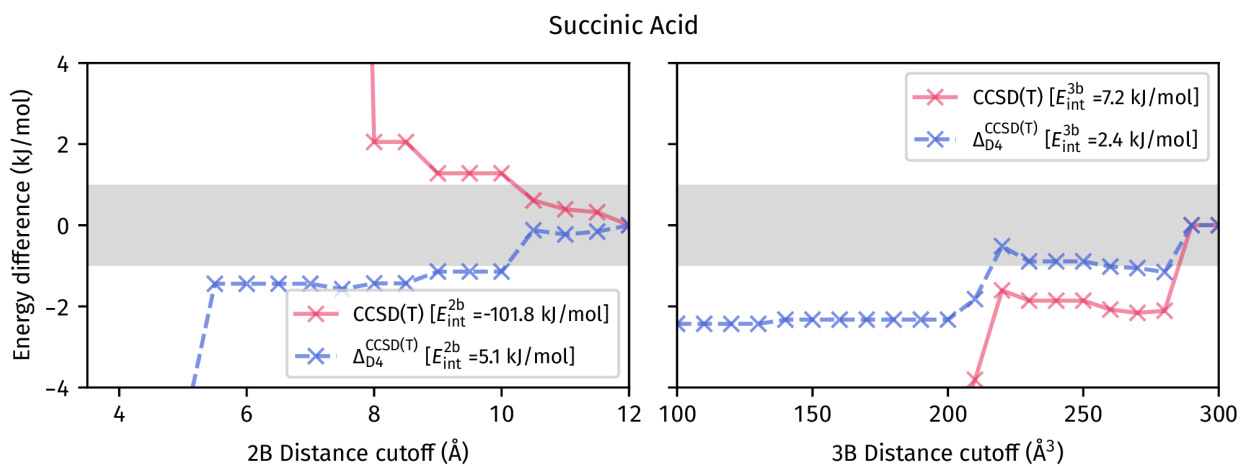


FIG. 22: The convergence of the 2B and 3B MBE components to the E_{latt} of succinic acid.

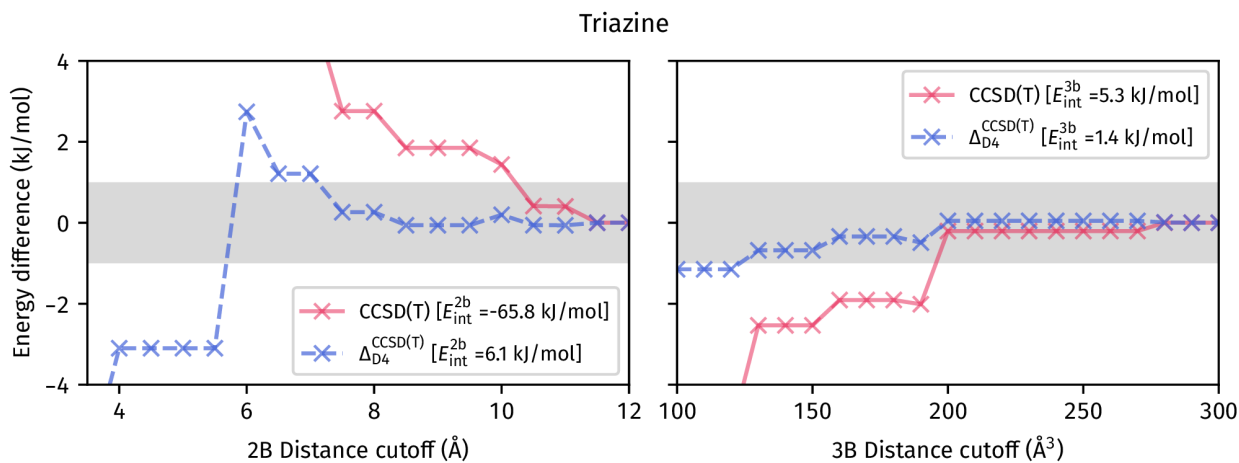


FIG. 23: The convergence of the 2B and 3B MBE components to the E_{latt} of triazine.

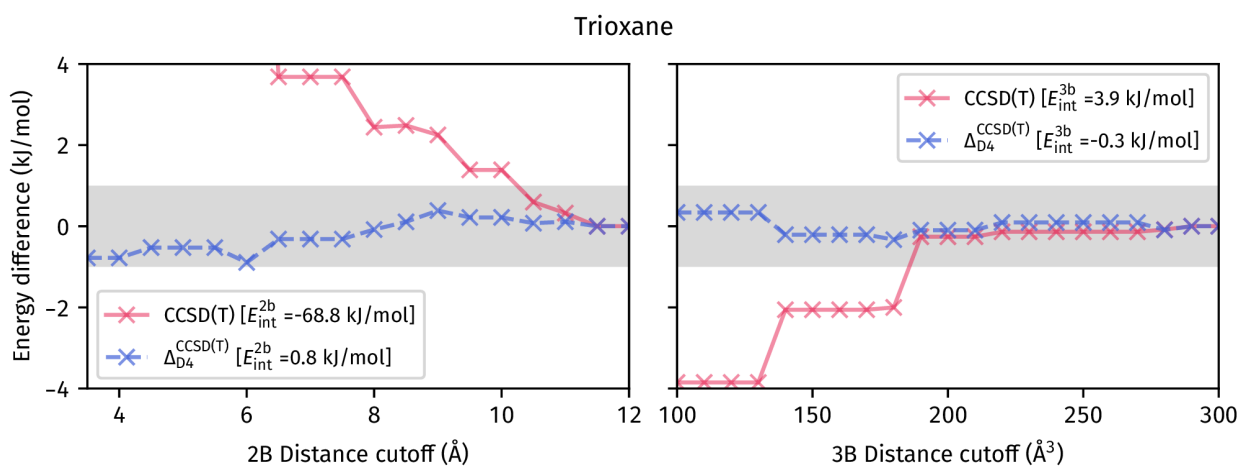


FIG. 24: The convergence of the 2B and 3B MBE components to the E_{latt} of trioxane.

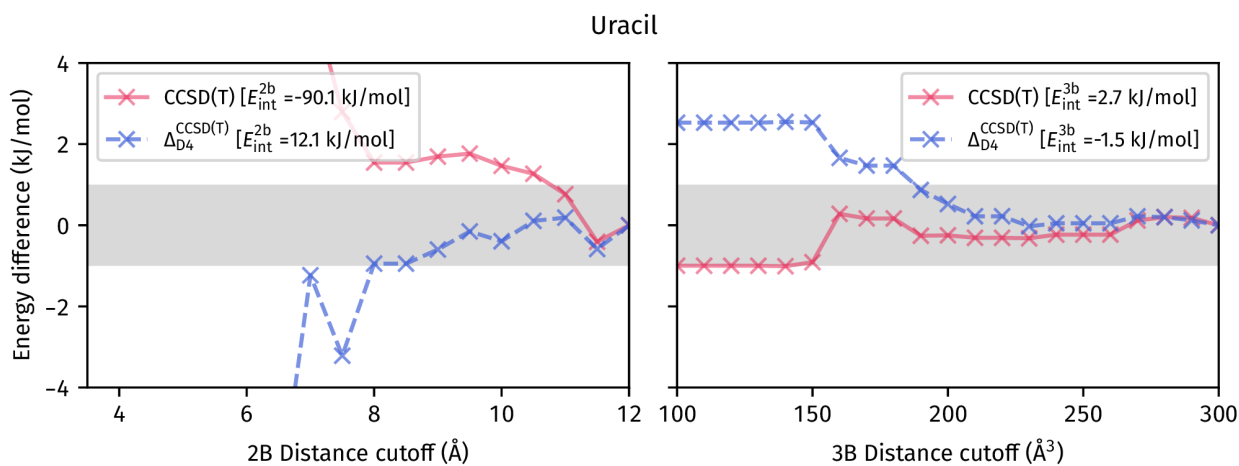


FIG. 25: The convergence of the 2B and 3B MBE components to the E_{latt} of uracil.

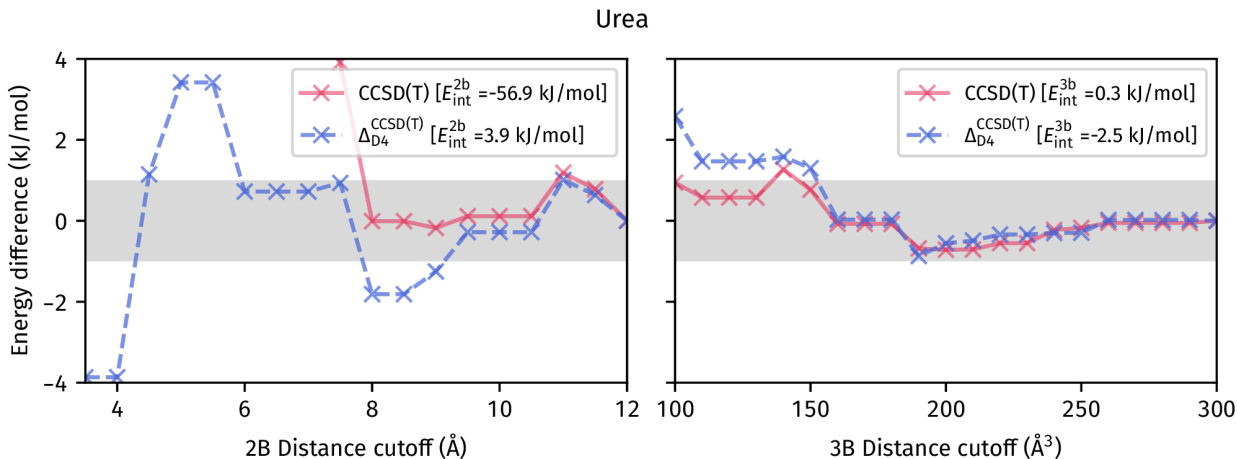


FIG. 26: The convergence of the 2B and 3B MBE components to the E_{latt} of urea.

C. Identifying symmetrically and translationally redundant terms

So far, we have dealt with physical approaches to remove or decrease the number of calculations required to reach convergence of the MBE. Here, we will consider mathematical or machine-learning means to identify equivalent subsystems due to symmetry so that there are no redundant calculations. As illustrated in Figure 27, within this work, we use the periodic MBE approach developed by Herman and Xantheas [51] to remove terms which are translationally equivalent relative to a full enumeration of the MBE, followed by a Coulomb-matrix descriptor to further filter the remaining terms. This entire process is automated within the pMBE code on Github that will be available upon publication. In Tables 4 and 5, we tabulate the cumulative number of 2B and 3B terms, respectively, as a function of distance cutoff. For the former, we use the distance between the center of mass of the two molecules while in the latter, we use the product of the (three) pairwise distances between the three molecules.

1. Periodic MBE

The periodic MBE (shortened to pMBE) leverages the inherent translational symmetry of the periodic system. That said, the maximum reduction in the number of subsystems (in comparison to a full enumeration) is by a factor of n where n is the order of the expansion. For a unit cell of 1 molecule (i.e., hexamine), the reduction in the 2- and 3-body terms is exactly a factor of 2 and 3, respectively. When the n -body terms are enumerated for each monomer in the unit cell

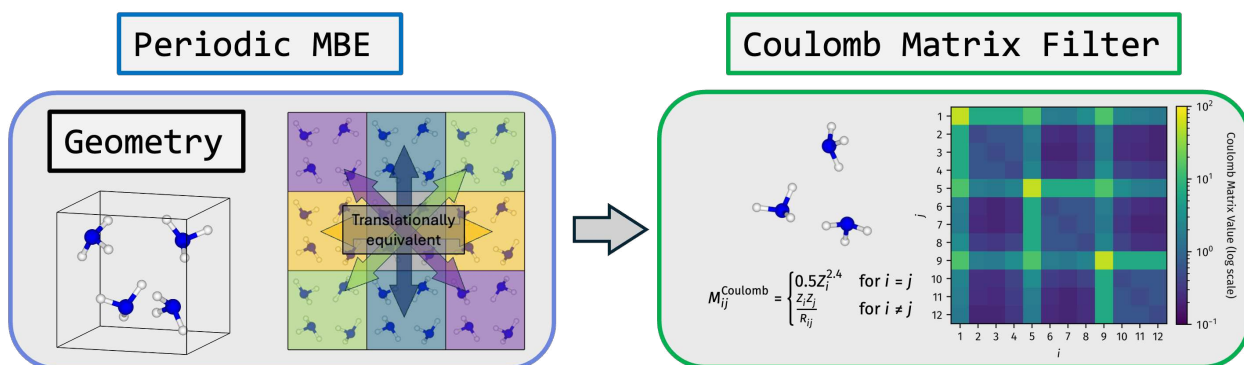


FIG. 27: A schematic of the workflow to generate the dimers and trimers in the MBE. This entire workflow is implemented and automated in the pMBE Github code (available upon publication)

(as is necessary to account for the differing molecular environments in the unit cells of several ice polymorphs), the factor that the terms are reduced are slightly less than n due to the dimers, trimers, etc. that exist within the same unit cell. Naturally, for the case where the n -body terms are enumerated for a single molecule in the unit cell, the savings are dependent on the size of the unit cell. For larger unit cells, the translational symmetry cannot be leveraged as effectively, leading to a smaller reduction of subsystems in comparison to smaller unit cells.

As input, the code requires a unit cell structure, unit cell vectors, and the cutoff distance for the many-body term of interest. It typically takes a fraction of a second on a laptop to enumerate the subsystems necessary to compute the n -body component of the lattice energy. The output of the pMBE code is an SQLite3 database which, for each body term, provides: (1) the Atomic Simulation Environment `Atoms` object (containing the atomic elements and positions) (2) cutoff distance and (3) weight contribution to the lattice energy.

2. Coulomb-matrix filter

The Coulomb-matrix filter can be used to further decrease the number of subsystems taken from the pMBE, decreasing the number of 2B terms by half and in some highly symmetric systems, the number of terms are decreased significantly further. For example, in hexamine at a 2B cutoff of 12 Å, the pMBE approach decreases the number of 2B terms from 50 to 25, with the Coulomb-matrix filter further decreasing this down to 4. The cost savings are even more prominent for 3B terms, where with respect to a full enumeration, the Coulomb matrix filter decreases the number of terms 3B terms within a 300 Å³ cutoff for CO₂ from 1050 down to 56. We note that this approach has also been explored by the CrystaLattE [84] package from Sherrill

and co-workers.

The Coulomb matrix for the combined 2B, 3B (or more) system is defined as:

$$M_{ij}^{\text{Coulomb}} = \begin{cases} 0.5Z_i^{2.4} & \text{for } i = j \\ \frac{Z_i Z_j}{R_{ij}} & \text{for } i \neq j \end{cases}, \quad (8)$$

where i and j are the indices of two atoms. We sort the row and columns of the matrix by its l^2 -norm to ensure permutation symmetry, before flattening the matrix into a one-dimensional array (called the Coulomb array). We use the DScibe Python package [85, 86] to generate these Coulomb arrays. We further regularize the Coulomb matrix by adding the distance cutoff (R_{12} and $R_{12} * R_{23} * R_{13}$ for 2B and 3B systems, respectively, where R_{12} is the distance between the centers of masses of monomers 1 and 2) to the front of this array. Finally, we compare and group the Coulomb arrays using the Density-Based Spatial Clustering of Applications with Noise (DBSCAN) approach [87], as provided by the `scikit-learn` package in Python. Below, we provide an example of the Python code to apply the Coulomb Matrix Filter to filter out the ASE database generated by the pMBE code:

TABLE 4: The number of two-body (2B) terms as a function of distance between the center of mass of the two molecules that make up the dimer subsystem.

2B distance (Å)		5	6	7	8	9	10	11	12
1,4-cyclohexanedione	Full Enumeration	2	6	14	14	16	26	46	50
	pMBE	2	6	11	11	12	18	35	39
	pMBE + Coulomb	1	3	7	7	8	13	23	25
Acetic Acid	Full Enumeration	6	12	22	30	36	62	76	100
	pMBE	5	10	18	25	31	55	69	91
	pMBE + Coulomb	3	6	11	15	18	31	38	49
Adamantane	Full Enumeration	0	0	12	12	14	18	18	42
	pMBE	0	0	10	10	11	13	13	33
	pMBE + Coulomb	0	0	2	2	3	4	4	7
Ammonia	Full Enumeration	12	24	42	60	86	128	158	212
	pMBE	12	21	39	51	73	115	142	184
	pMBE + Coulomb	2	4	7	9	13	18	22	27
Anthracene	Full Enumeration	0	6	6	6	8	18	22	34
	pMBE	0	5	5	5	6	15	17	25
	pMBE + Coulomb	0	2	2	2	3	6	8	13
Benzene	Full Enumeration	0	12	14	16	16	34	50	66
	pMBE	0	12	13	14	14	31	45	57
	pMBE + Coulomb	0	3	4	5	5	10	15	21
CO ₂	Full Enumeration	12	18	42	54	78	86	134	176
	pMBE	12	15	39	45	69	73	121	160
	pMBE + Coulomb	1	2	4	6	8	10	14	17
Cyanamide	Full Enumeration	9	16	29	42	53	81	104	136
	pMBE	9	16	27	40	51	76	99	127
	pMBE + Coulomb	5	9	16	23	29	42	55	70
Cytosine	Full Enumeration	2	6	10	20	24	32	48	58
	pMBE	1	5	9	18	22	29	43	52
	pMBE + Coulomb	1	3	5	10	12	16	24	29

Continued on next page

TABLE 4: (continued)

Ethyl carbamate	Full Enumeration	3	5	8	20	22	30	48	60
	pMBE	3	4	7	15	17	23	34	45
	pMBE + Coulomb	3	4	7	15	17	23	34	45
Formamide	Full Enumeration	7	16	27	39	53	73	100	134
	pMBE	6	15	25	35	48	64	89	116
	pMBE + Coulomb	5	11	17	23	32	45	62	85
Hexamine	Full Enumeration	0	0	14	14	14	26	26	50
	pMBE	0	0	7	7	7	13	13	25
	pMBE + Coulomb	0	0	2	2	2	3	3	4
Imidazole	Full Enumeration	5	11	17	22	31	48	66	85
	pMBE	5	10	16	20	29	42	57	74
	pMBE + Coulomb	3	7	11	14	20	30	41	51
Naphthalene	Full Enumeration	0	6	6	12	16	24	36	46
	pMBE	0	5	5	10	12	18	26	35
	pMBE + Coulomb	0	2	2	4	6	9	14	17
Oxalic Acid α	Full Enumeration	8	12	16	26	38	58	70	86
	pMBE	8	12	14	23	33	51	61	73
	pMBE + Coulomb	2	3	5	8	12	18	22	28
Oxalic Acid β	Full Enumeration	4	14	16	20	40	50	70	92
	pMBE	4	11	12	16	30	37	53	70
	pMBE + Coulomb	1	5	6	7	15	19	26	34
Pyrazine	Full Enumeration	2	12	16	26	26	32	52	80
	pMBE	1	10	12	21	21	24	42	60
	pMBE + Coulomb	1	3	5	7	7	10	13	20
Pyrazole	Full Enumeration	5	12	16	16	34	48	68	72
	pMBE	5	12	15	15	32	46	64	68
	pMBE + Coulomb	4	10	13	13	24	36	51	54
Succinic Acid	Full Enumeration	0	8	8	20	26	26	46	64
	pMBE	0	8	8	20	25	25	43	61

Continued on next page

TABLE 4: (continued)

	pMBE + Coulomb	0	3	3	7	9	9	17	25
	Full Enumeration	2	8	14	22	28	34	54	72
Triazine	pMBE	2	8	14	21	27	30	50	68
	pMBE + Coulomb	1	2	3	5	6	7	10	13
	Full Enumeration	2	8	14	20	28	34	58	64
Trioxane	pMBE	2	8	14	20	27	30	54	60
	pMBE + Coulomb	1	2	3	4	6	7	11	12
	Full Enumeration	2	4	13	23	25	30	47	63
Uracil	pMBE	1	3	12	21	23	28	42	56
	pMBE + Coulomb	1	3	8	15	16	19	30	40
	Full Enumeration	10	14	14	30	42	60	76	96
Urea	pMBE	9	11	11	21	33	46	58	76
	pMBE + Coulomb	3	4	4	8	10	14	16	20

TABLE 5: The number of three-body (3B) terms as a function of the product of the pairwise distances between the center of mass of the three molecules that make up the trimer subsystem.

3B distance (\AA^3)		120	150	180	210	240	270	300
1,4-cyclohexanedione	Full Enumeration	0	0	3	15	27	48	60
	pMBE	0	0	2	10	18	32	40
	pMBE + Coulomb	0	0	1	5	9	16	20
Acetic Acid	Full Enumeration	30	45	87	135	177	204	279
	pMBE	20	31	59	97	131	150	205
	pMBE + Coulomb	10	15	30	47	64	76	106
Adamantane	Full Enumeration	0	0	0	0	0	0	24
	pMBE	0	0	0	0	0	0	16
	pMBE + Coulomb	0	0	0	0	0	0	2
Ammonia	Full Enumeration	195	321	519	846	1125	1314	1683
	pMBE	165	261	414	666	897	1062	1353
	pMBE + Coulomb	19	28	43	69	91	108	136
Anthracene	Full Enumeration	0	0	6	6	12	12	18
	pMBE	0	0	4	4	8	8	12
	pMBE + Coulomb	0	0	1	1	2	2	4
Benzene	Full Enumeration	0	0	30	36	42	78	102
	pMBE	0	0	28	32	36	68	92
	pMBE + Coulomb	0	0	5	6	7	14	18
CO ₂	Full Enumeration	132	150	222	366	510	834	1050
	pMBE	120	132	180	300	396	648	840
	pMBE + Coulomb	8	10	14	22	29	45	56
Cyanamide	Full Enumeration	87	123	198	261	393	540	696
	pMBE	84	120	187	249	365	495	639
	pMBE + Coulomb	26	38	54	71	110	148	188
Cytosine	Full Enumeration	9	12	24	42	48	60	93
	pMBE	5	7	15	27	33	43	67
	pMBE + Coulomb	3	4	8	14	16	20	31

Continued on next page

TABLE 5: (continued)

Ethyl carbamate	Full Enumeration	6	15	21	24	39	66	84
	pMBE	4	10	14	16	26	43	53
	pMBE + Coulomb	2	5	7	8	13	22	28
Formamide	Full Enumeration	63	102	165	237	333	435	555
	pMBE	48	80	135	194	268	349	442
	pMBE + Coulomb	21	34	55	78	108	142	179
Hexamine	Full Enumeration	0	0	0	0	0	36	36
	pMBE	0	0	0	0	0	12	12
	pMBE + Coulomb	0	0	0	0	0	1	1
Imidazole	Full Enumeration	6	30	57	84	117	150	168
	pMBE	5	27	49	72	99	129	141
	pMBE + Coulomb	2	10	19	28	38	49	55
Naphthalene	Full Enumeration	0	6	6	12	12	18	30
	pMBE	0	4	4	8	8	12	20
	pMBE + Coulomb	0	1	1	2	2	4	6
Oxalic Acid α	Full Enumeration	24	42	78	114	138	210	234
	pMBE	24	36	68	100	124	172	196
	pMBE + Coulomb	4	7	14	20	24	38	42
Oxalic Acid β	Full Enumeration	12	42	60	114	138	192	246
	pMBE	8	28	38	74	90	116	146
	pMBE + Coulomb	2	8	11	20	24	32	41
Pyrazine	Full Enumeration	3	15	51	63	75	87	87
	pMBE	1	9	29	37	45	49	49
	pMBE + Coulomb	1	2	6	7	9	11	11
Pyrazole	Full Enumeration	6	36	42	93	109	138	184
	pMBE	6	34	40	88	102	130	172
	pMBE + Coulomb	4	23	27	57	66	86	115
Succinic Acid	Full Enumeration	0	6	6	36	60	69	105
	pMBE	0	6	6	36	58	66	102

Continued on next page

TABLE 5: (continued)

	pMBE + Coulomb	0	1	1	6	10	13	19
Triazine	Full Enumeration	3	21	39	75	75	75	117
	pMBE	2	20	38	74	74	74	114
	pMBE + Coulomb	1	2	3	6	6	6	10
	Full Enumeration	0	21	39	57	75	75	111
Trioxane	pMBE	0	20	38	56	74	74	104
	pMBE + Coulomb	0	3	5	9	10	10	16
	Full Enumeration	6	12	30	45	63	70	106
Uracil	pMBE	3	7	19	30	44	52	75
	pMBE + Coulomb	2	4	16	23	31	35	50
	Full Enumeration	24	42	78	135	183	219	255
Urea	pMBE	16	28	52	81	113	133	157
	pMBE + Coulomb	3	6	10	19	23	27	31
	Full Enumeration	24	42	78	135	183	219	255

D. Optimizing the local natural orbital approximation for the MBE

A key development within this work is the optimization of some of the approximations in the local natural orbital methods to further improve its application to the three-body terms in the many-body expansion. The correlation energy contribution of the three-body terms and the LNO errors in them are individually very small. However, adding a large number of these terms and the overall very high accuracy goals of this project motivated improvements targeting the 3B contributions.

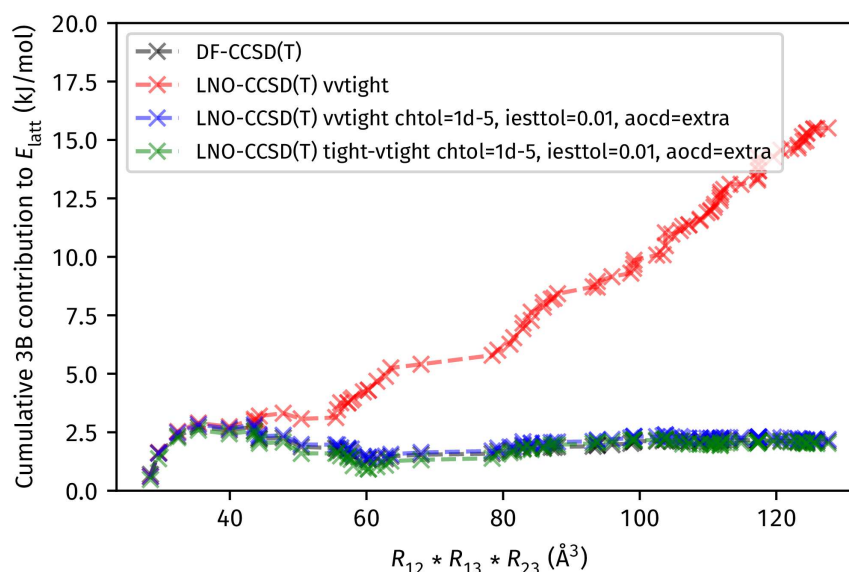


FIG. 28: LNO error in the three-body term to ice VIII for the aug-cc-pVDZ basis set compared to the canonical density-fitted (DF-)CCSD(T) reference.

As shown in Figure 28, up to medium range of 40–50 Å³, previous LNO-CCSD(T) results also provided accurate cumulative 3B contributions compared to approximation free DF-CCSD(T) references. At this point, the cumulative 3B contributions are also converged well within 1 kJ/mol due to the rapid decay of these terms beyond 40–50 Å³. Going beyond that, the previous LNO-CCSD(T) results exhibited increasing errors originating from the buildup of small numerical noise from the rapidly increasing number of 3B contributions. Detailed investigation revealed that this behavior originates from two usually very reliable approximations.

First, the accuracy of the Cholesky-decomposition factorization of MP2 denominations has an effect on the the local MP2 part of the correlation energies, that is usually very small and cancels excellently upon formation of energy differences.[88, 89] However, for the high relative accuracy requirement posed by the small 3B terms, this approximation was tightened via setting

`chtol=1d-5`. In the updated LNO-CCSD(T) implementation, this setting is automatically adjusted, as it is tied to the `lcorthr` keyword governing the local correlation threshold settings.[42]

The second adjustment is related to the use of counterpoise corrections to increase the basis set convergence. For example for water 3B terms, ghost AOs are put on the position of some of the water atom centers when computing dimer and monomer contributions. In this ghost positions the density of electrons becomes particularly small, especially with increasing trimer distances. The composition of the AO basis set used for expanding the localized orbitals are designed to introduce cost saving approximations, when we recognize the very small population of the localized orbitals on the some of the ghost AO centers. Previously, we extended this approach by considering the expected size of also the AO integrals on these ghost AO centers as an additional criteria.[90] This criteria is adjusted to be more precise via the `iestto1=0.01` and `aocd=extra` settings in the updated LNO-CCSD(T) version. [41, 42]

An additional benefit of these developments is that the LNO thresholds (`lcorthr`) required for convergence can be loosened. In particular, we find that `Tight` or `vTight` settings are sufficient for converging two- and three-body terms, in contrast to the `vvTight` settings used in previous work [58]. For lattice energies in the X23 and ICE13 datasets, we extrapolate from `Tight` to `vTight`, while relative energies of pharmaceutical polymorphs require only `Tight`, discussed in the next section. As shown in Table 6, these choices lead to substantial cost savings. For example, `Tight` calculations are roughly an order of magnitude faster and require 5–6 \times less memory than `vvTight` for anthracene dimer and trimer calculations, making them far more affordable and suitable for commodity hardware.

TABLE 6: Computational walltime and memory requirements for LNO-CCSD(T) calculations on a dimer and trimer of anthracene with various LNO thresholds. These estimates are given for a calculation involving 32 cores on an Intel Icelake node with 400 GB of available memory.

		Loose	Normal	Tight	vTight	vvTight
System	Metric					
Dimer	Walltime (min)	121	233	763	2473	7005
	Memory (Mb)	1328	3517	10696	26351	52202
Trimer	Walltime (min)	465	840	2595	9493	33822
	Memory (Mb)	1524	4652	15618	42048	90182

3. COST-EFFICIENT ELECTRONIC STRUCTURE PARAMETERS

It is important to ensure that the electronic structure parameters in the final LNO-CCSD(T) calculations are sufficiently accurate to reach e.g., 1 kJ/mol accuracy while being efficient enough to study large pharmaceutical-sized molecular crystals. In this section, we will study the effect of the basis set and local correlation thresholds. The required settings depend on the type of calculations, where the higher body-order terms in the MBE generally require smaller basis sets and the calculation of relative energies, as opposed to lattice energies, also allows for smaller basis sets and local thresholds.

A. Lattice energy

1. Basis set dependence

We show the convergence of the 2B contribution to E_{latt} for the aug-cc-pVXZ set of basis sets for $X = D, T$ and Q , and also consider two-point complete basis set (CBS) extrapolations for the D/T and T/Q combinations in Table 7. This was all performed with the Boys and Bernardi counterpoise corrections [91]. Taking the CBS(aug-cc-pVDZ/aug-cc-pVTZ) as the (most converged) reference, there is a strong basis set dependence of the 2B terms, where aug-cc-pVDZ is more than 10 kJ/mol away, while CBS(aug-cc-pVDZ/aug-cc-pVTZ) is sufficient to be within 0.6 kJ/mol of the CBS(aug-cc-pVTZ/aug-cc-pVQZ).

TABLE 7: Effect of basis set to the two-body contribution of the E_{latt} of ice VIII.

	2B contribution to E_{latt} (kJ/mol)
CCSD(T) aug-cc-pVDZ	-20.7
CCSD(T) aug-cc-pVTZ	-27.6
CCSD(T) aug-cc-pVQZ	-29.6
CCSD(T) CBS(aug-cc-pVDZ/aug-cc-pVTZ)	-31.6
CCSD(T) CBS(aug-cc-pVTZ/aug-cc-pVQZ)	-31.0

In Table 8, we show the basis set convergence for 12 ice phases. It confirms the weak basis set dependence of 3B terms, with aug-cc-pVDZ being only 0.1 kJ/mol away from the CBS estimates. It also highlights the necessity of performing basis set extrapolations for 2B terms, as even the QZ basis set is off by 1.5 kJ/mol on average.

TABLE 8: Three-body contributions have a significantly smaller basis set dependence than two-body contributions to the E_{latt} of ice phases. These tests are for the aug-cc-pVXZ ($X = \text{D, T, Q}$) basis sets and their CBS, T/Q for 2B and D/T for 3B terms, extrapolations.

	2B			3B		
	TZ	QZ	CBS	DZ	TZ	CBS
Ih	-20.3	-22.5	-24.0	0.1	0.1	0.1
II	-23.1	-25.2	-26.7	1.6	1.7	1.7
III	-22.2	-24.4	-26.0	0.6	0.7	0.7
IV	-24.1	-26.1	-27.6	1.3	1.4	1.5
VI	-25.3	-27.5	-29.0	1.8	1.9	1.9
VIII	-27.6	-29.6	-31.0	2.3	2.4	2.5
IX	-21.4	-23.6	-25.1	1.0	1.0	1.1
XI	-20.7	-23.0	-24.6	0.0	0.0	0.0
XIII	-23.3	-25.5	-27.0	1.3	1.4	1.5
XIV	-24.4	-26.6	-28.1	1.7	1.8	1.9
XV	-24.8	-26.9	-28.4	1.7	1.8	1.9
XVII	-19.7	-21.9	-23.5	0.2	0.3	0.3
MAD	3.7	1.5	0.0	0.1	0.0	0.0

In Table 9, we show the basis set convergence for the benzene E_{latt} within the X23 dataset. It can be seen that the basis set dependence is much weaker, where the aug-cc-pVTZ basis set is within 1 kJ/mol away from the CBS limit, with a similar weak basis set dependence for the 3B terms, showing no change to less than 0.1 kJ/mol for aug-cc-pVDZ.

To summarize, we conclude from these tests on the ice phases and benzene that the CBS(DZ/TZ) or CBS(TZ/QZ) with the aug-cc-pVXZ family of basis sets is needed to consistently achieve sub-kJ/mol accuracy on 2B terms. On the other hand, even aug-cc-pVDZ is sufficient for the 3B terms. These conclusions reflect observations from several previous studies [48, 92, 93]

TABLE 9: Convergence of 2B with basis set: aug-cc-pVTZ, aug-cc-pVQZ and CBS(aug-cc-pVTZ/aug-cc-pVQZ) as well as 3B with basis set: aug-cc-pVDZ, aug-cc-pVTZ and CBS(aug-cc-pVDZ/aug-cc-pVTZ) for the MP2 level of theory.

		MP2 (kJ/mol)
	TZ	-22.5
2B	QZ	-22.9
	CBS	-23.2
	DZ	0.5
3B	TZ	0.5
	CBS	0.5

2. Effect of core electrons

For Ice VIII, we have also investigated the effect of core electrons on the 2B contribution to the lattice energy. We expect core-electron effects to be strongest out of all the systems we study because this system is a high-pressure dense phase of ice. This means incorporating the 1s electrons on the O atoms in the correlation treatment together with corresponding polarized weighted core valence basis sets at the CBS(aug-cc-pwCVTZ/aug-cc-pwCVQZ) level. As shown in Table 10, we find that differences w.r.t. a standard valence electron-only treatment are smaller than 0.3 kJ/mol, indicating that these effects are small for ice phases. As such, we do not expect the core electrons to have a significant contribution to the lattice energy and can be safely neglected when aiming for sub-kJ/mol accuracy.

TABLE 10: Effect of core correlation to the two-body contribution of the E_{latt} of ice VIII.

		2B contribution to E_{latt} (kJ/mol)
CCSD(T)	CBS(aug-cc-pVTZ/aug-cc-pVQZ)	-31.0
CCSD(T)	smallcore CBS(aug-cc-pwCVTZ/aug-cc-pwCVQZ)	-31.3

3. Beyond-CCSD(T) contributions

We further consider the effect of higher order correlations beyond CCSD(T) for ice VIII, performing calculations with CCSDT(Q) using the aug-cc-pVDZ basis set in Table 10. These effects are found to be small for ice VIII, at less than 0.2 kJ/mol. Thus, we expect that these effects can be mostly neglected when aiming for sub-kJ/mol accuracy.

TABLE 11: Effect of higher order correlation to the two-body contribution of the E_{latt} of ice VIII.

	2B contribution to E_{latt} (kJ/mol)
CCSD(T) aug-cc-pVDZ	-20.7
CCSDT(Q) aug-cc-pVDZ	-20.9

4. Convergence with many-body terms in the MBE

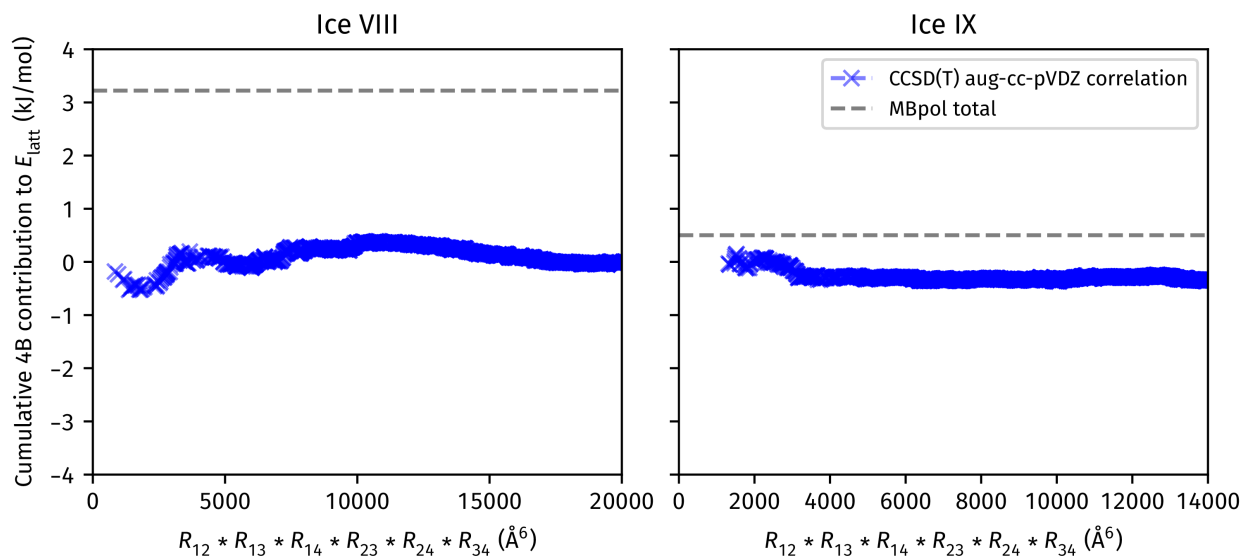


FIG. 29: The convergence with distance cutoff for the four-body contribution of the CCSD(T) correlation energy to E_{latt} for ice VIII and IX. These are compared to the converged total energy contribution approximated by MB-pol estimates from Ref. 51.

We have considered only 2B and 3B contributions to the MBE so far. Ice VIII is a system where higher-order terms in the many-body expansion, such as the four-body (4B) contribution can have a significant contribution to the lattice energy. This contribution is significant for

the *total* energy (taken for MB-pol from Ref. 51), but we show here that it is small for the CCSD(T) correlation energy, meaning most of the contribution comes from the HF energy. As shown in Figure 29, the corresponding contribution from the CCSD(T) correlation energy is small, being less than 0.5 kJ/mol compared to the 3.2 kJ/mol for the total 4B contribution (approximated using MB-pol). We also computed this contribution for ice IX, finding a similarly small contribution at ~ 0.4 kJ/mol. Overall, these results indicate that we can neglect many-body contributions beyond the 3B term for the molecular crystals we have studied throughout this work.

5. Local approximation convergence

We look at the convergence with local natural orbital (LNO) approximations thresholds for the (pre-defined) `Tight` and `vTight` settings, together with the local approximation free (LAF) extrapolation, comparing these to the canonical results for the `aug-cc-pVTZ`, `aug-cc-pVQZ` and `CBS(aug-cc-pVTZ/aug-cc-pVQZ)` basis sets. This has been compared for the 12 phases of ice in Tables 12 and 13 for the 2B and 3B contributions, respectively. The errors are generally small, being on average less than 1 kJ/mol for the 2B contribution. This error gets halved, to an MAD of 0.5 kJ/mol for the `vTight` LNO threshold and is further halved to ~ 0.2 kJ/mol with the LAF extrapolation. In general we find that the errors do not change much between different basis set choices. For the 3B terms, the dependence on the LNO thresholds is weaker, coming to only a maximum MAD of 0.3 kJ/mol across 12 phases of ice due to the already small contribution of this term.

In Table 14, we have also compared these LNO thresholds with the `aug-cc-pVDZ` basis set for the 2B and 3B terms for benzene. Similarly, it can be seen that for the 2B terms, the LAF can come into near exact agreement with canonical estimates. For the 3B terms, the results appear to already be well-converged to within 0.5 kJ/mol with the `Tight` LNO thresholds and do not improve by going to `vTight` or LAF treatments.

Overall, these tests indicate that an LAF extrapolation treatment benefits 2B terms when aiming for sub-kJ/mol accuracy while its effects are negligible or worse for 3B terms, where `Tight` or `vTight` settings are sufficient already.

TABLE 12: Convergence of 2B contribution for 12 ice phases with LNO thresholds: Tight, vTight and extrapolated locality approximation free (LAF) for aug-cc-pVTZ, aug-cc-pVQZ and CBS(aug-cc-pVTZ/aug-cc-pVQZ) basis sets

	TZ				QZ				CBS			
	Tight	vTight	LAF	Canonical	Tight	vTight	LAF	Canonical	Tight	vTight	LAF	Canonical
Ih	-19.5	-19.9	-20.1	-20.3	-21.6	-22.1	-22.4	-22.5	-23.1	-23.7	-24.0	-24.0
II	-21.9	-22.5	-22.8	-23.1	-24.0	-24.7	-25.0	-25.2	-25.5	-26.2	-26.5	-26.7
III	-21.5	-21.7	-21.8	-22.2	-23.6	-23.9	-24.1	-24.4	-25.0	-25.5	-25.7	-26.0
IV	-23.1	-23.5	-23.7	-24.1	-25.0	-25.6	-25.8	-26.1	-26.4	-27.1	-27.4	-27.6
VI	-24.0	-24.7	-25.1	-25.3	-26.1	-26.9	-27.2	-27.5	-27.6	-28.4	-28.8	-29.0
VIII	-26.2	-27.0	-27.4	-27.6	-28.1	-29.0	-29.4	-29.6	-29.5	-30.4	-30.9	-31.0
IX	-20.6	-20.9	-21.0	-21.4	-22.7	-23.1	-23.2	-23.6	-24.2	-24.6	-24.8	-25.1
XI	-19.9	-20.3	-20.5	-20.7	-22.1	-22.6	-22.9	-23.0	-23.6	-24.3	-24.6	-24.6
XIII	-22.3	-22.7	-23.0	-23.3	-24.3	-24.9	-25.2	-25.5	-25.8	-26.4	-26.7	-27.0
XIV	-23.2	-23.8	-24.0	-24.4	-25.3	-25.9	-26.2	-26.6	-26.8	-27.4	-27.7	-28.1
XV	-23.6	-24.2	-24.6	-24.8	-25.6	-26.4	-26.7	-26.9	-27.1	-27.9	-28.2	-28.4
XVII	-18.9	-19.3	-19.6	-19.7	-21.1	-21.6	-21.9	-21.9	-22.6	-23.2	-23.5	-23.5
MAD	1.0	0.5	0.3	0.0	1.1	0.5	0.2	0.0	1.1	0.5	0.2	0.0

TABLE 13: Convergence of 3B contribution for 12 ice phases with LNO thresholds: Tight, vTight and extrapolated locality approximation free (LAF) for aug-cc-pVDZ, aug-cc-pVTZ and CBS(aug-cc-pVDZ/aug-cc-pVTZ) basis sets

	DZ				TZ				CBS			
	Tight	vTight	LAF	Canonical	Tight	vTight	LAF	Canonical	Tight	vTight	LAF	Canonical
Ih	0.6	0.3	0.1	0.1	-0.0	0.2	0.3	0.1	-0.4	0.1	0.4	0.1
II	1.5	1.7	1.8	1.6	1.5	1.7	1.8	1.7	1.5	1.7	1.8	1.7
III	0.6	0.7	0.8	0.6	0.7	0.8	0.8	0.7	0.8	0.8	0.8	0.7
IV	1.2	1.3	1.3	1.3	1.6	1.5	1.4	1.4	1.8	1.6	1.5	1.5
VI	1.5	1.8	2.0	1.8	1.7	1.9	2.0	1.9	1.8	2.0	2.0	1.9
VIII	3.0	2.6	2.4	2.3	2.7	2.3	2.1	2.4	2.6	2.1	1.9	2.5
IX	1.0	1.1	1.1	1.0	1.4	1.0	0.8	1.0	1.6	0.9	0.6	1.1
XI	0.2	0.2	0.2	0.0	-0.2	-0.0	0.1	0.0	-0.5	-0.2	-0.0	0.0
XIII	0.9	1.4	1.7	1.3	1.4	1.4	1.5	1.4	1.7	1.5	1.3	1.5
XIV	1.5	1.8	1.9	1.7	1.6	1.8	1.8	1.8	1.7	1.8	1.8	1.9
XV	1.4	1.8	2.0	1.7	1.8	1.8	1.8	1.8	2.0	1.9	1.8	1.9
XVII	-0.2	0.3	0.6	0.2	0.0	0.3	0.5	0.3	0.1	0.3	0.4	0.3
MAD	0.3	0.1	0.2	0.0	0.2	0.1	0.1	0.0	0.3	0.1	0.2	0.0

TABLE 14: Convergence of 2B and 3B contributions, for the benzene molecular crystal in the X23 dataset, with LNO thresholds: Tight, vTight and extrapolated locality approximation free (LAF) for aug-cc-pVDZ basis set

	2B				3B			
	Tight	vTight	LAF	Canonical	Tight	vTight	LAF	Canonical
CCSD(T) aug-cc-pVDZ (kJ/mol)	-70.7	-70.2	-70.0	-70.0	4.7	4.6	4.5	5.1

6. Final parameters

Based on the observations made within the preceding sections for the MBE treatment of the lattice energy E_{latt} , we come up with several approaches for computing E_{latt} that can retain a high level of accuracy. The procedures are as follows:

- **Canonical** — This is the most accurate as it makes extensive use of canonical CCSD(T). We use for the following basis sets for the many-body terms:
 - 1B terms: CBS(aug-cc-pVQZ/aug-cc-pV5Z)
 - 2B terms: CBS(aug-cc-pVTZ/aug-cc-pVQZ)
 - 3B terms: CBS(aug-cc-pVDZ/aug-cc-pVTZ)
- **LAF** — In this more economical approach, we use LNO-CCSD(T) and aim to reach the local approximation free limit by extrapolating using Tight and vTight settings. The exact same sets of AO basis functions are used as for the Canonical approach.
- **Composite** — To further lower costs, we make use of a composite procedure whereby the canonical MP2 is used to correct for both the local (i.e., LNO) approximation errors as well as for basis set incompleteness effects. One way to explain how it works (using the 2B terms as an example) is that we start from a CBS(aug-cc-pVTZ/aug-cc-pVQZ) extrapolated canonical MP2 estimates, using the same basis set combinations as listed above, and add on correction between LNO-CCSD(T) and local MP2 (LMP2) at the smaller aug-cc-pVTZ basis set.

$$\begin{aligned}
 E_{\text{latt}}^{\Delta\text{MP2}} &= E_{\text{latt}}^{\text{MP2}}[\text{CBS}(\text{aug-cc-pVTZ}/\text{aug-cc-pVQZ})] \\
 &\quad \left[+ E_{\text{latt}}^{\text{LAF LNO-CCSD(T)}}[\text{aug-cc-pVTZ}] \right. \\
 &\quad \left. - E_{\text{latt}}^{\text{LAF LMP2}}[\text{aug-cc-pVTZ}] \right] \quad (9)
 \end{aligned}$$

Alternatively, this may also be thought as starting from a LAF extrapolated LNO-CCSD(T) estimate at the aug-cc-pVTZ basis set with a subsequent correction from canonical CBS(aug-cc-pVTZ/aug-cc-pVQZ) MP2 to correct for local approximation errors and basis set errors in LMP2 aug-cc-pVTZ:

$$\begin{aligned}
 E_{\text{latt}}^{\Delta\text{MP2}} &= E_{\text{latt}}^{\text{LAF LNO-CCSD(T)}}[\text{aug-cc-pVTZ}] \\
 &\quad \left[+ E_{\text{latt}}^{\text{MP2}}[\text{CBS}(\text{aug-cc-pVTZ}/\text{aug-cc-pVQZ})] \right. \\
 &\quad \left. - E_{\text{latt}}^{\text{LAF LMP2}}[\text{aug-cc-pVTZ}] \right]. \quad (10)
 \end{aligned}$$

This procedure is expected to work very well for the LNO-CCSD(T) implementation within MRCC because the LMP2[88, 89] energy is exactly the second-order part of LNO-CCSD(T) [36–38], thus their local approximations also match and consequently, both can be consistently improved by the canonical MP2 correction.

In Table 15, we have compared the lattice energy for these three approaches across 12 ice phases in their small-sized unit cells. Table 16 gives the same estimates for the medium-sized unit cells to assess whether there might be a build-up in errors when more terms have to be computed. [94] We find that compared to the canonical results, the LAF approach introduces errors of only 0.2 kJ/mol, while Composite introduces errors of 0.3 kJ/mol in terms of MAD across the 12 ice phases. We find no change in errors when using medium-sized unit cells, indicating no build up of errors, arising because the lattice energy is a per molecule quantity.

TABLE 15: Comparison of various approaches [Canonical (Can.), LAF and Composite (Comp.) described in the text] for computing the lattice energy of several ice phases in their small-sized unit cells.

	1B			2B			3B			Total		
	Can.	LAF	Comp.	Can.	LAF	Comp.	Can.	LAF	Comp.	Can.	LAF	Comp.
Ih	-8.0	-8.0	-8.1	-24.0	-24.0	-23.7	0.1	0.4	0.1	-31.9	-31.6	-31.7
II	-7.1	-7.1	-7.2	-26.7	-26.5	-26.4	1.7	1.8	1.8	-32.1	-31.8	-31.8
III	-8.0	-8.0	-8.1	-26.0	-25.7	-25.6	0.7	0.8	0.7	-33.3	-32.9	-33.0
IV	-7.1	-7.1	-7.1	-27.6	-27.4	-27.3	1.5	1.5	1.5	-33.2	-33.0	-32.9
VI	-6.8	-6.8	-6.8	-29.0	-28.8	-28.7	1.9	2.0	2.0	-33.8	-33.5	-33.5
VIII	-5.3	-5.3	-5.3	-31.0	-30.9	-30.7	2.5	1.9	2.6	-33.8	-34.3	-33.4
IX	-7.5	-7.5	-7.6	-25.1	-24.8	-24.8	1.1	0.6	1.1	-31.6	-31.7	-31.3
XI	-8.6	-8.6	-8.6	-24.6	-24.6	-24.2	0.0	-0.0	0.0	-33.1	-33.2	-32.8
XIII	-6.9	-6.9	-6.9	-27.0	-26.7	-26.7	1.5	1.3	1.5	-32.4	-32.3	-32.1
XIV	-6.6	-6.6	-6.7	-28.1	-27.7	-27.8	1.9	1.8	1.9	-32.9	-32.6	-32.5
XV	-6.5	-6.5	-6.6	-28.4	-28.2	-28.1	1.9	1.8	1.9	-33.1	-33.0	-32.8
XVII	-8.4	-8.4	-8.4	-23.5	-23.5	-23.1	0.3	0.4	0.3	-31.6	-31.5	-31.3
MAD	0.0	0.0	0.0	0.0	0.2	0.3	0.0	0.2	0.0	0.0	0.3	0.3

We have also tested these approaches for the benzene molecular crystal in Table 17. We find that the Composite procedure is accurate to within 0.1 kJ/mol w.r.t. the canonical result.

TABLE 16: Comparison of various approaches [Canonical (Can.), LAF and Composite (Comp.) described in the text] for computing the lattice energy of several ice phases in their medium-sized unit cells.

	1B			2B			3B			Total		
	Can.	LAF	Comp.	Can.	LAF	Comp.	Can.	LAF	Comp.	Can.	LAF	Comp.
Ih	-8.6	-8.6	-8.6	-23.8	-23.9	-23.4	0.1	0.4	0.1	-32.2	-32.0	-31.9
III	-7.5	-7.5	-7.6	-25.5	-25.2	-25.1	0.6	0.8	0.6	-32.4	-31.9	-32.1
IV	-7.0	-7.0	-7.0	-27.3	-27.0	-27.0	1.3	1.1	1.3	-33.0	-32.9	-32.7
VII	-5.6	-5.6	-5.6	-31.8	-31.7	-31.5	3.2	3.1	3.2	-34.2	-34.2	-33.9
XVII	-8.4	-8.4	-8.4	-23.4	-23.5	-23.0	0.2	0.4	0.2	-31.5	-31.5	-31.2
MAD	0.0	0.0	0.0	0.0	0.2	0.3	0.0	0.2	0.0	0.0	0.2	0.3

This comes from a cancellation of ~ 0.6 kJ/mol errors on the 2B and 3B contributions to the total lattice energy. The LAF approach is about 2.2 kJ/mol off from the canonical estimates and this arises from errors in the 3B contribution, while there is agreement to within 0.1 kJ/mol on the 2B terms. It seems that the LAF extrapolation formula, while working for 2B terms, is less successful for 3B terms, as we have observed in Section 3A5.

TABLE 17: Convergence of the LNO-MBE-CCSD(T) lattice energy of benzene with respect to the LNO threshold, compared to the canonical result. All values are in kJ/mol.

	1B	2B	3B	Total
Tight	-1.3	-80.0	3.6	-77.7
vTight	-1.3	-79.3	5.8	-74.8
LAF	-1.3	-78.9	6.8	-73.4
Composite	-1.3	-79.6	5.3	-75.7
Canonical	-1.3	-79.0	4.7	-75.6

B. Relative energy

1. Final parameters

Compared to the lattice energies, relative energies are expected to be easier to converge since there can be cancellation of errors (e.g., in basis set, MBE, or local approximation) between the two polymorphs being compared. Within this section, we will demonstrate this for the relative energy between ice forms Ih and VIII as well as the experimental and vanEijck-3 forms of molecule X from the third Crystal Structure Prediction (CSP) Blind Test [11]. Its easier convergence means that it is possible to come up with cheaper procedures than what was discussed for the lattice energy that can scale up towards larger molecular crystal systems. Specifically, we show in Table 18 that the Composite with the original basis sets (dubbed ‘Full’) can be loosened towards using smaller basis sets (dubbed ‘Reduced’) and less tight LNO approximations for the various terms that make up the Composite relative energy:

$$E_{\text{rel}}^{\text{final}} = E_{\text{rel}}^{\text{LNO-CCSD(T)}} + [E_{\text{rel}}^{\text{MP2}} - E_{\text{rel}}^{\text{LMP2}}]. \quad (11)$$

In this ‘Reduced’ basis set, for the 2B terms, we use aug-cc-pVDZ and aug-cc-pVTZ pair as opposed to the aug-cc-pVTZ and aug-cc-pVQZ pair. For the 3B terms, we introduce the jul-cc-pVDZ and jul-cc-pVTZ pairs, where the ‘jul’ basis sets remove the diffuse augmentation functions on the H atoms for an overall smaller basis set. Additionally, we have also used canonical MP2 to correct CCSD(T) with Tight LNO thresholds as opposed to LAF extrapolated (from the Tight and vTight threshold pair).

TABLE 18: The basis sets used for the original – termed ‘Full’ – Composite procedure in Section 3 A 5 for computing the lattice energy and the cheaper procedure – termed ‘Reduced’ for computing relative energy.

Approach	Quantity	1B contribution		2B contribution		3B contribution	
		Basis	LNO	Basis	LNO	Basis	LNO
Composite Full	$E_{\text{rel}}^{\text{LNO-CCSD(T)}}$	aug-cc-pVQZ	LAF	aug-cc-pVTZ	LAF	aug-cc-pVDZ	LAF
	$E_{\text{rel}}^{\text{MP2}}$	aug-cc-pVQZ	LAF	aug-cc-pVTZ	LAF	aug-cc-pVDZ	LAF
	$E_{\text{rel}}^{\text{LMP2}}$	CBS(aug-cc-pVQZ/5Z)	Canonical	CBS(aug-cc-pVTZ/QZ)	Canonical	CBS(aug-cc-pVDZ/TZ)	Canonical
Composite Reduced	$E_{\text{rel}}^{\text{LNO-CCSD(T)}}$	jul-cc-pVTZ	Tight	aug-cc-pVDZ	Tight	jul-cc-pVDZ	Tight
	$E_{\text{rel}}^{\text{MP2}}$	jul-cc-pVTZ	Tight	aug-cc-pVDZ	Tight	jul-cc-pVDZ	Tight
	$E_{\text{rel}}^{\text{LMP2}}$	CBS(jul-cc-pVTZ/QZ)	Canonical	CBS(aug-cc-pVDZ/TZ)	Canonical	CBS(jul-cc-pVDZ/TZ)	Canonical

2. Experimental and vanEijck-3 forms of molecule X

Molecule X from the third CSP Blind Test has represented a challenge for many DFAs [12, 15] due to its conformational flexibility, which requires an accurate treatment of both the intermolecular and intramolecular interactions. In particular, the relative energy between the experimental and vanEijck-3 form of molecule X has been challenging to predict.

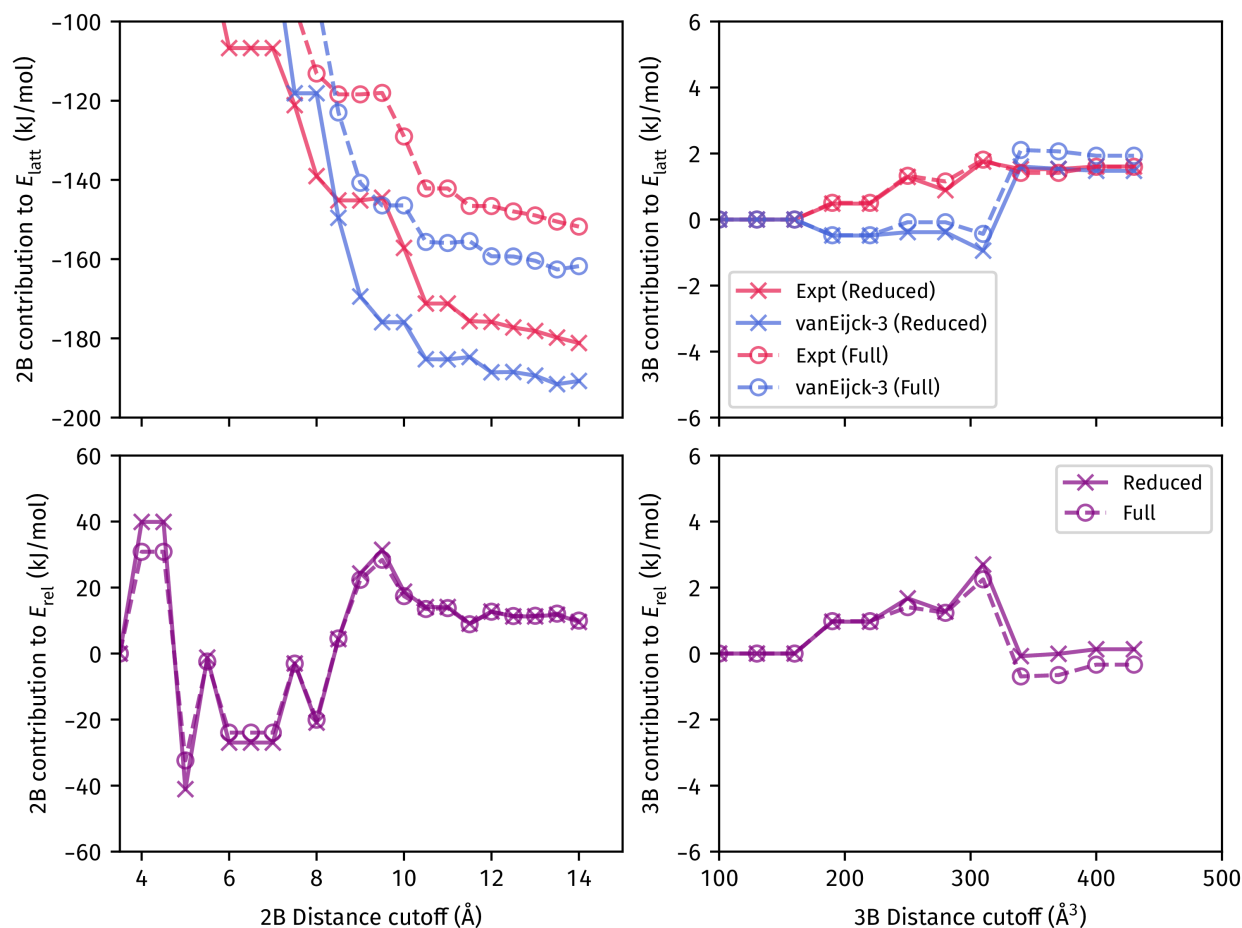


FIG. 30: Demonstrating the quicker convergence of the relative energy E_{rel} between the experimental and vanEijck-3 polymorphs of molecule X over the lattice energy E_{latt} of these individual polymorphs for both the two-body (2B) and three-body (3B) contributions of the correlation energy to the many-body expansion (MBE).

In Figure 30, we demonstrate the convergence of the 2B and 3B contributions to the lattice energy E_{latt} from the correlation energy of the (aforementioned) two polymorphs of molecule X as well as their relative energy E_{rel} . It can be seen that in terms of absolute value, the use of the Reduced basis sets leads to a large ~ 30 kJ/mol difference compared to the Full basis sets for the 2B terms. However, when we consider energy differences, it is less than 0.5 kJ/mol for the

2B contribution, highlighting the near-perfect cancellation of errors. This is similarly observed for the 3B contributions, albeit to a much smaller extent.

In Table 19, we show that the relative energy difference between the vanEijck-3 and experiment forms are to within 0.6 kJ/mol of each other, regardless of the errors in the absolute E_{latt} . Overall, this highlights that we can expect cancellation in errors between the local approximation as well as the basis set when computing relative energies. Furthermore, it can be seen that the relative energy convergences significantly quicker with cutoff than the absolute contribution to the lattice energy.

TABLE 19: Convergence of the relative energies between the experimental and vanEijck-3 polymorphs of X arising from CCSD(T) correlation with respect to basis set size. Both the results with the ‘Reduced’ basis set (used in the main text) and ‘Full’ basis sets are given. All values are in kJ/mol.

		1B	2B	3B	Total
	Experimental	-0.0	-152.4	1.6	-150.8
Reduced basis	vanEijck-3	0.6	-165.1	1.9	-162.6
	E_{rel}	-0.6	12.8	-0.3	11.8
	Experimental	-0.0	-181.2	1.6	-179.6
Full basis	vanEijck-3	1.2	-190.8	1.5	-188.1
	E_{rel}	-1.2	9.6	0.1	8.5

3. *Ice Ih and VIII*

The relative energy between Ice Ih and VIII represents a particularly challenging task for the MBE because there is significantly different many-body behavior between the two phases, the former being a low-pressure/density phase while the latter is a high-pressure/density phase. In Figure 31, we show the contribution from the 2B and 3B terms to the total lattice energies of Ih and VIII. It can be seen that Ih has almost no contributions to the CCSD(T) correlation energy from three-body terms while VIII has significant contributions from three-body terms. Furthermore, there is also a large difference in density between the two systems, whereby ice Ih has a density of 0.93 g/cm^3 at 10 K [95] and low pressures, while ice VIII has a density of 1.49 g/cm^3 at zero temperature and pressure [96]. Thus, there is also a different convergence behavior of the 2B and 3B terms with cutoff distance. Given these considerations, we expect the relative energy between ice Ih and VIII represents a system that can really stress-test the MBE approach.

In Table 20, we compare the relative energy between forms VIII and Ih using the 'Reduced' basis set Composite approach with respect to the several treatments with the 'Full' basis set used for the lattice energy in Section 3 A 6. It can be seen that this cheaper treatment can obtain the relative energy to within 1.1 kJ/mol of the range of values from the (more expensive) approaches used for the lattice energy. This error largely comes from the three-body term, which is underestimated by the Composite Reduced approach. We also observe similar large errors with the LAF Full basis treatment, suggesting that it is hard to leverage cancellation of errors arising from the local approximation due to the different density behaviors.

To summarize, we find that relative energies can still be obtained to within 1 kJ/mol even for these challenging pair of polymorphs. We do not expect systems with such differences in character and density to be compared under general circumstances, as they would appear under different thermodynamic conditions. For typical systems, we expect a better control of errors, as observed for the molecule X polymorphs.

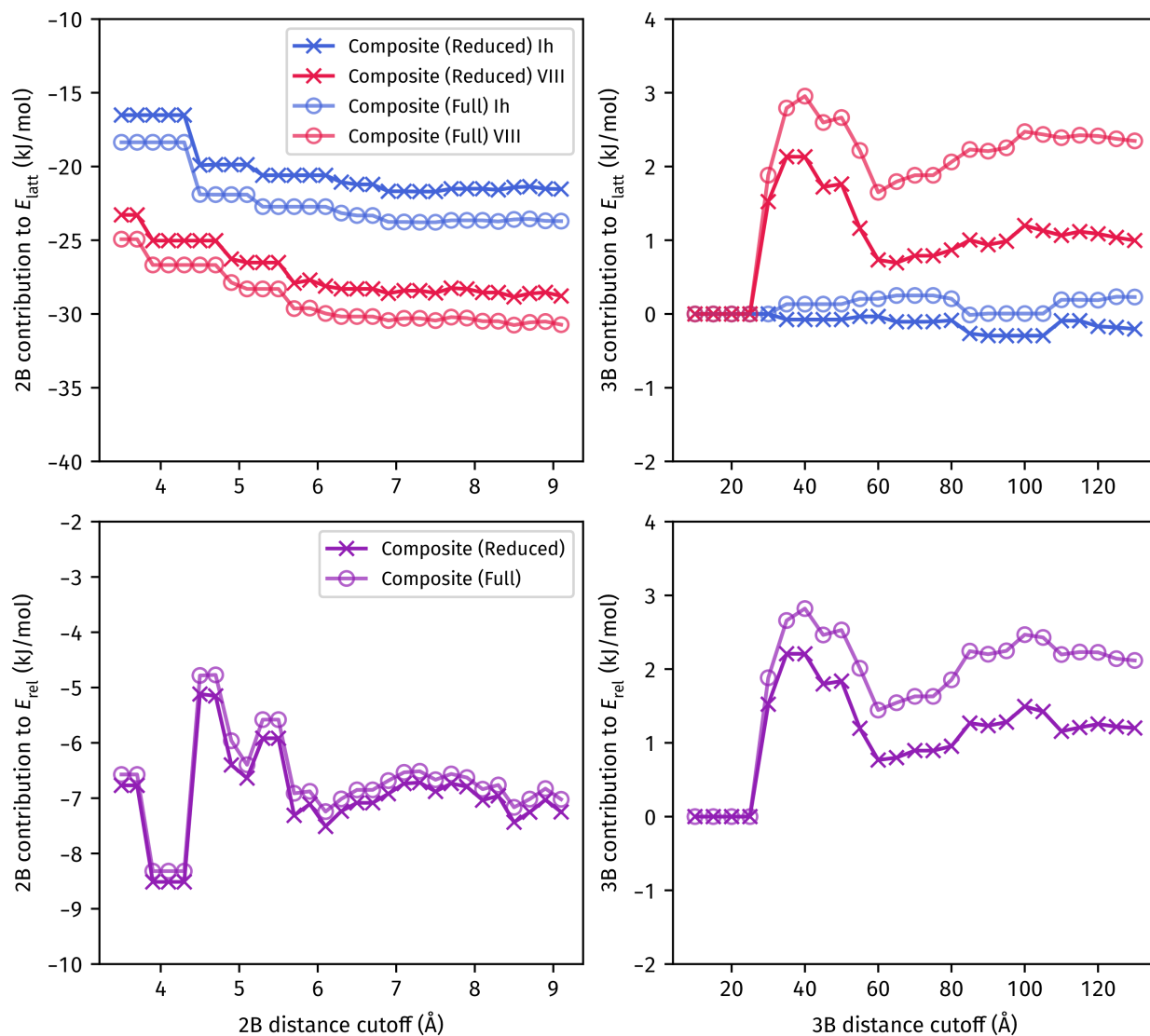


FIG. 31: Convergence of the 2B and 3B terms to the MBE for ice Ih (left) and VIII (right) for different local threshold procedures to LNO-CCSD(T): Tight, vTight and local approximation free (LAF) extrapolation.

TABLE 20: The MBE contributions to the lattice energy of ice Ih and VIII for several LNO approximations (Tight, vTight and LAF extrapolated) to the CCSD(T) in the Composite 'Reduced' approach.

		Ih E_{latt}	VIII E_{latt}	(VIII - Ih) E_{rel}
1B	Composite Reduced	-7.9	-5.2	2.7
	LAF Full	-8.0	-5.3	2.8
	Canonical Full	-8.0	-5.3	2.8
	Composite Full	-8.1	-5.3	2.8
2B	Composite Reduced	-21.5	-28.8	-7.2
	LAF Full	-24.0	-30.9	-6.9
	Canonical Full	-24.0	-31.0	-7.0
	Composite Full	-23.7	-30.7	-7.0
3B	Composite Reduced	-0.3	1.3	1.6
	LAF Full	0.4	1.9	1.5
	Canonical Full	0.1	2.5	2.4
	Composite Full	0.1	2.6	2.5
Total	Composite Reduced	-29.8	-32.7	-2.9
	LAF Full	-31.6	-34.3	-2.7
	Canonical Full	-31.9	-33.8	-1.8
	Composite Full	-31.7	-33.4	-1.8

4. LATTICE ENERGY OF X23 DATASET

Within this section, we will arrive at our final LNO-MBE-CCSD(T) estimates of the lattice energy for the X23 dataset, comparing it to experimental lattice energies (corrected from sublimation enthalpies) and quantum diffusion Monte Carlo (DMC) estimates from the literature.

A. Experimental analysis

Experiments do not measure the lattice energy, but instead the sublimation enthalpy ΔH , which include temperature and vibrational contributions. Thus, these sublimation enthalpies must be converted to lattice energies (calculating the temperature contribution E_{temp} from simulations) for an apples-to-apples comparison to our LNO-MBE-CCSD(T) estimates. Additionally, for each of 23 systems within the X23 dataset, there are often several experimental measurements [97–100] made with different instruments and techniques as well as at different years throughout time. These experiments can vary quite significantly, as discussed in Ref. 1, with ranges of over 10 kJ/mol on the sublimation enthalpy for some studies. A good estimate of for the error bars on the average of the experiments is also required to enable proper comparison to the simulations.

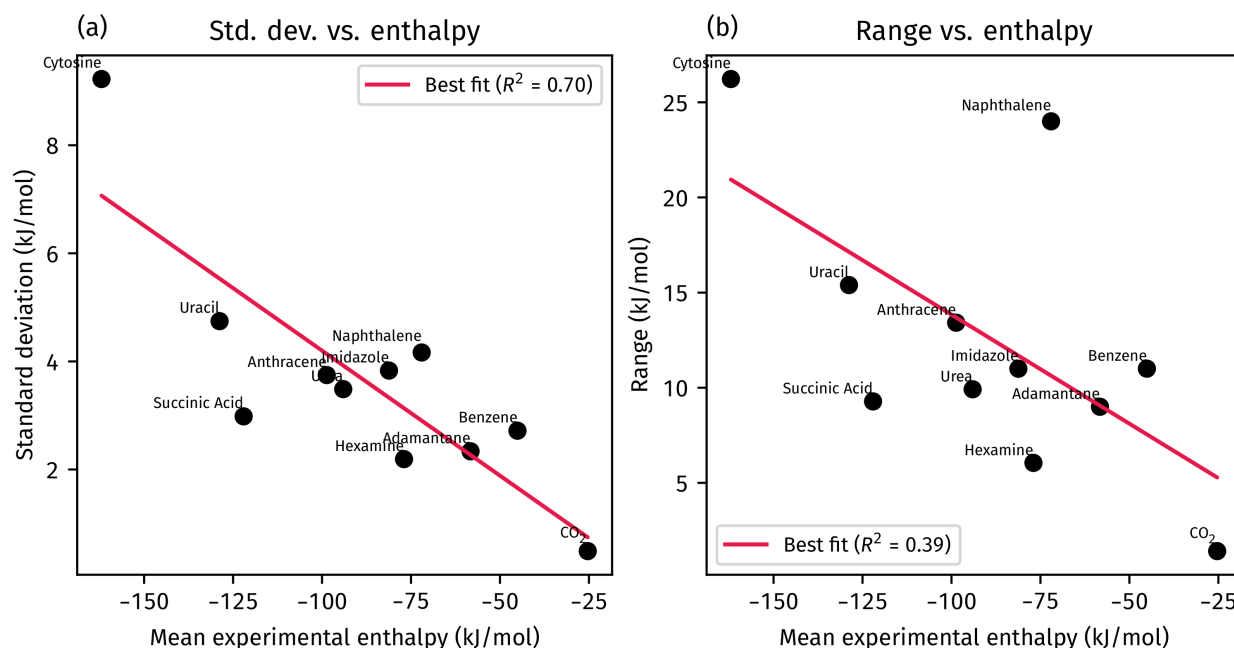


FIG. 32: Correlation between the ΔH and (a) standard deviation as well as (b) range for the set of X23 systems with 5 or more experimental measurements.

We consider two approaches to estimate the error on the mean value of the experimental

sublimation enthalpy. For the systems with 5 or more experimental measurements, we take the standard deviation as the error, quoting 2σ errors to account for 95% confidence interval. For the remaining systems, we make a prediction of the 2σ standard deviation. In Figure 32a, we show that there is a good correlation between the value of the mean experimental sublimation enthalpy as well as the standard deviation, with an R^2 of 0.70 for the set of systems with 5 or more sublimation enthalpy measurements. The line of best fit we obtain has the following equation (in kJ/mol units):

$$\sigma_{\text{predicted}} = -0.0462642 \times \Delta H_{\text{mean}} + -0.427082. \quad (12)$$

In panel b, we also consider the correlation with the range of the sublimation enthalpy measurements, finding significantly worse correlation with R^2 of 0.39.

To convert the sublimation enthalpies ΔH into lattice energies E_{latt} , we have used recent [101] temperature corrections E_{temp} calculated using machine-learned interatomic potentials (MLIPs) trained to DFT data: The chosen DFT functional within this work is vdW-DF2 [27], which has been shown to demonstrate excellent agreement to DMC estimates for the X23 dataset. Specifically, we take sublimation enthalpy values computed using path-integral molecular dynamics (PIMD) in Table S32 of the Supplementary Material for Ref. 101 simulations, accounting fully for anharmonicity and nuclear quantum effects. The temperature correction is calculated as:

$$E_{\text{temp}} = \Delta H - E_{\text{latt}}. \quad (13)$$

As described in Ref. 101, such an approach is particularly important for systems such as succinic acid due to its conformational flexibility and anharmonicity. The final experimental estimate of the lattice energy and error bars are given in Table 21

TABLE 21: Compilation of experimental lattice energies of the X23 set, together with the mean and (analyzed) error estimate. All values are in kJ/mol.

Systems	Enthalpy measurements	E_{temp} [101]	Mean enthalpy	2σ	Predicted 2σ	Range	Lattice energy	Error	Error type
1,4-cyclohexanedione	-84.2, -75.0, -84.0	6.4	-81.1	-	6.6	-	-87.5	6.6	Predicted
Acetic Acid	-66.2, -68.7	5.0	-67.5	-	5.4	-	-72.4	5.4	Predicted

Continued on next page

TABLE 21: (continued)

Adamantane	-58.5, -59.6, -56.0, -55.3 -59.5, -60.2, -59.8, -54.2 -59.2, -59.0, -53.0, -58.0 -59.0, -60.0, -55.0, -59.0 -60.0, -60.0, -62.0	6.7	-58.3	4.7	4.5	9.0	-64.9	4.7	Real
Ammonia	-31.1	5.8	-31.1	-	2.0	-	-36.8	2.0	Predicted
Anthracene	-98.8, -98.5, -99.1, -96.2 -99.7, -103.5, -97.1, -103.3 -100.7, -101.1, -99.5, -103.3 -95.6, -91.9, -91.9, -96.1 -100.6, -98.1, -95.9, -102.6 -101.3, -99.2, -90.6, -104.1 -99.3, -102.9, -102.9, -93.1 -91.3, -94.2, -98.8, -98.0 -100.0, -96.0, -99.0, -104.0 -103.0	5.6	-98.7	7.5	8.3	13.4	-104.2	7.5	Real
Benzene	-41.5, -45.0, -45.1, -52.5 -48.0, -45.6, -43.8, -42.3 -44.6, -46.6, -44.5, -42.5 -44.3	7.7	-45.1	5.4	3.3	11.0	-52.8	5.4	Real
CO ₂	-26.1, -24.7, -25.5, -25.5 -25.0	3.8	-25.3	1.0	1.5	1.4	-29.1	1.0	Real
Cyanamide	-75.8, -75.0	4.2	-75.4	-	6.1	-	-79.6	6.1	Predicted
Cytosine	-168.8, -155.3, -149.8, -155.0 -167.0, -176.0	5.3	-162.0	18.5	14.1	26.2	-167.2	18.5	Real
Ethyl carbamate	-77.2, -72.3, -89.1, -76.0	6.2	-78.6	-	6.4	-	-84.9	6.4	Predicted
Formamide	-72.2, -71.7, -72.4	6.5	-72.1	-	5.8	-	-78.6	5.8	Predicted
Hexamine	-78.7, -77.0, -79.1, -74.0 -80.0, -75.0, -75.0	6.7	-77.0	4.4	6.3	6.0	-83.7	4.4	Real

Continued on next page

TABLE 21: (continued)

Imidazole	-83.1, -80.8, -83.0, -74.0 -85.0	4.6	-81.2	7.7	6.7	11.0	-85.8	7.7	Real
Naphthalene	-87.8, -72.3, -73.0, -79.0 -71.3, -73.7, -71.0, -72.5 -75.9, -73.3, -72.5, -72.7 -77.1, -72.0, -71.2, -74.2 -73.3, -74.6, -72.6, -67.5 -63.8, -72.8, -71.8, -66.0 -65.7, -68.7, -72.0, -72.2 -70.0, -72.0, -73.0, -72.0 -72.0, -72.0, -73.0, -64.0 -66.0	5.3	-72.0	8.3	5.8	24.0	-77.3	8.3	Real
Oxalic Acid α	-93.7, -94.0	2.5	-93.8	-	7.8	-	-96.4	7.8	Predicted
Oxalic Acid β	-93.6	1.0	-93.6	-	7.8	-	-94.6	7.8	Predicted
Pyrazine	-56.3	6.9	-56.3	-	4.4	-	-63.2	4.4	Predicted
Pyrazole	-73.9, -72.2, -74.0, -69.0	4.1	-72.3	-	5.8	-	-76.3	5.8	Predicted
Succinic Acid	-128.7, -119.4, -121.7, -119.6 -123.0, -122.0, -120.0	-5.2	-122.0	6.0	10.4	9.3	-116.8	6.0	Real
Triazine	-56.9, -54.2	6.6	-55.6	-	4.3	-	-62.2	4.3	Predicted
Trioxane	-56.7, -55.6, -56.5, -56.2	7.8	-56.2	-	4.3	-	-64.1	4.3	Predicted
Uracil	-127.4, -130.8, -129.3, -134.3 -122.2, -123.8, -137.6, -128.9 -122.6, -131.0	4.5	-128.8	9.5	11.1	15.4	-133.3	9.5	Real
Urea	-95.8, -96.0, -95.5, -92.3 -88.7, -97.8, -96.4, -88.9 -89.2, -95.5, -98.6	5.2	-94.1	7.0	7.8	9.9	-99.2	7.0	Real

B. Periodic HF

The first step to our final LNO-MBE-CCSD(T) lattice energy is the calculation of the Hartree-Fock (HF) using the periodic plane-wave implementation in VASP (described in Section 1 B 1). The lattice energy is defined as:

$$E_{\text{latt}} = E_{\text{crys}} - E_{\text{gas}}, \quad (14)$$

where E_{crys} is the total energy per molecule in the crystal phase while E_{gas} is that for the molecule in the (isolated) gas phase. Achieving accurate estimates of the lattice energy requires hard PAW potentials [102, 103] with a (1) large energy cutoff of 1000 eV together with a (2) converged k -point mesh. We follow a composite scheme to reach both criteria, which goes as:

- The main calculation is performed with hard PAW potentials (with 1000 eV energy cutoff) and a moderate k -point spacing of 0.25 \AA^{-1} .
- The Δ_k correction towards denser k -point spacing of 0.18 \AA^{-1} (on top of a spacing of 0.25 \AA^{-1}) is performed using standard (Std) PAW potentials and a 520 eV energy cutoff.

These separate estimates are given in Table 22. In general, it can be seen that the first calculation is sufficient for accuracy of within 0.2 kJ/mol for all of the systems, making the Δ correction relatively negligible. It also highlights in the importance of hard PAW potentials as the standard PAW potentials can differ by as much as 7 kJ/mol for some of the X23 systems.

As described in the main text, one of the new developments we leverage is new implementations over the past decade that use graphic processing units [104] (GPU) together with the Adaptively Compressed Exchange [21] (ACE) operator. We report the GPU costs (in GPUh) for the individual contributions in Table 23. Overall, it can be seen that for the dominant hard PAW calculations, the cost is less than 5 GPUh on average, with a maximum of 25 GPUh for Trioxane. In fact, the cost for the negligible Δ_k correction is more, at a sum of ~ 11 GPU on average.

TABLE 22: Contributions that make up the final HF lattice energies for the X23 set. All values are in kJ/mol.

	Hard (KSPACING=0.25)	Std (KSPACING=0.25)	Std (KSPACING=0.18)	Δ_k	Final
1,4-cyclohexanedione	-3.4	-5.7	-5.4	0.2	-3.2
Acetic Acid	-17.4	-20.1	-20.1	0.0	-17.4
Adamantane	41.5	41.5	41.4	-0.1	41.5
Ammonia	-9.1	-9.4	-9.4	-0.0	-9.1
Anthracene	54.9	55.0	55.0	-0.0	54.9
Benzene	23.0	23.0	23.0	-0.1	22.9
CO ₂	-3.4	-4.3	-4.3	-0.0	-3.5
Cyanamide	-29.9	-30.7	-30.8	-0.1	-29.9
Cytosine	-48.0	-51.1	-51.1	0.0	-48.0
Ethyl carbamate	-17.4	-19.7	-19.8	-0.0	-17.4
Formamide	-30.3	-33.0	-33.1	-0.0	-30.4
Hexamine	18.0	18.2	18.2	-0.1	18.0
Imidazole	-14.3	-14.7	-14.7	-0.0	-14.3
Naphthalene	43.7	43.8	43.8	-0.0	43.7
Oxalic Acid α	-35.3	-40.7	-40.8	-0.0	-35.3
Oxalic Acid β	-28.2	-33.4	-33.5	-0.0	-28.2
Pyrazine	14.5	14.1	14.0	-0.0	14.5
Pyrazole	-3.8	-4.2	-4.2	-0.0	-3.9
Succinic Acid	-22.6	-26.9	-27.1	-0.2	-22.7
Triazine	2.4	1.8	1.8	-0.0	2.4
Trioxane	6.2	4.2	4.2	0.0	6.2
Uracil	-38.5	-42.6	-42.7	-0.1	-38.6
Urea	-45.4	-49.4	-49.7	-0.3	-45.6

TABLE 23: Estimated computational cost (in GPUh) for the composite VASP calculations used to compute the HF lattice energies of the X23 dataset on an NVIDIA A100 GPU. The three different settings correspond to different PAW potentials and plane-wave cutoffs (with k -point spacing given in parenthesis), as described in the text.

	Hard (0.25)	Std (0.25)	Std (0.18)
1,4-cyclohexanedione	3.4	1.6	11.2
Acetic Acid	2.9	1.4	8.5
Adamantane	1.4	0.7	4.7
Ammonia	0.2	0.2	0.9
Anthracene	4.0	1.7	7.1
Benzene	2.4	0.9	4.5
CO ₂	0.5	0.2	1.2
Cyanamide	4.3	2.0	17.3
Cytosine	4.2	1.7	10.4
Ethyl carbamate	2.6	1.4	15.0
Formamide	2.3	1.2	6.8
Hexamine	1.8	1.0	4.7
Imidazole	2.2	1.1	7.8
Naphthalene	3.9	1.9	6.0
Oxalic Acid α	5.6	2.7	10.7
Oxalic Acid β	3.9	1.9	9.2
Pyrazine	1.8	1.0	5.0
Pyrazole	9.8	3.5	22.2
Succinic Acid	2.5	1.2	7.9
Triazine	8.3	2.6	7.4
Trioxane	24.8	8.4	26.3
Uracil	14.3	5.4	8.9
Urea	0.7	0.3	1.6
Average	4.7	1.9	8.9

C. MBE cWFT correlation

We have used the Composite approach with 'Full' basis set described in Section 3 A 6 to calculate the 1B, 2B and 3B contributions from the correlation energy to the lattice energy, which we report in Table 24. We have reported several post-HF methods besides CCSD(T), such as second-order Møller-Plesset perturbation theory [43] (MP2) as well as coupled cluster theory with single and double excitations. Within the Composite approach, MP2 is devoid of local approximations, while CCSD and CCSD(T) make use of the LNO approximation. We leave comparisons of the performance of these methods to Section 10 and discuss general trends here.

We find that the 2B contribution makes up the bulk of the lattice energy, being an order of magnitude or more than the 3B contributions. MP2 generally predicts less-repulsive values (by an average of 2.6 kJ/mol) on the 3B contributions than CCSD or CCSD(T) due to missing (repulsive) three-body dispersion effects [105]. Conversely, CCSD can reproduce 3B contributions well [106] to a mean absolute deviation (MAD) of 0.6 kJ/mol and tends to underbind the 2B contributions significantly by an MAD of 13.8 kJ/mol which is equivalent to the mean-signed deviation. MP2 has an MAD of 6.9 kJ/mol on the 2B terms and most of this comes from an overbinding of dispersion-bound compounds [107].

TABLE 24: The MBE contributions to the lattice energy of the X23 set for several correlated wave-function theory methods in the Composite 'Full' basis approach. All values are in kJ/mol. We also report the mean signed deviation (MSD) and mean absolute deviation (MAD) of MP2 and CCSD compared to CCSD(T).

	MP2				CCSD				CCSD(T)			
	1B	2B	3B	Total	1B	2B	3B	Total	1B	2B	3B	Total
1,4-cyclohexanedione	-6.4	-86.7	0.7	-92.5	-4.5	-71.3	3.0	-72.8	-5.8	-86.4	3.6	-88.6
Acetic Acid	-4.8	-49.1	0.8	-53.1	-3.7	-42.1	2.2	-43.6	-4.5	-50.5	2.6	-52.4
Adamantane	-0.4	-115.3	1.2	-114.4	-0.6	-94.5	4.3	-90.9	-1.0	-113.1	4.7	-109.3
Ammonia	-0.9	-27.6	0.4	-28.1	-0.9	-24.2	1.3	-23.8	-1.1	-28.7	1.4	-28.4
Anthracene	-2.4	-212.0	1.8	-212.5	-1.8	-141.0	4.4	-138.4	-2.7	-171.7	5.3	-169.1
Benzene	-1.0	-92.7	2.1	-91.6	-0.9	-66.3	4.6	-62.6	-1.3	-79.6	5.3	-75.7
CO ₂	0.1	-26.8	1.0	-25.7	0.1	-22.4	2.0	-20.2	0.1	-26.9	2.3	-24.5
Cyanamide	-3.4	-59.6	2.2	-60.8	-2.1	-43.4	3.8	-41.7	-2.5	-53.5	4.1	-51.9
Cytosine	-10.7	-113.7	-0.1	-124.4	-8.3	-88.5	3.3	-93.5	-10.3	-107.5	3.8	-114.1
Ethyl carbamate	-2.9	-64.9	0.3	-67.4	-2.3	-56.1	2.1	-56.3	-3.0	-67.1	2.5	-67.6
Formamide	-7.9	-41.8	0.2	-49.5	-6.0	-37.0	2.0	-41.0	-7.5	-44.8	2.6	-49.7
Hexamine	-0.9	-111.7	1.0	-111.6	-0.5	-90.8	3.7	-87.6	-0.7	-108.9	4.0	-105.6
Imidazole	-5.0	-84.6	1.1	-88.4	-3.6	-61.5	3.4	-61.6	-4.5	-74.1	3.9	-74.6
Naphthalene	-1.4	-159.7	1.2	-159.9	-1.2	-109.0	2.8	-107.5	-1.8	-132.2	3.2	-130.8
Oxalic Acid α	1.8	-71.1	4.1	-65.3	1.5	-58.4	4.6	-52.2	2.4	-71.6	5.1	-64.1
Oxalic Acid β	-3.5	-73.5	5.3	-71.7	-2.7	-59.8	4.9	-57.5	-2.7	-74.3	6.5	-70.5
Pyrazine	-2.4	-96.3	1.8	-96.8	-1.8	-67.7	5.4	-64.0	-2.6	-81.7	6.4	-77.9
Pyrazole	-4.0	-86.5	1.7	-88.8	-2.9	-62.9	3.8	-62.0	-3.7	-75.6	4.3	-75.1
Succinic Acid	-7.7	-100.8	3.2	-105.3	-6.3	-83.8	6.0	-84.1	-7.5	-101.8	7.2	-102.2
Triazine	-2.8	-71.0	2.2	-71.6	-2.0	-54.2	4.5	-51.8	-2.9	-65.8	5.3	-63.4
Trioxane	-4.7	-67.7	1.5	-70.9	-3.9	-58.4	3.2	-59.0	-5.1	-68.8	3.9	-70.1
Uracil	-12.3	-94.3	-0.5	-107.1	-8.8	-73.1	1.7	-80.1	-11.2	-90.1	2.7	-98.6
Urea	-5.8	-53.7	-2.6	-62.1	-3.9	-47.3	0.6	-50.6	-4.5	-56.9	0.3	-61.2
MSD	-0.2	-5.6	-2.6	-8.4	0.8	13.8	-0.6	14.0	0.0	0.0	0.0	0.0
MAD	0.4	6.9	2.6	8.5	0.8	13.8	0.6	14.0	0.0	0.0	0.0	0.0

D. Effects from CCSD(cT)-fit

As discussed in the main text, there are discrepancies between DMC and LNO-MBE-CCSD(T) for $\pi - \pi$ dispersion-bound complexes such as naphthalene and anthracene of over 10 kJ/mol. This is in line with observations by Al-Hamdani and Nagy *et al.* [108], which found even larger discrepancies for the interaction energy between $\pi - \pi$ bound supramolecules including coronene and circumcoronene. It is currently a matter of open debate where these errors lie [109–112], with studies indicating either errors in the DMC nodal surface [113] or level of convergence up to the perturbative triples (T) contribution [109] in CCSD(T).

Schäfer *et al.* [109] have suggested that part of this discrepancy arises from missing contributions in (T) that can be accounted by the (cT) approach. They have demonstrated that there exists an empirical relationship between the (cT) and the (T) correlation energy contributions for dispersion-dominated complexes. This empirical relationship makes use of the MP2, CCSD and (T) correlation energies, with a (cT)-fit of the form:

$$\frac{(T)}{(cT)\text{-fit}} = a + b \cdot \frac{\text{MP2 corr.}}{\text{CCSD corr.}}, \quad (15)$$

where a and b were parameters fitted from a set of dispersion-bound complexes. While this means that CCSD(cT)-fit should only be applied to study dispersion-bound systems, we find that it does not affect performance for H-bonded systems both within this work and for dimers of the S66 dataset [114], while giving improvements in agreement to DMC for dispersion-bound systems.

In Table 25, we have computed the MBE contributions of the CCSD(cT)-fit correlation energy and compared it to CCSD(T). Its effect is small for the 1B and 3B terms and the general trend is to weaken the 2B contributions, leading to a MSD and MAD of 1.7 kJ/mol w.r.t. the CCSD(T) estimate. Importantly, this is most prominent for dispersion-bound systems such as anthracene and naphthalene, amounting to 5.1 kJ/mol and 3.7 kJ/mol, respectively. As seen in Figure 33, in both cases, this brings CCSD(cT)-fit closer in the direction of the DMC estimates than CCSD(T), albeit not fully in exact agreement with DMC, commensurate with observations by Schäfer *et al.* [109]. This in turn has improved the MAD from 3.1 kJ/mol to 2.5 kJ/mol for the entire X23 dataset (Table 26). On the other hand, other studies suggest that beyond CCSD(cT) effects from quadruple excitations move the CC results back close to CCSD(T) for π - π dimers,[110] so one cannot provide more conclusive results at the moment.

TABLE 25: The MBE contributions to the lattice energy of the X23 set between CCSD(T) and CCSD(cT)-fit in the Composite 'Full' basis approach. All values are in kJ/mol. We also report the mean signed deviation (MSD) and mean absolute deviation (MAD) compared to CCSD(T).

	CCSD(T)				CCSD(cT)-fit			
	1B	2B	3B	Total	1B	2B	3B	Total
1,4-cyclohexanedione	-5.8	-86.4	3.6	-88.6	-5.6	-84.8	3.7	-86.7
Acetic Acid	-4.5	-50.5	2.6	-52.4	-4.4	-49.7	2.7	-51.5
Adamantane	-1.0	-113.1	4.7	-109.3	-1.0	-111.1	4.8	-107.2
Ammonia	-1.1	-28.7	1.4	-28.4	-1.1	-28.3	1.5	-27.9
Anthracene	-2.7	-171.7	5.3	-169.1	-2.6	-166.6	5.4	-163.8
Benzene	-1.3	-79.6	5.3	-75.7	-1.3	-77.7	5.4	-73.6
CO ₂	0.1	-26.9	2.3	-24.5	0.1	-26.4	2.4	-24.0
Cyanamide	-2.5	-53.5	4.1	-51.9	-2.4	-52.0	4.1	-50.2
Cytosine	-10.3	-107.5	3.8	-114.1	-10.1	-105.2	3.9	-111.3
Ethyl carbamate	-3.0	-67.1	2.5	-67.6	-2.9	-66.1	2.6	-66.4
Formamide	-7.5	-44.8	2.6	-49.7	-7.3	-44.1	2.7	-48.8
Hexamine	-0.7	-108.9	4.0	-105.6	-0.6	-107.0	4.0	-103.5
Imidazole	-4.5	-74.1	3.9	-74.6	-4.3	-72.3	4.0	-72.6
Naphthalene	-1.8	-132.2	3.2	-130.8	-1.7	-128.5	3.3	-127.0
Oxalic Acid α	2.4	-71.6	5.1	-64.1	2.3	-70.1	5.1	-62.7
Oxalic Acid β	-2.7	-74.3	6.5	-70.5	-2.7	-72.7	6.4	-69.0
Pyrazine	-2.6	-81.7	6.4	-77.9	-2.5	-79.6	6.5	-75.6
Pyrazole	-3.7	-75.6	4.3	-75.1	-3.6	-73.8	4.3	-73.0
Succinic Acid	-7.5	-101.8	7.2	-102.2	-7.4	-99.9	7.3	-100.1
Triazine	-2.9	-65.8	5.3	-63.4	-2.8	-64.4	5.4	-61.8
Trioxane	-5.1	-68.8	3.9	-70.1	-5.0	-67.9	3.9	-69.0
Uracil	-11.2	-90.1	2.7	-98.6	-10.8	-88.0	2.9	-96.1
Urea	-4.5	-56.9	0.3	-61.2	-4.4	-56.1	0.5	-60.0
MSD	0.0	0.0	0.0	0.0	0.1	1.7	0.1	1.9
MAD	0.0	0.0	0.0	0.0	0.1	1.7	0.1	1.9

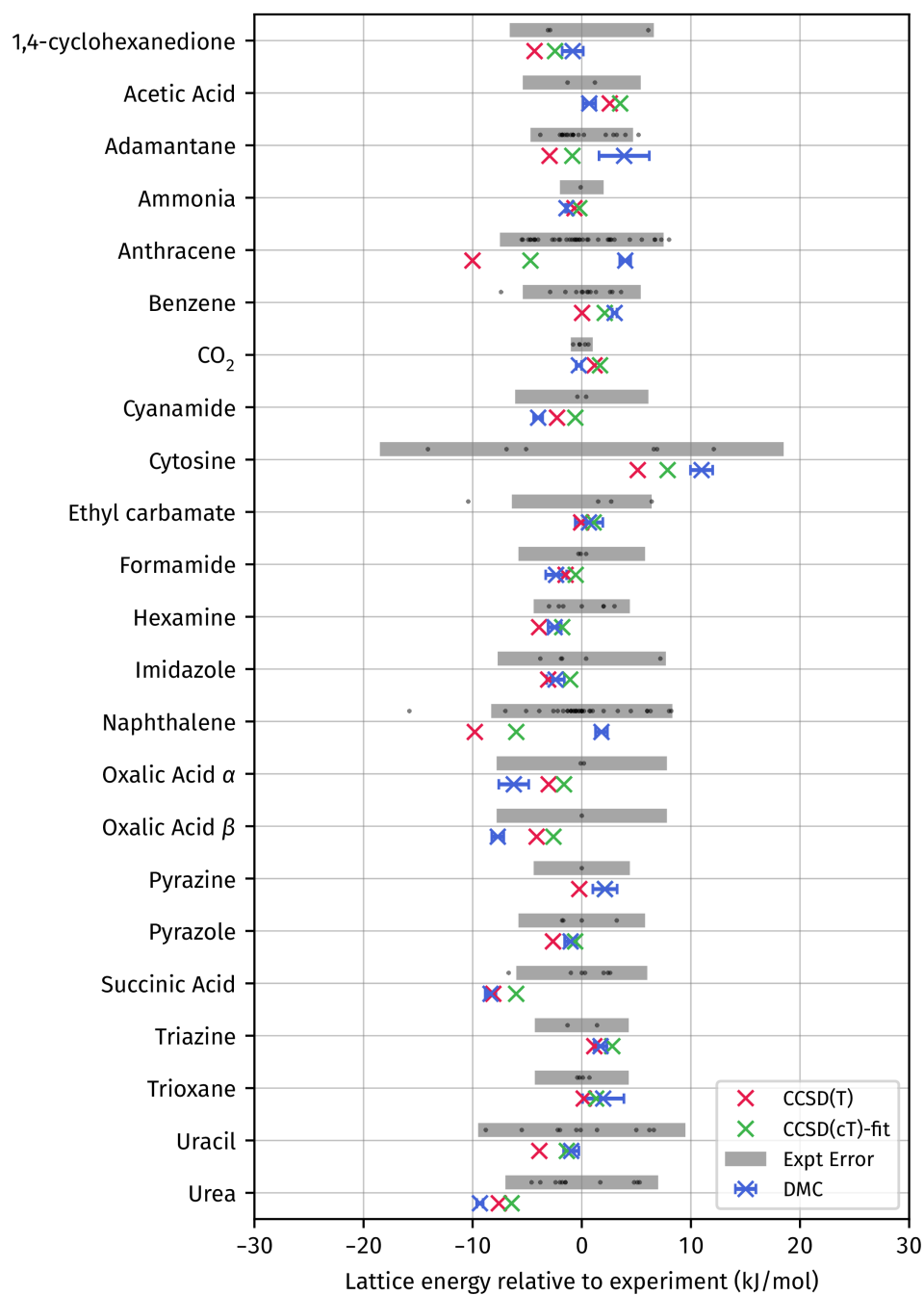


FIG. 33: Comparing the relative differences of DMC, CCSD(T) and CCSD(cT)-fit w.r.t. the experimental mean and error.

E. Final estimates and comparison to DMC

In Table 26, we compare the final (LNO-MBE-)CCSD(T) and CCSD(cT)-fit estimates to both DMC and experiments. Within this context, it's not clear what should be used as the reference, given the large error bars on the experimental lattice energies and the open question on whether CCSD(T) or DMC has larger error bars. Regardless, the agreement between all of the approaches is great, reaching sub-chemical accuracy of below 4 kJ/mol regardless of whether the experiment, LNO-MBE-CCSD(T) or DMC are used as the reference. For experiments, both DMC and LNO-MBE-CCSD(T) have an MAD of 3.4 kJ/mol w.r.t. experiments, although the large error bars of experiments (the majority exceeding 4 kJ/mol) will make it difficult to assess the accuracy between these methods at this level of precision.

When comparing the LNO-MBE-CCSD(T) estimates to DMC (compared visually in Figure 34), it can be seen that there is a tendency to predict stronger binding, with an MSD of -1.8 kJ/mol. As shown in Table 27, this stronger binding comes predominantly from the vdW dispersion-bound systems (as defined in Ref. 4). We have compared the lattice energy between LNO-MBE-CCSD(T) and DMC for this set of systems and it can be seen that the MSD [negative indicating stronger binding of CCSD(T)] lies close in magnitude of the MAD. This trend is in agreement with a recent comparison of dimers of different binding characters in Ref. 114, which indicates stronger binding of CCSD(T) w.r.t. DMC.

In Table 28, we have also compared the lattice energies between DMC and LNO-MBE-CCSD(T) for the subset of systems with predominantly H-bonding character [4]. It follows similar trends for those recently observed for dimers [114] whereby CCSD(T) predicts weaker binding than DMC, indicated by a positive MSD that is very close in magnitude to the MAD.

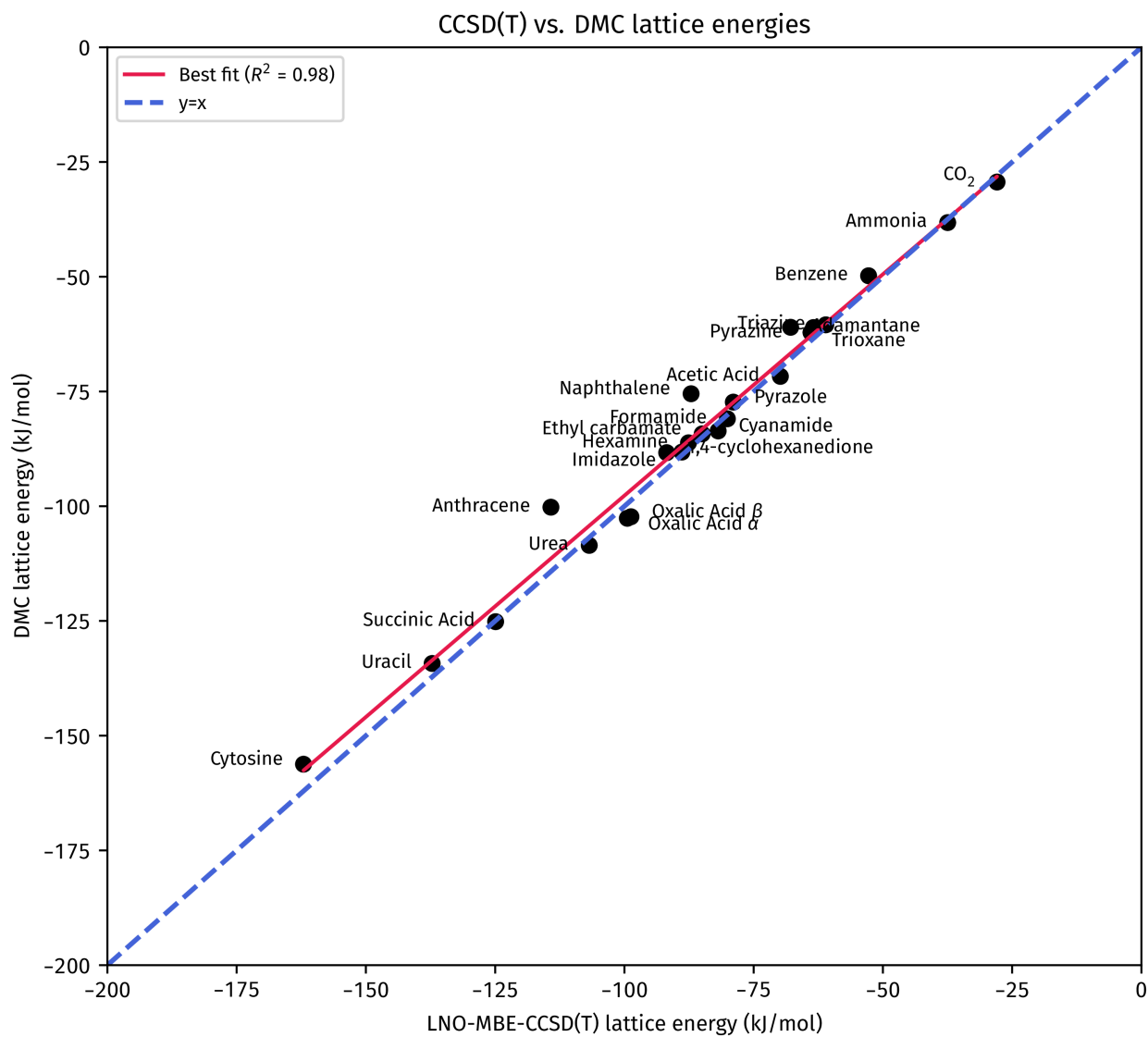


FIG. 34: Parity plot of the LNO-MBE-CCSD(T) and DMC lattice energies for the X23 dataset.

TABLE 26: Final lattice energy (in kJ/mol) for the X23 dataset computed with different methods, compared to experimental values. The DMC values are taken from Ref. 1. The mean absolute deviation (MAD) is also reported with respect to (LNO-MBE-)CCSD(T), experiment and DMC.

	CCSD(T)	CCSD(cT)-fit	DMC	DMC Error	Expt	Expt Error
1,4-cyclohexanedione	-91.8	-89.9	-88.3	1.0	-87.5	6.6
Acetic Acid	-69.8	-68.9	-71.7	0.6	-72.4	5.4
Adamantane	-67.9	-65.8	-61.0	2.3	-64.9	4.7
Ammonia	-37.5	-37.0	-38.2	0.1	-36.8	2.0
Anthracene	-114.2	-108.9	-100.2	0.5	-104.2	7.5
Benzene	-52.8	-50.7	-49.8	0.2	-52.8	5.4
CO ₂	-27.9	-27.4	-29.4	0.2	-29.1	1.0
Cyanamide	-81.9	-80.2	-83.6	0.4	-79.6	6.1
Cytosine	-162.1	-159.3	-156.2	1.0	-167.2	18.5
Ethyl carbamate	-85.0	-83.8	-84.2	1.3	-84.9	6.4
Formamide	-80.1	-79.2	-81.0	1.0	-78.6	5.8
Hexamine	-87.6	-85.5	-86.2	0.6	-83.7	4.4
Imidazole	-88.9	-86.9	-88.2	0.8	-85.8	7.7
Naphthalene	-87.1	-83.3	-75.5	0.5	-77.3	8.3
Oxalic Acid α	-99.4	-98.0	-102.6	1.4	-96.4	7.8
Oxalic Acid β	-98.7	-97.2	-102.3	0.6	-94.6	7.8
Pyrazine	-63.4	-61.1	-61.1	1.1	-63.2	4.4
Pyrazole	-78.9	-76.9	-77.3	0.5	-76.3	5.8
Succinic Acid	-124.9	-122.8	-125.2	0.5	-116.8	6.0
Triazine	-61.1	-59.4	-60.5	0.6	-62.2	4.3
Trioxane	-63.9	-62.8	-62.1	1.9	-64.1	4.3
Uracil	-137.2	-134.7	-134.3	0.7	-133.3	9.5
Urea	-106.8	-105.6	-108.5	0.3	-99.2	7.0
MAD [CCSD(T)]	0.0	1.9	3.1	-	3.4	-
MAD (Expt)	3.4	2.6	3.4	-	0.0	-
MAD (DMC)	3.1	2.5	0.0	-	3.4	-
MSD (DMC)	-1.8	0.1	0.0	-	0.7	-

TABLE 27: Lattice energy (in kJ/mol) for the vdW-bonded subset of the X23 dataset computed with different methods, compared to experimental values. The DMC values are taken from Ref. 1. The mean absolute deviation (MAD) is also reported with respect to (LNO-MBE-)CCSD(T), experiment and DMC.

	CCSD(T)	CCSD(cT)-fit	DMC	DMC Error	Expt	Expt Error
1,4-cyclohexanedione	-91.8	-89.9	-88.3	1.0	-87.5	6.6
Adamantane	-67.9	-65.8	-61.0	2.3	-64.9	4.7
Anthracene	-114.2	-108.9	-100.2	0.5	-104.2	7.5
Benzene	-52.8	-50.7	-49.8	0.2	-52.8	5.4
CO ₂	-27.9	-27.4	-29.4	0.2	-29.1	1.0
Hexamine	-87.6	-85.5	-86.2	0.6	-83.7	4.4
Naphthalene	-87.1	-83.3	-75.5	0.5	-77.3	8.3
Pyrazine	-63.4	-61.1	-61.1	1.1	-63.2	4.4
Pyrazole	-78.9	-76.9	-77.3	0.5	-76.3	5.8
Triazine	-61.1	-59.4	-60.5	0.6	-62.2	4.3
Trioxane	-63.9	-62.8	-62.1	1.9	-64.1	4.3
MAD [CCSD(T)]	0.0	2.3	4.4	-	3.3	-
MAD (Expt)	3.3	2.4	2.1	-	0.0	-
MAD (DMC)	4.4	2.6	0.0	-	2.1	-
MSD (DMC)	-4.1	-1.8	0.0	-	-1.3	-

TABLE 28: Lattice energy (in kJ/mol) for the H-bonded subset of the X23 dataset computed with different methods, compared to experimental values. The DMC values are taken from Ref. 1. The mean absolute deviation (MAD) is also reported with respect to (LNO-MBE-)CCSD(T), experiment and DMC.

	CCSD(T)	CCSD(cT)-fit	DMC	DMC Error	Expt	Expt Error
Acetic Acid	-69.8	-68.9	-71.7	0.6	-72.4	5.4
Ammonia	-37.5	-37.0	-38.2	0.1	-36.8	2.0
Cyanamide	-81.9	-80.2	-83.6	0.4	-79.6	6.1
Ethyl carbamate	-85.0	-83.8	-84.2	1.3	-84.9	6.4
Formamide	-80.1	-79.2	-81.0	1.0	-78.6	5.8
Oxalic Acid α	-99.4	-98.0	-102.6	1.4	-96.4	7.8
Oxalic Acid β	-98.7	-97.2	-102.3	0.6	-94.6	7.8
Succinic Acid	-124.9	-122.8	-125.2	0.5	-116.8	6.0
Urea	-106.8	-105.6	-108.5	0.3	-99.2	7.0
MAD [CCSD(T)]	0.0	1.3	1.6	-	3.3	-
MAD (Expt)	3.3	2.5	4.5	-	0.0	-
MAD (DMC)	1.6	2.7	0.0	-	4.5	-
MSD (DMC)	1.5	2.7	0.0	-	4.2	-

F. Comparison to other work

In Table 29, we compare LNO-MBE-CCSD(T) (as well as experiment and DMC) to several previous works employing beyond-DFT methods:

- Syty *et al.* [58] have been able to study the entire X23 dataset through a multilevel approach, which performs LNO-CCSD(T) for 1B and short-range 2B terms within the MBE, while an energy-corrected RPA (RPA+ph) is used for longer-range dimers and short-range trimers, and periodic HF to cover remaining contributions. The `vvTight` thresholds were used on LNO-CCSD(T) for most systems, but this was decreased to `vTight` for anthracene.
- Červinka *et al.* [115] studied a subset of the X23 dataset (alongside several other small crystalline molecules), utilizing a MBE approach up to 3B contributions, followed by calculating electrostatic interactions using atomic partial charges.
- Klimeš applied RPA with singles correlation energy contributions at the GW singles excitations (GWSE) level under periodic boundary conditions to study a subset of X23.
- Sherrill and co-workers have performed MBE calculations with CCSD(T) for the two-body contributions [77] of the entire X23 dataset and three-body contributions for a subset [78, 79]. We include estimates for three dispersion-bound systems as higher-body terms are expected to be required for H-bonded systems. To get the final lattice energy, we have added 1B contributions calculated within this work.

Our LNO-MBE-CCSD(T) approach achieves good agreement to the previous works. Against the estimates by Syty *et al.*, it achieves a mean absolute deviation (MAD) of 2.0 kJ/mol, while DMC achieves 3.1 kJ/mol and experimental agreement is 4.3 kJ/mol. Similarly, for the other aforementioned studies, our LNO-MBE-CCSD(T) approach achieves the best agreement compared to DMC and experiment.

TABLE 29: Comparison of reference literature lattice energies (in kJ/mol) for X23. The mean absolute deviation (MAD) is reported with respect to LNO-MBE-CCSD(T), experiment and DMC [1].

	Multilevel Syty <i>et al.</i> [58]	CCSD(T) 1B+2B+3B+ELST (>3B) MBE (Červinka [115])	RPA+GWSE (Klimeš [2])	HMBI CCSD(T) 1B+2B+FF(>2B) (Wen and Beran [80])	CCSD(T) 1B+2B+3B MBE (Sherrill <i>et al.</i> [77, 78])
1,4-cyclohexanedione	-94.4	-	-	-	-
Acetic Acid	-71.2	-70.6	-	-	-
Adamantane	-66.0	-	-69.4	-	-
Ammonia	-37.6	-39.1	-37.2	-40.2	-
Anthracene	-111.4	-	-112.7	-	-
Benzene	-51.6	-	-55.3	-54.0	-53.8
CO ₂	-29.4	-21.2	-28.4	-29.5	-28.7
Cyanamide	-82.6	-	-79.7	-	-
Cytosine	-163.1	-	-	-	-
Ethyl carbamate	-86.5	-	-	-	-
Formamide	-84.0	-89.9	-	-80.4	-
Hexamine	-88.0	-	-	-	-
Imidazole	-88.4	-	-	-90.8	-
Naphthalene	-82.5	-	-81.7	-	-
Oxalic Acid α	-103.0	-	-96.3	-	-
Oxalic Acid β	-101.6	-	-96.1	-	-
Pyrazine	-64.3	-	-	-	-
Pyrazole	-79.3	-	-	-	-
Succinic Acid	-128.2	-	-	-	-
Triazine	-60.3	-	-	-	-52.2
Trioxane	-67.8	-	-	-	-
Uracil	-139.7	-	-	-	-
Urea	-111.0	-	-102.5	-	-
MAD [CCSD(T)]	2.0	70 4.7	2.4	1.5	3.6
MAD (Expt)	4.3	5.8	2.6	2.4	3.8
MAD (DMC)	3.1	4.8	5.7	1.9	4.3

G. Validating CCSD(T) estimates

As we have briefly discussed in Section 2 B that the standard MBE of the CCSD(T) correlation energy can be enhanced by using subtractive embedding (by calculating $\Delta_{D4}^{CCSD(T)}$ on top of the D4 dispersion). On top of its improved convergence speed with distance cutoff, this also offers an alternative approach for validation. In the limit of infinite 2B and 3B cutoffs (assuming negligible contribution from 4B terms), we expect both approaches to converge towards the same value. In Table 30, we have compared both approaches for the same set of 2B and 3B cutoffs. The differences between the two are very small, with an MAD of 0.4 kJ/mol, reassuring the estimates the MBE estimates we have made of the correlation energy.

TABLE 30: Lattice energy (in kJ/mol) for the X23 dataset when LNO-MBE-CCSD(T) is corrected with (and without) the D4 dispersion correction.

	Without D4	With D4	Difference
1,4-cyclohexanedione	-91.8	-92.2	0.4
Acetic Acid	-69.8	-70.3	0.5
Adamantane	-67.9	-67.5	-0.3
Ammonia	-37.5	-38.6	1.1
Anthracene	-114.2	-113.9	-0.3
Benzene	-52.8	-52.8	0.0
CO ₂	-27.9	-27.9	-0.0
Cyanamide	-81.9	-82.4	0.5
Cytosine	-162.1	-161.9	-0.2
Ethyl carbamate	-85.0	-85.0	0.1
Formamide	-80.1	-80.8	0.7
Hexamine	-87.6	-88.1	0.5
Imidazole	-88.9	-88.8	-0.1
Naphthalene	-87.1	-83.8	-3.3
Oxalic Acid α	-99.4	-99.3	-0.1
Oxalic Acid β	-98.7	-98.8	0.1
Pyrazine	-63.4	-63.5	0.0
Pyrazole	-78.9	-78.5	-0.4
Succinic Acid	-124.9	-125.0	0.1
Triazine	-61.1	-61.5	0.4
Trioxane	-63.9	-64.1	0.2
Uracil	-137.2	-137.2	-0.0
Urea	-106.8	-107.0	0.2
Mean	-	-	0.4

5. COST COMPARISON FOR X23 DATASET

In this section, we will compare the cost to perform LNO-MBE-CCSD(T) against standard approaches such as periodic GGA-DFT (with the PBE DFA) and for hybrid-DFT (with the PBE0 DFA). Furthermore, we will compare it to fixed-node quantum diffusion Monte Carlo (DMC), which has become a relatively mature high-level theory that has been applied to many molecular crystals in the past [1, 7, 116, 117]. We will use the 23 molecular crystals within the X23 dataset to assess the cost to perform these calculations as they feature a diverse range of elements commonly found in molecular crystals together with varying system and unit cell sizes.

We report the cost for each of the 23 molecular crystals as well as their average in Table 31. For each of the approaches, we have made our best attempts to calculate costs from a seasoned user of the corresponding approach, based on our collective expertise, which we will discuss in Secs. 5 A, 5 B and 5 C for DFT, LNO-MBE-CCSD(T) and DMC, respectively. In particular, we have reported several costs for LNO-MBE-CCSD(T), defined by ‘low’, ‘moderate’, which loosen both the 2B and 3B cutoffs in the MBE relative to the original ‘high’ estimate. The cutoffs are specified in Section 5 B, where we show that ‘low’ and ‘moderate’ lead to mean absolute deviations (MADs) of 2 and 1 kJ/mol against ‘high’, respectively. We note here that these metrics utilize the subtractive embedding of D4 dispersion described in Section 2 B due to its improved convergence behavior. Similarly, for DMC, we present costs for increasing precision, namely with a standard deviation 2σ of the energy estimation of 4, 2 and 1 kJ/mol (where a 95% confidence interval corresponds to the interval $E \pm 2\sigma$).

The cost of the ‘high’ LNO-MBE-CCSD(T) are already relatively cheap and comparable to periodic HF, where the former has costs ranging from 277 to 21941 CPUh while the latter has costs ranging from 93 to 11773 CPUh. Already, this cost is highly economical, particularly within the context of crystal structure prediction (CSP), where it has been recently suggested [118] that the threshold for a computational method to be economically viable is ‘about one day on 1,000 cores’ (amounting to 24,000 CPUh) within a final screening stage. In the case of Firaha *et al.* [118], such a threshold was for going beyond static electronic energies towards free energies but we expect that it could be similarly important to get LNO-MBE-CCSD(T) lattice energies. Going to the ‘moderate’ or ‘low’ LNO-MBE-CCSD(T) approaches leads to significantly cheaper costs, with the ‘medium’ coming to an average cost of 1906 CPUh, while ‘low’ brings this down to an average of 502 CPUh, with the majority (20 out of the 23) of systems requiring fewer than 1000 CPUh. Importantly, this makes the cost cheaper than HF or hybrid DFT. The GGA-DFT

TABLE 31: Estimated computational cost (in CPUh) for the different methods used to compute the lattice energies of the X23 dataset. The LNO-MBE-CCSD(T) costs are given for the low (2B cutoff of 6.5 Å and 3B cutoff of 100 Å³), moderate (2B cutoff of 9.0 Å and 3B cutoff of 200 Å³) and high (2B cutoff of 12.0 Å and 3B cutoff of 300 Å³) models. The DMC costs are estimated for a standard deviation of 2σ of 1, 2 and 4 kJ/mol, respectively.

	HF	DFT (GGA)	CCSD(T) [low]	CCSD(T) [moderate]	CCSD(T) [high]	DMC [4]	DMC [2]	DMC [1]
1,4-cyclohexanedione	1297	3	800	2276	7824	1984	23818	317584
Acetic Acid	1684	4	139	878	2195	433	5198	69307
Adamantane	365	3	624	1795	5585	4334	52013	693512
Ammonia	93	1	50	193	411	18	219	2925
Anthracene	2496	6	2822	6586	21941	2065	24791	330552
Benzene	1201	4	241	1000	2802	1221	14657	195439
CO ₂	162	1	24	116	277	160	1926	25689
Cyanamide	1993	5	137	465	1149	349	4198	55984
Cytosine	2778	6	754	5566	10764	1285	15430	205738
Ethyl carbamate	1048	3	484	1604	4160	1044	12528	167046
Formamide	1149	3	180	662	1505	366	4395	58600
Hexamine	1104	4	548	1045	2637	2191	26293	350579
Imidazole	1308	4	274	1575	3242	764	9178	122386
Naphthalene	1148	4	1238	3758	11119	2627	31534	420464
Oxalic Acid α	2411	3	128	1154	2263	1845	22146	295291
Oxalic Acid β	1677	2	293	1351	2495	1329	15952	212701
Pyrazine	798	3	212	991	1750	886	10636	141823
Pyrazole	6483	8	409	2836	5588	764	9178	122386
Succinic Acid	916	5	356	1050	4786	1182	14195	189276
Triazine	6337	5	238	640	1025	886	10636	141823
Trioxane	11773	10	194	1135	1830	1601	19214	256190
Uracil	7081	9	1297	6717	13454	1285	15430	205738
Urea	170	2	168	456	736	290	3481	46414
Mean	2412	4	502	1906	4762	1257	15089	201193

remains the cheapest approach by far but that comes with an accuracy trade-off as shown in Section 10.

Compared to the LNO-MBE-CCSD(T) costs, the DMC costs are larger. For a 95% confidence interval of 1 kJ/mol, it would cost $\sim 200,000$ CPUh on average. If less accuracy is needed, the cost is on average $\sim 15,000$ and $\sim 1,300$ CPUh for a 2 and 4 kJ/mol error respectively. For relative energies between some polymorphs (particularly competing polymorphs), the differences may be 1 kJ/mol or less, necessitating that level of statistical accuracy on the DMC calculations.

A. Calculating cost of hybrid DFT

As our HF calculations were actually performed on GPUs (see Section 4 B) and it is challenging to make a one-to-one comparison with costs on CPU, we reperformed these calculations on the CPU. Both the HF and DFT (GGA) calculations were performed in Quantum Espresso [33], where we have also accelerated the calculations with the Adaptively Compressed Exchange [21] (ACE) operator. This is expected to speed up costs by ≈ 3 . These costs were estimated on 48-core Cascadelake nodes with 768 GB of RAM.

B. Calculating cost of LNO-MBE-CCSD(T)

For the X23 dataset, all LNO-MBE-CCSD(T) calculations were performed on nodes involving 2×18 2.1 GHz Intel Xeon E5-2695 (Broadwell) series processors with 256 GB of RAM in total. For the X23 dataset, each calculation was performed on 8-cores with 46 GB of RAM allocated. Our costs include not only the cost to perform the LNO-CCSD(T) calculations, but also the composite correction using the MP2 as well within the Composite procedure with 'Full' basis sets (see Section 3 A 6). These costs exclude the underlying costs to perform the periodic HF calculations because their costs are negligible compared to the CCSD(T) calculations with the help of GPUs (see Section 4 B). It also enables fairer comparison to DMC calculations, where the costs to (1) generate the DFT trial wave-function and (2) optimizing the Jastrow factor have been neglected during the cost analysis.

As discussed in the preceding section, we have defined several presets of 2B and 3B cutoffs assuming a D4 dispersion embedding (due to its faster convergence):

- low — 2B cutoff of 6.5 \AA and 3B cutoff of 100 \AA^3 ,
- moderate — 2B cutoff of 9.0 \AA and 3B cutoff of 200 \AA^3 ,

TABLE 32: Lattice energy (in kJ/mol) for the X23 dataset with the large (2B cutoff of 12.0 Å and 3B cutoff of 300 Å³) LNO-MBE-CCSD(T) model, and the medium (2B cutoff of 6.5 Å and 3B cutoff of 100 Å³) as well as small models (2B cutoff of 9.0 Å and 3B cutoff of 200 Å³).

	Small	Medium	Large
1,4-cyclohexanedione	-92.9	-92.2	-92.2
Acetic Acid	-70.9	-69.5	-70.3
Adamantane	-65.4	-66.9	-67.5
Ammonia	-37.4	-37.9	-38.6
Anthracene	-110.4	-111.3	-113.9
Benzene	-53.2	-52.3	-52.8
CO ₂	-28.4	-28.3	-27.9
Cyanamide	-82.9	-81.8	-82.4
Cytosine	-163.8	-157.5	-161.9
Ethyl carbamate	-83.7	-85.1	-85.0
Formamide	-76.8	-81.1	-80.8
Hexamine	-85.1	-85.3	-88.1
Imidazole	-87.8	-87.9	-88.8
Naphthalene	-81.7	-82.7	-83.8
Oxalic Acid α	-102.5	-99.1	-99.3
Oxalic Acid β	-101.2	-98.1	-98.8
Pyrazine	-64.4	-63.4	-63.5
Pyrazole	-78.5	-78.1	-78.5
Succinic Acid	-128.9	-128.5	-125.0
Triazine	-61.4	-61.5	-61.5
Trioxane	-64.1	-63.8	-64.1
Uracil	-141.6	-137.2	-137.2
Urea	-103.7	-108.8	-107.0
MAD	1.8	1.0	0.0

- high — 2B cutoff of 12.0 Å and 3B cutoff of 300 Å³.

The cost for each molecular crystal within the X23 dataset is shown in Table 32.

C. Calculating the cost of DMC

Diffusion Monte Carlo (DMC) estimations are affected by systematic and random errors. Systematic errors arise from approximations in the approach; the crucial ones are the fixed-node (FN) approximation, the use of pseudopotentials (PPs), and the finite-timestep (τ) approximation. The first two (FN and PP) are difficult to investigate because they cannot be reduced systematically; they can only be assessed by performing sets of calculations with different nodal surfaces and different PPs. For this reason, we treat FN and PP errors as a feature of the method that may affect its accuracy. By contrast, the finite- τ error can be made negligible by performing simulations at decreasing τ and either extrapolating to $\tau \rightarrow 0$ or choosing a τ such that the timestep bias is negligible for the target. This comes at the price of increased computational cost, which scales approximately as $1/\tau$ for a DMC simulation at timestep τ (see below).

Random errors are due to the stochastic nature of the approach and are estimated in each simulation from the standard deviation σ of the estimator. The smaller σ , the higher the precision. The stochastic error can be reduced to any target by increasing sampling, with $\sigma \propto (\text{sampling})^{-1/2}$ (and thus $\sigma \propto T^{-1/2}$ in computational time; see below). Consequently, reducing σ by a factor x costs about x^2 more compute. There is no point in having a tiny stochastic error but a large timestep bias (or vice versa): simulations should be planned so that both errors are comparable and sufficiently small for the desired precision and accuracy; otherwise total DMC cost will be unnecessarily large.

When the final estimator is a combination of results from multiple DMC runs, the overall stochastic error is obtained by propagating the independent errors. This is the case for lattice energies E_{latt} of molecular crystals, computed as the difference $E_{\text{latt}} = E_{\text{crys,1mol}} - E_{\text{gas}}$ between the energy per molecule of the crystal and the gas-phase molecular energy. If the two are estimated independently with stochastic errors $\sigma_{\text{crys,1mol}}$ and σ_{gas} , then $\sigma_{\text{latt}} = \sqrt{\sigma_{\text{crys,1mol}}^2 + \sigma_{\text{gas}}^2}$.

Despite having the same target precision, the costs of $E_{\text{crys,1mol}}$ and E_{gas} are not comparable. The crystal calculation is typically much more expensive, whereas the gas-phase calculation is often negligible or a small overhead. This follows from DMCs scaling with system size and from the fact that $E_{\text{crys,1mol}}$ is obtained from a periodic simulation cell containing several molecules. The simulated cell is not necessarily the primitive cell because finite-size errors (FSEs) can bias

the result. Two strategies are common: (i) brute-force extrapolation by computing a sequence of supercells and extrapolating to the thermodynamic limit, or (ii) applying finite-size corrections to each simulated cell. Several FSE corrections exist; see Refs. 119–123. Applying an FSE correction to a small cell is far cheaper than supercell extrapolation but is only as reliable as the correction itself; any bias propagates to $E_{\text{crys,1mol}}$ and therefore to E_{latt} . If only a single cell is used there is no internal check of the corrections reliability. Using multiple cells reduces the correction magnitude (it vanishes in the thermodynamic limit) but increases cost toward that of an explicit extrapolation. For molecular crystals there is evidence that the model periodic Coulomb (MPC)-based correction[121–123] is reliable whenever the inscribed-sphere radius of the WignerSeitz cell of the supercell is $\gtrsim 5 \text{ \AA}$; see Ref. [117]. Our cost estimates below assume this setup.

We evaluate the computational cost for DMC lattice energies of the X23 molecular crystals as reported in Table 31. This evaluation is based on calculations performed on the Peta4-Skylake nodes of the University of Cambridge CSD3 HPC system (Intel Xeon Scalable Skylake processors), published in Refs. 1, 117. The Cascade Lake nodes used for hybrid DFT estimates (Section 5 A) are slightly newer; we expect broadly comparable performance.

a. Stochastic cost model. Let σ be the target stochastic error for the total energy of a system. The DMC energy is the average over N_s electronic configurations $\{X_i\}_{i=1}^{N_s}$ sampled by DMC of the local energy $E_L[X_i]$: $E_{\text{DMC}} = \frac{1}{N_s} \sum_{i=1}^{N_s} E_L[X_i]$. If the $E_L[X_i]$ were independent, the error would be $\sqrt{\text{Var}(E_L)/N_s}$. Because configurations are correlated, we introduce an effective sample size $N_{\text{eff}} < N_s$ and estimate the error as $\sigma_{\text{DMC}} = \sqrt{\text{Var}(E_L)/N_{\text{eff}}}$. To achieve a target σ for a given $\text{Var}(E_L)$, we therefore require $N_{\text{eff}} = \text{Var}(E_L)/\sigma^2$.

A DMC run begins with $n_w(t=0)$ walkers. The algorithm generates new configurations from the previous iteration, and a population-control step keeps the walker count close to a target n_w^{target} each iteration. After equilibration, the sampling phase consists of $N_{\text{iter}} = N_s/n_w^{\text{target}}$ iterations. Within an iteration, walkers are (approximately) independent; correlations are significant between consecutive iterations. Define the autocorrelation $\rho(k) = \gamma(k)/\gamma(0)$, with $\gamma(k) = \text{Cov}(\langle E_L \rangle_t, \langle E_L \rangle_{t+k})$ over sampling iterations (after discarding equilibration). Let $N_{\text{ac}} = 1 + 2 \sum_{k=1}^{\infty} \rho(k)$ be the integrated autocorrelation time in units of iterations. Then

$$\frac{N_s}{N_{\text{eff}}} \approx N_{\text{ac}} \quad \Rightarrow \quad N_{\text{eff}} \approx \frac{\tau}{t_{\text{ac}}} N_s,$$

where we used the empirical observation that $N_{\text{ac}} \propto 1/\tau$ and define a (system-dependent) correlation time $t_{\text{ac}} = \tau N_{\text{ac}}$ (constant for a given system, in atomic units of time). Hence the

required sampling for target σ is

$$N_s = \frac{t_{\text{ac}}}{\tau} \frac{\text{Var}(E_L)}{\sigma^2}, \quad N_{\text{iter}} = \frac{1}{n_w^{\text{target}}} \frac{t_{\text{ac}}}{\tau} \frac{\text{Var}(E_L)}{\sigma^2}.$$

The wall time per iteration, T_{iter} , is proportional to n_w^{target} and only weakly dependent on τ in common implementations (nonlocal PP treatments can add a weak τ -dependence). Writing $T_{\text{iter}} = n_w^{\text{target}} T_w$, where T_w is the time to advance one walker by one iteration, the total cost (neglecting equilibration) scales as $1/\tau$ and $1/\sigma^2$.

Let T_{DMC} be the computational cost in *CPU hours* (core-hours) for a DMC simulation with timestep τ achieving error σ :

$$T_{\text{DMC}} = \frac{T_w}{3600} \frac{t_{\text{ac}}}{\tau} \frac{\text{Var}(E_L)}{\sigma^2}.$$

(The factor $1/3600$ converts seconds to hours if T_w is measured in seconds.) The variance $\text{Var}(E_L)$ is extensive (for a fixed wavefunction/PP setup), roughly proportional to the number of electrons N_e : $\text{Var}(E_L) \approx N_e V_{1e}$, with V_{1e} the average variance per electron. In many DMC implementations,

$$T_w = C (N_e^2 + \epsilon N_e^3),$$

where C and ϵ are system- and architecture-dependent (typically $\epsilon \lesssim 10^{-3}$). Thus,

$$T_{\text{DMC}}(\sigma, \tau) = \frac{C}{3600} (N_e^3 + \epsilon N_e^4) \frac{t_{\text{ac}}}{\tau} \frac{V_{1e}}{\sigma^2}. \quad (16)$$

For the X23 systems on the Peta4-Skylake cluster[101], analysis of our runs indicates broadly similar C , ϵ , t_{ac} , and V_{1e} across crystals. We adopt the averages: $\tilde{C} = 2.4 \times 10^{-6}$ s, $\tilde{\epsilon} = 4 \times 10^{-4}$, $\tilde{V}_{1e} = 0.026$ a.u., and $\tilde{t}_{\text{ac}} = 0.73$ a.u. (atomic units of time). Note that Eq. 16 shows the scaling of DMC with the number of simulated electrons. Since $\epsilon \sim 10^{-4}$, DMC scales with N_e^3 for typically simulated systems with fewer than $\sim 10^4$ electrons. The scaling is instead $o(N_e^4)$ for $N_e \gtrsim 10^4$.

The DMC cost for a lattice-energy evaluation is the sum of the costs for $E_{\text{crys,1mol}}$ and E_{gas} computed via Eq. (16). In the crystal, the periodic cell contains N_{mol} molecules, so $N_e = N_{\text{mol}} N_{e,1\text{mol}}$ and $E_{\text{crys,1mol}} = E_{\text{crys}}/N_{\text{mol}}$. To achieve $\sigma_{\text{crys,1mol}}$ *per molecule*, we target a stochastic error on the total cell energy of $\sigma_{\text{crys}} = N_{\text{mol}} \sigma_{\text{crys,1mol}}$. If our target σ and the timestep τ are the same on the gas-phase and on the periodic cell simulations, the crystal simulation is roughly N_{mol} times more expensive than the gas-phase one, as implied by Eq. (16). Therefore, considering the overall cost of both simulations, it can be shown that the most efficient setup for the simulations (i.e., the setup minimising the stochastic error on the lattice energy given the

overall computational cost) is to set $\sigma_{\text{crys,1mol}}^2 \sim \frac{\sqrt{N_{\text{mol}}}}{1+\sqrt{N_{\text{mol}}}} \sigma_{\text{latt}}^2$ and $\sigma_{\text{mol}}^2 \sim \frac{1}{1+\sqrt{N_{\text{mol}}}} \sigma_{\text{latt}}^2$, being σ_{latt} our target stochastic error on the lattice energy evaluation.

b. Choice of timestep. The timestep bias decreases with τ . From the analysis reported in the SI of Ref. 1 for X23 molecular crystals, typical bounds are: $\tau = 0.03$ a.u. \Rightarrow bias < 2 kJ/mol; $\tau = 0.01$ a.u. \Rightarrow bias < 1 kJ/mol; $\tau = 0.003$ a.u. \Rightarrow bias < 0.5 kJ/mol. These τ values were used for the DMC[4], DMC[2], DMC[1] entries in Table 31.

6. LATTICE AND RELATIVE ENERGY OF ICE13 DATASET

In this section, we report the final lattice energy estimates computed by the MBE for the ICE13 dataset and compare it to both experiment and DMC. We also compute the relative energies w.r.t. ice Ih for the other 12 phases. Throughout this section, we use experimental lattice energies from Whalley [96], which have been extrapolated to zero temperature and pressure, with zero-point energies removed.

A. Final lattice energies

In Table 33, we have collated the LNO-MBE-CCSD(T) estimates for the Small, Medium and Large unit cells. As mentioned in the main text, there are significant errors in the lattice energy predicted for ice VII for the Small unit cell due to the large dipole moment within the unit cell. Thus, when comparing to e.g., DMC calculations, we instead use values from the Medium cell for ice VII, while reporting the Small unit cell for all other phases. These estimates are given under ‘Final’.

The lattice energies predicted between the Small, Medium or Large unit cells are generally within 1 kJ/mol and oftentimes much better than that. Besides the noted difference for ice VII, the differences can arise due to differences in the ferroelectric character of the unit cells or because the small unit cell uses the Canonical approach described in Section 3A6, while the other unit cell sizes uses the LAF approach.

We have also included estimates for both MP2 and CCSD (just showing the Final set). It can be seen that going towards CCSD(T) is absolutely necessary, with MP2 and CCSD both performing worse compared to DMC. In fact, CCSD performs poorly, with an MAD of ~ 6.3 kJ/mol across the 13 ice polymorphs. MP2 performs better, with an MAD of ~ 1 kJ/mol.

As shown in Table 34, we find that the differences between CCSD(T) and DMC are sufficiently small that the MAD (across the 13 ice phases) on E_{latt} are similar to within 0.5 kJ/mol when used to benchmark several density functional approximations taken from Ref. 7. A more detailed comparison of DFAs is given in Section 10.

TABLE 33: Lattice energies of the ICE13 set from DMC [7], Experiment [96] and LNO-MBE-CCSD(T). We consider the Small, Medium and Large unit cell sizes for LNO-MBE-CCSD(T) and also a Final estimate that corrects for errors in ice VII when using a Small unit cell. We also give Final estimates at the MP2 and CCSD levels. All values are in kJ/mol.

Ice Phase	DMC (Unitcell)	Experiment	CCSD(T) [Small cell]	CCSD(T) [Medium cell]	CCSD(T) [Large cell]	CCSD(T) [Final]	CCSD [Final]	MP2 [Final]
Ih	-59.5 ± 0.1	-58.9 ± 1.0	-59.3	-58.4	-58.3	-59.3	-53.5	-59.2
II	-59.1 ± 0.1	-58.8 ± 1.0	-58.3	N/A	N/A	-58.3	-52.5	-57.7
III	-58.2 ± 0.1	-57.9 ± 1.0	-57.3	-57.0	-56.8	-57.3	-51.3	-57.1
IV	-55.6 ± 0.1	N/A	-56.0	-55.5	-54.8	-56.0	-50.0	-55.3
VI	-57.7 ± 0.1	-57.2 ± 1.0	-56.9	N/A	-56.2	-56.9	-50.8	-56.1
VII	-54.5 ± 0.1	-54.7 ± 1.0	-57.2	-54.6	-54.4	-54.6	-48.5	-53.1
VIII	-55.2 ± 0.1	-55.7 ± 1.7	-55.6	N/A	N/A	-55.6	-49.6	-54.3
IX	-58.9 ± 0.1	-58.5 ± 1.0	-57.7	N/A	N/A	-57.7	-52.0	-57.4
XI	-59.3 ± 0.1	N/A	-59.3	N/A	N/A	-59.3	-53.3	-59.4
XIII	-57.3 ± 0.1	N/A	-57.4	N/A	N/A	-57.4	-51.6	-56.9
XIV	-57.8 ± 0.1	N/A	-56.9	N/A	N/A	-56.9	-51.0	-56.2
XV	-57.7 ± 0.1	N/A	-56.9	N/A	N/A	-56.9	-50.9	-56.1
XVII	-57.7 ± 0.1	N/A	-57.7	-57.4	-57.1	-57.7	-52.0	-57.8
MAD (DMC)						0.5	6.3	0.9
MAD (Exp)	0.4					0.4	6.2	1.1

TABLE 34: Mean absolute deviations (MAD) with respect to LNO-MBE-CCSD(T) and DMC [7] for several DFT functionals on the lattice energies of the ICE13 set. All values are in kJ/mol.

	MAD [DMC]	MAD [CCSD(T)]
PBE-D3(BJ)	7.9	8.3
optB86b-vdW	9.3	9.7
SCAN+rVV10	9.6	9.9
revPBE0-D3	1.5	1.2
B3LYP-D4	2.3	2.6

B. Final relative energies

The relative energy between ice polymorphs lie within a small 5 kJ/mol range for both LNO-MBE-CCSD(T) and DMC as shown in Figure 35. This makes it a stringent test system, where minute differences can have ramifications in the resulting ice phase diagram [124–126]. Within this figure, we also highlight a range of DFT values, which can span more than 20 kJ/mol on the relative energy depending on the chosen functional, taken from Ref. 7.

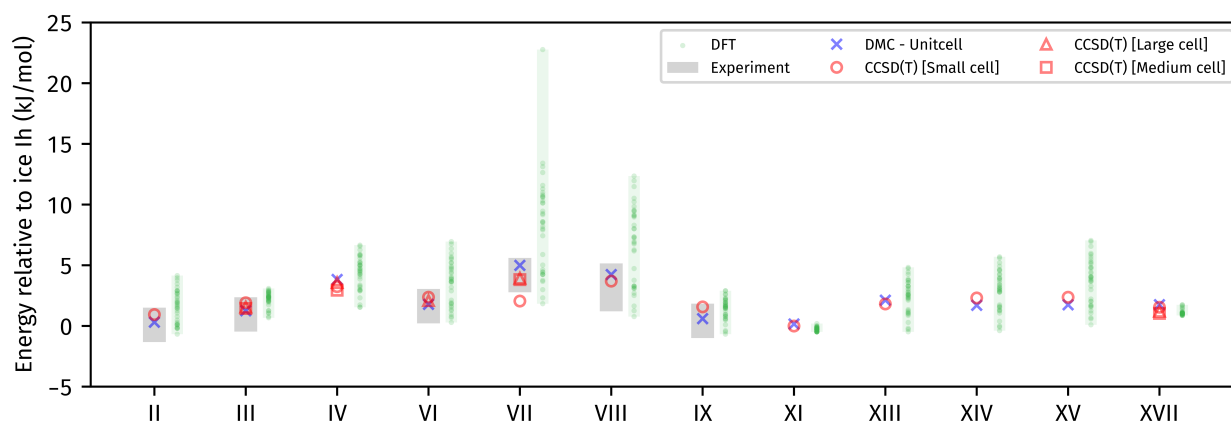


FIG. 35: Comparison of the energy relative to ice Ih for the 13 phases of ice. Besides estimates from LNO-MBE-CCSD(T), we include DMC and DFT estimates from Ref. 7 and experimental values from Ref. 96.

We compare the mean absolute deviation for the 12 phases of ice (excluding Ih) against DMC and experiment in Table 35. To be consistent with DMC, we use results for the small unit cell, except for ice VII, where we used the medium cell, and dub this combined set of numbers ‘Final’.

The resulting MAD against DMC is better than 1 kJ/mol, at 0.6 kJ/mol. The MAD against experiment for DMC and LNO-MBE-CCSD(T) are 0.5 kJ/mol and 0.8 kJ/mol respectively, both within the expected error range for experiment. Here, it is interesting to note that despite its poor performance on the lattice energy, CCSD performs exceptionally well for relative energies, with similar MADs (w.r.t. DMC and experiment) as CCSD(T). For this quantity, MP2 performs worse, with an MAD of 0.8 kJ/mol and 1.5 kJ/mol relative to DMC and experiment, respectively.

TABLE 35: Relative lattice energies of the ICE13 set with respect to ice Ih from DMC [7], Experiment [96] and LNO-MBE-CCSD(T). We consider the Small, Medium and Large unit cell sizes for LNO-MBE-CCSD(T) and also a Final estimate that corrects for errors in ice VII when using a Small unit cell. We also give Final estimates at the MP2 and CCSD levels. All values are in kJ/mol. All values are in kJ/mol.

Ice Phase	DMC (Unitcell)	Experiment	CCSD(T) [Small cell]	CCSD(T) [Medium cell]	CCSD(T) [Large cell]	CCSD(T) [Final]	CCSD [Final]	MP2 [Final]
II	0.3 ± 0.1	0.1 ± 1.4	0.9	N/A	N/A	0.9	1.0	1.5
III	1.2 ± 0.1	0.9 ± 1.4	1.9	1.4	1.6	1.9	2.1	2.1
IV	3.8 ± 0.1	N/A	3.2	2.9	3.6	3.2	3.5	3.9
VI	1.8 ± 0.1	1.6 ± 1.4	2.4	N/A	2.1	2.4	2.7	3.1
VII	5.0 ± 0.1	4.2 ± 1.4	2.0	3.8	3.9	3.8	4.9	6.1
VIII	4.2 ± 0.1	3.2 ± 2.0	3.7	N/A	N/A	3.7	3.9	4.9
IX	0.6 ± 0.1	0.4 ± 1.4	1.6	N/A	N/A	1.6	1.5	1.8
XI	0.2 ± 0.1	N/A	-0.0	N/A	N/A	-0.0	0.2	-0.2
XIII	2.1 ± 0.1	N/A	1.8	N/A	N/A	1.8	1.9	2.3
XIV	1.7 ± 0.1	N/A	2.3	N/A	N/A	2.3	2.5	2.9
XV	1.7 ± 0.1	N/A	2.4	N/A	N/A	2.4	2.5	3.1
XVII	1.8 ± 0.1	N/A	1.5	1.0	1.2	1.5	1.5	1.4
MAD (DMC)						0.6	0.5	0.8
MAD (Exp)	0.5					0.8	0.9	1.5

We compare the MADs predicted for a subset of DFAs from Ref. [7] against both DMC and LNO-MBE-CCSD(T) for predicting relative energies for the ICE13 dataset in Table 51. This highlights that the precision in both DMC and CCSD(T) are sufficiently accurate that they will discern good-performing DFAs. In fact, the differences between DMC and LNO-MBE-CCSD(T) are now smaller, with MADs differing on average ~ 0.1 kJ/mol to either DMC or LNO-MBE-CCSD(T) across the DFAs. A more detailed comparison of DFAs is given in Section 10.

TABLE 36: Mean absolute deviations (MAD) with respect to LNO-MBE-CCSD(T) and DMC [7] for several DFT functionals on the relative lattice energies of the ICE13 set (using ice Ih as the reference). All values are in kJ/mol. All values are in kJ/mol.

	MAD [DMC]	MAD [CCSD(T)]
PBE-D3(BJ)	3.5	3.3
optB86b-vdW	0.5	0.7
SCAN+rVV10	0.7	0.7
revPBE0-D3	1.0	1.0
B3LYP-D4	1.9	1.7

7. TOWARDS OPTIMIZED DENSITY FUNCTIONAL APPROXIMATIONS FOR MOLECULAR CRYSTALS

The large set of LNO-MBE-CCSD(T) lattice energy estimates we have generated make for useful benchmarks. This can be used to assess the performance of density functional approximations (DFAs), as we will do in Section 10. In addition, these benchmarks can be used to parametrize new density functional approximations, as has been common using small dimer binding energies [127, 128] but has been absent for molecular crystals to date. In particular, our LNO-MBE-CCSD(T) estimates provide low-errors compared to the large (error) range of possible experimental data for several systems within the X23 dataset.

In this section, we have focused efforts on optimizing the parametrization of the XDM parameters for B86bPBE50 [29] to our LNO-MBE-CCSD(T) X23 data, which we will dub B86bPBE50-revXDM. This base DFA was selected because its large amount of exact exchange makes it more resilient towards delocalization errors [129] which may be prominent when tackling the flexible pharmaceutical-size molecular crystals that we will study later. Furthermore, we have optimized the XDM parameters specifically for the compact `lightdense` basis sets in FHI-AIMS. These basis sets are particularly ideal as they are less susceptible to basis set superposition error at small sizes [130]. Inspired by the “-3c” approaches [131] and others [132], we hope to capture the basis set incompleteness errors within the XDM term. Overall, the development of such a cheap approach would make it useful for crystal structure prediction, where it might be used to screen thousands of polymorphs (at as low a cost as possible). Additionally, this also makes it useful in the context of training machine-learned interatomic potentials (MLIP) to obtain thermal contributions – particular for large pharmaceutical molecular crystals – as we will do later.

The XDM dispersion is computed as a damped asymptotic pairwise term,

$$E_{\text{XDM}} = - \sum_{n=6,8,10} \sum_{i>j} \frac{C_{n,ij}}{R_{ij}^n + R_{\text{vdW},ij}^n}, \quad (17)$$

which is added to the base density functional energy (in our case B86bPBE50 with ‘lightdense’ basis sets),

$$E = E_{\text{base}} + E_{\text{XDM}}. \quad (18)$$

Here, i and j run over atoms, R_{ij} are interatomic distances, $C_{n,ij}$ are dispersion coefficients, and the damping lengths are

$$R_{\text{vdW},ij} = a_1 R_{c,ij} + a_2. \quad (19)$$

These a_1 and a_2 coefficients are what needs to be parameterized or optimized.

In Figure 36, we plot the B86bPBE50-XDM mean absolute deviation (MAD) against our LNO-MBE-CCSD(T) benchmarks for the X23 dataset for a range of a_1 and a_2 parameters. We used meV units ($1 \text{ kJ/mol} = 10.4 \text{ meV}$) to make differences easier to discern. We start with a wide search of the a_1 and a_2 parameters at the top panel, covering a range between $0.70 - 1.00 \text{ \AA}$ and $0.80 - 1.60 \text{ \AA}$, in intervals of 0.02 and 0.05 \AA , respectively. We then perform a focused search between $0.66 - 0.80 \text{ \AA}$ and $1.40 - 1.80 \text{ \AA}$ in the middle panel, as that region was found to have the lowest MAD. Subsequently, we perform a final detailed search in the bottom panel (involving intervals of 0.01 and 0.02 \AA for a_1 and a_2 , respectively) to identify $a_1 = 0.74$ and $a_2 = 1.72$ as the most optimal parameters, with an MAD of 18.9 meV and root mean square deviation of 24.7 meV . As shown in Table 37, this improves over the default parameters for the `lightdense` basis set with B86bPBE50 significantly, which has an MAD of 45.3 meV , higher than chemical accuracy. We note here that this MAD differs from that in Table 49 because that utilized a two step process to correct for errors in the basis set (using the cheaper B86bPBE-XDM) functional, as described in Section 1 B 2.

A recurring challenge, as we have highlighted in the main text and also illustrated in Ref. 29 is that methods which describe molecular crystals in the X23 dataset do not necessarily describe the ice polymorphs in the ICE13 dataset well. In Table 38, we have also calculated the MAD for the lattice energies of the ICE13 dataset and it can be seen that the agreement remains excellent, improving over the default XDM parameters, with MAD better than the best DFA observed in Ref. 7.

Finally, we briefly discuss the low cost of B86bPBE50-revXDM, shown for the X23 data in Table 39. The cost is on average 10 CPU core-hours (CPUh) for the X23 dataset, in a tight range between 5–17 CPUh. This cost is comparable to a GGA with plane-waves, as shown in Section 5 while being much cheaper than the corresponding hybrid calculations.

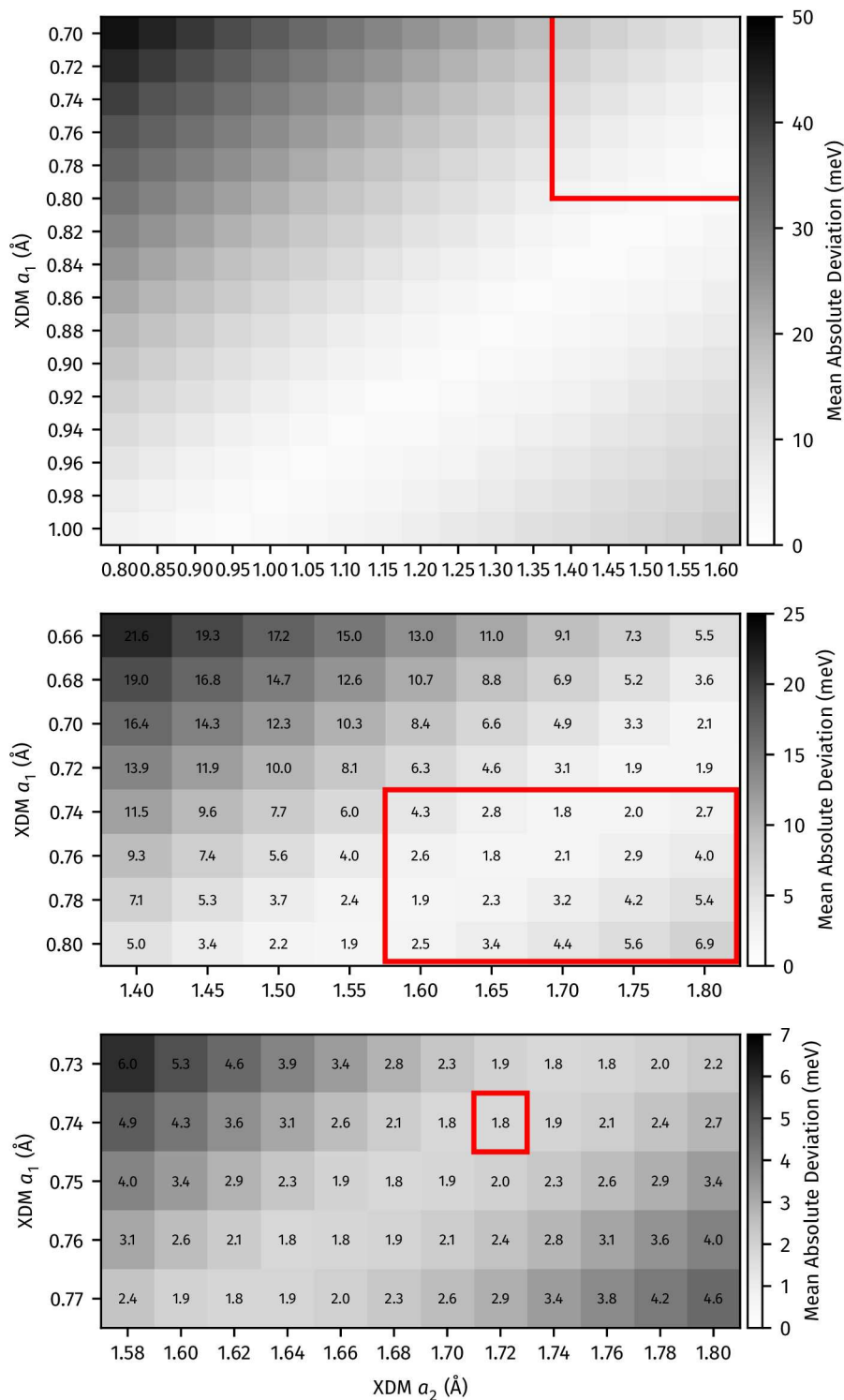


FIG. 36: Optimizing the XDM a_1 and a_2 coefficients against the X23 dataset. This was performed in a three step process starting from a large (top panel), medium (middle panel) and small (bottom panel) of values to come to the final coefficients to within one decimal place. We used meV units (1 kJ/mol= 10.4 meV) to make differences easier to discern.

TABLE 37: Comparison of X23 lattice energies (kJ/mol) calculated with B86bPBE50-XDM using the 'lightdense' basis sets and associated XDM parameters against B86bPBE50-revXDM parameters ($a_1 = 0.74 \text{ \AA}$ and $a_2 = 1.72 \text{ \AA}$) with 'lightdense' basis sets in FHI-aims. The reference (LNO-MBE-CCSD(T)) lattice energies are also shown.

	CCSD(T)	B86bPBE50-XDM (lightdense)	B86bPBE50-revXDM
1,4-cyclohexanedione	-92.2	-85.6	-91.2
Acetic Acid	-70.3	-69.5	-73.6
Adamantane	-67.5	-59.2	-63.5
Ammonia	-38.6	-34.4	-36.5
Anthracene	-113.9	-106.0	-112.8
Benzene	-52.8	-50.2	-53.4
CO ₂	-27.9	-24.6	-27.7
Cyanamide	-82.4	-79.7	-82.8
Cytosine	-161.9	-154.0	-160.4
Ethyl carbamate	-85.0	-79.6	-84.2
Formamide	-80.8	-76.2	-79.8
Hexamine	-88.1	-86.7	-91.2
Imidazole	-88.8	-86.1	-89.6
Naphthalene	-83.8	-78.0	-82.8
Oxalic Acid α	-99.3	-97.3	-104.0
Oxalic Acid β	-98.8	-94.8	-101.4
Pyrazine	-63.5	-59.8	-63.8
Pyrazole	-78.5	-76.0	-79.6
Succinic Acid	-125.0	-123.8	-131.4
Triazine	-61.5	-56.3	-60.1
Trioxane	-64.1	-58.0	-63.4
Uracil	-137.2	-132.4	-138.7
Urea	-107.0	-100.4	-104.5
MAD (kJ/mol)		4.4	1.8

TABLE 38: Comparison of ICE13 lattice energies (in kJ/mol) calculated with B86bPBE50-XDM using the ‘lightdense’ basis sets and associated XDM parameters against B86bPBE50-revXDM parameters ($a_1 = 0.74 \text{ \AA}$ and $a_2 = 1.72 \text{ \AA}$) obtained in this work, against the DMC-ICE13 reference values.

	DMC	B86bPBE50-XDM (lightdense)	B86bPBE50-revXDM
Ih	-59.5	-59.7	-60.9
II	-59.1	-57.5	-59.1
III	-58.2	-56.9	-58.3
IV	-55.6	-54.4	-56.1
VI	-57.7	-55.0	-56.8
VII	-54.5	-50.9	-53.0
VIII	-55.2	-52.0	-54.1
IX	-58.9	-57.6	-59.1
XI	-59.3	-59.6	-60.8
XIII	-57.3	-56.5	-58.2
XIV	-57.7	-55.9	-57.6
XV	-57.7	-55.1	-56.9
XVII	-57.7	-58.4	-59.5
MAD (kJ/mol)		1.6	0.8

TABLE 39: Computational cost in CPU core-hours (CPUh) required for B86bPBE50-revXDM calculations with 'lightdense' basis sets in FHI-aims for the X23 set on 128 cores for the molecular calculations and 512 cores for the molecular crystal calculations. These were performed on AMD EPYC 7742 2.25 GHz processors.

System	B86bPBE50-revXDM CPUh
1,4-cyclohexanedione	9
Acetic Acid	8
Adamantane	11
Ammonia	5
Anthracene	12
Benzene	9
CO ₂	6
Cyanamide	10
Cytosine	14
Ethyl carbamate	7
Formamide	8
Hexamine	11
Imidazole	9
Naphthalene	11
Oxalic Acid α	11
Oxalic Acid β	7
Pyrazine	7
Pyrazole	15
Succinic Acid	8
Triazine	13
Trioxane	17
Uracil	14
Urea	7
Mean	10

8. RELATIVE ENERGY CALCULATIONS ON PHARMACEUTICAL MOLECULAR CRYSTALS

In this section, we tabulate the relative energy between pairs of challenging polymorphs for four different molecular crystals, with the largest (Axitinib and Rotigotine) being comparable in size to those found in pharmaceutical drugs. The molecular crystals and their polymorphs are as follows:

1. **ROY** — There are 14 known forms of ROY [133], nearly half of which were only proposed since 2019. Importantly, it has been a significant challenge for DFT [134] to get the difference between forms R and Y correctly, where the latter is the experimentally predicted form at ambient conditions [135, 136].
2. **Rotigotine** — Used as a dopamine agonist to treat Parkinson's (and restless leg) disease [137] under the brand name Neupro. Rotigotine was thought to exist as only one polymorph form (I) since its release in 1985. However, in 2008, the appearance of a more stable (and less soluble) polymorph (II) led to a massive batch recall [138], with implications towards public health and the economy.
3. **Axitinib** — Sold under the brand name Inlyta and used to treat kidney cancer [139] with potential applications for treating breast cancer as well [140]. Axitinib represents another large pharmaceutical-sized molecular crystal where the energy difference between its various polymorphs has served as a major challenge for DFAs [141].
4. **Molecule X from the third Blind Test** — This small molecular crystal featured in an early Blind Test [11]. For this system, the energy differences between the experimentally observed and vanEijck-3 forms [12] are small and prone to change with the chosen DFA. This system was mostly included as its small size (and small energy difference) makes it ideal for benchmarking out electronic structure parameters in Section 3 B 2

A. Convergence of 2B and 3B terms as a function of cutoff

In Figs. 37 to 40, we demonstrate the convergence of the 2B and 3B terms for molecular crystal polymorphs (cutoffs specified in Section 1D). We also plot the convergence of the difference between the polymorph pairs. In general, we find that the relative energy converges faster with distance cutoff for both the 2B and 3B terms. For example, for ROY, a 2B (center-of-mass) cutoff of up to 16 Å is required to converge the 2B cutoff of polymorph to within 1 kJ/mol, while the relative energy between R and Y converges by a 12 Å cutoff. Similarly, the 3B cutoff also converges faster, requiring around 600 Å³ to converge for polymorph Y, while it is converged by 450 Å³ for the relative energy. This faster convergence is observed for the other molecular crystals as well.

For all molecular crystal polymorphs, we find that performing a subtractive embedding to the CCSD(T) correlation energy with D4 improves the convergence of the 2B terms with cutoff, mirroring the observations found in Section 2B for the X23 dataset. Importantly, this also further decreases the required distance cutoff to converge the relative energy. For example, for Rotigotine, the relative energy between forms I and II is converged to within 1 kJ/mol by 12 Å while 14 Å is required without the D4 subtractive embedding.

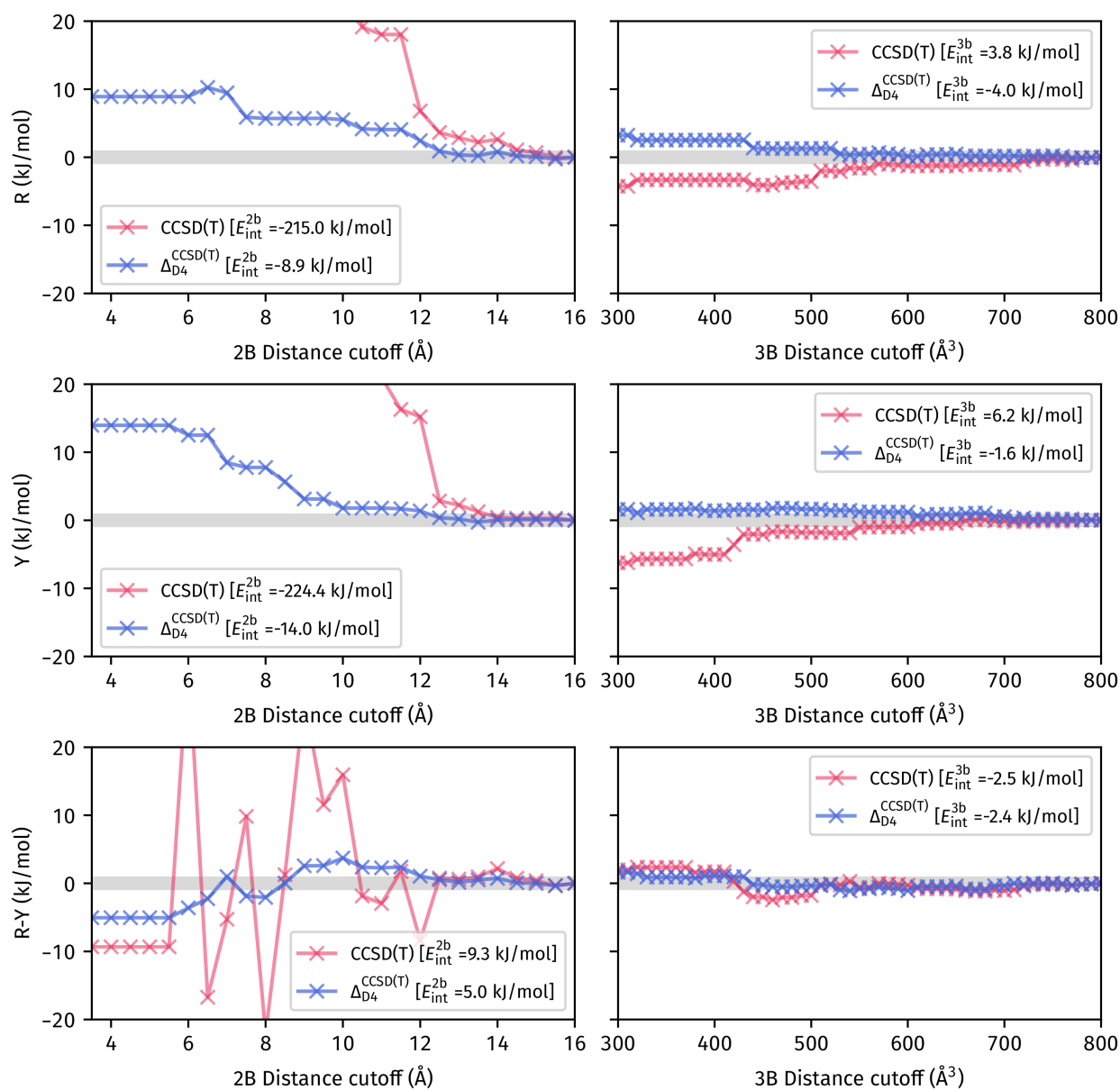


FIG. 37: Convergence of the 2B and 3B MBE components of ROY R and Y as well as the difference between forms R and Y.

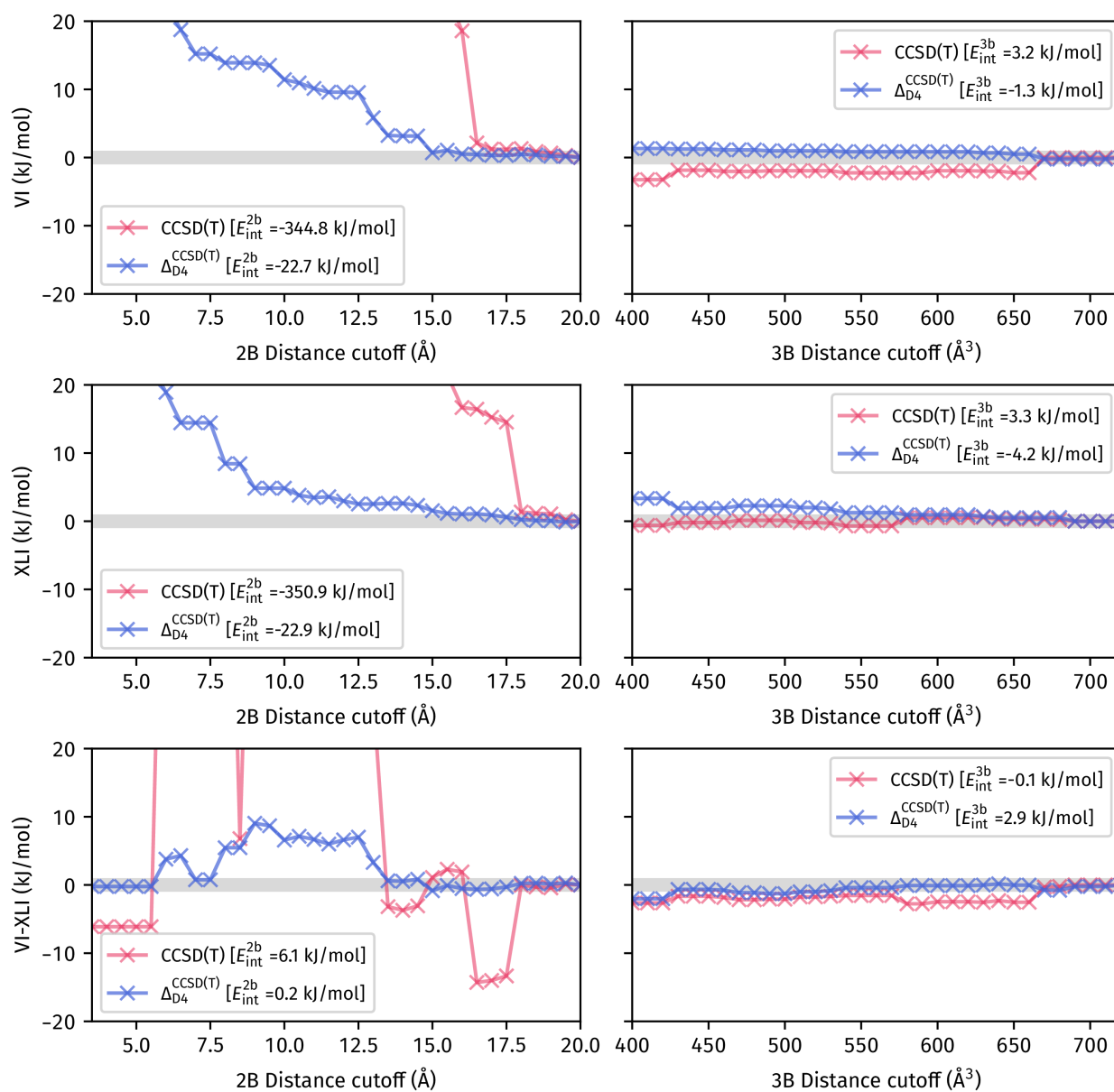


FIG. 38: Convergence of the 2B and 3B MBE components of Axitinib VI and XLI as well as the difference between forms VI and XLI.

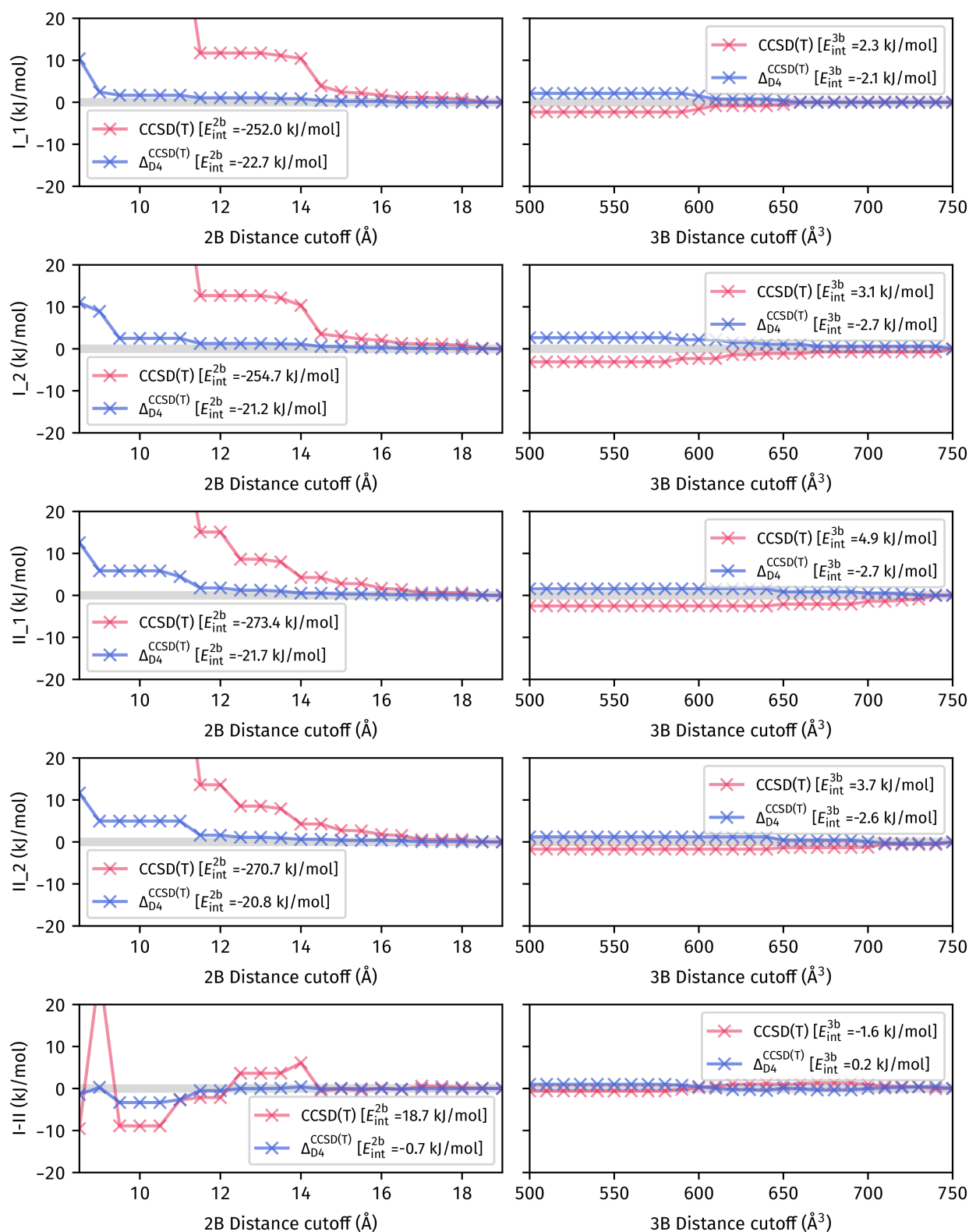


FIG. 39: Convergence of the 2B and 3B MBE components of Rotigotine I_1 , I_2 , II_1 , II_2 as well as the difference between forms I and II.

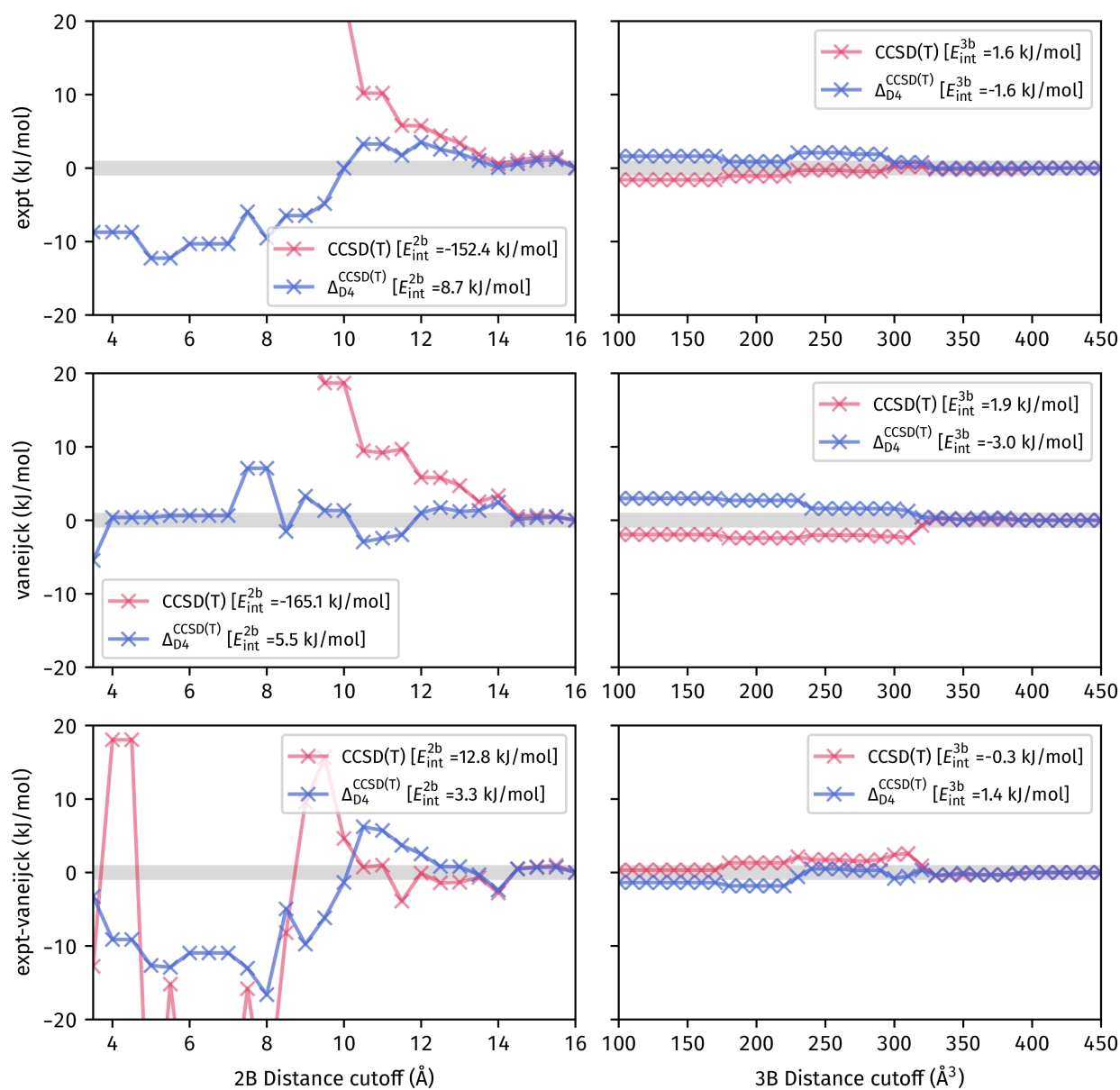


FIG. 40: Convergence of the 2B and 3B MBE components for the experiment and vanEijck-3 forms of molecule X from the third Blind test, as well as the difference between these two forms.

B. MBE contributions to the relative energies

We summarize the final 1B, 2B, 3B contributions to the LNO-MBE-CCSD(T) (correlation energy) MBE as well as the periodic HF estimates in Tables 40 to 43. We include results both with and without incorporating subtractive embedding using D4.

TABLE 40: Contributions to the CCSD(T) relative energies between the R and Y polymorphs of ROY from the many-body expansion (MBE) up to 3-body terms. Both the results without and with (corrections from HF with) D4 dispersion corrections are given. 1B terms are computed relative to the monomer taken from polymorph Y. All values are in kJ/mol.

D4 Correction	without D4						with D4					
	HF	CCSD(T) corr				Final	HF	CCSD(T) corr - D4				Final
MBE Level	Periodic	1B	2B	3B	Sum	Total	Periodic	1B	2B	3B	Sum	Total
R	-31437.1	-4.6	-215.0	3.8	-215.8	-31653.0	-31978.3	-4.2	-8.9	-4.0	-17.1	-31995.4
Y	-31435.7	-0.0	-224.3	6.2	-218.1	-31653.9	-31980.6	-0.0	-14.0	-1.6	-15.6	-31996.1

TABLE 41: Contributions to the CCSD(T) relative energies between the I and II polymorphs of Rotigotine from the many-body expansion (MBE) up to 3-body terms. Both the results without and with (corrections from HF with) D4 dispersion corrections are given. 1B terms are computed relative to the monomer taken from polymorph II₁. All values are in kJ/mol.

D4 Correction	without D4						with D4					
	HF	CCSD(T) corr				Final	HF	CCSD(T) corr - D4				Final
MBE Level	Periodic	1B	2B	3B	Sum	Total	Periodic	1B	2B	3B	Sum	Total
I ₁	-46115.9	-1.4	-252.0	2.3	-251.1	-46367.0	-46865.8	-0.6	-22.7	-2.1	-25.5	-46891.3
I ₂	-46114.5	0.1	-254.7	3.1	-251.5	-46366.0	-46866.9	-0.7	-21.2	-2.6	-24.6	-46891.4
II ₁	-46105.4	-0.0	-273.4	4.9	-268.6	-46373.9	-46874.7	0.0	-21.7	-2.7	-24.4	-46899.1
II ₂	-46104.8	-1.3	-270.7	3.8	-268.2	-46373.0	-46874.3	0.5	-20.9	-2.6	-22.9	-46897.2

TABLE 42: Contributions to the CCSD(T) relative energies between the VI and XLI polymorphs of Axitinib from the many-body expansion (MBE) up to 3-body terms. Both the results without and with (corrections from HF with) D4 dispersion corrections are given. 1B terms are computed relative to the monomer taken from polymorph XLI. All values are in kJ/mol.

D4 Correction	without D4						with D4					
	HF	CCSD(T) corr				Final	HF	CCSD(T) corr - D4				Final
MBE Level	Periodic	1B	2B	3B	Sum	Total	Periodic	1B	2B	3B	Sum	Total
VI	-51601.7	1.9	-344.9	3.2	-339.7	-51941.4	-52506.3	-6.3	-22.7	-1.3	-30.3	-52536.6
XLI	-51600.3	0.0	-350.9	3.3	-347.6	-51948.0	-52517.0	0.0	-22.9	-4.2	-27.1	-52544.1

TABLE 43: Contributions to the CCSD(T) relative energies between the experimental and vanEijck-3 polymorphs of X from the many-body expansion (MBE) up to 3-body terms. Both the results without and with (corrections from HF with) D4 dispersion corrections are given. 1B terms are computed relative to the monomer taken from the vanEijck-3 polymorph. All values are in kJ/mol.

D4 Correction	without D4						with D4					
	HF	CCSD(T) corr				Final	HF	CCSD(T) corr - D4				Final
MBE Level	Periodic	1B	2B	3B	Sum	Total	Periodic	1B	2B	3B	Sum	Total
expt	-30679.5	-0.0	-152.4	1.6	-150.8	-30830.3	-31124.8	-0.0	8.7	-1.6	7.1	-31117.8
vaneijck	-30669.8	0.6	-165.1	1.9	-162.6	-30832.4	-31123.0	0.4	5.5	-3.0	2.9	-31120.1

C. Final relative energies

We report the final relative energies between the polymorph pairs in Table 44 for all four molecular crystals. These are compared to experimental values, where we have performed the conversion from relative sublimation enthalpies to relative energies using molecular dynamics simulations with machine-learning interatomic potentials in Section 9. For LNO-MBE-CCSD(T), the agreement with experiments is excellent, being within 0.5 kJ/mol for all systems (barring X, where there isn't any experimental values). We are able to obtain two values of the relative energy, given both with and without subtracting D4 embedding. These values are close to one another, being within 1 kJ/mol (and often much less) for all of the systems, giving confidence in the estimates provided.

We also report relative energies predicted by CCSD and MP2. It can be seen that both MP2 and CCSD are unable to consistently agree with experiments. For example, there is a ~ 5 kJ/mol error on MP2 for the VI-XLI relative energy of Axitinib and ~ 3 kJ/mol error on CCSD for Rotigotine (I-II).

We also briefly discuss our results for molecule X. Our results are the highest level of accuracy [CCSD(T)] for this system so far. It is in agreement with previous studies that the vanEijck-3 and experimental forms are very competitive in stability, with CCSD predicting them to nearly degenerate. However, both CCSD(T) and MP2 suggests that the vanEijck-3 form is more stable by 2 kJ/mol. This, combined with the fact that free energy contributions [12] further favors the vanEijck-3 form suggest that it may indeed be more stable than the experimental crystal form.

TABLE 44: Final relative energies between the most stable polymorphs of each pharmaceutical molecule studied here with different levels of theory, both without and with (corrections from HF with) D4 dispersion corrections. All values are in kJ/mol.

	Experiment (kJ/mol)	without D4			with D4		
		MP2	CCSD	CCSD(T)	MP2	CCSD	CCSD(T)
ROY R - Y	1.2 \pm 0.5 [142]	1.6	2.0	0.9	1.5	1.8	0.8
Axitinib VI - XLI	7.5 \pm 0.8 [143]	11.4	5.8	6.6	12.4	6.8	7.5
Rotigotine I - II	7.0 \pm 0.5 [10]	7.8	4.4	7.0	7.6	4.1	6.8
X vanEijck-3 - Expt	N/A	-2.5	-0.0	-2.1	-2.8	-0.3	-2.4

D. Density functional approximation comparison

In Table 45, we have compared the relative energies predicted by the polymorph pairs between the 4 molecular crystals, reporting their difference w.r.t. the LNO-MBE-CCSD(T) values in Table 44 (the average of when ‘Without D4’ and ‘With D4’ subtractive embedding).

Overall, we find that there is significant discrepancy between CCSD(T) and the DFAs. For example, for ROY, only one DFA [B86bPBE50-revXDM] can correctly predict the stability of form Y over R. Similarly, this is also a challenging property to predict for Axitinib, with some DFAs predicting errors in excess of 8 kJ/mol; these are DFAs such as B86bPBE-XDM as well as r²SCAN-D4, which perform well on absolute lattice energies for the X23 dataset. Rotigotine represents a relatively simple system to get right, with many DFAs lying within 1 kJ/mol.

TABLE 45: Relative lattice energies (in kJ/mol) for polymorph pairs of the four molecular crystals with various density functional approximation, together with their error with respect to the CCSD(T) estimates.

	ROY		Axitinib		Rotigotine		X	
	E_{rel}	Error	E_{rel}	Error	E_{rel}	Error	E_{rel}	Error
PBE-D3(BJ)	-6.2	-7.0	-2.4	-9.5	5.1	-1.8	0.8	3.1
PBE-TS	0.0	-0.8	0.0	-7.0	0.0	-6.9	0.0	2.2
revPBE-D30	-5.7	-6.5	7.8	0.8	7.6	0.8	1.1	3.3
B86bPBE-XDM	-5.9	-6.7	-2.0	-9.0	7.4	0.5	1.6	3.8
r ² SCAN-D4	-6.3	-7.1	-1.6	-8.6	7.3	0.4	0.2	2.5
optB86b-vdW	-5.8	-6.6	0.6	-6.5	11.9	5.0	2.4	4.6
vdW-DF2	-6.3	-7.1	0.6	-6.4	10.0	3.1	0.5	2.7
B86bPBE25-XDM	-2.5	-3.3	1.3	-5.7	7.9	1.0	1.4	3.6
B86bPBE50-XDM	-0.1	-0.9	3.4	-3.7	8.1	1.2	0.6	2.8
B86bPBE50-revXDM	1.4	0.6	3.3	-3.8	7.5	0.6	0.3	2.5
PBE0-MBD	-2.7	-3.6	1.4	-5.7	7.3	0.4	0.7	2.9

E. Estimation of geometrical errors

As discussed in Section 1 A, we utilized DFT-optimized geometries for the pharmaceutical polymorphs [ROY (R and Y), Axitinib (VI and XLI), Rotigotine (I and II) and Molecule X (van-Eijck and experimental)] for our LNO-MBE-CCSD(T) calculations. Obtaining CCSD(T)-optimized geometries would be highly challenging as energy gradients are generally unavailable in most codes. As such, we are limited towards using geometries generated by a lower level of theory such as DFT. There is thus an error in the resulting E_{rel} arising from the use of a DFT geometry.

Here, we aim to find the typical errors expected from utilizing an inconsistent level of theory by considering 6 DFT functionals (selected from DFAs discussed in the next section): B86bPBE-XDM, B86bPBE25-XDM, B86bPBE50-XDM, PBE-D3(BJ), PBE-MBD and PBE0-MBD. We relaxed each of the polymorph geometries with these 6 different DFAs, to obtain a “true” E_{rel} with the consistent DFA for the geometry. We then obtained 5 other “approximate” E_{rel} for each geometry on the other DFAs. The difference between the approximate and true E_{rel} is plotted in Figure 41, with the mean absolute deviation from the true E_{rel} given. The MAD given along the column to the right is a measure of how sensitive a DFA is to the geometry, while the MAD given along the row at the bottom is a measure of the error expected when applying an inconsistent level of theory to a DFA's geometry.

We find that the geometrical errors are small, on the order of 0.5 kJ/mol or less. This is most significant for ROY, while the other systems have MADs mostly in the 0.1 to 0.2 kJ/mol range. B86bPBE50-XDM appears to be the most sensitive DFA to the geometry, probably arising from its higher exact exchange fraction, as evidenced by the fact that it is strongly affected in ROY — a system where delocalization error is prominent.

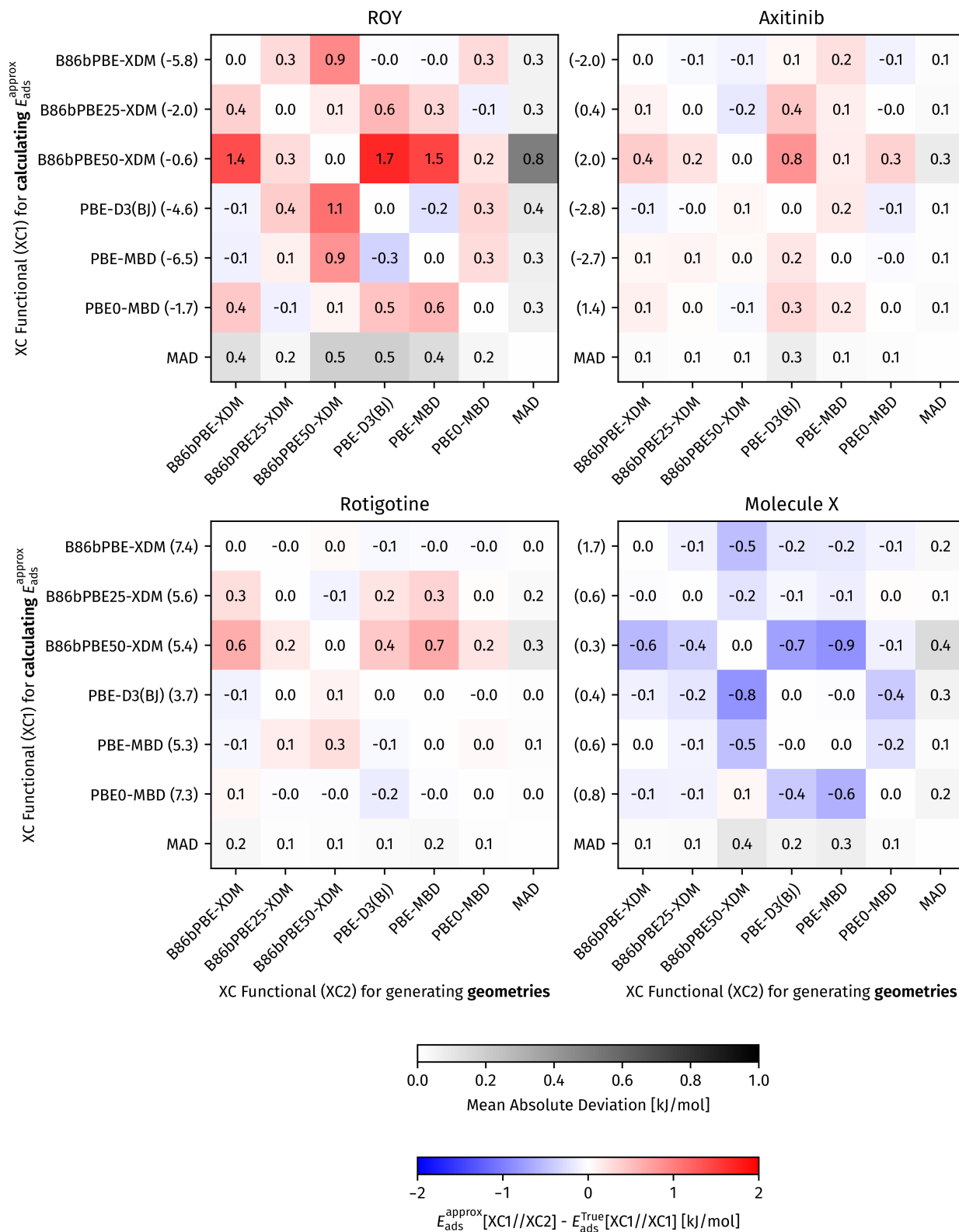


FIG. 41: Estimating the errors in E_{rel} for using inconsistent geometries for the polymorph pairs of ROY (R-Y), Axitinib (VI-XLI), Rotigotine (I-II) and Molecule X (van-Eijck-experimental). We considered 6 DFAs. For the geometry generated by each DFA (on the x-axis), an approximate E_{rel} is computed for the other DFAs and compared to the true estimate with the appropriate geometry. The difference in E_{rel} is plotted, with a corresponding mean absolute deviation given in the bottom row.

9. THERMAL CONTRIBUTIONS FROM MACHINE-LEARNING INTERATOMIC POTENTIALS

Experimental techniques typically measure the sublimation enthalpy, where the thermal and vibrational contributions must be removed if we want to make a direct ‘apples-to-apples’ comparison to the lattice energies (or relative energies) computed directly from our simulation methods. However, computing these contributions rigorously may not be trivial. Even for several systems [101] within the X23 dataset (notably succinic acid), the standard quasi-harmonic approximation (QHA) may lead to significant errors (~ 10 kJ/mol). Incorporating anharmonicity requires performing classical molecular dynamics (MD) or path-integral MD (PIMD) to further incorporate quantum nuclear effects. However, these methods are computationally prohibitive, requiring hundreds of thousands of force evaluations.

We leverage recent developments in machine learning interatomic potentials (MLIPs) by Della Pia *et al.* [101] to overcome the cost to perform (PI)MD. We have modified this framework to enable tackling multiple polymorphs simultaneously. Furthermore, its accuracy is improved further through the use of B86bPBE50-revXDM discussed in Section 7. We will use this approach to calculate the thermal contributions to the relative energy for the ROY (R and Y) and Axitinib (XLI and VI) polymorphs. For Rotigotine Forms I and II, we have taken the thermal contributions calculated by Mortazavi *et al.* [10].

A. The framework

Here, we describe our extensions to the previous framework of Della Pia *et al.* [101] to compute relative energies between molecular crystal polymorphs – commonly the energy of interest for crystal structure prediction. This previous work focused on relatively rigid molecules, which does not represent the interplay of intra- and intermolecular interactions commonly found in many organic crystal polymorphs. Our extensions to the framework enable us to study the relative enthalpies between polymorph pairs of Axitinib and ROY, both systems which exemplify not only a strong interplay of intra- and intermolecular interactions but are also challenges to density functional approximations. We observe that no significant increases in data are needed to tackle these more flexible systems.

The framework we use is illustrated in Figure 42. The framework goes over several generations, with the aim to converge the target property of interest. In our work, it will be the relative

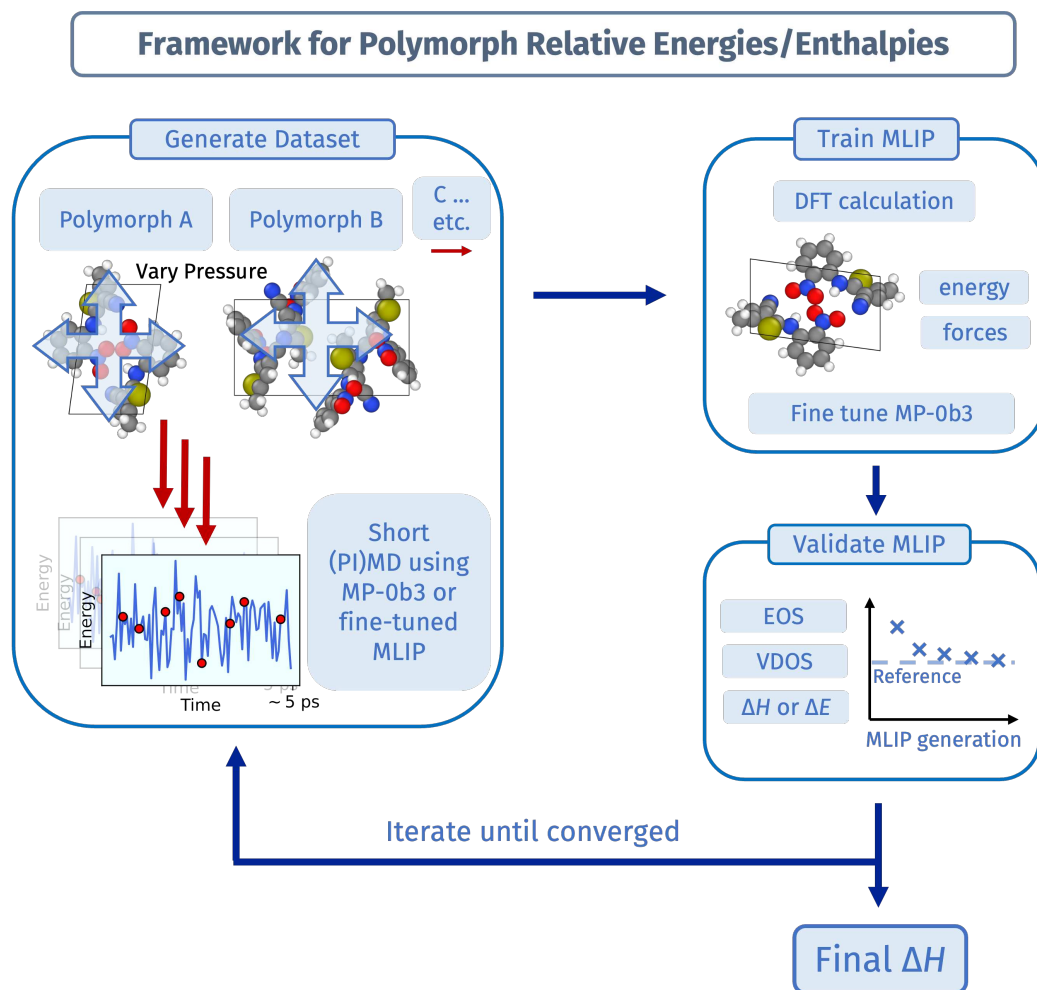


FIG. 42: Illustrating the framework used to train DFT-level MLIPs for flexible polymorphs.

enthalpy from molecular dynamics simulations. We start by generating structures across a range of 5 densities, from relaxations at pressures of -4, -2, -1, 0, 1, 2 and 4 kbar. For each of these pressures, we will perform short NVT (path-integral) molecular dynamics simulations. We will start with the MACE-MP-0b3 MLIP [144] – a foundational model trained to PBE [5] data – which we finetune at each subsequent generation with additionally generated data (including the data from previous generations).

While we have focused on a pair of polymorphs within this work, it is straightforward to tackle a larger number of polymorphs by incorporating data from those additional polymorphs. In the future, we will look into generalizing this approach to be able to study unseen polymorphs of molecular crystals.

B. Computational and dataset details

We refer to the reader to the Methods section in Ref. 101 for all the computational details on the MACE [144] MLIP architecture (and corresponding hyperparameters) and how we calculate the sublimation enthalpy from (path-integral) molecular dynamics as well as the quasi-harmonic approximation (QHA). The final dataset we used consisted of 5 generations, whereby the first generation was generated by MD simulations using MACE-MP-0b3 foundation model with the other generations using the subsequently trained models. This resulted in 888 structures for both Axitinib and ROY, amounting to 37,320 and 21,725 CPUh in total, respectively, on Intel Xeon Gold 6248 2.5GHz processors. We used the primitive unit cells of each polymorph, corresponding to 4 (184 atoms) and 2 (92 atoms) molecules for forms XLI and VI of Axitinib, respectively, and also 4 (108 atoms) and 2 (54 atoms) molecules for forms Y and R of ROY.

C. Convergence of the relative sublimation enthalpies

We use several metrics to assess the convergence of our MLIPs, including the vibrational density of states (VDOS), equation of state (EOS) as well as directly computing the relative enthalpy ΔH .

We have computed the VDOS for the 5 generations of MLIPs for the polymorphs of ROY and Axitinib in Figs. 43 and 44, respectively. By visual inspection, it can be seen (particularly at the higher frequency peaks) that from generation 3 onwards, there is little noticeable change in the VDOS for the polymorphs of both ROY and Axitinib.

In Figs. 45 and 46, we show the convergence of EOS for the polymorphs of ROY and Axitinib. Besides the generation 1 MLIP, which were trained only to PBE-level structures generated from the original MACE-MP-0b3, the other generations are able to reach close to 3 meV per molecule (~ 0.3 kJ/mol) on the EOS relative to the B86bPBE50-revXDM DFA.

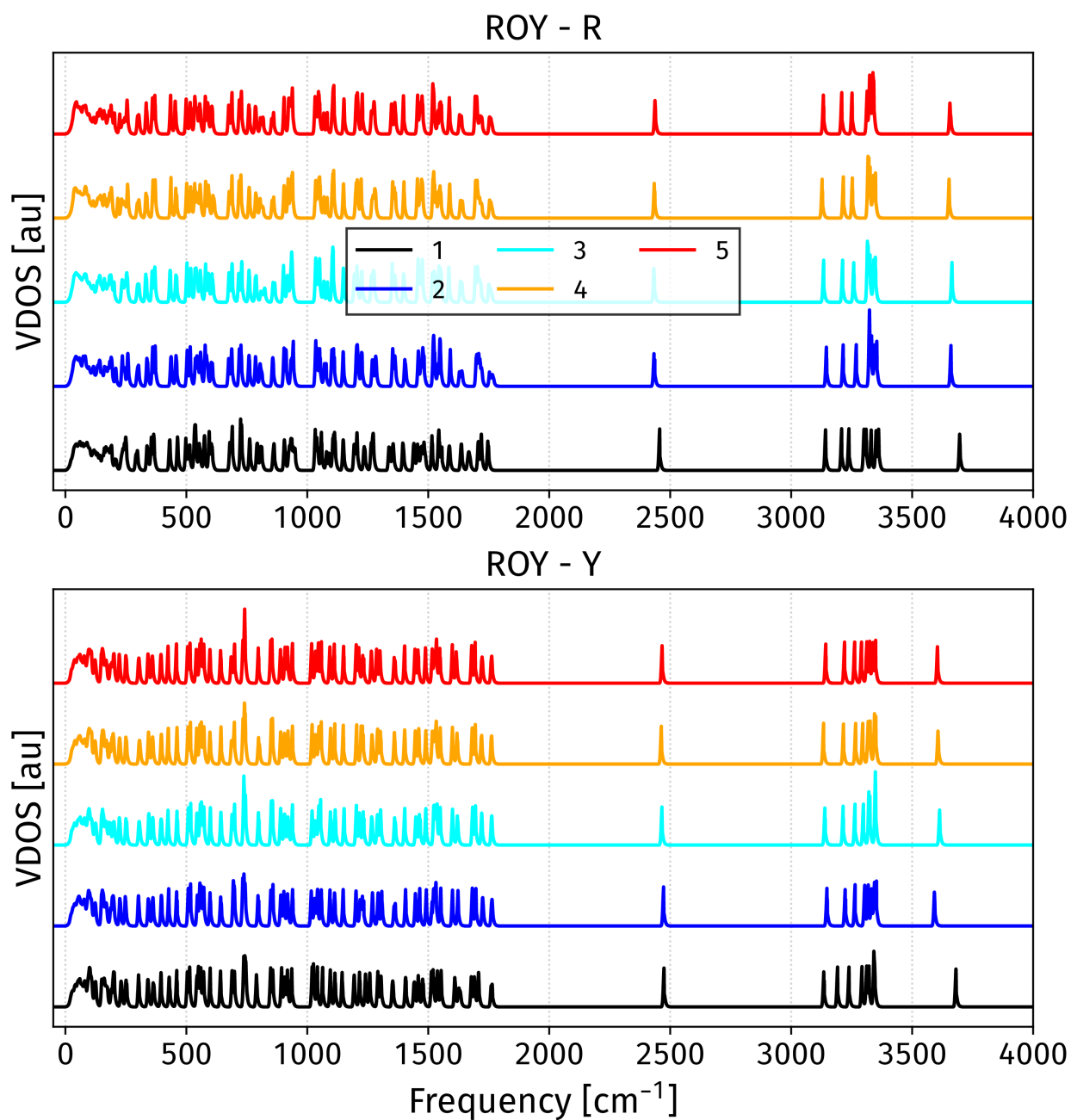


FIG. 43: Convergence of the vibrational density of states for ROY forms R (upper panel) and XLI (lower panel) with MLIP generations.

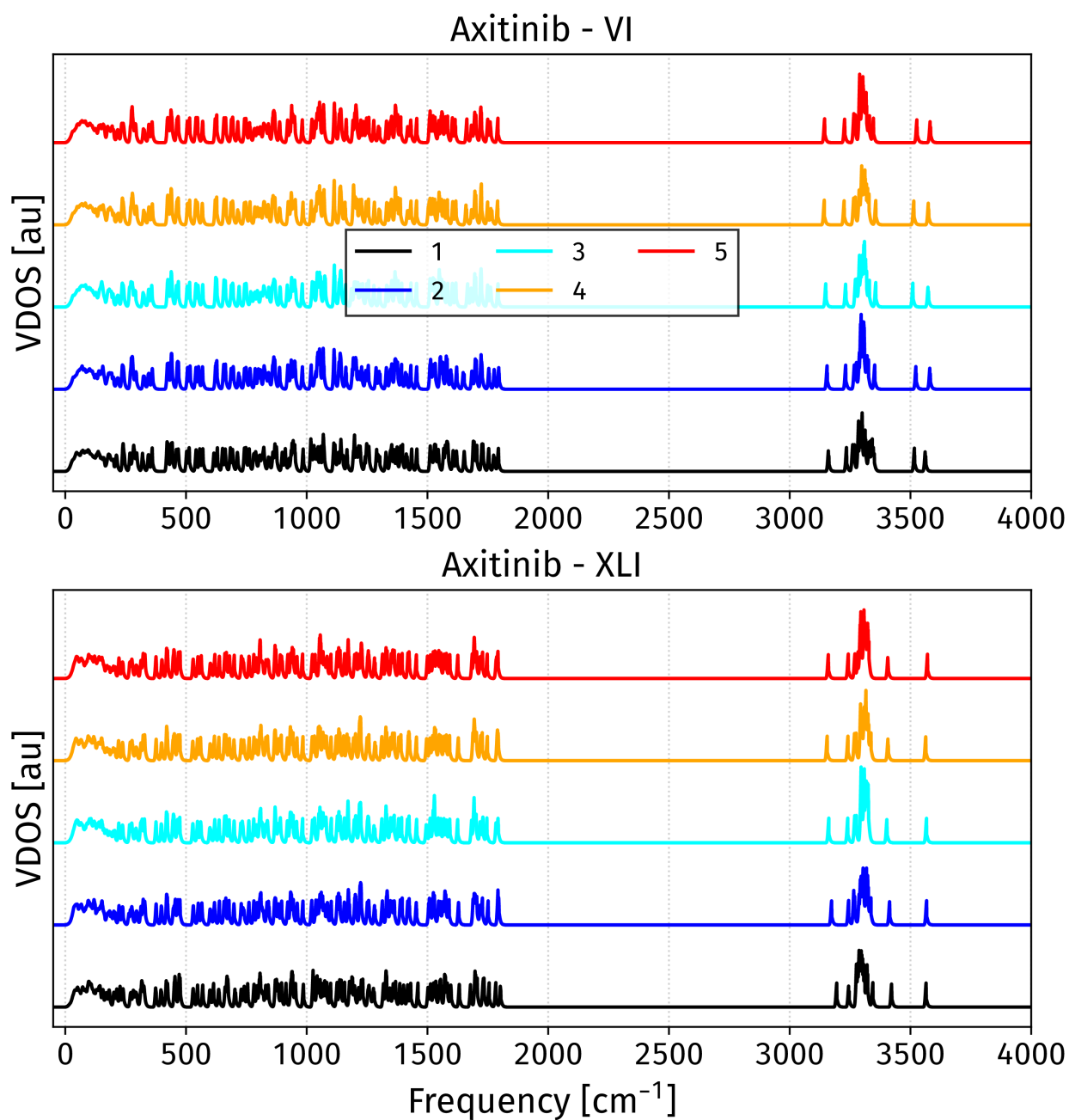


FIG. 44: Convergence of the vibrational density of states for Axitinib forms VI (upper panel) and XLI (lower panel) with MLIP generations.

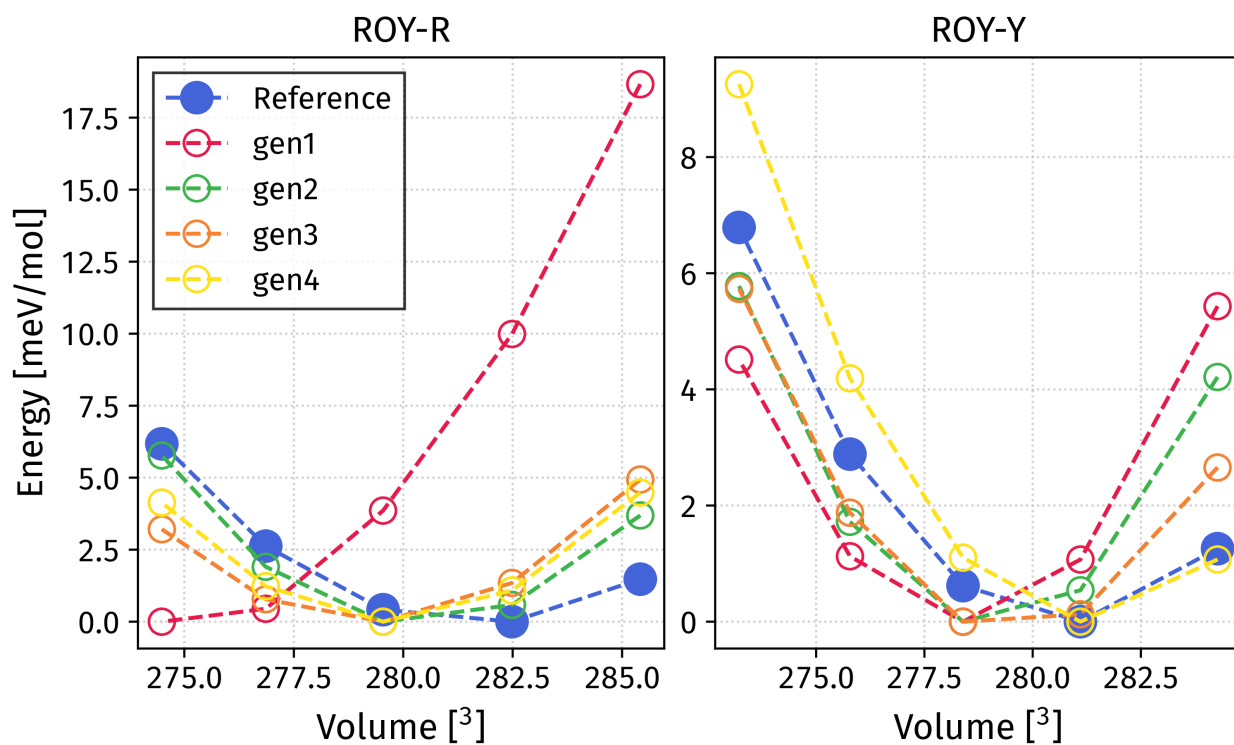


FIG. 45: Convergence of the equation of states for ROY forms R (left panel) and Y (right panel) with MLIP generations.

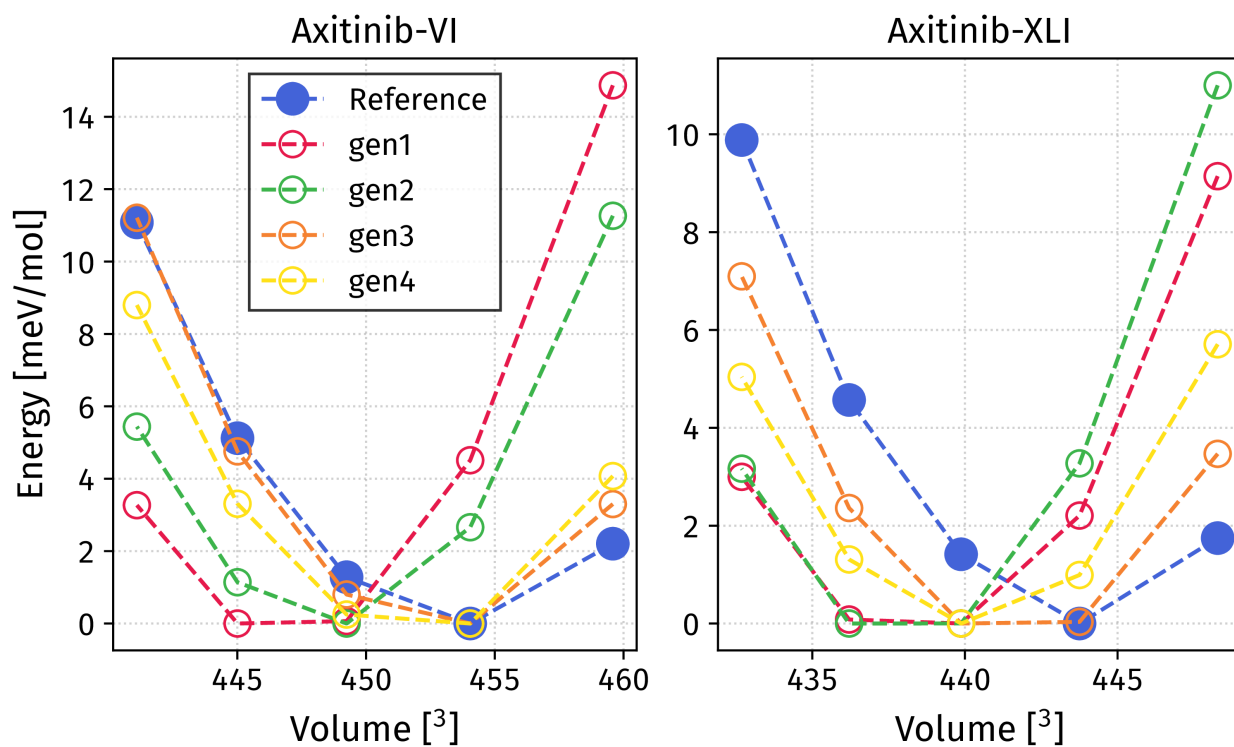


FIG. 46: Convergence of the equation of states for Axitinib forms VI (left panel) and XLI (right panel) with MLIP generations.

We finally look at relative energy in Figs. 47 and 48 for ROY and Axitinib. We consider various related quantities:

- ΔE — the relative energy at 0K.
- $\Delta E + \text{ZPE}$ — the relative energy at 0K with zero-point energy contributions calculated using the harmonic approximation.
- QHA — the relative enthalpy calculated using the quasi-harmonic approximation.
- MD — the relative enthalpy calculated using classical molecular dynamics.
- PIMD — the relative enthalpy calculated using path-integral molecular dynamics.

These estimates are tabulated in Table 46. It can be seen that for all of these relative energy quantities, there is a convergence to within 0.5 kJ/mol by the generation 3 MLIP onwards. For both systems, the finite-temperature effects, going up to ΔH^{MD} are small compared to ΔE , being less than 0.5 kJ/mol for both ROY and Axitinib.

For the the final (fifth) generation, we have also computed PIMD estimates to ΔH . The error bars are generally larger due to the significantly higher computational costs compared to MD. For ROY, we see that the MD and PIMD ΔH estimates are within their respective error bars. For Axitinib, there is some effect (of the order of 1 kJ/mol) due to nuclear quantum effects but overall, these differences are not significant given the experimental value of ΔH (7.5 kJ/mol).

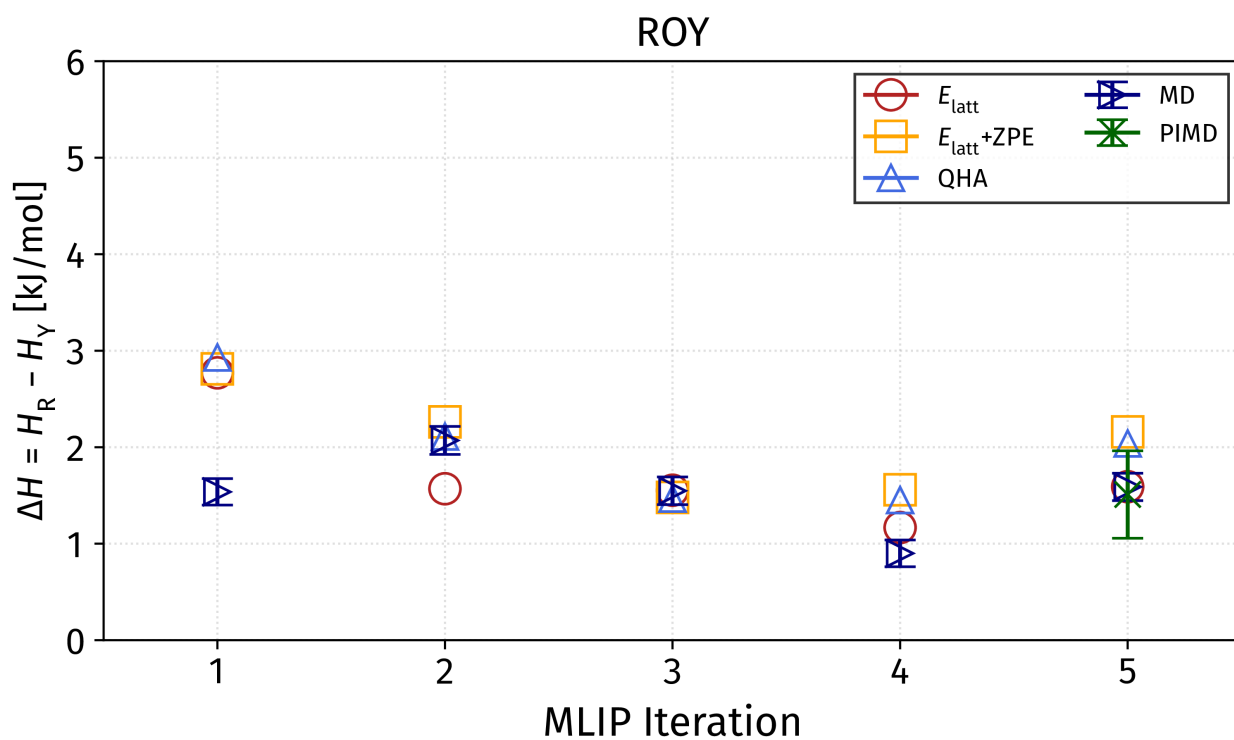


FIG. 47: Convergence of the relative energy between ROY forms R and Y with MLIP generations.

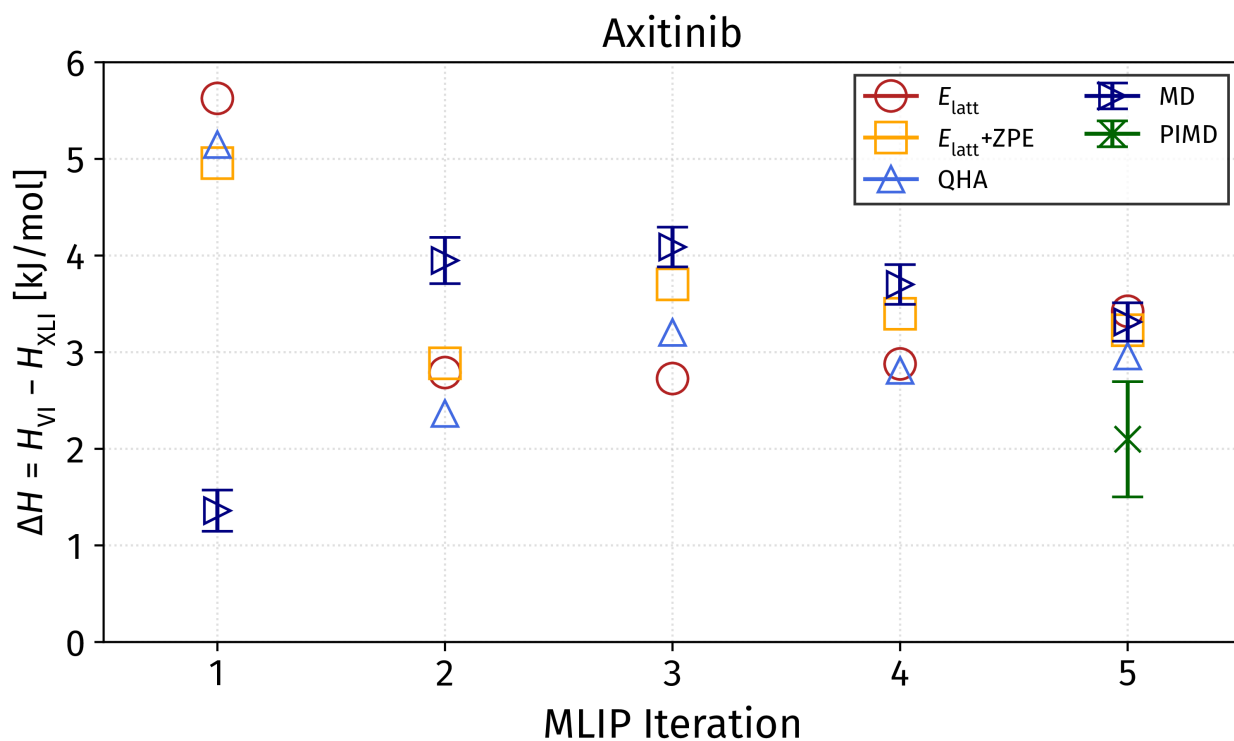


FIG. 48: Convergence of the relative energy between Axitinib forms VI and XLI with MLIP generations.

TABLE 46: Relative between ROY (forms R and Y) and Axitinib (forms VI and XLI) as predicted by MLIPs of different generations. All values are in kJ/mol. Statistical uncertainties (1σ) are reported for MD and PIMD results.

		MLIP Generation				
		1	2	3	4	5
ROY	Elatt	2.8	1.6	1.6	1.2	1.6
	Elatt + ZPE	2.8	2.3	1.5	1.6	2.2
	QHA	2.9	2.1	1.5	1.5	2.0
	MD DeltaH	1.5±0.1	2.1±0.1	1.5±0.1	0.9±0.1	1.6±0.1
	PIMD DeltaH	-	-	-	-	1.5±0.5
Axitinib	Elatt	5.6	2.8	2.7	2.9	3.4
	Elatt + ZPE	5.0	2.9	3.7	3.4	3.2
	QHA	5.1	2.4	3.2	2.8	3.0
	MD DeltaH	1.4±0.2	3.9±0.2	4.1±0.2	3.7±0.2	3.3±0.2
	PIMD DeltaH	-	-	-	-	2.1±0.6

D. Final experimental relative energy estimates

We report the final thermal contributions (calculated with MD) in Table 47, which we used to correct the experimental ΔH measurements. In general, we set 0.5 kJ/mol error bars on the experimental ΔH values. This is based upon the study by Campeta *et al.* [143], which shows that experimental differential scanning calorimetry (DSC) can give values in the range of ~ 1 kJ/mol for across several measurements for a single polymorph. This is in line with previous works that highlight errors up to 5% on DSC measurements [145]. For axitinib specifically, we set the error bar to 0.8 kJ/mol due to the increased errors found specifically for form VI by Campeta *et al.* [143]. We use the (classical) MD estimates of ΔH for ROY and Rotigotine, which has been shown to agree with the PIMD estimates. For rotigotine, we report ΔE and ΔH values taken from Mortazavi *et al.* [10], where the enthalpy is estimated from vibrational free energies within the harmonic approximation.

TABLE 47: DFT static relative energy and relative enthalpy from MD simulations. Their difference is used to correct experimental enthalpies for the polymorph pairs of rotigotine (I and II), axitinib (VI and XLI) and ROY (R and Y).

	DFT ΔE	DFT ΔH^{MD}	Expt. ΔH	Expt. ΔE
Rotigotine	7.1	7.6	7.5±0.5 [10]	7.0±0.5
Axitinib	3.4	3.3	7.3±0.8 [143]	7.5±0.8
ROY	1.6	1.6	1.2±0.5 [142]	1.2±0.5

10. BENCHMARKING DENSITY FUNCTIONAL AND WAVE FUNCTION METHODS

We have benchmarked the performance of a selection of density functional approximations (DFAs) in this section for the X23 and ICE13 datasets. While not aiming to cover all possible DFAs, the DFAs we have selected encompass a broad set of exchange-correlation functionals (across Jacob's ladder [146]) and dispersion corrections [72]. These are as follows:

- PBE-D3(BJ) – PBE [5] with Grimmes D3 dispersion using the BeckeJohnson damping.
- PBE-TS – PBE with the pairwise Tkatchenko and Scheffler [6], formally equivalent to Grimmes D2 dispersion but with charge-density dependent dispersion coefficients and damping function.
- PBE-MBD – PBE together with a many-body dispersion by Tkatchenko *et al.* [31]. This uses the “rsSCS” formulation.
- revPBE-D3(0) – revPBE [23] together with Grimme's D3 dispersion using zero damping.
- B86bPBE-XDM – B86b exchange and PBE correlation with exchangehole dipole moment (XDM) dispersion correction [13].
- r²SCAN-D4 – Regularized SCAN meta-GGA functional [24, 25] with Grimmes D4 dispersion correction [73], including environment-dependent atomic charges.
- optB86b-vdW – Optimized B86b exchange combined with nonlocal van der Waals correlation (vdW-DF) as developed by Klimeš *et al.* [3].
- vdW-DF2 – Second version of the nonlocal van der Waals density functional (vdW-DF2) of Lee *et al.* [28]
- B86bPBE25-XDM – Hybrid B86bPBE functional with 25% Hartree-Fock exchange, combined with XDM dispersion correction.
- B86bPBE50-XDM – Hybrid B86bPBE functional with 50% Hartree-Fock exchange, combined with XDM dispersion correction.
- PBE0-MBD – Hybrid PBE0 functional combined with many-body dispersion (MBD) correction within the rsSCS formulation.

A. X23 lattice energy

We tabulate the lattice energies of the DFAs in Tables 48 and 49 for the semilocal and hybrid DFAs, respectively. We also give the mean absolute deviation (MAD) against experimental, DMC and LNO-MBE-CCSD(T) references for each DFA. In general, the trends are well-captured irrespective of the reference methods used. For example, the DFA with the largest error (optB86b-vdW) is the same for all three methods. However, for the DFAs with small errors, with MAD below 4 kJ/mol, it may be more difficult to identify the best DFA. For example, B86bPBE25-XDM gives the best performance w.r.t. LNO-MBE-CCSD(T), but r²SCAN-D4 is the best according to DMC, while B86bPBE25-XDM is the best when compared to experiments.

TABLE 48: Comparison of several semilocal density functional approximations to experiments, LNO-MBE-CCSD(T) and DMC (in kJ/mol) for the X23 dataset

	PBE-D3(BJ)	PBE-TS	PBE-MBD	revPBE-D3(0)	B86bPBE-XDM	r ² SCAN-D4	optB86b-vdW	vdW-DF2
1,4-cyclohexanedione	-88.6	-105.6	-91.9	-90.6	-88.4	-90.6	-115.1	-99.5
Acetic Acid	-74.3	-81.9	-76.4	-67.7	-73.5	-74.9	-87.3	-73.4
Adamantane	-71.4	-105.5	-77.7	-73.9	-70.5	-63.5	-98.9	-82.0
Ammonia	-42.6	-43.7	-42.3	-38.4	-40.5	-40.5	-44.1	-39.7
Anthracene	-106.7	-135.9	-107.6	-115.1	-102.6	-103.1	-135.3	-103.7
Benzene	-54.9	-66.7	-54.5	-58.4	-51.6	-51.2	-67.3	-54.4
CO ₂	-24.2	-24.6	-23.1	-22.6	-24.6	-28.9	-34.5	-32.8
Cyanamide	-92.7	-93.4	-91.4	-84.5	-89.2	-91.0	-99.3	-86.9
Cytosine	-160.4	-172.5	-161.0	-153.7	-156.8	-159.9	-179.2	-152.6
Ethyl carbamate	-87.8	-98.5	-90.9	-82.6	-86.3	-85.8	-104.6	-91.1
Formamide	-82.3	-85.9	-82.4	-75.9	-80.5	-81.8	-90.0	-79.7
Hexamine	-86.3	-115.5	-90.7	-87.2	-87.9	-84.6	-112.5	-92.7
Imidazole	-92.1	-101.7	-93.4	-87.4	-90.9	-89.6	-103.0	-87.2
Naphthalene	-80.1	-101.2	-80.7	-86.8	-76.6	-77.4	-101.3	-77.9
Oxalic Acid α	-91.0	-98.4	-94.1	-83.2	-93.6	-103.8	-116.7	-104.1
Oxalic Acid β	-94.8	-102.3	-97.4	-87.4	-96.7	-105.5	-119.3	-102.6
Pyrazine	-65.3	-74.8	-62.5	-63.1	-62.7	-60.4	-78.2	-66.0
Pyrazole	-81.0	-88.7	-82.2	-78.7	-79.1	-78.4	-91.6	-76.0
Succinic Acid	-130.5	-146.8	-135.8	-120.4	-130.6	-136.4	-156.7	-124.8
Triazine	-60.2	-67.3	-57.1	-58.4	-57.8	-57.2	-73.7	-64.6
Trioxane	-58.2	-75.3	-63.8	-59.0	-62.1	-58.3	-80.2	-72.9
Uracil	-137.2	-148.2	-137.7	-128.7	-134.5	-138.5	-156.5	-133.8
Urea	-108.0	-111.9	-109.8	-100.0	-105.1	-110.5	-117.7	-104.0
MAD [CCSD(T)]	3.9	12.4	4.2	4.2	3.5	4.1	17.1	5.0
MAD [DMC]	4.4	14.6	5.4	5.9	2.9	2.8	18.9	4.4
MAD [Expt]	4.8	15.0	5.9	5.2	3.8	4.8	19.7	5.3

TABLE 49: Comparison of several hybrid density functional approximations to experiments, LNO-MBE-CCSD(T) and DMC (in kJ/mol) for the X23 dataset

	B86bPBE25-XDM	B86bPBE50-XDM	PBE0-MBD
1,4-cyclohexanedione	-88.5	-89.7	-94.2
Acetic Acid	-71.9	-71.3	-76.1
Adamantane	-68.2	-64.7	-77.3
Ammonia	-36.7	-33.9	-39.0
Anthracene	-106.5	-107.9	-115.2
Benzene	-52.1	-51.6	-56.4
CO ₂	-24.1	-23.9	-23.7
Cyanamide	-85.2	-82.2	-88.3
Cytosine	-155.9	-155.5	-162.8
Ethyl carbamate	-83.7	-81.8	-89.9
Formamide	-78.2	-76.7	-81.4
Hexamine	-89.3	-90.5	-95.3
Imidazole	-88.7	-86.3	-92.6
Naphthalene	-79.2	-80.1	-85.9
Oxalic Acid α	-94.7	-97.4	-97.9
Oxalic Acid β	-94.9	-95.0	-98.2
Pyrazine	-61.3	-59.6	-62.9
Pyrazole	-77.5	-76.0	-82.0
Succinic Acid	-127.8	-127.1	-136.0
Triazine	-57.2	-56.9	-58.0
Trioxane	-60.4	-59.4	-64.5
Uracil	-134.0	-133.8	-139.6
Urea	-103.5	-103.1	-109.4
MAD [CCSD(T)]	3.0	3.4	3.5
MAD [DMC]	2.8	3.2	5.8
MAD [Expt]	3.1	3.3	6.3

B. ICE13 lattice energy and relative energy

We compare the lattice energy and relative energy predicted by the DFAs for the ICE13 dataset in Tables 50 and 51, respectively. Their MAD against both DMC and LNO-MBE-CCSD(T) are also tabulated. The conclusions drawn from comparisons to LNO-MBE-CCSD(T) are similar to DMC, highlighting the high precision in both the DMC and LNO-MBE-CCSD(T) estimates. In general, the MAD for the deviation between a DFA and LNO-MBE-CCSD(T) is within 0.5 kJ/mol the deviation against DMC as well. For example, in agreement with Ref. 7, we find that revPBE-D3 with zero-damping performs really well at predicting both the absolute lattice energy and the relative energy.

-
- [1] F. Della Pia, A. Zen, D. Alfè, and A. Michaelides, How accurate are simulations and experiments for the lattice energies of molecular crystals?, *Phys. Rev. Lett.* **133**, 046401 (2024).
 - [2] J. Klimeš, Lattice energies of molecular solids from the random phase approximation with singles corrections, *J. Chem. Phys.* **145**, 094506 (2016).
 - [3] J. Klimeš, D. R. Bowler, and A. Michaelides, Chemical accuracy for the van der Waals density functional, *J. Phys.: Condens. Matter* **22**, 022201 (2010).
 - [4] A. M. Reilly and A. Tkatchenko, Understanding the role of vibrations, exact exchange, and many-body van der Waals interactions in the cohesive properties of molecular crystals, *J. Chem. Phys.* **139**, 024705 (2013).
 - [5] J. P. Perdew, K. Burke, and M. Ernzerhof, Generalized gradient approximation made simple, *Phys. Rev. Lett.* **77**, 3865 (1996).
 - [6] A. Tkatchenko and M. Scheffler, Accurate molecular van der Waals interactions from ground-state electron density and free-atom reference data, *Phys. Rev. Lett.* **102**, 073005 (2009).
 - [7] F. Della Pia, A. Zen, D. Alfè, and A. Michaelides, DMC-ICE13: Ambient and high pressure polymorphs of ice from diffusion Monte Carlo and density functional theory, *J. Chem. Phys.* **157**, 134701 (2022).
 - [8] M. Matsumoto, T. Yagasaki, and H. Tanaka, GenIce: Hydrogen-disordered ice generator, *J. Comp. Chem.* **39**, 61 (2018).
 - [9] M. Matsumoto, T. Yagasaki, and H. Tanaka, Novel algorithm to generate hydrogen-disordered ice structures, *J. Chem. Inf. Model.* **61**, 2542 (2021).

TABLE 50: Comparison of several density functional approximations to LNO-MBE-CCSD(T) and DMC (in kJ/mol) for the ICE13 dataset

	PBE-D3(BJ)	PBE-TS	PBE-MBD	revPBE-D3(0)	B86bPBE-XDM	r ² SCAN-D4	optB86b-vdW	vdW-DF2	B86bPBE25-XDM	B86bPBE50-XDM	PBE0-MBD
Ih	-70.4	-69.5	-70.5	-59.1	-68.2	-66.5	-68.7	-59.5	-60.7	-55.3	-63.0
II	-66.6	-67.8	-67.4	-57.8	-65.3	-65.8	-67.9	-60.2	-58.7	-54.0	-61.3
III	-67.5	-67.4	-67.8	-56.7	-65.6	-64.6	-67.5	-58.4	-58.1	-52.7	-60.6
IV	-64.1	-65.3	-64.8	-55.1	-62.7	-63.2	-65.8	-58.0	-55.9	-51.0	-58.4
VI	-64.0	-65.9	-64.9	-56.2	-63.0	-64.4	-66.9	-59.2	-56.5	-51.9	-59.1
VII	-57.9	-59.1	-59.2	-55.0	-57.6	-61.6	-63.0	-56.6	-52.2	-48.7	-54.6
VIII	-58.9	-60.4	-60.2	-55.8	-58.7	-62.7	-64.0	-57.8	-53.3	-49.9	-55.8
IX	-67.7	-68.0	-68.2	-57.5	-66.0	-65.4	-68.3	-59.9	-58.9	-53.7	-61.4
XI	-70.9	-70.0	-71.0	-59.3	-68.6	-66.9	-69.2	-59.5	-60.8	-55.1	-63.2
XIII	-66.0	-67.3	-66.7	-56.7	-64.6	-65.1	-67.7	-60.0	-57.9	-53.0	-60.5
XIV	-65.2	-66.8	-65.9	-56.3	-64.0	-64.9	-67.5	-59.9	-57.3	-52.5	-59.9
XV	-63.8	-65.7	-64.7	-56.1	-62.8	-64.3	-66.7	-59.3	-56.5	-52.0	-59.0
XVII	-69.3	-68.5	-69.5	-58.0	-67.2	-65.5	-67.3	-58.1	-59.5	-54.0	-61.9
MAD [CCSD(T)]	8.3	9.1	9.0	0.5	7.0	7.5	9.7	1.7	1.0	4.6	2.7
MAD [DMC]	8.0	8.7	8.6	0.9	6.6	7.1	9.4	1.4	1.0	5.0	2.3

TABLE 51: Comparison of several density functional approximations to LNO-MBE-CCSD(T) and DMC [7] (in kJ/mol) for the relative energy of the ICE13 dataset

	PBE-D3(BJ)	PBE-TS	PBE-MBD	revPBE-D3(0)	B86bPBE-XDM	r ² SCAN-D4	optB86b-vdW	vdW-DF2	B86bPBE25-XDM	B86bPBE50-XDM	PBE0-MBD
II	3.8	1.8	3.1	1.3	2.9	0.7	0.8	-0.7	2.0	1.3	1.7
III	2.9	2.1	2.7	2.3	2.6	1.9	1.2	1.0	2.5	2.6	2.4
IV	6.3	4.2	5.7	4.0	5.5	3.3	3.0	1.5	4.8	4.3	4.6
VI	6.4	3.7	5.6	2.8	5.2	2.1	1.9	0.3	4.2	3.4	3.9
VII	12.5	10.5	11.3	4.1	10.6	4.9	5.8	2.9	8.5	6.6	8.4
VIII	11.5	9.1	10.3	3.3	9.5	3.8	4.8	1.6	7.3	5.3	7.2
IX	2.7	1.5	2.3	1.6	2.2	1.2	0.5	-0.4	1.8	1.6	1.6
XI	-0.5	-0.5	-0.5	-0.2	-0.4	-0.3	-0.5	-0.0	-0.1	0.2	-0.2
XIII	4.4	2.2	3.8	2.3	3.6	1.5	1.0	-0.5	2.8	2.3	2.6
XIV	5.2	2.7	4.5	2.7	4.2	1.7	1.3	-0.4	3.4	2.7	3.2
XV	6.6	3.8	5.8	2.9	5.4	2.3	2.1	0.1	4.2	3.3	4.0
XVII	1.1	1.1	1.0	1.0	1.0	1.0	1.5	1.4	1.2	1.3	1.2
MAD [CCSD(T)]	3.3	1.6	2.7	0.4	2.4	0.3	0.7	1.6	1.5	0.8	1.4
MAD [DMC]	3.4	1.7	2.9	0.8	2.6	0.5	0.5	1.5	1.7	1.0	1.5

- [10] M. Mortazavi, J. Hoja, L. Aerts, L. Quéré, J. van de Streek, M. A. Neumann, and A. Tkatchenko, Computational polymorph screening reveals late-appearing and poorly-soluble form of rotigotine, *Commun. Chem.* **2**, 70 (2019).
- [11] G. M. Day, W. D. S. Motherwell, H. L. Ammon, S. X. M. Boerrigter, R. G. Della Valle, E. Venuti, A. Dzyabchenko, J. D. Dunitz, B. Schweizer, B. P. van Eijck, P. Erk, J. C. Facelli, V. E. Bazterra, M. B. Ferraro, D. W. M. Hofmann, F. J. J. Leusen, C. Liang, C. C. Pantelides, P. G. Karamertzanis, S. L. Price, T. C. Lewis, H. Nowell, A. Torrisi, H. A. Scheraga, Y. A. Arnautova, M. U. Schmidt, and P. Verwer, A third blind test of crystal structure prediction, *Acta Cryst. B* **61**, 511 (2005).
- [12] S. R. Whittleton, A. Otero-de-la-Roza, and E. R. Johnson, Exchange-hole dipole dispersion model for accurate energy ranking in molecular crystal structure prediction II: Nonplanar molecules, *J. Chem. Theory Comput.* **13**, 5332 (2017).
- [13] A. D. Becke and E. R. Johnson, Exchange-hole dipole moment and the dispersion interaction revisited, *J. Chem. Phys.* **127**, 154108 (2007).
- [14] A. Otero-de-la-Roza and E. R. Johnson, Van der Waals interactions in solids using the exchange-hole dipole moment model, *J. Chem. Phys.* **136**, 174109 (2012).
- [15] C. Greenwell and G. J. O. Beran, Inaccurate conformational energies still hinder crystal structure prediction in flexible organic molecules, *Cryst. Growth Des.* **20**, 4875 (2020).
- [16] G. J. O. Beran, I. J. Sugden, C. Greenwell, D. H. Bowskill, C. C. Pantelides, and C. S. Adjiman, How many more polymorphs of ROY remain undiscovered, *Chem. Sci.* **13**, 1288 (2022).
- [17] G. S. Fanourgakis and S. S. Xantheas, The flexible, polarizable, thole-type interaction potential for water (TTM2-F) revisited, *J. Phys. Chem. A* **110**, 4100 (2006).
- [18] G. Kresse and J. Hafner, Ab initio molecular dynamics for liquid metals, *Phys. Rev. B* **47**, 558 (1993).
- [19] G. Kresse and J. Furthmüller, Efficiency of ab-initio total energy calculations for metals and semiconductors using a plane-wave basis set, *Comput. Mater. Sci.* **6**, 15 (1996).
- [20] G. Kresse and J. Furthmüller, Efficient iterative schemes for ab initio total-energy calculations using a plane-wave basis set, *Phys. Rev. B* **54**, 11169 (1996).
- [21] L. Lin, Adaptively compressed exchange operator, *J. Chem. Theory Comput.* **12**, 2242 (2016).
- [22] S. Grimme, J. Antony, S. Ehrlich, and H. Krieg, A consistent and accurate ab initio parametrization of density functional dispersion correction (DFT-D) for the 94 elements H-Pu, *J. Chem. Phys.* **132**, 154104 (2010).

- [23] Y. Zhang and W. Yang, Comment on “Generalized gradient approximation made simple”, *Phys. Rev. Lett.* **80**, 890 (1998).
- [24] J. W. Furness, A. D. Kaplan, J. Ning, J. P. Perdew, and J. Sun, Accurate and numerically efficient r^2 SCAN meta-generalized gradient approximation, *J. Phys. Chem. Lett.* **11**, 8208 (2020).
- [25] J. Ning, M. Kothakonda, J. W. Furness, A. D. Kaplan, S. Ehlert, J. G. Brandenburg, J. P. Perdew, and J. Sun, Workhorse minimally empirical dispersion-corrected density functional with tests for weakly bound systems: r^2 SCAN+rVV10, *Phys. Rev. B* **106**, 075422 (2022).
- [26] J. Klimeš, D. R. Bowler, and A. Michaelides, Van der Waals density functionals applied to solids, *Phys. Rev. B* **83**, 195131 (2011).
- [27] I. Hamada, Van der Waals density functional made accurate, *Phys. Rev. B* **89**, 121103 (2014).
- [28] K. Lee, É. D. Murray, L. Kong, B. I. Lundqvist, and D. C. Langreth, Higher-accuracy van der Waals density functional, *Phys. Rev. B* **82**, 081101 (2010).
- [29] A. J. A. Price, A. Otero-de-la-Roza, and E. R. Johnson, XDM-corrected hybrid DFT with numerical atomic orbitals predicts molecular crystal lattice energies with unprecedented accuracy, *Chem. Sci.* **14**, 1252 (2023).
- [30] C. Adamo and V. Barone, Toward reliable density functional methods without adjustable parameters: The PBE0 model, *J. Chem. Phys.* **110**, 6158 (1999).
- [31] A. Tkatchenko, R. A. DiStasio, R. Car, and M. Scheffler, Accurate and efficient method for many-body van der Waals interactions, *Phys. Rev. Lett.* **108**, 236402 (2012).
- [32] V. Blum, R. Gehrke, F. Hanke, P. Havu, V. Havu, X. Ren, K. Reuter, and M. Scheffler, *Ab Initio* molecular simulations with numeric atom-centered orbitals, *Comput. Phys. Commun.* **180**, 2175 (2009).
- [33] P. Giannozzi, S. Baroni, N. Bonini, M. Calandra, R. Car, C. Cavazzoni, D. Ceresoli, G. L. Chiarotti, M. Cococcioni, I. Dabo, A. D. Corso, S. de Gironcoli, S. Fabris, G. Fratesi, R. Gebauer, U. Gerstmann, C. Gougoussis, A. Kokalj, M. Lazzeri, L. Martin-Samos, N. Marzari, F. Mauri, R. Mazzarello, S. Paolini, A. Pasquarello, L. Paulatto, C. Sbraccia, S. Scandolo, G. Sclauzero, A. P. Seitsonen, A. Smogunov, P. Umari, and R. M. Wentzcovitch, QUANTUM ESPRESSO: A modular and open-source software project for quantum simulations of materials, *J. Phys.: Condens. Matter* **21**, 395502 (2009).
- [34] G. Prandini, A. Marrazzo, I. E. Castelli, N. Mounet, and N. Marzari, Precision and efficiency in solid-state pseudopotential calculations, *npj Comput. Mater.* **4**, 72 (2018).

- [35] P. R. Nagy and M. Kállay, Optimization of the linear-scaling local natural orbital CCSD(T) method: Redundancy-free triples correction using Laplace transform, *J. Chem. Phys.* **146**, 214106 (2017).
- [36] P. R. Nagy, G. Samu, and M. Kállay, Optimization of the linear-scaling local natural orbital CCSD(T) method: Improved algorithm and benchmark applications, *J. Chem. Theory Comput.* **14**, 4193 (2018).
- [37] P. R. Nagy and M. Kállay, Approaching the basis set limit of CCSD(T) energies for large molecules with local natural orbital coupled-cluster methods, *J. Chem. Theory Comput.* **15**, 5275 (2019).
- [38] P. R. Nagy, State-of-the-art local correlation methods enable affordable gold standard quantum chemistry for up to hundreds of atoms, *Chem. Sci.* **15**, 14556 (2024).
- [39] K. Raghavachari, G. W. Trucks, J. A. Pople, and M. Head-Gordon, A fifth-order perturbation comparison of electron correlation theories, *Chem. Phys. Lett.* **157**, 479 (1989).
- [40] M. Kállay, P. R. Nagy, D. Mester, Z. Rolik, G. Samu, J. Csontos, J. Csóka, P. B. Szabó, L. Gyevi-Nagy, B. Hégyel, I. Ladjánszki, L. Szegedy, B. Ladóczki, K. Petrov, M. Farkas, P. D. Mezei, and Á. Ganyecz, The MRCC program system: Accurate quantum chemistry from water to proteins, *J. Chem. Phys.* **152**, 074107 (2020).
- [41] D. Mester, P. R. Nagy, J. Csóka, L. Gyevi-Nagy, P. B. Szabó, R. A. Horváth, K. Petrov, B. Hégyel, B. Ladóczki, G. Samu, B. D. Lőrincz, and M. Kállay, Overview of developments in the MRCC program system, *J. Phys. Chem. A* **129**, 2086 (2025).
- [42] M. Kállay, P. R. Nagy, D. Mester, L. Gyevi-Nagy, J. Csóka, P. B. Szabó, Z. Rolik, G. Samu, J. Csontos, B. Hégyel, Á. Ganyecz, I. Ladjánszki, L. Szegedy, B. Ladóczki, K. Petrov, M. Farkas, P. D. Mezei, and R. A. Horváth, MRCC, a quantum chemical program suite. See <https://www.mrcc.hu/> (Accessed Jan 1, 2025).
- [43] Chr. Møller and M. S. Plesset, Note on an approximation treatment for many-electron systems, *Phys. Rev.* **46**, 618 (1934).
- [44] K. A. Peterson and T. H. Dunning, Accurate correlation consistent basis sets for molecular core-valence correlation effects: The second row atoms Al–Ar, and the first row atoms B–Ne revisited, *J. Chem. Phys.* **117**, 10548 (2002).
- [45] F. Neese and E. F. Valeev, Revisiting the atomic natural orbital approach for basis sets: Robust systematic basis sets for explicitly correlated and conventional correlated *ab initio* methods?, *J. Chem. Theory Comput.* **7**, 33 (2011).

- [46] F. Weigend, M. Häser, H. Patzelt, and R. Ahlrichs, RI-MP2: Optimized auxiliary basis sets and demonstration of efficiency, *Chem. Phys. Lett.* **294**, 143 (1998).
- [47] A. Hellweg, C. Hättig, S. Höfener, and W. Klopper, Optimized accurate auxiliary basis sets for RI-MP2 and RI-CC2 calculations for the atoms Rb to Rn, *Theor. Chem. Acc.* **117**, 587 (2007).
- [48] J. P. Heindel and S. S. Xantheas, The many-body expansion for aqueous systems revisited: I. Water–water interactions, *J. Chem. Theory Comput.* **16**, 6843 (2020).
- [49] J. P. Heindel and S. S. Xantheas, The many-body expansion for aqueous systems revisited: II. Alkali metal and halide ion–water interactions, *J. Chem. Theory Comput.* **17**, 2200 (2021).
- [50] K. M. Herman, J. P. Heindel, and S. S. Xantheas, The many-body expansion for aqueous systems revisited: III. Hofmeister ion–water interactions, *Phys. Chem. Chem. Phys.* **23**, 11196 (2021).
- [51] K. M. Herman and S. S. Xantheas, A formulation of the many-body expansion (MBE) for periodic systems: Application to several ice phases, *J. Phys. Chem. Lett.* **14**, 989 (2023).
- [52] K. Szalewicz, Symmetry-adapted perturbation theory of intermolecular forces, *WIREs Comput. Mol. Sci.* **2**, 254 (2012).
- [53] G. R. Medders, V. Babin, and F. Paesani, Development of a “first-principles” water potential with flexible monomers. III. Liquid phase properties, *J. Chem. Theory Comput.* **10**, 2906 (2014).
- [54] X. Zhu, M. Riera, E. F. Bull-Vulpe, and F. Paesani, MB-pol(2023): Sub-chemical accuracy for water simulations from the gas to the liquid phase, *J. Chem. Theory Comput.* **19**, 3551 (2023).
- [55] A. Hermann, Ground-state properties of crystalline ice from periodic Hartree–Fock calculations and a coupled-cluster-based many-body decomposition of the correlation energy, *Phys. Rev. Lett.* **101**, 10.1103/PhysRevLett.101.183005 (2008).
- [56] M. J. Gillan, D. Alfè, P. J. Bygrave, C. R. Taylor, and F. R. Manby, Energy benchmarks for water clusters and ice structures from an embedded many-body expansion, *J. Chem. Phys.* **139**, 114101 (2013).
- [57] J. P. Heindel and S. S. Xantheas, Molecular dynamics driven by the many-body expansion (MBE-MD), *J. Chem. Theory Comput.* **17**, 7341 (2021).
- [58] K. Syty, G. Czekają, K. N. Pham, and M. Modrzejewski, Multi-level coupled-cluster description of crystal lattice energies, *J. Chem. Theory Comput.* **21**, 5533 (2025).
- [59] C. Müller and D. Usyat, Incrementally corrected periodic local MP2 calculations: I. The cohesive energy of molecular crystals, *J. Chem. Theory Comput.* **9**, 5590 (2013).
- [60] G. J. O. Beran and K. Nanda, Predicting organic crystal lattice energies with chemical accuracy, *J. Phys. Chem. Lett.* **1**, 3480 (2010).

- [61] S. Wen, K. Nanda, Y. Huang, and G. J. O. Beran, Practical quantum mechanics-based fragment methods for predicting molecular crystal properties, *Phys. Chem. Chem. Phys.* **14**, 7578 (2012).
- [62] C. Červinka and G. J. O. Beran, Ab initio prediction of the polymorph phase diagram for crystalline methanol, *Chem. Sci.* **9**, 4622 (2018).
- [63] J. Košata, P. Merkl, P. Teeratchanan, and A. Hermann, Stability of hydrogen hydrates from second-order Møller–Plesset perturbation theory, *J. Phys. Chem. Lett.* **9**, 5624 (2018).
- [64] O. A. Loboda, G. A. Dolgonos, and A. D. Boese, Towards hybrid density functional calculations of molecular crystals via fragment-based methods, *J. Chem. Phys.* **149**, 124104 (2018).
- [65] J. Hoja, A. List, and A. D. Boese, Multimer embedding approach for molecular crystals up to harmonic vibrational properties, *J. Chem. Theory Comput.* **20**, 357 (2024).
- [66] M. A. Neumann, Tailor-made force fields for crystal-structure prediction, *J. Phys. Chem. B* **112**, 9810 (2008).
- [67] G. J. O. Beran, Approximating quantum many-body intermolecular interactions in molecular clusters using classical polarizable force fields, *J. Chem. Phys.* **130**, 164115 (2009).
- [68] S. L. Price, M. Leslie, G. W. A. Welch, M. Habgood, L. S. Price, P. G. Karamertzanis, and G. M. Day, Modelling organic crystal structures using distributed multipole and polarizability-based model intermolecular potentials, *Phys. Chem. Chem. Phys.* **12**, 8478 (2010).
- [69] J. Nyman, O. S. Pundyke, and G. M. Day, Accurate force fields and methods for modelling organic molecular crystals at finite temperatures, *Phys. Chem. Chem. Phys.* **18**, 15828 (2016).
- [70] D. H. Bowskill, I. J. Sugden, S. Konstantinopoulos, C. S. Adjiman, and C. C. Pantelides, Crystal structure prediction methods for organic molecules: State of the art, *Annu. Rev. Chem. Biomol. Eng.* **12**, 593 (2021).
- [71] S. Grimme, Semiempirical GGA-type density functional constructed with a long-range dispersion correction, *J. Comp. Chem.* **27**, 1787 (2006).
- [72] S. Grimme, A. Hansen, J. G. Brandenburg, and C. Bannwarth, Dispersion-corrected mean-field electronic structure methods, *Chem. Rev.* **116**, 5105 (2016).
- [73] E. Caldeweyher, S. Ehlert, A. Hansen, H. Neugebauer, S. Spicher, C. Bannwarth, and S. Grimme, A generally applicable atomic-charge dependent London dispersion correction, *J. Chem. Phys.* **150**, 154122 (2019).
- [74] Y. Muto, Force between nonpolar molecules, *Proc. Phys.-Math. Soc. Jpn.* **17**, 629 (1943).
- [75] B. M. Axilrod and E. Teller, Interaction of the van der Waals type between three atoms, *J. Chem. Phys.* **11**, 299 (1943).

- [76] A. L. Ringer and C. D. Sherrill, First principles computation of lattice energies of organic solids: The benzene crystal, *Chem. - Eur. J.* **14**, 2542 (2008).
- [77] C. T. Sargent, D. P. Metcalf, Z. L. Glick, C. H. Borca, and C. D. Sherrill, Benchmarking two-body contributions to crystal lattice energies and a range-dependent assessment of approximate methods, *J. Chem. Phys.* **158**, 054112 (2023).
- [78] Y. Xie, Z. L. Glick, and C. D. Sherrill, Assessment of three-body dispersion models against coupled-cluster benchmarks for crystalline benzene, carbon dioxide, and triazine, *J. Chem. Phys.* **158**, 094110 (2023).
- [79] P. M. Nelson and C. D. Sherrill, Convergence of the many-body expansion with respect to distance cutoffs in crystals of polar molecules: Acetic acid, formamide, and imidazole, *J. Chem. Phys.* **161**, 214105 (2024).
- [80] S. Wen and G. J. O. Beran, Accurate molecular crystal lattice energies from a fragment QM/MM approach with on-the-fly ab initio force field parametrization, *J. Chem. Theory Comput.* **7**, 3733 (2011).
- [81] J. Hofierka and J. Klimeš, Binding energies of molecular solids from fragment and periodic approaches, *Electron. Struct.* **3**, 034010 (2021).
- [82] M. Modrzejewski, S. Yourdkhani, and J. Klimeš, Random phase approximation applied to many-body noncovalent systems, *J. Chem. Theory Comput.* **16**, 427 (2020).
- [83] M. Modrzejewski, S. Yourdkhani, S. Śmiga, and J. Klimeš, Random-phase approximation in many-body noncovalent systems: Methane in a dodecahedral water cage, *J. Chem. Theory Comput.* **17**, 804 (2021).
- [84] C. H. Borca, B. W. Bakr, L. A. Burns, and C. D. Sherrill, CrystaLattE: Automated computation of lattice energies of organic crystals exploiting the many-body expansion to achieve dual-level parallelism, *J. Chem. Phys.* **151**, 144103 (2019).
- [85] L. Himanen, M. O. J. Jäger, E. V. Morooka, F. Federici Canova, Y. S. Ranawat, D. Z. Gao, P. Rinke, and A. S. Foster, DSCRIBE: Library of descriptors for machine learning in materials science, *Comput. Phys. Commun.* **247**, 106949 (2020).
- [86] J. Laakso, L. Himanen, H. Homm, E. V. Morooka, M. O. J. Jäger, M. Todorović, and P. Rinke, Updates to the DSCRIBE library: New descriptors and derivatives, *J. Chem. Phys.* **158**, 234802 (2023).
- [87] E. Schubert, J. Sander, M. Ester, H. P. Kriegel, and X. Xu, DBSCAN revisited, revisited: Why and how you should (still) use DBSCAN, *ACM Trans. Database Syst.* **42**, 19:1 (2017).

- [88] P. R. Nagy, G. Samu, and M. Kállay, An integral-direct linear-scaling second-order Møller–Plesset approach, *J. Chem. Theory Comput.* **12**, 4897 (2016).
- [89] P. B. Szabó, J. Csóka, M. Kállay, and P. R. Nagy, Linear-scaling open-shell MP2 approach: Algorithm, benchmarks, and large-scale applications, *J. Chem. Theory Comput.* **17**, 2886 (2021).
- [90] P. R. Nagy, L. Gyevi-Nagy, B. D. Lőrincz, and M. Kállay, Pursuing the basis set limit of CCSD(T) non-covalent interaction energies for medium-sized complexes: Case study on the S66 compilation, *Molecular Physics* **121**, e2109526 (2023).
- [91] S. Boys and F. Bernardi, The calculation of small molecular interactions by the differences of separate total energies. Some procedures with reduced errors, *Mol. Phys.* **19**, 553 (1970).
- [92] R. M. Richard, K. U. Lao, and J. M. Herbert, Aiming for benchmark accuracy with the many-body expansion, *Acc. Chem. Res.* **47**, 2828 (2014).
- [93] R. M. Richard, B. W. Bakr, and C. D. Sherrill, Understanding the many-body basis set superposition error: Beyond Boys and Bernardi, *J. Chem. Theory Comput.* **14**, 2386 (2018).
- [94] A. Altun, S. Ghosh, C. Riplinger, F. Neese, and G. Bistoni, Addressing the system-size dependence of the local approximation error in coupled-cluster calculations, *J. Phys. Chem. A* **125**, 9932 (2021).
- [95] K. Röttger, A. Endriss, J. Ihringer, S. Doyle, and W. F. Kuhs, Lattice constants and thermal expansion of H₂O and D₂O ice Ih between 10 and 265 K, *Acta. Cryst. B* **50**, 644 (1994).
- [96] E. Whalley, Energies of the phases of ice at zero temperature and pressure, *J. Chem. Phys.* **81**, 4087 (1984).
- [97] H. G. M. De Wit, J. C. Van Miltenburg, and C. G. De Kruif, Thermodynamic properties of molecular organic crystals containing nitrogen, oxygen, and sulphur 1. Vapour pressures and enthalpies of sublimation, *J. Chem. Thermodyn.* **15**, 651 (1983).
- [98] M. A. V. Ribeiro da Silva, M. J. S. Monte, and J. R. Ribeiro, Thermodynamic study on the sublimation of succinic acid and of methyl- and dimethyl-substituted succinic and glutaric acids, *J. Chem. Thermodyn.* **33**, 23 (2001).
- [99] W. Acree, Jr. and J. S. Chickos, Phase transition enthalpy measurements of organic and organometallic compounds. Sublimation, vaporization and fusion enthalpies from 1880 to 2015. Part 1. C₁–C₁₀, *J. Phys. Chem. Ref. Data* **45**, 033101 (2016).
- [100] W. Acree, Jr. and J. S. Chickos, Phase transition enthalpy measurements of organic and organometallic compounds and ionic liquids. Sublimation, vaporization, and fusion enthalpies from 1880 to 2015. Part 2. C₁₁–C₁₉₂, *J. Phys. Chem. Ref. Data* **46**, 013104 (2017).

- [101] F. Della Pia, B. X. Shi, V. Kapil, A. Zen, D. Alfè, and A. Michaelides, Accurate and efficient machine learning interatomic potentials for finite temperature modelling of molecular crystals, *Chem. Sci.* **16**, 11419 (2025).
- [102] J. G. Brandenburg, T. Maas, and S. Grimme, Benchmarking DFT and semiempirical methods on structures and lattice energies for ten ice polymorphs, *J. Chem. Phys.* **142**, 124104 (2015).
- [103] S. Yourdkhani and J. Klimeš, Using noncovalent interactions to test the precision of projector-augmented wave data sets, *J. Chem. Theory Comput.* **19**, 8871 (2023).
- [104] M. Hacene, A. Anciaux-Sedrakian, X. Rozanska, D. Klahr, T. Guignon, and P. Fleurat-Lessard, Accelerating VASP electronic structure calculations using graphic processing units, *J. Comp. Chem.* **33**, 2581 (2012).
- [105] Y. Huang and G. J. O. Beran, Reliable prediction of three-body intermolecular interactions using dispersion-corrected second-order Møller-Plesset perturbation theory, *J. Chem. Phys.* **143**, 044113 (2015).
- [106] J. Řezáč, Y. Huang, P. Hobza, and G. J. O. Beran, Benchmark calculations of three-body intermolecular interactions and the performance of low-cost electronic structure methods, *J. Chem. Theory Comput.* **11**, 3065 (2015).
- [107] K. E. Riley, J. Řezáč, and P. Hobza, MP2.X: A generalized MP2.5 method that produces improved binding energies with smaller basis sets, *Phys. Chem. Chem. Phys.* **13**, 21121 (2011).
- [108] Y. S. Al-Hamdani, P. R. Nagy, A. Zen, D. Barton, M. Kállay, J. G. Brandenburg, and A. Tkatchenko, Interactions between large molecules pose a puzzle for reference quantum mechanical methods, *Nat. Commun.* **12**, 3927 (2021).
- [109] T. Schäfer, A. Irmeler, A. Gallo, and A. Grüneis, Understanding discrepancies in noncovalent interaction energies from wavefunction theories for large molecules, *Nat. Commun.* **16**, 9108 (2025).
- [110] V. Fishman, M. Lesiuk, J. M. L. Martin, and A. Daniel Boese, Another angle on benchmarking noncovalent interactions, *J. Chem. Theory Comput.* **21**, 2311 (2025).
- [111] S. Lambie, D. Kats, D. Usvyat, and A. Alavi, On the applicability of CCSD(T) for dispersion interactions in large conjugated systems, *J. Chem. Phys.* **162**, 114112 (2025).
- [112] K. U. Lao, Canonical coupled cluster binding benchmark for nanoscale noncovalent complexes at the hundred-atom scale, *J. Chem. Phys.* **161**, 234103 (2024).
- [113] S. Lambie, P. López-Ríos, D. Kats, and A. Alavi, Nodal error behind discrepancies between coupled cluster and diffusion Monte Carlo: AcOH dimer case study, *arXiv [physics.chem-phy]*,

[arXiv:2508.17937](https://arxiv.org/abs/2508.17937) (2025).

- [114] B. X. Shi, F. Della Pia, Y. S. Al-Hamdani, A. Michaelides, D. Alfè, and A. Zen, Systematic discrepancies between reference methods for noncovalent interactions within the S66 dataset, *J. Chem. Phys.* **162**, 144107 (2025).
- [115] C. Červinka, M. Fulem, and K. Růžička, CCSD(T)/CBS fragment-based calculations of lattice energy of molecular crystals, *J. Chem. Phys.* **144**, 064505 (2016).
- [116] K. Hongo, M. A. Watson, T. Iitaka, A. Aspuru-Guzik, and R. Maezono, Diffusion Monte Carlo study of para-diiodobenzene polymorphism revisited, *J. Chem. Theory Comput.* **11**, 907 (2015).
- [117] A. Zen, J. G. Brandenburg, J. Klimeš, A. Tkatchenko, D. Alfè, and A. Michaelides, Fast and accurate quantum Monte Carlo for molecular crystals, *Proc. Natl. Acad. Sci. U. S. A.* **115**, 1724 (2018).
- [118] D. Firaha, Y. M. Liu, J. van de Streek, K. Sasikumar, H. Dietrich, J. Helfferich, L. Aerts, D. E. Braun, A. Broo, A. G. DiPasquale, A. Y. Lee, S. Le Meur, S. O. Nilsson Lill, W. J. Lunsmann, A. Mattei, P. Muglia, O. D. Putra, M. Raoui, S. M. Reutzel-Edens, S. Rome, A. Y. Sheikh, A. Tkatchenko, G. R. Woollam, and M. A. Neumann, Predicting crystal form stability under real-world conditions, *Nature* **623**, 324 (2023).
- [119] H. Kwee, S. Zhang, and H. Krakauer, Finite-size correction in many-body electronic structure calculations, *Phys. Rev. Lett.* **100**, 126404 (2008).
- [120] S. Chiesa, D. M. Ceperley, R. M. Martin, and M. Holzmann, Finite-size error in many-body simulations with long-range interactions, *Phys. Rev. Lett.* **97**, 076404 (2006).
- [121] L. M. Fraser, W. M. C. Foulkes, G. Rajagopal, R. J. Needs, S. D. Kenny, and A. J. Williamson, Finite-size effects and Coulomb interactions in quantum Monte Carlo calculations for homogeneous systems with periodic boundary conditions, *Phys. Rev. B* **53**, 1814 (1996).
- [122] A. J. Williamson, G. Rajagopal, R. J. Needs, L. M. Fraser, W. M. C. Foulkes, Y. Wang, and M.-Y. Chou, Elimination of Coulomb finite-size effects in quantum many-body simulations, *Phys. Rev. B* **55**, R4851 (1997).
- [123] P. R. C. Kent, R. Q. Hood, A. J. Williamson, R. J. Needs, W. M. C. Foulkes, and G. Rajagopal, Finite-size errors in quantum many-body simulations of extended systems, *Phys. Rev. B* **59**, 1917 (1999).
- [124] A. Reinhardt and B. Cheng, Quantum-mechanical exploration of the phase diagram of water, *Nat. Commun.* **12**, 588 (2021).

- [125] L. Zhang, Phase diagram of a deep potential water model, *Phys. Rev. Lett.* **126**, [10.1103/PhysRevLett.126.236001](https://doi.org/10.1103/PhysRevLett.126.236001) (2021).
- [126] S. L. Bore and F. Paesani, Realistic phase diagram of water from “first principles” data-driven quantum simulations, *Nat. Commun.* **14**, 3349 (2023).
- [127] J. Řezáč, K. E. Riley, and P. Hobza, S66: A well-balanced database of benchmark interaction energies relevant to biomolecular structures, *J. Chem. Theory Comput.* **7**, 2427 (2011).
- [128] J. Řezáč, M. Dubecký, P. Jurečka, and P. Hobza, Extensions and applications of the A24 data set of accurate interaction energies, *Phys. Chem. Chem. Phys.* **17**, 19268 (2015).
- [129] K. R. Bryenton, A. A. Adeleke, S. G. Dale, and E. R. Johnson, Delocalization error: The greatest outstanding challenge in density-functional theory, *WIREs Comput. Mol. Sci.* **13**, e1631 (2023).
- [130] S. Yang, I. Y. Zhang, and X. Ren, Developing correlation-consistent numeric atom-centered orbital basis sets for krypton: Applications in RPA-based correlated calculations, *J. Chem. Phys.* **160**, 024112 (2024).
- [131] J. G. Brandenburg, M. Hochheim, T. Bredow, and S. Grimme, Low-cost quantum chemical methods for noncovalent interactions, *J. Phys. Chem. Lett.* **5**, 4275 (2014).
- [132] E. Keller, J. Morgenstein, K. Reuter, and J. T. Margraf, Small basis set density functional theory method for cost-efficient, large-scale condensed matter simulations, *J. Chem. Phys.* **161**, 074104 (2024).
- [133] J. Weatherston, M. R. Probert, and M. J. Hall, Polymorphic ROYalty: The 14th ROY polymorph discovered via high-throughput crystallization, *J. Am. Chem. Soc.* **147**, 11949 (2025).
- [134] B. Rana, G. J. O. Beran, and J. M. Herbert, Correcting π -delocalisation errors in conformational energies using density-corrected DFT, with application to crystal polymorphs, *Mol. Phys.* **121**, e2138789 (2023).
- [135] G. A. Stephenson, T. B. Borchardt, S. R. Byrn, J. Bowyer, C. A. Bunnell, S. V. Snorek, and L. Yu, Conformational and Color Polymorphism of 5-Methyl-2-[(2-nitrophenyl)amino]-3-thiophenecarbonitrile, *J. Pharm. Sci.* **84**, 1385 (1995).
- [136] L. Yu, G. A. Stephenson, C. A. Mitchell, C. A. Bunnell, S. V. Snorek, J. J. Bowyer, T. B. Borchardt, J. G. Stowell, and S. R. Byrn, Thermochemistry and conformational polymorphism of a hexamorphic crystal system, *J. Am. Chem. Soc.* **122**, 585 (2000).
- [137] O. Rascol and S. Perez-Lloret, Rotigotine transdermal delivery for the treatment of Parkinson’s disease, *Expert Opin. Pharmacother.* **10**, 677 (2009).

- [138] I. B. Rietveld and R. Céolin, Rotigotine: Unexpected polymorphism with predictable overall monotropic behavior, *J. Pharm. Sci.* **104**, 4117 (2015).
- [139] B. Rini, O. Rixe, R. Bukowski, M. D. Michaelson, G. Wilding, G. Hudes, O. Bolte, H. Steinfeldt, S. D. Reich, and R. Motzer, AG-013736, a multi-target tyrosine kinase receptor inhibitor, demonstrates anti-tumor activity in a Phase 2 study of cytokine-refractory, metastatic renal cell cancer (RCC), *J. Clin. Oncol.* **23**, 4509 (2005).
- [140] L. J. Wilmes, M. G. Pallavicini, L. M. Fleming, J. Gibbs, D. Wang, K.-L. Li, S. C. Partridge, R. G. Henry, D. R. Shalinsky, D. Hu-Lowe, J. W. Park, T. M. McShane, Y. Lu, R. C. Brasch, and N. M. Hylton, AG-013736, a novel inhibitor of VEGF receptor tyrosine kinases, inhibits breast cancer growth and decreases vascular permeability as detected by dynamic contrast-enhanced magnetic resonance imaging, *Magn. Reson. Imaging* **25**, 319 (2007).
- [141] G. J. O. Beran, From polymorphs to cocrystals and salts: Successfully predicting axitinib's challenging crystal forms, *Chem. Sci.* **16**, 23026 (2025).
- [142] L. Yu, Polymorphism in molecular solids: An extraordinary system of red, orange, and yellow crystals, *Acc. Chem. Res.* **43**, 1257 (2010).
- [143] A. M. Campeta, B. P. Chekal, Y. A. Abramov, P. A. Meenan, M. J. Henson, B. Shi, R. A. Singer, and K. R. Horspool, Development of a targeted polymorph screening approach for a complex polymorphic and highly solvating API, *J. Pharm. Sci.* **99**, 3874 (2010).
- [144] I. Batatia, D. P. Kovacs, G. Simm, C. Ortner, and G. Csanyi, MACE: Higher order equivariant message passing neural networks for fast and accurate force fields, in *Advances in Neural Information Processing Systems*, Vol. 35, edited by S. Koyejo, S. Mohamed, A. Agarwal, D. Belgrave, K. Cho, and A. Oh (Curran Associates, Inc., 2022) pp. 11423–11436.
- [145] S. Rudtsch, Uncertainty of heat capacity measurements with differential scanning calorimeters, *Thermochim. Acta Developments in Calorimetry 2001*, **382**, 17 (2002).
- [146] J. P. Perdew and K. Schmidt, Jacob's ladder of density functional approximations for the exchange-correlation energy, *AIP Conf. Proc.* **577**, 1 (2001).